

WOFEX 2018

proceedings of the 16th annual workshop

Faculty of Electrical Engineering and Computer Science,
VŠB – Technical University of Ostrava

ISBN 978-80-248-4206-6

WOFEX 2018 wofex

<http://wofex.vsb.cz/2018/>

16th annual workshop,
Ostrava, 10th September 2018
Proceedings of papers

Organized by

VŠB – Technical University of Ostrava
Faculty of Electrical Engineering and Computer Science



WOFEX 2018

© Michal Krátký, Jiří Dvorský, Pavel Moravec, editors

ISBN 978-80-248-4206-6

This work is subject to copyright. All rights reserved. Reproduction or publication of this material, even partial, is allowed only with the editors' permission.

Page count: 310
Impression: 200
Edition: 1st
First published: 2018

This proceedings was typeset by pdfL^AT_EX.

Published by Faculty of Electrical Engineering and Computer Science, VŠB – Technical University of Ostrava

Preface

The workshop WOFEX 2018 (PhD workshop of Faculty of Electrical Engineering and Computer Science) was held on September 10th September 2018 at the VŠB – Technical University of Ostrava. The workshop offers an opportunity for students to meet and share their research experiences, to discover commonalities in research and studentship, and to foster a collaborative environment for joint problem solving. PhD students are encouraged to attend in order to ensure a broad, unconfined discussion. In that view, this workshop is intended for students and researchers of this faculty offering opportunities to meet new colleagues.

This book of proceedings includes 46 papers of faculty PhD students and 4 papers of external authors. The proceedings of WOFEX 2018 are also available at the web site <http://wofex.vsb.cz/2018/>. I would like to thank the authors and the Organizing Committee from Department of Computer Science, namely Jiří Dvorský and Pavel Moravec, for their arduous editing work.

September 2018

Michal Krátký
Program Committee Chair
WOFEX 2018

Organization

Program Committee

Chair:

Michal Krátký (VŠB – Technical University of Ostrava)

Members:

Pavel Brandštetter (VŠB – Technical University of Ostrava)

Radim Briš (VŠB – Technical University of Ostrava)

Zdeněk Dostál (VŠB – Technical University of Ostrava)

Petr Chlebiš (VŠB – Technical University of Ostrava)

Stanislav Rusek (VŠB – Technical University of Ostrava)

Václav Snášel (VŠB – Technical University of Ostrava)

Vladimír Vašínek (VŠB – Technical University of Ostrava)

Organizing Committee

Jiří Dvorský (VŠB – Technical University of Ostrava)

Pavel Moravec (VŠB – Technical University of Ostrava)

Hana Dluhošová (VŠB – Technical University of Ostrava)

Workshop Location:

Campus of VŠB – Technical University of Ostrava

17. listopadu 15, 708 33 Ostrava–Poruba, Czech Republic

10th September 2018

<http://wofex.vsb.cz/2018/>

Table of Contents

Study Programme P2649 Electrical Engineering

Electrical Power Engineering (3907V001)

Measurement of watchdog lighting system in the area of electric station TR Čechy střed	1
<i>Richard Baleja, Tomáš Novák, and Karel Sokanský</i>	
Testing software goniophotometer for the purpose of evaluating the generation of obtrusive light	7
<i>Petr Běčák, Tomáš Novák, and Karel Sokanský</i>	
An Estimation of Appliance Impact on Frequency and Power Factor Parameters in Micro-Grid Environment	13
<i>Vojtěch Blažek, Michal Petružela, and Jan Vysocký</i>	
Localization of Current Fields in the Vicinity of a Railway Platform	21
<i>Jiří Cigánek</i>	
Intelligent Model for Power Load Forecasting	27
<i>Ibrahim S. Jahan and Stanislav Mišák</i>	
Possibilities of Optimizing Maintenance Strategies Applicable on Electrical Network in the Czech Republic	33
<i>David Lazecký</i>	
Alternative energy sources comparison for heating a residential house	39
<i>Tomáš Machů</i>	
Research on the Combination of Biogas Station and Photovoltaic Power Plant Operation	45
<i>Ladislav Novosád</i>	
Reliability of the PV system operation influencing connection to the distribution network	51
<i>Petr Seroišzka</i>	

Electrical Machines, Apparatus and Drives (2642V004)

An Implementation of the DTC Method with Direct Calculation of Voltage Vector	57
<i>Jakub Bača</i>	
Sensorless Induction Motor Drive Based on CB-MRAS Observer	63
<i>Jakub Bača, Petr Chamrád, and Daniel Kouřil</i>	

Electronics (2612V015)

Malfunction Simulation for Combustion Engines Powermanagement Systems	69
<i>Tomáš Harach</i>	
The Control and Regulation Processes of Electronic Diesel Control Systems	75
<i>Tomáš Klein</i>	
System architecture of experimental electric vehicle	81
<i>Martin Kořený</i>	
Development of the Application Software for Electrohydraulic Brakes System of the Electric Vehicle Democar	86
<i>Samuel Przewczek</i>	
AC Link Converters	92
<i>Jan Strossa and Petr Chlebiš</i>	

Technical Cybernetics (2612V045)

A Fuzzy Evaluation of Quality of Color Vision Testing	98
<i>Monika Borová and Michal Prauzek</i>	
Design of fuzzy controller for simple inverted pendulum	104
<i>Tomáš Dočekal and Štěpán Ožana</i>	
Evaluation platform for quadcopter control design	112
<i>Matěj Golembiovský</i>	
Chaotic properties of human gait	118
<i>Radek Halfar</i>	
A Priority Driven Embedded Device	123
<i>Karolína Janošová and Michal Prauzek</i>	
Use of Independent Component Analysis for Fetal ECG Processing	129
<i>René Jaroš and Radek Martinek</i>	
Comparison of Effectiveness of Image Processing on Different HW Platforms	135
<i>Jakub Kolařík, Radek Martinek, Jakub Štefanský and Petr Bílík</i>	
Model for autonomous classification of stage of heel bone fracture treatment using fixator based on X-ray images and Time iteration segmentation model	142
<i>David Oczka</i>	
Skin pigment evaluation using image processing	147
<i>Tomáš Ondraczka</i>	

Use of the IQRF and Node-RED technology	153
<i>Jiří Škovránek</i>	

Emergency Record Digitalization Using NFC Tags	159
<i>Tomáš Urbanczyk</i>	

Study Programme P1807 Computer Science, Communication Technology and Applied Mathematics

Computer Science (1801V001)

Simulation of Transactions Behavior in IOTA Network	165
<i>Tomáš Janečko</i>	

The Method of Vertical Cuts (MoVC) in Action Recognition	171
<i>Radek Šimkanič</i>	

Crowd Sourcing as an Improvement of N-Grams Text Document Classification Algorithm	178
<i>Petr Šaloun, David Andrešič, and Barbora Cigánková</i>	

The Comparison of Windows API Functions Usage between Malware and Legitimate Applications	184
<i>Filip Zatloukal</i>	

Computational and Applied Mathematics (1103V036)

Quasilinear boundary problem with p-Laplacian	190
<i>Michaela Bailová</i>	

Classification problem with multinomial regression and random forests . . .	196
<i>Michal Běloch</i>	

Parareal: From ODE to PDE	201
<i>Ladislav Foltyn</i>	

Semi-smooth Newton Method for Solving the Stokes Problem with the Stick-slip Boundary Condition	207
<i>Radek Kučera and Jan Pacholek</i>	

Parallel Runge-Kutta method in nonadiabatic molecular dynamics	213
<i>Stanislav Paláček</i>	

New upper bounds for the orders of (k, g) -graphs	219
<i>Tom Raiman</i>	

Prediction models in medical data analysis: methodology overview	224
<i>Adéla Vrtková</i>	

Orientations of Almost Regular Graphs	230
<i>Jakub Závada, Petr Kovář, Michal Kravčenko, Matěj Krbeček, Michael Kubesa, and Adam Silber</i>	

Communication Technology (2601V018)

Optical Vehicle-to-Vehicle (V2V) Communication: Analysis of Beam Homogeneity DRL Jaguar XK	235
<i>Peter Hajduk and Vladimír Vašínek</i>	

Implementation of a Thermally Loaded EDFA Amplifier into a WDM-PON Optical Network	240
<i>Jakub Kolář, Jan Látal, Anirban Dhar, and Zdeněk Wilček</i>	

Measurement of bulb lamp parameters made from PDMS and luminophore	246
<i>Martin Novák</i>	

YAG:Ce Phosphor Powders in Visible Light Communication Systems	252
<i>Tomáš Stratil, Jan Vitásek and Vladimír Vašínek</i>	

Measurement of IPTV qualitative parameters on EPON/VDSL2 topology	259
<i>Zdeněk Wilček and Jan Látal</i>	

Path Loss Predictions	265
<i>Yahia Zakaria, Lubomír Ivánek</i>	

The fiber-optic sensor as a detector of weak seismic waves	271
<i>Stanislav Žabka</i>	

External Authors

Use of a Flying Platform for Measuring of Electromagnetic Fields	276
<i>Lukasz Miszuda</i>	

Spectral analysis of high-voltage lines surroundings	282
<i>Jakub Osuchowski</i>	

Analysis of Improvement in Reaction Time With Prolonged Use of Android System Devices	288
<i>Agnieszka Rozanska</i>	

Crypto Mining Energy Consumption Problem	292
<i>Stawomir Szymocha</i>	

Author Index

Measurement of watchdog lighting system in the area of electric station TR Čechy střed

Richard Baleja, Tomáš Novák, and Karel Sokanský

Department of Electrical Power Engineering, FEECS,
VŠB – Technical University of Ostrava, 17. listopadu 15,
708 33 Ostrava – Poruba, Czech Republic
ba10034@vsb.cz

Abstract. The use of camera and security systems has been becoming a standard part of facilities equipment. Companies protect their property against potential damage and theft and also want to have information about who, when and where was located. These systems are especially used to protect strategic objects whose threat or destruction would have an obvious impact on a society. This group of buildings clearly includes electric stations where the eventual shutdown or destruction would result in a power outage in the regions or a total blackout of the whole country. Therefore, when designing security and camera systems, consideration should be given to all possibilities of space disturbance and to designing the system so that any intruder can be detected in time. In this paper, we will deal in detail with the watchdog lighting system of an electric station that works together with security camera systems.

Keywords: Luminance Camera, Colour Rendering Index, Watch Lighting System.

1 Introduction

The high-quality design of the lighting systems in the area of electric station is important especially for safety reasons. It is about the safety of the whole electric station, which should be protected against potential intruders, as well as the safety of employees who have to move in places with high voltage. This is not just a design watchdog lighting project to ensure the proper functioning of the security cameras, but also the design of lighting systems, whose role is to illuminate individual areas within the station. For example, these are entrance gates, roads, transformers and various measuring devices that need to be checked regularly. Lighting requirements are often very specific, and therefore, when designing the watchdog lighting systems, it is necessary to respect, in addition to Czech technical standards, technical standards that deal with the issue in more detail. ČEPS, a.s. in cooperation with VŠB TU - Ostrava, worked out a technical standard, which deals with the lighting issues at the premises of electric stations. This standard is available under the designation

TN/59/2016 Revision 3 Venkovní a vnitřní osvětlení v objektu elektrických stanic PS. According to this standard, outdoor lighting in electric stations is divided into three types, such as watchdog lighting, road lighting and operational lighting. This standard defines the requirements of each type of the lighting system and also describes its correct design.

2 Watchdog lighting and lighting requirements

Luminaires for public lighting are used for a watchdog lighting systems, either with high-pressure sodium lamps or with LED. The watchdog lighting serves to illuminate the perimeter of the premises of the electric station in order to ensure the functionality of the security camera systems of the security guard. The watchdog lighting is installed along the entire fence of the electric station, including the entrances to the houses and the central house, the entrances and along the fencing, which separates the foreign legal entity from ČEPS premises. Luminaires with the photometric distribution curve for public lighting systems are used for illuminating the strip along the fencing to provide the watchdog lighting system. The lighting points are located inside a station 2,5 to 4 meters from the fence. Luminaires are directed towards the fence.

Requirements for the watchdog lighting system are defined according to the technical standard TN/59/2016 of revision No. 3 as follows: the average maintained vertical illumination must be at least 10 lx. The illumination is evaluated from the point of view of the security camera at a height of 1 m above the terrain. The average maintained horizontal illumination of the reference section between the two light points must be at least 10 lx. Uniformity requirements for both cases are $U_o = 0.4$. The limit value of the glare rating limits GRL shall not be greater than 45. The colour rendering index of the lighting sources used must be at least 20. When lighting is proposed, it is recommended that the luminaires be placed in a higher vertical level as a security camera. Luminaires must be placed in such a way that they do not cause the camera to glare and cause the camera to pass into a saturated state.

The functionality of security cameras is that it picks up the luminances of illuminated objects. The greatest luminance is achieved when the luminous flux enters the illuminated object from the viewpoint of the camera. Standard cameras have a minimum sensitivity for colour mode $E = 0.4$ lx and for black and white mode $E = 0.05$ lx. This is illumination on the chip of security camera. In order to ensure the optimal and correct functioning of the camera and the contrast, it is necessary that the illumination value for the colour mode is at least 15 lx and for black and white 10 lx. This illumination must be at least 70% of the area occupied by the scene. To avoid overturning, and thus reduce an image resolution, it is necessary to balance the illumination, i.e. the ratio of maximum intensity to minimum intensity, in a ratio of 6: 1, at 4: 1 (zoomed out) points.

3 The measurement of watchdog lighting

In order to verify the quality of the proposed lighting systems, the light parameters are measured. The measurement is always carried out after eclipse to avoid the contribution of daylight. The measurements include all spaces and places that are in the electric station. These are premises of transformers, measuring devices, roads and so on.



Fig. 1. Area of TR electrical station TR Čechy střed

Several light parameters are measured for watchdog lighting system. It is the camera illuminance (vertical illuminance of the camera), the horizontal illuminance at ground level and the measuring of luminances from the view of the security camera. The values of illumination are measured using a luxmeter. The measurement of the vertical illumination is providing by using a tripod. Luminances are measured using a luminance camera located as close as possible to the security camera. From this position, the luminance analyses are made for the different distance of the figures from the security camera. The measurement of the lighting parameters was carried out at the electric station TR Čechy střed. The area of the electric station is illustrated in Figure 1. The red colour shows the line of the watchdog lighting. The yellow colour mark the areas of the electric substations, transformers and roads where the horizontal illumination was evaluated.

Due to the same height of luminaires and their pitch, only the reference sections were selected for the measurement. The position of the reference sections is marked in figure 1. (sections 2A, 2B and 2C).



Fig. 2. Watchdog lighting system in the area of electric station

As was mentioned above, the proper function of the security cameras depends on the luminances of objects. For this reason, the quality of the watchdog lighting was also verified by means of a luminance camera. The luminance camera was placed in the approximate position of the security camera so that the observation conditions of the luminance camera corresponded to the monitoring conditions of the security camera.

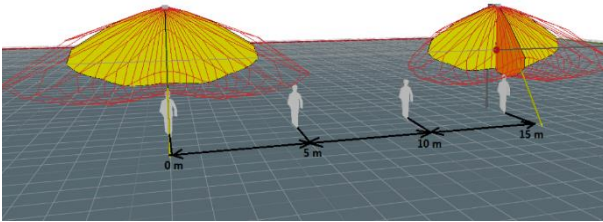


Fig. 3. Schematic outline of figures positions for the measurement of luminance analysis

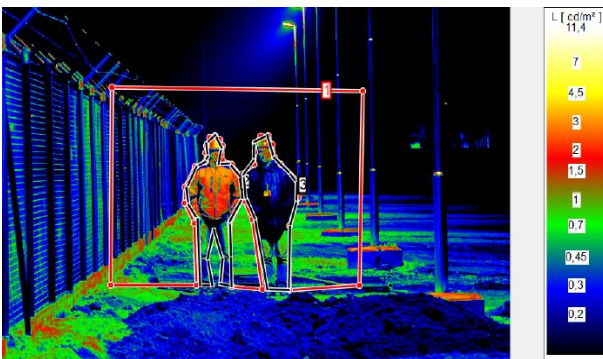


Fig. 4. Schematic outline of figures positions for the measurement of luminance analysis

To evaluate the luminance analysis, figures with different garment reflections, which gradually changed their positions at a spacing of approximately 5 m were used. For each reference section of the watchdog lighting, the luminance analysis was made for 4 positions of the figure. An example of the luminance analysis of the figures is shown in figure 4. The figure with a lighter clothing is placed on the left; the figure with a dark clothing is placed on the right. The following figure 5 shows a record from the security camera.



Fig. 5. Record from the security camera

Table 1. Calculated values from the luminance analysis of the figures on the position 2 according to figure 3.

	Luminance analysis of figures				
	<i>Average luminance of figurine</i>		<i>Average background luminance (cd/m²)</i>	<i>Contrast of figures and background</i>	
	<i>Left (cd/m²)</i>	<i>Right (cd/m²)</i>		<i>Left (-)</i>	<i>Right (-)</i>
<i>Position 2</i>	<i>1,14</i>	<i>0,31</i>	<i>0,33</i>	<i>2,45</i>	<i>0,06</i>

4 Conclusion

From the measured luminance analyses of the figures in the field of vision of the security camera, the contrasts between the background and the figurines were calculated. The calculated contrasts between the figure and the background are relatively low, so in some cases recording and recognizing pedestrians in the field of vision of the security camera can be difficult. From the measurements of the luminance contrast and based on the measured vertical illuminances of figures, in the case of measurements on the reference section 2A, 2B and 2C, it is obvious that the highest luminances values, contrast and also vertical illumination take the figures in position 2. For

designing watchdog lighting systems, it is preferable to use LED luminaires for better distribution of luminous flux through the lens. These days a large number of luminaires with different photometric distribution curves are available on the market. They are capable of distributing the luminous flux so that it can be used with the highest possible efficiency.

References

1. Technical standards of ČEPS a.s., TN/59/2016 Revision 3 Venkovní a vnitřní osvětlení v objektu elektrických stanic PS and is valid from 1.5.2016.
2. Ullman, I., Bos, P., Ullman, J.,: New outdoor lighting-Operation and maintenance, 17th International Scientific Conference on Electric Power Engineering, 2016, art. no. 7521823, ISBN 978-150900907-7.
3. Bos, P., Baleja, R., Sokanský, K., Novák, T., Ullman, I., New outdoor lighting-Operation and maintenance, 17th International Scientific Conference on Electric Power Engineering, 2016, art. no. 7521823, ISBN 978-150900907-7.

Testing software goniophotometer for the purpose of evaluating the generation of obtrusive light

Petr Běčák, Tomáš Novák, and Karel Sokanský

Department of Electrical Power Engineering, FEECS,
VŠB – Technical University of Ostrava, 17. listopadu 15,
708 33 Ostrava – Poruba, Czech Republic
petr.becak@vsb.cz

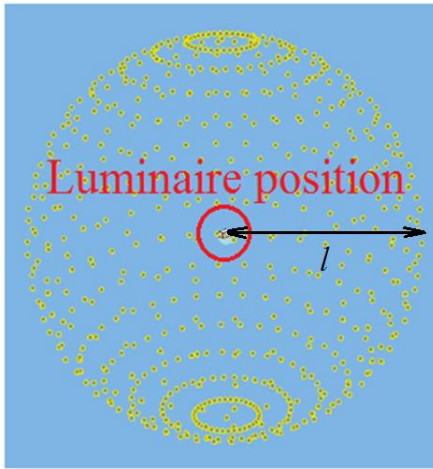
Abstract. The article focuses on a new methodology that can model the luminous flux generated on the night sky (the so-called obtrusive light). Specifically, it deals with the verification of the newly designed software goniophotometer implemented in Astra MS Software's - Building Design software. In particular, it is possible to calculate the emission of the luminous flux (direct and indirect) going into the upper half-space from lighting systems not only from public lighting. The first part of the paper deal with the verification of the software goniophotometer functionality by calculating the direct and indirect (reflected) component of the luminous flux. The superstructure was conceived as the possibility of inserting a network of calculating points in the shape of a sphere. The individual calculation points showing normal illuminance towards the centre of the sphere and can be imagined as a lux meter sensor. The main goal is calculating the radiation of the liminous flux flowing into the upper half-space from the outdoor lighting systems. It will be the basis for further astronomical calculations that focus on obtrusive light and increased sky luminance. Based on the testing, it will be possible to create model of lighting system in some city or district of the city by inserting LDT data of real luminaires, thus creating a real lighting system with real building models. From the resulting model, it will be possible to quantify the proportion of the direct and indirect luminous flux flowing into the upper half-space.

Keywords: software goniophotometer, luminous intensity curves, direct luminous flux, indirect (reflected) luminous flux, upper half-space, obtrusive light

1 Introduction

VŠB-TUO in cooperation with Astra MS Software, it was possible to insert computational points network in the shape of a sphere with computational points showing normal illumination in the direction to the center of the sphere. The system thus designed duplicates the function of a real goniophotometer, a photometric laboratory instrument that measures luminous intensity or luminous intensity curves [2]. The principle of a goniophotometer is that it allows to measure the luminous intensity in

different planes and at different angles, which can be easily interpreted by a sphere with a network of calculation points. The density of the calculation points can be entered in an angular step according to the standard luminaire measurement plan C, γ . The software goniophotometer principle is based on square law, as shown in the figures below.



$$E = \frac{I}{l^2}$$

E...Illuminance (lx)
I...Luminous intensity (cd)
l...Distance (m)

Fig. 1. Software goniophotometer principle with luminaire and square law.

All calculations in the program testing and computational procedures were performed with a maintenance factor of 1 so that input and output data could be compared, in particular from the point of view of the energy conservation law, and there was no aging of the luminaires and light sources [1].

2 Verifying the programme function – Measuring the direct component of luminaire luminous flux

Verification of the programme functionality was solved by comparing the luminous intensity curve of selected luminaire with that of the luminaire generated by a software goniophotometer. Comparison was made from the viewpoint of verifying the shape of the luminous intensity curve and from the viewpoint of the total luminous flux that is generated in the space from the obtained LDT data. LDT data represents Eulumdat photometric data of luminaires.

For the purpose of comparing the functionality of the program, the VYRTYCH 1VV-70S-DINGO-E was fitted with a 70 W high-pressure sodium discharge lamp. The luminaire has radiation pattern corresponding to the classical pattern of the street lighting luminaire, shown in Figure 2.

For the verification of the properties of the computational programme, the above specified luminaire was placed in the centre of the sphere formed by the calculation points distributed in planes C0 - C180 and C90 - C270 by 5 ° and in gamma planes

also by 5° . The radius of the computing sphere has been selected at 10 m so that the tested luminaire can be viewed as a point source. This was shown in Figure 1.

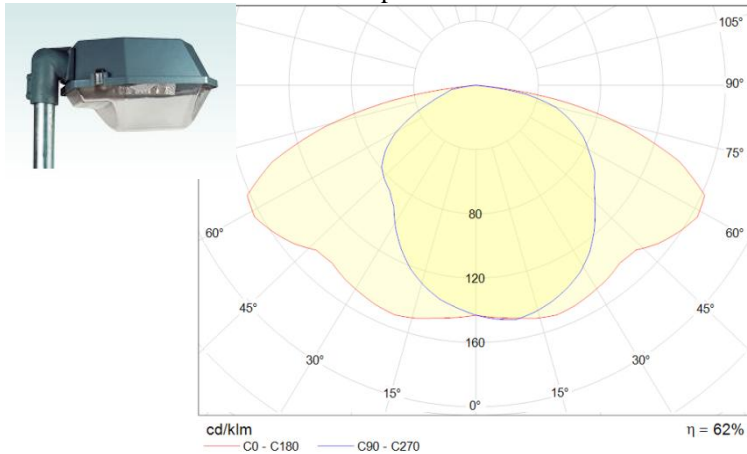


Fig. 2. Radiation pattern of the luminaire from manufacturer's LDT data, which was also verified during testing.

From the above-mentioned lighting and technical parameters of the original luminaire and the lighting and technical parameters of the luminaires obtained from a software goniophotometer, the following can be stated to verify the behaviour of the programme:

- By comparing the luminous flux of the original luminaire (3450 lm) and the luminous flux obtained by the method of the band factors from the luminous intensity curve of the newly measured (3390 lm) we concluded that the deviation at the above-described density of the calculation points is less than 2 %. This deviation is not determined by its own calculation, but by choosing the density of the calculation points and then converting the luminous flux from the luminances into the individual solid angles [3].
- Shape and size of luminances of the calculated radiation pattern corresponds to the original radiation pattern (shown in Figure 2) and it can be stated that the deviations from the original values are minimal and the behaviour of network of the calculation points can be also attributed. [1]

3 Verifying the programme function – Measuring the indirect (reflected) component of luminaire luminous flux

In the future, the purpose of this application is to use the calculation points for modelling radiation of luminous flux spreading into the upper half-space from outdoor lighting systems as the basis for further astronomical calculation [4] that focus on disturbing light and increased sky brightness. Therefore, it is necessary to address not only the direct component but also the component reflected from the objects located near the lighting systems. Verification of software function was also done using the calcu-

lation with the reflected luminous flux component for the identical luminaire tested for the direct component of the luminous flux, i.e. the VYRTYCH 1VV-70S-DINGO-E luminaire. The number of reflections was set to 3 in the software, which is sufficient enough for testing. The calculation points distributed in the planes were the same as the previous case. For the model, a reflecting surface with 100% reflection was used to avoid any loss during luminous flux reflection and total luminous flux coming out into the combination luminaire-reflective material was the same as the luminous flux coming out of the luminaire located in a system 1 m above the reflecting surface. Larger distance from a reflective surface (2 m or more) would result in a direct luminous flux in the half-space, which would be undesirable for the experiment. Due to the expected diffuse reflection of the simulated reflective area, we also expected a substantial change in radiation pattern from lower half-space radiation to upper half-space radiation, and a change in shape of the radiation pattern from wide pattern for street lighting to a pattern that approaches a diffusive radiator.

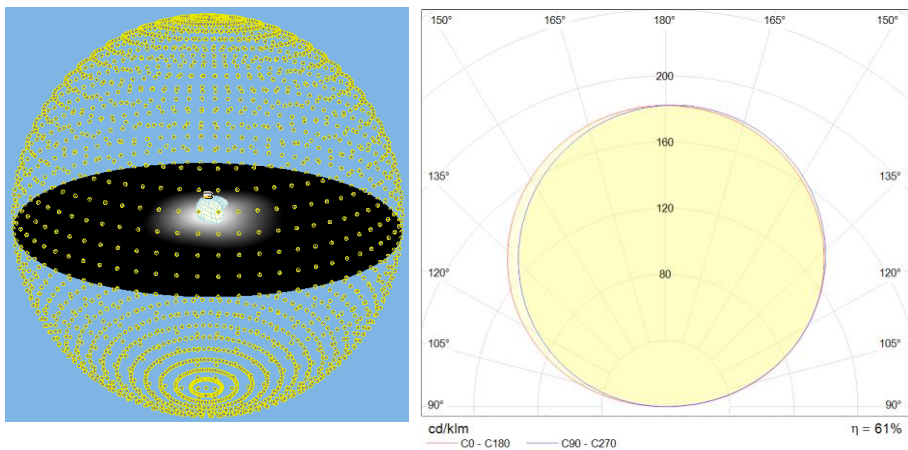


Fig. 3. Model situation of luminaire location against illuminated surface and radiation pattern of the fictitious luminaire into the upper half-space.

Based on the luminance data obtained from software goniophotometer for individual planes, the radiance pattern of the fictitious luminaire was obtained, all of whose luminous flux was reflected in the upper half-space where it was captured by the spherical computing network of the software goniophotometer. This pattern is illustrated in the Figure 3 (right).

- By comparing the luminous flux of the original luminaire (3450 lm) and the luminous flux obtained by the method of the band factors from the luminous intensity curve of the newly measured (3410 lm) we concluded that the deviation at the above-described density of the calculation points is again less than 2 %. This deviation is not determined by its own calculation, but by choosing of the calculation points, the dimensions of reflecting surfaces, and then converting the luminous flux from the luminances into the individual solid angles.

- Shape and size of luminous intensities of the calculated radiation pattern corresponds to the assumptions. The calculated luminous intensity curve radiates only to the upper half-space, and its shape approaches the diffusive (cosine) radiator. Expected deviations from the shape of the cosine function are visible from the curve unbalance and is caused by the unbalanced light radiation of the luminaire, and by using the reflective surface throughout the examined radius, the resulting combination of light radiation of luminaire and reflective surfaces does not act as a point source.[1]

4 Conclusion

Based on the above-mentioned testing, it has been confirmed that various lighting systems, or light sources, can be modeled and evaluate the extent to which are involved in the luminous flux generated on the sky. It is supposed, that the most important part of the obtrusive light is the lighting systems of the public lighting. However, other sources such as advertising areas - billboards, windows, headlamps of some cars, and so on need to be implemented in the calculations. The figure below shows an example of a real housing estate model with a real distribution of the lighting system made up of almost 200 public lighting luminaires. The luminaires are modeled and inserted using the manufacturer's LDT data, which is necessary for this calculation. The potential sources of obtrusive light mentioned above will be inserted into this model in the future.

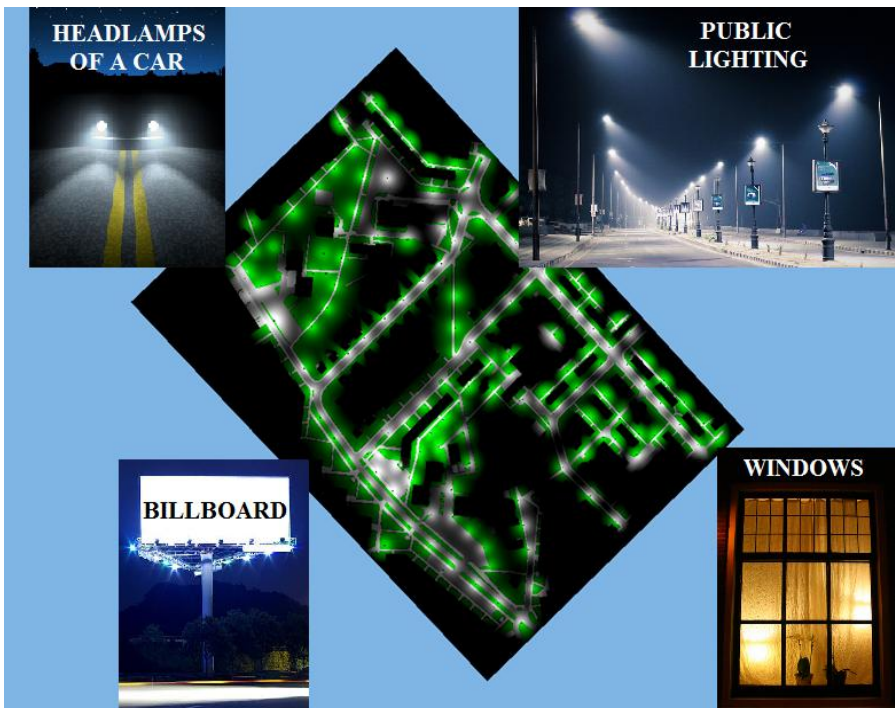


Fig. 5. Radiation of the luminous flux of a real housing estate model fitted by public lighting with an example of other possible sources of obtrusive light.

This example of the model situation helps to get an overview of the percentage of the luminous flux spreading into the upper half-space. Based on this model, it is possible to recalculate direct and reflected component of the luminous flux going into the upper half-space and also monitor the power consumption such lighting systems. We can also replace the sodium lighting system with the modern LED lighting system [5], [6] with the appropriate parameters and monitor the differences in radiated luminous flux into the upper half-space.

5 Acknowledgment

The article was prepared with the support of the SGS SP2018/117 - BroadbandLIGHT - Public Lighting in SMART City and VI20172019071 - Analysis of Visibility of Transport Infrastructure for Safety Increasing during Night, Sunrise and Sunset

6 References

- [1] P. Becak, T. Novak, R. Baleja, K. Sokansky, "Testing of the software goniophotometer in Wils - Building design computational programme", 2018, 19th International Scientific Conference on Electric Power Engineering, EPE 2018, DOI: 10.1109/EPE.2018.8395994
- [2] J. Sumpich, T. Novak, Z. Carbol, K. Sokansky, "Software calculation tool for light savings in the buildings compared with real measured data", 2013, 14th International Scientific Conference on Electric Power Engineering 2013, EPE 2013, Pages 677-680
- [3] L. Lipnický, D. Gašparovský, R. Dubníčka, "Influence of the calculation grid density to the selected photometric parameters for road lighting", Proceedings of 2016 IEEE Lighting Conference of the Visegrad Countries, Lumen 2016 Karpacz, Poland, DOI: 10.1109/LUMENV.2016.7745555
- [4] M. Kocifaj, F. Kundracik, "Modeling the night sky brightness distribution via new SkyGlow Simulator", Proceedings of 2016 IEEE Lighting Conference of the Visegrad Countries, Lumen 2016 Karpacz, Poland, DOI: 10.1109/LUMENV.2016.7745553
- [5] T. Pavelka, M. Ptacek, P. Baxant, "Static model of LED behaviour depending on operating conditions", Published in: Electric Power Engineering (EPE), 2016 17th International Scientific Conference, 2016 Prague, Czech Republic, DOI: 10.1109/EPE.2016.7521774
- [6] P. Žák, S. Vodráčková, "Conception of public lighting", Proceedings of 2016 IEEE Lighting Conference of the Visegrad Countries, Lumen 2016 Karpacz, Poland, DOI: 10.1109/LUMENV.2016.7745514

7 Publications

P. Becak, T. Novak, R. Baleja, K. Sokansky, "Testing of the software goniophotometer in Wils - Building design computational programme", 2018, 19th International Scientific Conference on Electric Power Engineering, EPE 2018, DOI: 10.1109/EPE.2018.8395994

An Estimation of Appliance Impact on Frequency and Power Factor Parameters in Micro-Grid Environment

Vojtěch Blažek, Michal Petružela, and Jan Vysocký

Department of Electrical Power Engineering, FEECS,
VŠB – Technical University of Ostrava, 17. listopadu 15,
708 33 Ostrava – Poruba, Czech Republic
{vojtech.blazek, michal.petruzela, jan.vysocky}@vsb.cz

Abstract. Nowadays, for many people living in a remote area, powering their homes or small businesses using a small renewable energy system that is not connected to the electricity grid is becoming an interesting option. Today, these systems can be driven by algorithms based on intelligent data-analysis methods, real-time optimizations, and predictive models. Systems, which use these algorithms, are called the Smart Grids. The smart-grid technology makes the electricity generation and consumption to be more effective, it has the potential to reduce greenhouse-gasses emissions and to improve environmental quality. For the correct design of the control algorithm, we need the appropriate data off the behavior of each device connected to the electrical system. Our paper presents an analysis of the various appliances impact on an off-grid electrical system. This analysis shows how the appliances affect frequency (FREQ) and power factor (PF) in an off-grid electrical system. The results of this analysis will be used to improve the control algorithm of the off-grid electrical system located on campus VŠB – Technical University of Ostrava.

Keywords: Off-grid electrical system, Frequency, Power factor, Power quality

1 Introduction

Our vision is that the off-grid system will become a fully autonomous energy platform with energy supply from the renewable sources (RESs) and with an application of an energy storage system. Now the platform is in development.

The stochastic character of the RESs which are system's source part causes the presence of a low to short-circuit power, which decreases the stability of power quality (PQ) parameters like the off-grid-system frequency (FREQ) [1], [2]. Part of the development is the measurement of the appliance behavior in this system.

Our objective is to find out which appliances have the impact on FREQ and power factor (PF) in the Off-grid system. This knowledge is important to be able to avoid poor PQ parameters. Poor PQ parameters may affect the operation of the other devices connected to the Off-grid [3]. The concept was proposed and designed in a study by Mišák

[4] [5]. This concept was titled as Active Demand Side Management (ADSM). ADSM includes the power quality forecasting module proposed by Vantuch et al. [5].

2 EXPERIMENT DESCRIPTION

Table 1. Feature values of the applied appliances further used for the estimation of their relevance

Appliance	Load (W)			PF	Characteristic			Power supply	
	avg	min	max		avg	Induc- tive	Capaci- tive	Resis- tive	Conti- uous
Mower	537.60	532.10	549.27	0.52	True	False	False	True	False
Drill	157.10	149.50	167.00	0.49	True	False	False	True	False
Kettle	619.10	617.00	628.30	1.00	False	False	True	True	True
Fridge	207.60	195.50	219.50	0.72	True	False	False	True	False
Switched mode power supply	410.00	409.70	420.20	0.78	False	True	False	True	True
AC heating	880.00	852.50	910.00	0.91	True	False	False	True	False
Micro- wave	203.00	76.80	1348.30	0.84	True	False	False	False	False
Boiler	307.00	305.80	346.50	0.99	False	False	True	True	False
TV	44.00	42.80	50.50	0.60	False	True	False	True	True
Lights	156.00	152.50	165.10	0.84	False	True	False	True	True

In the experiment, we used ten various usual appliances (see table 1) to create 120 combinations of three. There were always three appliances turned on because only one running appliance is uncommon in a house. Every combination was switched on at a defined time. Each combination was measured for 12 minutes. We omitted the first and last minute as a transient phenomenon. Appliances were supplied by batteries without connection to the external grid and RESs. During measure intervals, we measured PF and FREQ. When the measured interval had ended, batteries were charged from the external grid. Battery charging time was 18 minutes long to ensure that the desired state of charge (SoC) was always reached.

FREQ and PF values were measured by the power analyzer KMB SMC 144 with a one-minute timescale. For further analysis, we stored minimum, average and maximum measured values. We measured all combinations at two different battery SoCs (fully and half charged). At first, we measured system parameters with fully charged batteries (see table 1).

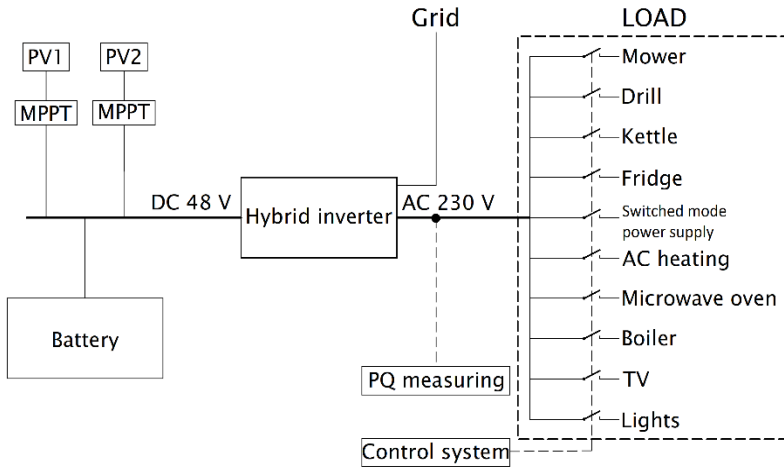


Fig. 1. Off-Grid scheme

The off-grid system under normal conditions is powered by two 2-kWp photovoltaic panels and NiCd batteries KPL 375 FERAK (see figure 1). The capacity of each battery is 375 Ah and the nominal voltage is 1.2 V. A total of 40 batteries are connected in series. Batteries are connected to DC bus. Photovoltaic panels and inverter Conext XW+ 8545 are also connected to this DC bus. This hybrid inverter transforms direct current to the alternating one for the appliances connected to Off-grid. The nominal power of the hybrid inverter is 6.8 kW. The grid's AC part and local appliances are connected to the hybrid inverter via a switchboard. The switchboard is controlled by a control system which utilizes an exact switching schedule. A power analyzer measures on the AC output of the hybrid inverter.

3 TESTING AND RESULTS

3.1 Power factor

Fig. 2 and fig .3 show PF values of each combination measured with the half and fully charged batteries.

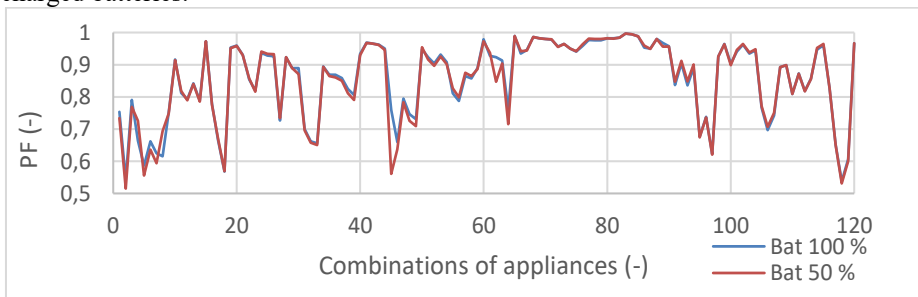


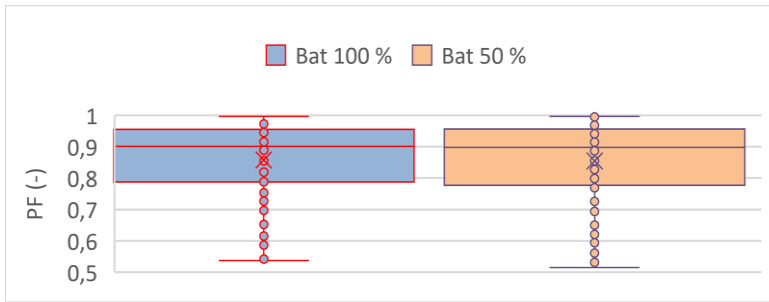
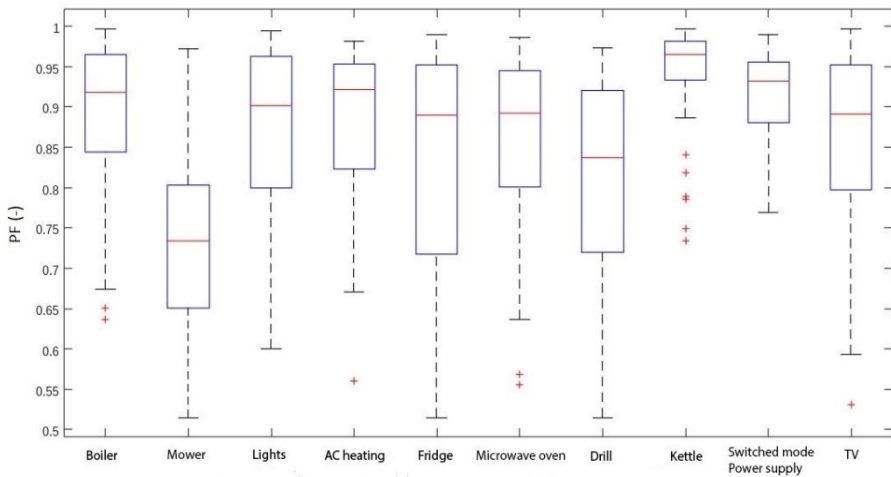
Fig. 2. Measured PF values**Fig. 3.** Box plot of measured PF values

Fig. 4 and fig. 5 show the data series of average PF values for SoC 50% and 100%. These data points were calculated for the individual measurement periods (each data point is calculated as the average value of one measurement-period values). Since the system was loaded by three different appliances during each measurement period, the average PF value is calculated for one given period and then it is assigned to the data series of all three appliances that were connected to the electrical system in the given period. Each appliance was switched on in 36 periods of total 120 periods.

**Fig. 4.** Box plot for all used appliances – impact of appliance operation on PF, SoC 50%

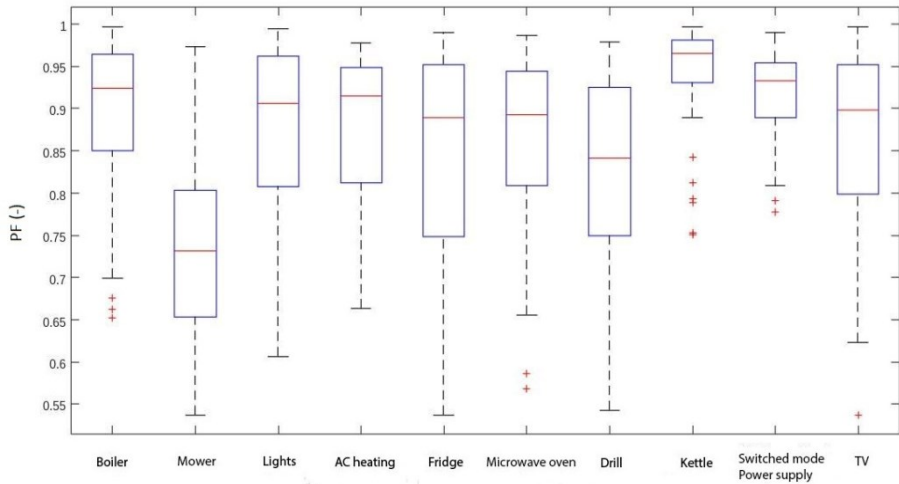


Fig. 5. Box plot for all used appliances – impact of appliance operation on PF, SoC 100%

Table 2 shows the arithmetic average of PF values of each combination for individual appliances.

Table 2. Arithmetic average of average power factor values for individual appliances during measurement

Appliances	Power factor (-)	
	SoC 100%	SoC 50%
Kettle	0.935	0.935
Switched mode power supply	0.914	0.913
Boiler	0.890	0.887
AC heating	0.873	0.875
Lights	0.870	0.869
TV	0.858	0.853
Microwave oven	0.857	0.854
Fridge	0.837	0.829
Drill	0.820	0.808
Mower	0.726	0.725

3.2 Frequency

Fig. 6 and fig. 7 show FREQ values of all combinations measured with the half and fully charged batteries. Measured FREQ values range from 50.0071 Hz to 50.0073 Hz for SoC 100% and from 50.0022 Hz to 50.0072 Hz for SoC 50%. Fig. 6 shows that the

average value of the frequency fluctuates more at SoC 50% than at SoC 100%. Measured FREQ values are in accordance with European Standard EN 50160: 2010 + A1: 2015.

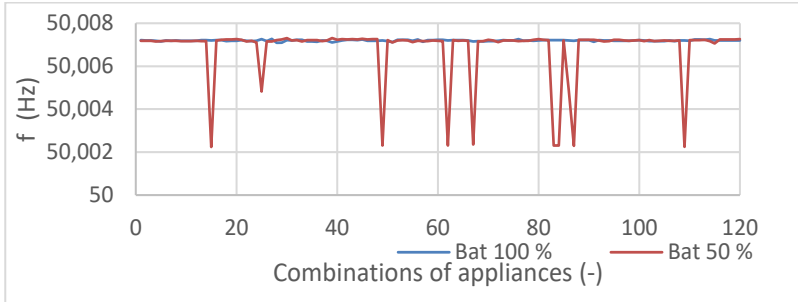


Fig. 6. Measured FREQ values

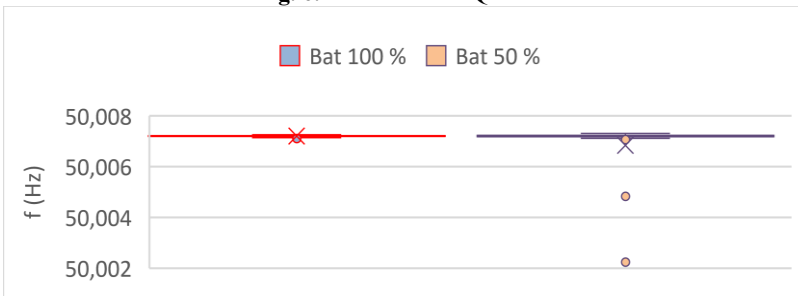


Fig. 7. Box plot of measured FREQ values

Fig. 8 and fig. 9 show the data series of average FREQ values for at SoC 50% and 100%, the data are presented for individual appliances. These data series were calculated analogously like the data series presented in fig. 4 and fig. 5.

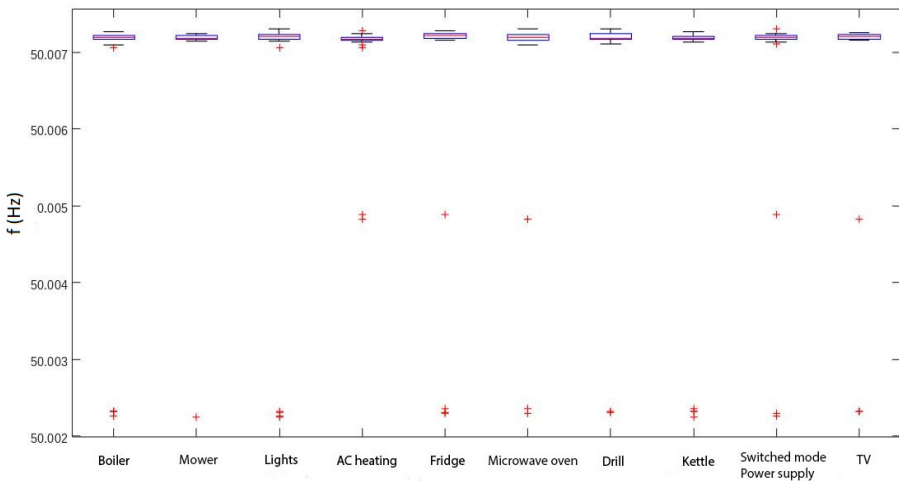


Fig. 8. Box plot for all used appliances – impact of appliance operation on FREQ, SoC 50%

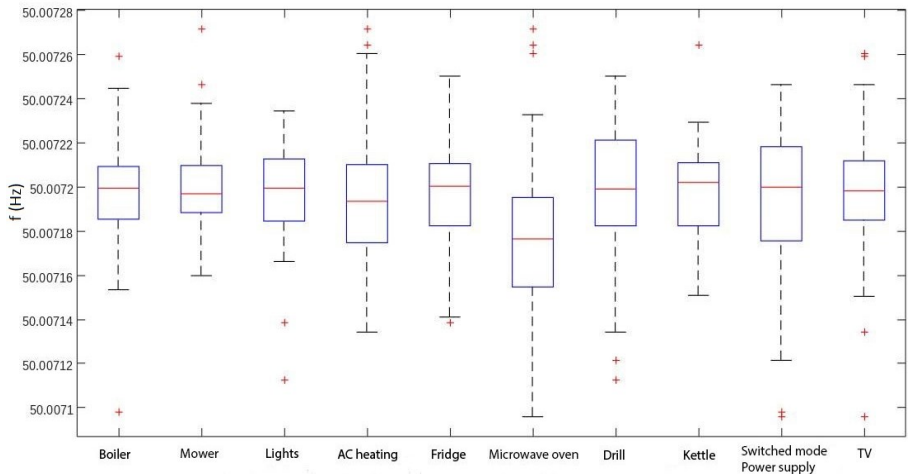


Fig. 9. Box plot for all used appliances – impact of appliance operation on $FREQ$, SoC 100%

Table 3 shows the arithmetic average of $FREQ$ values of each combination for individual appliances.

Table 3. Arithmetic average of average frequency for individual appliances during measurement

Appliances	Frequency (Hz)	
	SoC 100%	SoC 50%
Kettle	50.0072	50.0067
Switched mode power supply	50.0072	50.0069
Boiler	50.0072	50.0067
AC heating	50.0072	50.0070
Lights	50.0072	50.0067
TV	50.0072	50.0069
Microwave oven	50.0072	50.0069
Fridge	50.0072	50.0067
Drill	50.0072	50.0069
Mower	50.0072	50.0071

4 DISCUSSION AND CONCLUSIONS

The composition of turned-on appliances combination has minimal impact on $FREQ$ and PF and observed changes of these quantities' values were statistically insignificant. During the measurement at both SoCs 100% and 50%, the lowest PF value was measured when the electric mower was turned on, whilst the highest PF value was measured

when the kettle was turned on. This is in accordance with a generally considered assumption that the kettle is a resistive load. The comparison of the measured PF values indicates that the difference of the impact of the various-appliances operation on this quantity value for the system at SoC 50% or 100% is small and statistically insignificant. The impact on FREQ value is also small and statistically insignificant. Measured FREQ values are in accordance with European Standard EN 50160: 2010 + A1: 2015.

The longer-time measurement within a shorter time-scale will be our future work. This measurement should give us more precise values for further processing. Another task is to increase the number of used appliances number and perform new combinations. Our hybrid inverter has a nominal power of 6.8 kW and the power input of the largest load which was turned on during the measurement was 1.8 kW, so the inverter was operating in low load area.

Acknowledgment

This paper was supported by the following projects: LO1404: Sustainable development of ENET Centre; CZ.1.05/2.1.00/19.0389 Development of the ENET Centre research infrastructure; SP2018/58 Students Grant Competition and TACR TH01020426, Czech Republic and the Project LTII7023 "Energy Research and Development Information Centre of the Czech Republic" funded by Ministry of Education, Youth and Sports of the Czech Republic, program INTER-EXCELLENCE, subprogram INTER-INFORM.

References

1. Eckbert, D., Larsson-Edefors, P.: Interconnect-driven short-circuit power modeling. In: Digital Systems Design. Euromicro Symposium, pp. 414-421. IEEE (2001).
2. Saradarzadeh, M., Farhangi, S., Schanen, J.-L., Jeanin, P.-O., Frey, D., Combination of power flow controller and short-circuit limiter in distribution electrical network using a cascaded h-bridge distribution static synchronous series compensator. In: IET Generation, Transmission & Distribution, vol. 6, no. 11, pp. 1121-1131, IET Digital Library (2012)
3. Bhattacharyya, S., Myrzik, J. and Kling, W., Consequences of poor power quality – an overview. In: Universities Power Engineering, UPEC 2007 42nd international conference on, pp. 651-656. IEEE (2007)
4. Mišák, S., Stuchlý, J., Platoš, J., Krömer, P.: A heuristic approach to active demand side management in off-grid systems operated in a smart-grid environment. Energy and buildings, vol. 96, pp. 274-284 (2015).
5. Mišák, S., Stuchlý, J., Vramba, J., Prokop, L., Uher, M., Power Quality Analysis in Off-Grid Power Platform
6. Vantuch, T., Mišák, S., Jeżowicz, T., Buriánek, T., Snášel, V., The power quality forecasting model for off-grid system supported by multiobjective optimization. In: IEEE Transactions on Industrial Electronics, vol. 64, no. 12, pp. 9507-9516 (2017).

Localization of Current Fields in the Vicinity of a Railway Platform

Jiří Cigánek

Department of Electrical Engineering, FEECS,
VŠB – Technical University of Ostrava, 17. listopadu 15,
708 33 Ostrava – Poruba, Czech Republic
jiri.ciganek.fei@vsb.cz

Abstract. The article deals with an examination of current fields in the vicinity of a railway platform of the SUDOP type. It compares a fault-free state in which the rail is connected with a gabion through a lightning arrester and a case in which there occurs a breakdown of the lightning arrester.

Keywords: platform; current density; rail; gabion

1 Introduction

The occurrence of the so-called stray currents represents a major problem in the vicinity of a railway track. Stray current is a current which passes from a rail during the crossing of a railway vehicle into the earth and returns back to the power supply station. These currents disrupt concrete foundations in the vicinity of the railway substructure. Station platforms are some of the places through which these currents pass. This contribution deals with an examination of these fields in the railway platform of the SUDOP type. It compares a fault-free state in which a rail is connected with a gabion through a lightning arrester by means of a conductor and a case in which there occurs a breakdown of the lightning arrester. In this case there therefore occurs a significant voltage surge in the gabion and thus also passage of stray currents.

The term “platform” refers to a part of the railway substructure (a transport area and a pathway) intended for boarding or alighting of passengers and for handling of minor consignments. A gabion or a gabion structure is an element of a cube or cuboid shape made of a hexagonal steel wire mesh, welded steel nets or possibly high-strength polymer geogrids filled with natural aggregate, quarried rock, earth, recycled material, etc.

2 Mathematical Model

The basic field quantity describing current fields is a current density vector \mathbf{J} . It is a differential quantity and it therefore determines the quantity of the current flowing through the elementary area for every place of the solved space. The current density \mathbf{J} depends on the resistivity ρ , or rather on the conductivity σ according to the differential form of the Ohm's law.

$$\mathbf{J} = \sigma \mathbf{E} \quad (1)$$

In every place where it is possible to determine the intensity of the electric field \mathbf{E} and where the conductivity is known, it is also possible to determine the current density vector. Its direction in the isotropic medium is the same as the direction of the vector of the electric field intensity. The way to determine the current density vector is more complicated in the anisotropic medium where conductivity is in the form of a tensor. In most cases a tensor has only diagonal components, this means there are various conductivities in the direction of various coordinates, but the intensity of the electric field in the direction of one coordinate will not affect the current density in the direction of another coordinate, i.e. for example

$$J_x = \sigma_{xx} E_x, \quad J_y = \sigma_{yy} E_y, \quad J_z = \sigma_{zz} E_z, \quad (2)$$

The differential form of the Ohm's law is then

$$\mathbf{J} = \sigma \mathbf{E} = \sigma (-\text{grad } \varphi) \quad (3)$$

where

$$\sigma = \begin{bmatrix} \sigma_{ii} & 0 & 0 \\ 0 & \sigma_{jj} & 0 \\ 0 & 0 & \sigma_{kk} \end{bmatrix} \quad (4)$$

Electromagnetic problems associated with solving current fields in a railway superstructure and a substructure work generally with a resulting current, or current density, which is connected with intensity, or potential. Forced quantities are potentials or the primary (forced) intensity of the electric field \mathbf{E} . The primary intensity determines the distribution of charges and currents and it is used for specifying this distribution. For the purposes of an analysis it is possible to accept that the primary intensity determines the secondary distribution of charges and currents and thus the secondary intensity \mathbf{E}_{sec} , i.e.:

$$\nabla \times \mathbf{E} = -\partial \mathbf{B} / \partial t \quad (5)$$

$$\nabla \cdot \mathbf{D} = \rho_c \quad (6)$$

$$\nabla \times \mathbf{H} = \mathbf{J} \quad (7)$$

$$\nabla \cdot \mathbf{B} = 0 \quad (8)$$

where the symbol ρ_c does not stand for resistivity, but for the volume density of the total charge. Similarly to the intensity \mathbf{E} , the current density \mathbf{J} has also two components, i.e. forced current density \mathbf{J}_v and eddy current density $\sigma \mathbf{E}$. Material relationships must be added to these equations on the boundary

$$\mathbf{D} = \varepsilon \mathbf{E}, \quad \mathbf{B} = \mu \mathbf{H}, \quad \mathbf{J} = \sigma \mathbf{E} \quad (9)$$

A dynamic solution of Maxwell's equations includes also the influence of eddy currents and it is advisable to use here a continuous vector potential

$$\nabla \times \mathbf{A} = \mathbf{B} \quad (10)$$

$$\nabla \times \mathbf{H} = \mathbf{J}_v + \sigma \mathbf{E} = \mathbf{J}_v - \sigma \cdot \partial \mathbf{A} / \partial \tau \quad (11)$$

therefore
$$\nabla \times (\nabla \times \mathbf{A}) = \mu (\mathbf{J}_v - \sigma \cdot \partial \mathbf{A} / \partial \tau) \quad (12)$$

It is often advisable to perform the solution of direct-current fields for the scalar potential of the electric field. The advantage of using the scalar potential for large ground fields resides in the replacement of the vector field \mathbf{E} , which is given by 3 components, with only a single scalar variable. The boundary value problem is therefore described with one scalar variable φ and after its solution all components of the electric field intensity and subsequently also all components of the current density are obtained. The potential has an important role in connection with converting a spatial model into a circuit model described by a node voltage method.

The Laplace's equation in the Cartesian system applies to the scalar electric potential in homogeneous environments without sources:

$$\nabla^2 \varphi = \frac{\partial^2 \varphi}{\partial x^2} + \frac{\partial^2 \varphi}{\partial y^2} + \frac{\partial^2 \varphi}{\partial z^2} = 0 \quad (13)$$

The duality of the stationary current field with the electrostatic or magnetostatic field was used in modelling 3D direct-current fields of the railway electrification system.

3 Creating a Model

The Comsol Multiphysics program was chosen for the solution; this program makes it possible to use the finite element method to solve physical problems described by partial differential equations. These problems are generally solved on the basis of environment definitions which are described by partial differential equations and on boundary conditions entered in points, on edges or surfaces of a given model. The results can be obtained in several steps.

4 Defining the Parameters

The material parameters were defined by means of the electric conductivity σ and the relative permeability μ_r . These are the primary parameters for calculating the model. The conductor connecting the rail with the gabion was defined by means of the relative permeability $\mu_r = 4\ 000$ and the electric conductivity $\sigma = 1.12e7$ S/m. The insulation of the conductor was defined by $\mu_r = 1$ and $\sigma = 1e-12$ S/m. The material properties of the rail were defined by means of the measured BH characteristics. Table values of $\mu_r = 1$ and electric conductivity $\sigma = 10$ S/m were assigned to the concrete sleepers under the rail, the concrete footings under the platform and the platform itself. The gabion was defined with the values of relative permeability $\mu_r = 1$ and $\sigma = 4.1e6$ S/m. The most difficult task was to define various types of earth. It is problematic to

determine precisely the material properties of earth because its precise composition is unknown. The resistivity of earth depends on its composition; in the case of soil it can range between $\rho = 10^{-1} \div 10^2 \Omega\text{m}$; resistivity of clay is $\rho = 10 \div 10^2 \Omega\text{m}$ and resistivity of sand is $\rho = 10^2 \div 10^5 \Omega\text{m}$. A gravel subgrade will also have higher resistivity – in the range of $\rho = 10^2 \div 10^5 \Omega\text{m}$. The Comsol program requires entering of data by means of electric conductivity; resistivity was therefore converted to conductivity. In the present case the values for the earth were selected in the following way: compacted antifreeze material $\mu_t = 1$, $\sigma = 0.1 \text{ S/m}$, hard surface $\mu_t = 1$, $\sigma = 0.001 \text{ S/m}$.

5 Entering the Conditions

The conditions were entered in the following way: the condition of the electric potential $\varphi = 1\,000 \text{ V}$ was set for the upper surface of the rail. The electric potential value is the highest presumed value which can occur on the rail. The condition of a zero electric potential $\varphi = 0 \text{ V}$ was entered on the bottom side of the model. Other external boundaries were assigned the condition of electric insulation $\mathbf{n} \times \mathbf{J} = 0$.

6 Covering the Model with a Network

After the boundary conditions have been set, the model is prepared for generating a network in whose nodes the needed partial differential equations were calculated. The parameters for dividing the network can be set manually on the individual volumes, surfaces or lines. Furthermore, it is also possible to set the density of the network. The denser the network is, the more nodal points there are and the higher the number of the partial differential equations is. However, the calculation becomes more difficult at the same time. In our case a fine division corresponding to the number of approx. 750 000 nodal points was sufficient. As Figure 1 shows, the program makes the network intuitively denser in the smaller areas.

A stationary linear solver was used for the solution.

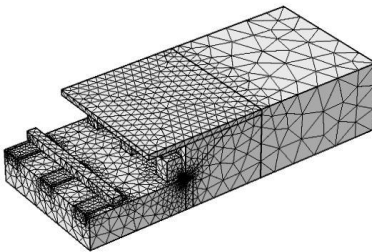


Fig. 1. The model covered with a network

7 Simulation Results

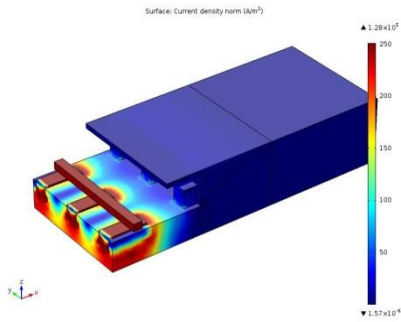


Fig. 2. Distribution of the current density, a fault-free state

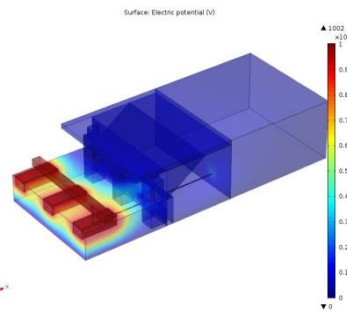


Fig. 3. Distribution of the electric potential, a faulty state

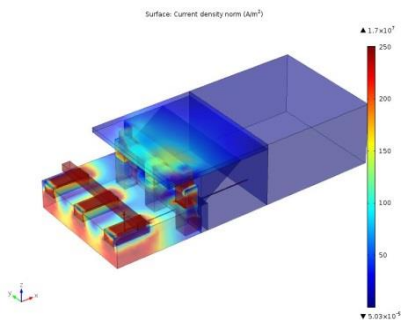


Fig. 4. Distribution of the current density, a faulty state

8 Conclusion

The aim was to prove if current density and consequently a stray current pass through concrete foundations. And if yes, what values they reach. This simulation was calculated with the maximum value of the electric potential on the rail, for example, during the passage of a train. The resulting values give an idea about the distribution of the current density and therefore about the passage of the current inside the concrete foundations and also in the earth under the platform. The simulated results confirm the supposition that the higher the value of the electric potential is, the higher the value of the normal current density is. As the models given above show, a stray current passes from the rail to the concrete sleeper and enters the earth. Then it passes through the vertical concrete foundations. A part of the current flows directly in the earth, while another part of the current flows through the surface of the platform and the gabion into the

earth. In the case of a fault-free state the current density values are very low and in some parts even negligible. However, despite this fact the current density value in the concrete foundations under the surface of the ground is approximately 150 A/m^2 . This certainly does not have a positive effect on the ageing of the concrete and there may occur degradation of the concrete in these places. Nevertheless, a much worse case occurs if there is a breakdown of the lightning arrester. In comparison with the fault-free state the current density values are very high in this case. The current density value in the platform increases by about 5 times. If the worst case is considered, the current density value in the concrete foundations increases by approximately 13 times, which represents a really very high value. As can be seen, this fact has an adverse effect on the concrete sleepers under the rail and also on the concrete foundations of the platform. One of the possible consequences of these stray currents is that their occurrence may cause degradation of the concrete and subsequently its cracking. The illustrative figure above shows how a stray current disrupts the concrete foundations in the vicinity of the railway substructure.

9 Bibliography

- [1] Paleček, Selected Chapters from Electrical Engineering Problems in Transportation Engineering university textbook, VŠB-TU Ostrava 1996
- [2] L. Ivánek, Models and Transfer Parameters for Propagation of Reverse Currents in Electric Traction post-doctoral thesis, Ostrava 1998
- [3] ČSN EN 50122-2 Railway applications – Fixed installations - Part 2: Protective provisions against the effects of stray currents caused by DC traction systems as amended
- [4] Promotion material from the company Humusoft
- [5] Materials of SŽDC.

Intelligent Model for Power Load Forecasting

Ibrahim S. Jahan and Stanislav Mišák

ENET Centre, VŠB – Technical University of Ostrava, 17. listopadu 15,
708 33 Ostrava – Poruba, Czech Republic
jahan_nw@yahoo.com, stanislav.misak@vsb.cz

Abstract. This study focuses on power load forecasting as parts of my thesis. The main goal of my thesis is to design a smart control system, which I plan to do in two main sections. The first section is about designing forecasting models, and the second section concentrates on designing an optimization model for re-configuration of a power distribution system. This article contributes to the first section of my thesis, where the second section is still in progress. Accurate and reliable load forecasting is a vital task as it may greatly influence the operation and management of electrical power generation systems. It is of a key importance when planning and controlling the power grid system. The load forecasting process makes part of a smart control system. In off-grid platforms, smart control systems are needed to keep the consumed power equal to generated power as well as to maintain the power quality at standard levels of power quality parameters. Many mathematical models have been designed for load forecasting. Still, the power load forecasting remains an open issue. In this article, we introduce an intelligent approach that predicts electrical load using data taken from an off-grid platform. The proposed approach builds on four models, namely K-means with ANN, K-means with DT, K-medoids with ANN, and K-medoids with DT. The article describes the design of these four forecasting models and compares them. The simulation results of the four models were evaluated and compared using mean absolute percentage error (MAPE) criteria. The best forecasting results were obtained using K-medoids clustering combined with ANN, where the MAPE was about 8%.

Keywords: Forecasting, power load, renewable energy, smart grid.

1 Introduction

Electrical load forecasting is used by power generation companies to estimate the total needed power to supply customers. Load forecasting helps companies to take important decisions to decrease the power production cost and to increase the accuracy of the power utility. Among others, these decisions concern power production and purchase, load switch, and infrastructure development [1]. Electricity generated from off-grid systems is particularly instable due to the changeability of the weather conditions. To ensure a stable flow of electrical power to users, smart control systems are vital for off-grids. In general, a smart control system of an off-grid system [2], [3] has

four main components: power generation forecasting, power load forecasting, power quality parameters forecasting, and an optimization model [3]. According to the results from the first three components, power generation forecasting, power load forecasting, and power quality parameters forecasting, the optimization model will shift home appliances to run at more suitable times. In an off-grid system, shifting home appliances to run at specific time periods contributes to the quality of the electrical power.

2 Mathematical Formulation

2.1 K-Means Clustering

K-means [4] is one of the basic unsupervised learning methods for data analysis by grouping the data samples. The main idea is to measure the distance between the centre points (centroids), and data points, and to assign every data sample to one cluster of minimum distance. In K-means, the following equation for Euclidean Distance, Equation (1) is used [5].

$$s = \sqrt{\sum_{i=1}^m (k_i - x_i)^2} \quad (1)$$

Where m – is the number of data points in one data sample.

2.2 K-medoids Clustering

K-medoids Clustering [4] is a modified version of K-means algorithm. K-means and K-medoids divide the data set in a set number of groups. The cluster center is called a medoid. Medoids are representative objects of a data set or a cluster with a data set whose average dissimilarity to all the objects in the cluster is minimal [6]. Medoids are similar in concept to means or centroids, but medoids are always restricted to be members of the data set [5].

2.3 Artificial Neural Networks

An artificial neural network (ANN) [7] is a mathematical model which tries to mimic the biological neurons in solving complex issues. ANNs are designed to solve a specific problem and are constructed from huge numbers of units called neurons. The numbers and connections between the neurons in an ANN depend on the purpose. The neurons in an ANN arrange in three layers: input layer, output layer, and hidden layer placed between the input and output layer. The input layer takes and sends the input signal to the hidden layer. In the hidden layer, the data processing may be organized in more than one layer. The last is the output layer from the neural system. Like a human brain, an ANN learns by examples in the learning phase. The basic principle of the neural networks is adjusting the weights between the neurons according to

learning examples till the ANN learns all data samples in the training phase. Later on, one can test and use the trained network to test a data set in the testing phase. ANN was applied successfully in several applications, such as speech and image recognition, EEG and ECG classification, forecasting, etc. More details on ANNs can be found in [8].

2.4 Decision Trees

A decision tree (DT) [9] is a powerful machine learning technique which can be used either for classification or for regression purposes. A DT is a supervisor learning technique which tries to find relations between the input variables and the numerical target output to be used to predict a numerical output unlike a classification tree which predicts a class target output. Regression and classification trees work in a similar way. The main idea of a DT is to split a data set into branches till the final branch node is reached. After training the decision tree and splitting the data set, the result is a tree which includes a decision node and a leaf node. The decision node has at least two or more outputs which will feed the next nodes on the succeeding level, while the leaf node has one output which represents the final decision value (as the electrical power load in our experiment). In classification DT, information gain (IG) is used to split the data set, while in regression decision tree standard deviation is used to split the data set. More details on DT can be found in [5].

3 A structural Model for power load forecasting in off-grid system

3.1 Data set

The data set used in this article was taken from the off-grid platform constructed at the Faculty of Electrical Engineering and Computer Science at VSB-Technical University of Ostrava, the Czech Republic. This data set includes several variables related to meteorology and power data. In our experiment, we used index day, normalized temperature, normalized humidity, wind speed, normalized pressure, and one, two, three steps back of power load. These are used as input variables, while the power load is used as the output. The data set used to train our model was from 23/05/2017 to 18/06/2017. In the testing phase, one-day ahead (19/06/2017) was used to test the model and predict the power load.

3.2 Experiment Setup

The experiments were carried out in three steps as follows. In the first step, the weather data were clustered into groups using K-means and K-medoids. In the second step, the distances between the samples and each cluster center were measured using Squared Euclidean Distance Equation (1). These distances represented the new features of the data set. In the third step, the new features were fed into the regression model with the smoothed actual power load for training the model. We applied the

smoothing because the measured data come from one household and contain rapid peaks which are generated by switching on and off devices with high load. The input power load was smoothed using a moving average technique. In the testing phase, only the distances are fed into the regression model to predict the load in the future time. The features used in this experiment are: index day - any working day = 1, weekend = 0, normalized temperature, normalized humidity, wind speed, normalized pressure, and one, two, three steps back of the power load, as can be seen in Figure 1. The experiments were carried out using four models: K-means with DT, K-means with ANN, K-medoids with DT, and K-medoids with ANN.

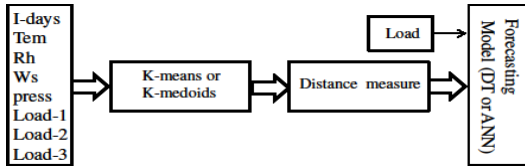


Fig. 1. Diagram of the proposed system

3.3 Discussion and Results

The results of the four models are compared using mean absolute percentage error (MAPE) as in the following Equation (2).

$$MAPE = \frac{100}{l} \sum_{t=1}^l \left(\frac{a_t - p_t}{a_t} \right) \quad (2)$$

Where- a_t - is the actual value of the power load, p_t - is the forecasted value of the power load, l - is the number of forecasted samples in testing dataset.

The results of MAPE values of K-means (with DT or ANN) and K-medoids (with DT or ANN) are listed in Table 1. The first two columns represent the results of K-means with DT and ANN, while the second two columns represent the results of K-medoids with DT and ANN.

Table 1. Forecasting results of K-means, K-medoids with DT and ANN

No of Clusters	DT MAPE	ANN MAPE	DT MAPE	ANN MAPE
5	163.00%	270.00%	440.61%	47.95%
10	46.74%	36.73%	494.28%	8.08%
15	263.77%	30.80%	153.21%	29.23%
20	185.47%	40.87%	257.29%	27.38%
25	261.72%	47.26%	437.33%	30.31%
30	221.17%	52.29%	60.54%	31.00%
35	464.30%	49.50%	454.92%	39.50%
40	142.56%	32.94%	481.29%	38.20%
45	745.15%	39.04%	503.35%	63.60%
50	458.09%	28.76%	446.19%	29.04%

The number of original features of the data set is 8 features as mentioned above, namely index day, normalized temperature, normalized humidity, wind speed, normalized pressure, and one, two, three steps back of the power load. These features were converted into distances. The forecasting models - DT and ANN were fed with the new different number of features from 5 to 50 features which represented the distances between each data sample and each cluster center. The number of the new features depends on the number of the clusters - for example, when 5 clusters are used 5 features are fed into the forecasting model when 50 clusters are used 50 features are fed into the forecasting model. Therefore the number of clusters affects the forecasting results as can be seen in the results listed in Table 1. The experiment was repeated with different numbers of clusters- 5, 10, 15, . . . , 50, for the purpose of comparing the performance of the four models with different numbers of fed data features. The best results of K-medoids were achieved with 10 clusters combined with ANN, which was about 8.08%, as can be seen in Figure 3. It shows the difference between the actual load and the output of the proposed model. The values of the MAPE error achieved from ANN were lower than other values obtained from DT for all cluster numbers.

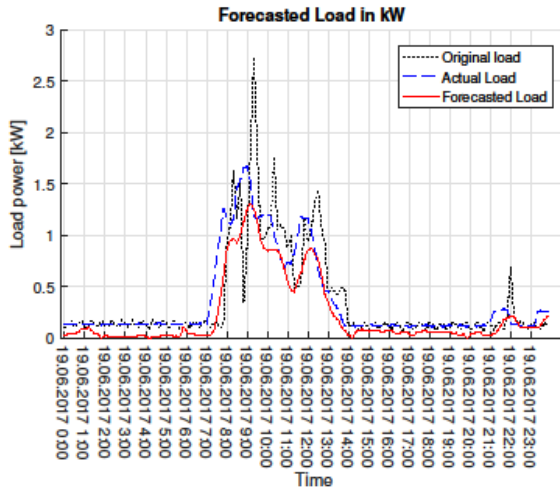


Fig. 2. Power Forecasting Results

In this study, the numerical results of both DT and ANN in Table 1, show that the ANN performance outperformed DT in load forecasting. The main goal of the contribution is not only to improve the forecasting accuracy, but also find and open an alternative process for power load forecasting which may help the future research to develop new forecasting models.

4 Conclusion

Accurate power load forecasting models are important for the operation and control of power systems as they ensure the supply of accurate and reliable electricity

to users. Load forecasting models are important parts of smart control systems of the power utility, which aim to balance the consumed power and generated power as well as to maintain power quality parameters at standard levels. Despite a number of previous studies focused on the design of various load forecasting models, the challenge remains to design and apply efficient techniques in real time. In this study, we designed a load forecasting model by combining the cluster method K-means and K-medoids with artificial neural network and decision tree. The designed method was constructed in four models: Kmeans with artificial neural network, K-means with decision tree, K-medoids with artificial neural network, and K-medoids with decision tree. The simulation results of the four methods were compared, and it shows that K-medoids with artificial neural network rendered the best results.

Acknowledgements

This work was conducted in the framework of the project LO1404 TUCENET – Sustainable Development of Centre ENET, and the project CZ.1.05/2.1.00/19.0389.CZ.1.05/2.1.00/19.0389- Research Infrastructure Development of the CENET, Czech Science Foundation under the grant no. GJ16-25694Y and in part by the Grant of SGS No. SP2018/126, VSB-Technical University of Ostrava, Czech Republic.

References

1. E. A. Feinberg, and D. Genethliou, "Load forecasting," in *Applied mathematics for restructured electric power systems*, Springer US, pp. 269–285, 2005.
2. S. Misak, and L. Prokop, "Off-grid power systems," in *IEEE Environment and electrical engineering (EEEIC)*, pp. 14–17, May 2010.
3. S. Misak, L. Prokop, and P. Bilik, "Power quality analysis in off-grid power system," in *IEEE ELEKTRO*, pp. 337–342, May 2014.
4. D. MacKay. *An Example Inference Task: Clustering*. In *Information Theory, Inference and Learning Algorithms*. Cambridge University Press, Cambridge, 2003, pp. 284–292.
5. T. Hastie, R. Tibshirani, and J. Friedman. *The Elements of Statistical Learning*. Springer-Verlag New York, 2009.
6. A. Struyf, M. Hubert, P. Rousseeuw, "Clustering in an Object-Oriented Environment," in *Journal of Statistical Software*, vol. 1 (4), pp 1–30, 1997.
7. P. J. Werbos, "Beyond Regression: New Tools for Prediction and Analysis," in *the Behavioral Sciences*, 1975.
8. J. M. Zurada, "Introduction to Artificial Neural System," West Publishing Co., St. Paul, MN, USA, 1992.
9. J. R. Quinlan, "Simplifying decision trees," in *International Journal of Man-Machine Studies*, vol. 27 (3), pp. 221–234, September 1987.

Possibilities of Optimizing Maintenance Strategies Applicable on Electrical Network in the Czech Republic

David Lazecký

Department of Electrical Power Engineering, FEECS,
VŠB – Technical University of Ostrava, 17. listopadu 15,
708 33 Ostrava – Poruba, Czech Republic
david.lazecky.st@vsb.cz

Abstract. The paper describes current results of student's research in field of maintenance strategies optimization. The maintenance strategies are described and possible optimization techniques are shown in the paper. The issues of implementation in Czech environment are discussed in the conclusion, and they will be subject of further research.

Keywords: Electrical networks, maintenance strategies, optimization, RCM

1 Introduction

An evaluation of safety and reliability evolved with description and assessment of malfunctions that were recorded in operators' databases. Malfunction prediction became possible when manufacturing processes moved from hand-made production to assembly-line production. Since every activity introduces some level of risk, technologies and strategies for risk evaluation and optimization have been developed. The same problem is connected with every piece of equipment ever produced.

Maintenance strategies are interconnected with reliability its evaluation and prediction. The process of reliability evaluation started in the 1960s in an air transport industry in the USA. At the same time, first failure databases started to collect data. Later, other industries began to implement such procedures and evaluation as well as filling their own databases. The rise of personal computing made the processes of exploration and assessment easily available for everyone who has access to such database.

The reliability of an electrical system could be described as an ability to provide electrical energy to all connected customers continuously. The ability is evaluated according to specified parameters. In case of exceeding any of the parameters, the distribution company is penalized (so-called undelivered energy). The evaluation of the undelivered energy is based on the results of the reliability outcomes.

Mathematical description of a single device or whole system is based on well-known "bathtub curve". For a distribution system in standard operation mode, mostly the second and third sections apply (coincidental and wearing malfunctions).

2 Maintenance Strategies

The processes of aging and wearing start when an electrical device is installed and put into service. Unless these changes are controlled, they could cause malfunction or breakdown of the device. Insufficiently coordinated and calculated changes in the system can also cause malfunctions of devices that have not been designed for a new network state. Therefore, the main task of maintenance and diagnostics should be to check the correct function and parameters of all individual devices in the network in order to ensure the maximum reliability of the entire electrical system.

The overview of maintenance strategies is depicted in the diagram below. Two main directions of the strategies based on approach to failure occurrence are shown (preventive maintenance vs. corrective maintenance).

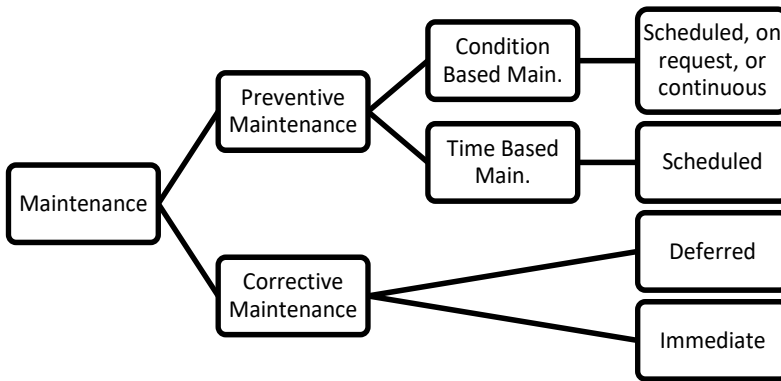


Fig. 1. Maintenance strategies overview

2.1 Corrective Maintenance

This strategy uses the easiest possible access to element failure. A device is operated until it fails. Depending on the type of fault, *Immediate* or *Deferred* solution is used (repair or replacement). This solution corresponds to the significance of the device in the fault within the electrical system and is based on a pre-ensured assessment of the risk that this approach will cause.

This strategy is not used by Czech electrical distributors.

2.2 Preventive Maintenance

Time Based Maintenance (TBM), the strategy can also be called *planned preventive maintenance*. The procedure expects maintenance-related activities at predetermined time intervals - astronomical time, operating time, or operating cycles. Individual operations and times are based on manufacturer or industry standards. Although the strategy works for regular device control, it does not take into account the current status of other elements, their importance within the system, or address the issue of

efficient use of workforce resources or operational experience. However, in case of non-efficiently used financial and human resources, it ensures high security and productivity of the maintained system.

Condition Based Maintenance (CBM) or *predictive maintenance*. This is an extension of the TBM strategy by non-intrusive test methods and device's current state assessment during standard operation (in most cases). TBM provides the basis, which, together with the parameters of the device operation, the experience and the measurement outputs, evaluates the assumed current condition of the device and recommends maintenance if needed. This is a relatively costly strategy that requires installation and operation of diagnostic devices. Therefore, it is economical only in case of expensive and very important devices (especially transformers).

Reliability Centered Maintenance (RCM). The strategy combines the principles of previous maintenance strategies (it assesses the current state of the device, its system importance, fault history and overall operating costs) and, using mathematical models, sets the optimal maintenance plan to maintain system reliability at the current state, while minimizing maintenance costs. The strategy also distinguishes disturbances due to the impact on the operation of the entire system and environment. Obviously, the severity of the malfunction could also affect the range of instruments that will be used to prevent the malfunction. In other words, serious consequences will be solved much more intensely and more acutely than those with small or negligible consequences.

3 Maintenance Optimization

The goal of optimization in today's world is to find the minimal costs, to maximize the trouble-free use of the system and thus the profit and/or balance activities of maintaining a reliable power system with total costs (time, technology, financial, etc.) to this level of reliability. With gradually evolving technologies of monitoring, testing, management and safety, it is possible to add additional factors to the evaluation and optimization procedures, which may influence the resulting form of the optimized process or product.

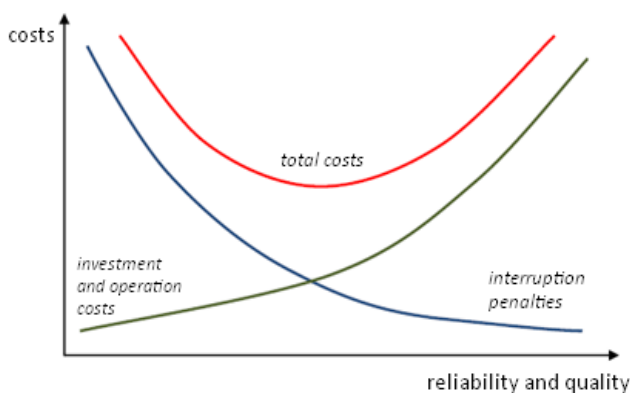


Fig. 2. Dependency between costs and reliability (and quality of distribution)

There are several ways to resolve the problem of the maintenance optimization. For example: time optimization goes in the direction of maximum utilization of employees' time for productive work, economic optimization tries to find the best number of employees for a certain area of distribution network or the lowest penalties for undelivered energy, and technical optimization's directive is to reach the best condition of all used devices.

Based on the technical state, it is possible to optimize maintenance in two main directions. The graph below shows the basic evaluation of the physical state of the element (failure rate) and the significance of the element within the system. On the vertical axis on the right, the maintenance frequency is also displayed. (It could be explained as the standard RCM chart.)

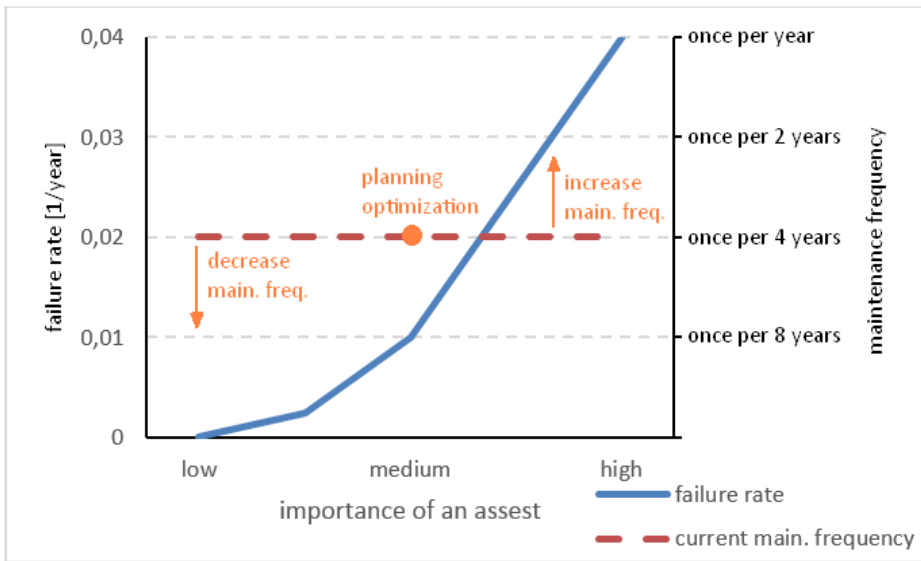


Fig. 3. Evaluation of device's technical state and importance vs. maintenance frequency

3.1 Planning Optimization

Optimization by matching visits of scheduled maintenance and device diagnostics is applicable to any maintenance strategy. In principle, it maximizes the use of the planned shutdown time for all non-intermittent activities (the greatest benefit) and possible better organization of work. The problem can be the coordination of individual actions.

The optimization requires a unified software solution for the activities planning. In case of better communication among all departments involved in the maintenance (or diagnostics) planning, the optimization should provide reduction of network shutdowns and better network parameters.

3.2 Maintenance Interval Optimization

On the basis of the technical condition assessment and future forecasts, it is theoretically possible to change the maintenance interval. It requires just a very good description of the current state and a high-quality prediction model.

Extension of the maintenance interval would be possible for network elements that are new or in very good technical condition, theoretically, even twice the original time. This would bring about a significant reduction in the costs of planned maintenance but, due to a longer maintenance period, the number of faults might increase.

Reduction of the interval is advantageous for the highly used devices and devices in poor technical condition, but for which there is no (for any reason) planned replacement/refurbishment. The benefit, in this case, would be increased reliability and reduction of repair costs. The negative would be increasing maintenance costs alone (and probably more workers).

The interval optimisation could be done for example by implementing RCM strategy. The requirements, software and implementation are described in [4].

4 Conclusion

The problem of implementation of described maintenance strategies in the Czech distribution system is based on differences between reliability and safety procedures. The difference is in the specification of each category. Safety procedures and their intervals are specified by Czech national standards, so, from the current and near-future point of view, they are set and cannot be changed. On the other hand, reliability procedures and intervals are specified by networks' operators, so that they can be revised quite easily.

The state of student's current research is in dividing procedures into above-described categories and in implementing described strategies on the specified network station.

When the separation of the procedures is done, the research should progress to the step of finding a solution for interval optimisation. The problem will be solved on the basis of evaluating strategies and finding the best solution for a chosen distribution station. The problem of planning software unification will not be solved, only some recommendations might be made.

In case of acceptance and implementation of RCM strategy (all requirements specified in [4] are met), the solution for the planning process is already prepared. The whole problem of optimisation is complicated by the fact that interval optimisation contradicts planning optimisation, but it represents a challenging innovation, especially in Czech conditions, that is worth of further research.

Acknowledgements. This research was partially supported by the SGS grant from VSB-TU Ostrava (No. SP2018/61) and by the project TUCENET (No. LO1404).

References

1. Smith, David J. *Reliability, Maintainability and Risk: Practical Methods for Engineers*; Ninth Edition. Oxford, UK: Butterworth-Heinemann, 2017. ISBN 978-0-08-102010-4.
2. ČSN EN 13306 (010660) A Údržba - Terminologie údržby. Praha: Úřad pro technickou normalizaci, metrologii a státní zkušebnictví, 2011. Available at: <http://csnonline.agentura-cas.cz/>
3. Conseil international des grands réseaux électriques. Comité d'études B3. Saving Through Optimised Maintenance in Air Insulated Substations. Cigré, 2016. ISBN 978-2-85873-363-7.
4. Lazecky, D., Kral, V., Rusek, S., Gono, R. Software solution design for application of reliability centered maintenance in preventive maintenance plan, *Proceedings of the 2017 18th International Scientific Conference on Electric Power Engineering, EPE 2017*, Kouty nad Desnou, Czech Republic. ISBN: 978-150906405-2, DOI: 10.1109/EPE.2017.7967354
5. Kelly, Anthony. *Strategic Maintenance Planning*. First Edition. Oxford, UK: Butterworth-Heinemann, 2006. ISBN 978-0-75-066992-4.
6. Tůma, Jiří. *Spolehlivost v elektroenergetice*. Praha: CONTE, 2006. ISBN 80-239-6483-6.
7. Gill, Paul (2008). *Electrical Power Equipment Maintenance and Testing*, Second Edition. Boca Raton, USA: CRC Press, 2008. ISBN 978-1-57444-656-2.

Publications

Lazecky, D., Kral, V., Rusek, S., Gono, R. Software solution design for application of reliability centered maintenance in preventive maintenance plan, *Proceedings of the 2017 18th International Scientific Conference on Electric Power Engineering, EPE 2017*, Kouty nad Desnou, Czech Republic. ISBN: 978-150906405-2, DOI: 10.1109/EPE.2017.7967354

Lazecky, D. Analysis of the Failure Rate of MV Circuit Breakers, *Proceedings of the 15th Annual Workshop WOFEX 2017*, Ostrava, Czech Republic. FEEDS, VŠB - Technical University of Ostrava ISBN: 978-80-248-4056-7

Lazecky, D. Comparison of Maintenance Strategies among Selected Electrical Companies, *Proceedings of the 14th Workshop ELNET 2017*, Ostrava, Czech Republic. FEEDS, VŠB -Technical University of Ostrava ISBN: 978-80-248-4154-0

Alternative energy sources comparison for heating a residential house

Tomáš Machů

Department of Electrical Power Engineering, FEECS,
VŠB – Technical University of Ostrava, 17. listopadu 15,
708 33 Ostrava – Poruba, Czech Republic
tomas.machu.st@vsb.cz

Abstract. This article deals the design of four alternative heat sources for a given object. The object is a residential house that is in the project phase. In the first part is necessary to find out heat loss of a family house. This part is also about designing of warm water floor heating. Design of heat loss and heating system is realized in program TechCON. The next part is about four heating sources. In the article are described a properties of heating sources. It is a geo-thermal heat pump, micro-cogeneration unit, heat pump air/water and under-floor heating film. The main task is to find out which of the sources is the most appropriate.

Keywords: Alternative sources, heating, heat pump, micro-cogeneration, mi-cro-CHP, underfloor heating foil, TechCON software,

1 Introduction

When building a family house, every owner is interested in choosing the right source of heating. In this article I deal with a particular object. This is a new family house project. The residential house has two floors, the second floor is considered as another child unit in the future. The heating system is warm water underfloor heating. Total electricity consumption for non-heating purposes is 2.2 MWh / year.

2 Calculation in TechCON

For the correct size of the selected heat sources, it is necessary to determine the thermal loss of the family house. This was detected using TechCON. This is a graphical computing software designed for the design and processing of central heating, to which all important data on both the object and its surroundings is entered. The most important part is the house itself. Therefore, the total heat loss was $\Phi = 10,885$ kW. This will determine the annual heat demand for heating, which is 22,1 MWh and an annual heat demand for DHW heating of 6,116 MWh. The total heat demand is therefore the sum of these two components, respectively $Q_r = 28,225$ MWh/year. [1], [2]

$$Q_{vyt,r} = \frac{\varepsilon}{\eta_o \cdot \eta_r} \cdot \frac{24 \cdot \Phi \cdot D}{(t_{is} - (-t_e))} = \frac{0,75}{1 \cdot 0,98} \cdot \frac{24 \cdot 10885 \cdot 3870,4}{(20 - (-15))}$$

$$= 22,109 \text{ MWh/rok}$$

Kde: ε – Correction coefficient (-), η_o – Service efficiency (-), η_r – Efficiency of heating distribution (-), t_{is} – Average indoor temperature ($^{\circ}\text{C}$), t_e – outdoor temperature ($^{\circ}\text{C}$), D – number day of grade (Kelvin-day), Φ - Heat loss of house (W)

TechCON includes all the important information about both the object and its surroundings eg: the lowest outdoor temperature, average outdoor heating temperature, number of days for heating, etc. The most important part is the house itself. It is necessary to define the dimensions of all translucent and opaque structures such as windows, walls, floors and others. If a given object is available in computer form (CAD system), it is possible to take the object and insert it directly into the TechCon program. If all necessary data is entered into the program, the heat loss of the family house will be calculated. Figure 1 shows the floor plan of one room of a family house, respectively. living room. The picture shows the projected hot water heating. The pitch between tubes is 30 cm. On the left side of the picture are room data such as floor area, room volume, proposed room temperature and heating power in the room. In the fact, this is one pipe that is connected at the beginning of the room at two points, namely in the hot water supply and the outlet of so-called return water. [1], [2], [11]

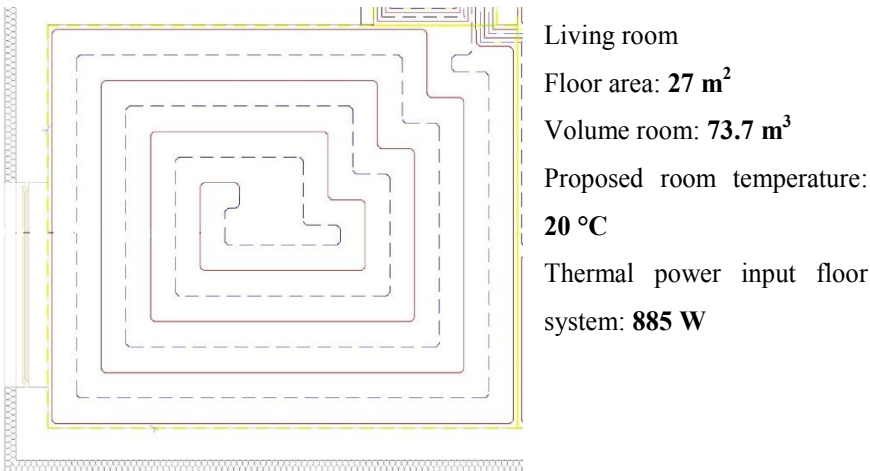


Fig. 1. Floor plan of the room with designed floor heating using the software TechCON

3 Alternative sources of heating

In this chapter, I will deal with individual alternative heating sources, such as geothermal heat pump, micro-cogeneration unit, heat pump air/water and underfloor heating foil. We will describe their individual parts, nominal values and other important features.

3.1 Var.1 – Geothermal heat pump

The first source of heating is the geothermal heat pump or also earth/water heat pump, the first word being heat sources, geothermal wells and second warm water underfloor heating. This heat pump has a rated thermal output of 12 kW. The product is supplied with a reheating electric boiler and a water heater. The depth of the geothermal borehole is 205 meters. One important factor is the heating factor, known as SCOP. Seasonal Coefficient of Performance (SCOP) of this heat pump has a value 4.53. Another important concept that we encounter at the heat pump is so-called bivalent operation, which is determined by the outside temperature. For our considered object, resp. family house, annual electricity consumption of 7.82 MWh/year, while it is contemplated that the additional electric boiler will be in service for 9 days. The total investment is 471 155 crowns, operating cost 31 529 crowns/year. This price includes the price of electricity consumption of a family house. [1], [4], [6]

3.2 Var.2 – Micro-cogeneration unit

The second comparative alternative source is a micro-cogeneration unit (micro-CHP). First, high-potential heat energy is used to perform the work, and then heat is used from micro-CHP losses. The micro name, which is in the name of the unit, means that it is a low-power cogeneration unit up to 30 kW. The heart of micro-CHP is Stirling's engine, with a rated electric power of 1 kW and a heat output of 6 kW. The primary energy supplied to the unit is natural gas. The micro-CHP is supplemented by a condensing gas boiler with a rated thermal output of 20 kW. Since micro-CHP also produces electric current, an electric current accumulator is connected to the system, with an accumulation of up to 5.5 kWh. Thus, the family house will be independent of the supply of electricity from the distribution network. The total gas consumption is 41,12 MWh/year. The total investment is 873 579 crowns, operating costs 60 514 crowns/year. This price includes the price of electricity consumption of a family house. In terms of electrical reliability, the house is connected to a distribution network. [1], [5], [11]

3.3 Var.3 - Heat pump air / water

The third alternative source is the air / water heat pump. Heat pumps do not require expensive earthworks and are therefore much less demanding on investment. This heat pump has a rated output of 12 kW at 7 ° C. The product is supplied with an electric boiler and a water heater. Bivalent temperature was determined at -8 ° C. The number of days when the temperature is below -8 ° C is 17 days (2012-2017). One

important factor is the heating factor COP, from which we find out Seasonal Coefficient of Performance SCOP. His value is $SCOP = 3,91$. The annual power consumption of the air / water heat pump is 8,36 MWh/year. Total investment is 244 605 crowns, operating cost 32 965 crowns. This price includes the price of electricity consumption of a family house. [1], [10]

3.4 Var.4 – Underfloor heating foil

The fourth source one are underfloor heating foil (UHF) or also infrared heating films. UHF for this facility is considered as floor heating with a heating output of 80 a 220 W/m². It is powered by AC 230V. The DHW heating (hot water) is provided by a 200 liter water heater. Another important point is the consumption of UHF. It can be assumed that the required heat is equal to the electrical energy consumed. The total electricity consumption of infrared heating is 29,53 MWh/year (the consumption of DHW with losses is considered). The total investment is 90 052 crowns, operating costs 87 928 crowns. This price includes the price of electricity consumption of a family house. [7], [8], [9]

4 Comparison of technical and economic

For the future owner, perhaps the most important question is how much the given heat source will cost, so how much does the investment cost and what are the operating costs. Figure 2 shows graphs showing a comparison of total costs. The slope of the curve is given by the amount of operating costs, the higher they are, the steeper the straight line and vice versa. From this data, it is clear that the total cost of the micro-CHP is greater than a year earlier (until the 20th years), than heat pumps and infrared heating.

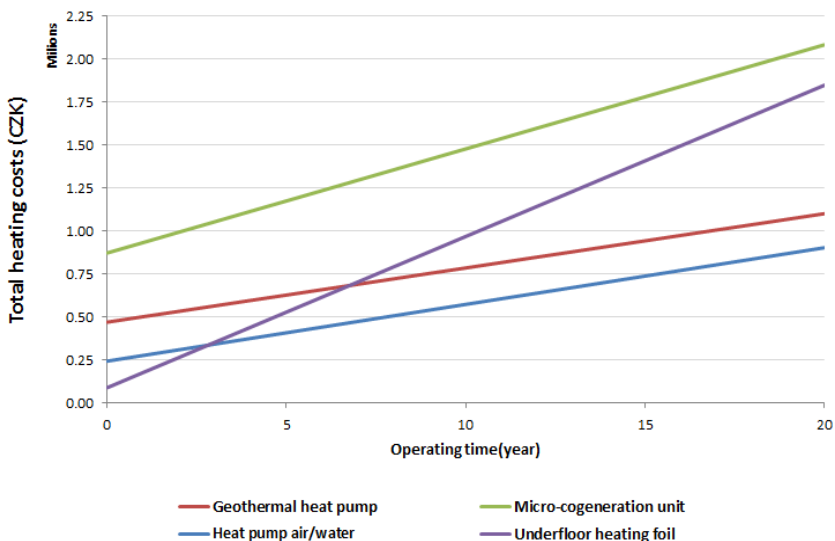


Fig. 2. Total costs for 20 years of operation

The technical comparison can be divided into several criteria. For example, in terms of efficiency, durability, etc. Micro-CHP efficiency is around 96-98%. For heat pumps, the heating factor called COP is given, as mentioned in the previous chapter. From this point of view, the best heat pump is, since the electrical energy is about 4 times smaller than the thermal energy. UHF transforms all of its energy into heat, have 100% efficiency. Regarding the lifetime, the micro-CHP is considered to be 18-20 years, the heat pump 20-25 years and the UHF 30-50 years. Of all the knowledge and calculations contained in this work, the most suitable source of heating for this house is the air/water heat pump. For even better comparison, I used multi-criteria analyzes. This is the TOPSIS method and CDA method. Criteria and the determination of their weights are important parameters (Table 1). The owner put his emphasis on the economic side. The greatest importance is placed on operating costs, followed by investment costs. This is due to the fact that for the owners, the lower operating costs are more advantageous than the lower investment costs.

Table 1.: Scales of Criteria

Criteria	Scales of Criteria
f_1 – Investment cost – NI	0,35
f_2 – Operating cost – NP	0,4
f_3 – Lifetime	0,2
f_4 – Sound pressure level - Noise	0,05

Table 2 lists individual variants from best to worst. Both variants directly confirm what has already been found in the previous comparison of total cost. Thus, the most suitable heating source is the air / water heat pump. The geothermal heat pump follows. On the other hand, the worst source of heating is clearly a micro-CHP for both methods. [1], [2], [6], [11]

Table 2.: Overall assessment according to the given method

VARIANTS	TOPSIS	CDA
Var.3 – Heat pump air/water	0,823	1,407
Var.1 – Geothermal heat pump	0,700	1,629
Var.4 – Underfloor heating foil	0,491	3,661
Var.2 – Micro-cogeneration unit	0,309	4,641

5 Conclusion

This article is about the comparison of alternative sources of heating for a residential house. Comparable variants are the geothermal heat pump, the micro-CHP, heat pump air/water and the underfloor heating foils. Each of the variants has its pros and cons.

For example, the cheapest heating source is the UHF, while the most expensive is the micro-CHP. In terms of annual operating costs, the most favourable geothermal heat pump vice versa the most expensive is UHF. The longest lifetime has UHF, and up to 50 years. On the contrary, the shortest lifetime has a micro-CHP. Compared the total cost it is obvious that the most suitable heating source is the heat pump air/water. It is given to low operating costs and low investment costs. On the contrary, the largest total cost is the micro-CHP. To refine a comparison, I used a comparison of a multi-criteria analysis using two methods. These are the TOPSIS method and the CDA method. The decisive parameters are the criteria, which I mentioned in the previous chapter. Both methods confirmed that the most suitable source of heating is the heat pump air/water. This article could help future owners choose a suitable heating source for family houses.

Publications

1. Machů, Hradílek: Alternative Energy Sources Comparison for Heating a Residential House, ELNET 2017, pp. 1–9, ISBN 978–80–248–4154–0. VSB – Technical University of Ostrava, FEECS, 2017.
2. Machů, Hradílek: Srovnání alternativních zdrojů pro vytápění rodinného domu, 39. NEKONVENČNÍ ZDROJE ELEKTRICKÉ ENERGIE, str. 75-78, Hustopeče 2018. ISBN 978-80-02-02786-7.

References

1. MACHŮ, Tomáš. Alternativní zdroj energie pro rodinný dům. Ostrava, 2017.
2. TechCON. TechCON [online]. Bratislava: ATCON SYSTEMS [cit. 2017-10-23]. Dostupné z: <http://www.techcon.sk/index.php?page=pinfo>
3. NIBE: Instalační příručka, NIBE F1226 Tepelné čerpadlo země/voda.
4. HRADÍLEK, Zdeněk, Ilona LÁZNIČKOVÁ a Vladimír KRÁL. Elektrotepelná technika. Vyd. 1. Praha: České vysoké učení technické v Praze, 2011, 264 s. ISBN 978-80-01-04938-9.
5. VIESSMANN: Projekční návod - Vitotwin 300-W. 2012.
6. HRADÍLEK, Zdeněk. Elektroenergetika distribučních a průmyslových zařízení. Ostrava: Vydala VŠB-TU Ostrava ve vydavatelství Montanex, 2008. ISBN 978-80-7225-291-6.
7. Druhy topných fólií - Heathome - zdravé teplo domova ... Heathome - kvalitní, úsporné a zdravé podlahové vytápění - Heathome - zdravé teplo domova ... [online]. [cit. 2018-03-26]. Dostupné z: <https://heathome.cz/content/9-druhy-topnych-folii>
8. O topných fóliích - Heathome - zdravé teplo domova ... Heathome - kvalitní, úsporné a zdravé podlahové vytápění - Heathome - zdravé teplo domova ... [online]. [cit. 2018-03-26]. Dostupné z: <https://heathome.cz/content/10-o-topnych-folii>
9. Infrapanely: Vyplatí se jako hlavní zdroj vytápění? | Nazeleno.cz. Úspory energie, izolace, zdravý životní styl, biopotraviny, ekologie | Nazeleno.cz [online]. [cit. 2018-03-26]. Dostupné z: <https://www.nazeleno.cz/vytapeni/primotopy/infrapanely-vyplati-se-jako-hlavni-zdroj-vytapeni.aspx>
10. Tepelné čerpadlo vzduch-voda NIBE F2040. Benátky nad Jizerou, 2015.
11. WANG, Lingfeng. Modeling and control of sustainable power systems: towards smarter and greener electric grids. Heidelberg: Springer, c2012. Green energy and technology. ISBN 978-3-642-22903-9.

Research on the Combination of Biogas Station and Photovoltaic Power Plant Operation

Ladislav Novosád

Department of Electrical Power Engineering, FEECS,
VŠB – Technical University of Ostrava, 17. listopadu 15,
708 33 Ostrava – Poruba, Czech Republic
ladislav.novosad.st@vsb.cz

Abstract. This article deals with the combination of renewable energy sources in distribution grid. In this particular case, it concerns a combination of operation or cooperation of biogas stations with photovoltaic power plants. The biogas plant in this case represents a stable renewable energy source that can be regulated to a certain extent. On the contrary, the photovoltaic power plant is characterized as a considerably stochastic, unregulated power source. The aim of this article is to present some possible ways of mutual cooperation of the above-mentioned power sources or to point out their advantages and disadvantages.

Keywords: biogas, biogas station, combination, accumulation, photovoltaic plant, co-generation units, regulation

1 Introduction

As stated above, the aim of the article below is to analyse the possibilities of cooperation of renewable energy sources (RES); specifically, a combination of a biogas station (BGS) equipped with co-generation units (CGU) and photovoltaic power plants (PPP). The biogas stations are designed as continuous operation power sources, and, unlike water, wind or photovoltaic power plants, they supply electricity to the distribution grid (DG) steadily and almost continuously throughout the day. An advantage over other RES, such as photovoltaic (PPP) and wind (WPP) power plants, is the minimum dependence of power production on the current weather conditions or daily cycles (day-night). The power generation from BGS can be relatively simple to regulate. On the other hand, photovoltaic power plants are sources heavily dependent on weather and daily cycles and the nature of their power generation can negatively affect the entire DG.

However, it is necessary to state that current economic BGS support (fixed purchase price) is not set for the use of BGS as a regulatory element in the DG. For this reason, we will only deal with the technical possibilities of combining the above-mentioned sources. The legislative and economic aspects of this cooperation will not be addressed in this article.

2 Biogas stations

Biogas stations can be simply characterized as a comprehensive set of facilities for storage, processing, conversion and energy use of biomass. Input raw material, the biomass, is processed in BGS by anaerobic processes to get biogas. Biogas is mainly made of methane (CH₄) and carbon dioxide (CO₂) and can be used for example to produce electricity and thermal energy using CGU.

3 Energy potential of biogas stations in distribution grid

To understand the importance of biogas station potential as power sources, it is necessary to know their current state or their energy potential in the Czech Republic. There are 567 biogas stations in the Czech Republic with a total installed capacity of 360MW (the data are available for 2016). The BGSs are located throughout the Czech Republic. Renewable sources, including BGSs, covered 12.97% of electricity consumption in the Czech Republic and produced a total of 9,395.4 GWh of electricity in 2016. The share of biogas in total production from RES was about 24.8% in terms of the total electricity produced. [4,5]

4 Photovoltaic plants in distribution grids

The power supply or power generation of photovoltaic power plants (PPP) is considerably stochastic and unpredictable in the long term. Dynamic change of power supply from PPP is caused by a sudden change in the intensity of solar radiation - e.g. sudden cloud change. The actual course of stochastic changes in PPP production also leads to high demands on DG control. High PPP production can cause shutting down the blocks of conventional power sources to a cold state, which has an adverse impact on their higher wear and longevity. As a rule, existing sources were not designed for these conditions. Moreover, the higher regulatory demands have an adverse economic impact. The power imbalance between power consumption and power generation that is triggered by PPP operation affects the system services that have to even up these power changes. Thus, there is a higher demand for power reserves and hence for support services. Maintaining high power reserves in production blocks is highly uneconomic, and the power supply from some RESs has a negative impact on the cost of regulatory energy. [1,5]

5 Possibilities of PPP and BGS cooperation

Some PPP operating disadvantages or problems mentioned above could be eliminated to a certain extent by a suitable combination of each of these electricity sources in DS. The accumulation of electricity and its subsequent utilization appear as a possible solution from the point of view of solving the above mentioned problems. A certain form of energy storage in biogas, which can be relatively easily accumulated directly in BGS, can be a possible solution regarding the BGS and PPP operation. Biogas accumulation

is based on the assumption of using gasometers with much larger capacity than those they are currently equipped with. Energy stored in the form of biogas can then simply be used for the various possibilities of cooperation between BGS and PPP.



Fig. 1. Position of PPP in area of Czech Republic

An important factor for the cooperation of BGS and PPP is the location of sources. A situation when a PPP is located near a BGS is frequent. An example of this may be the installation of PPP in the BPS Loděnice compound where PPPs are installed directly at the BGS site; see the following Figure 3.

6 Regulation of CGU in cooperation with PPP for the purpose of constant power supply to DG

The most appropriate option to use the potential of BGS in cooperation with PPP is their cooperation based on the regulation of CGU output for the steady supply of electricity to DG. The sources would have to be at least virtually interconnected or controlled and a method for regulating the power value or course of the sources would have to be selected with respect to the control. The following three methods appear to be the real possibilities of CGU regulation:

- reg. of CGU in cooperation with PPP for the purpose of constant power supply
- regulation based on specific consumption at the site (island operation)
- regulation according to daily DG load diagram

However, it is necessary to take into account the current operation of the entire BGS technology, the technical properties of CGU and the method of using the produced forms of electricity and thermal energy in each way proposed. Thermal energy is used for the BGS technology or for heating nearby buildings. Therefore, when designing CGU regulation, it is necessary to take into account the supply of thermal energy from the considered BGS, which will account for about 20-30% of all produced thermal energy. [2]

6.1 CGU continuous (dynamic) control

This mode of control is the most acceptable in terms of the assumption of a constant supply of electricity to a given part of Dg (transformer, node, etc.). The required output control from the backup source, represented by a CGU in this case, is done smoothly according to a specific requirement for the required control output. However, it is necessary to determine the output value which the regulation will be designed for. Furthermore, it is necessary to take into account the technical possibilities of CGUs or their operational efficiency. We will consider the possibility of CGU regulation in the range of about 50-100% of nominal electrical output.

7 Example of cooperation between specific BGS and PPP

A virtual combination of the two sources described above was created to illustrate the possibilities of cooperation between BGS and PPP. The basic data on PPP and BGS operation are taken from previously performed measurements on BGS. BGS will have a total installed power of approx. 1100kW. Electricity and thermal energy will be produced in 4 CGUs with an output of 1x 350kWe + 3x 250kWe for this BGS. According to the above mentioned parameters, we will consider the maximum stable supplied power of all CGUs of 1000kWe as the assumption of 100% reliable supply from the BGS. The CGU regulation option will be set in the range of 550-1000Kw (50-100% for each CGU) with regard to their efficacy and preserving sufficient thermal energy. Furthermore, we will assume the use of the most suitable type of regulation, namely continuous (dynamic) CGU regulation. In order to determine the basic characteristics of PPP production, the actual long-term measured data from the PPP having an electrical output of 1.1MWp will be used. Considering the seasonal variability of power supply to DG, we will use a sample of 3 days in June and 3 days in November. These time periods were selected at random. The June time period characterizes the possibility of PPP and BGS cooperation during the high PPP production potential, contrarily to the November time period.

Both the above sources will virtually cooperate into one point of the DG, specifically 04/22kV distribution transformer, for simplification purposes.

7.1 Cooperation of BGS and PPP without CGU regulation

Example supply from PPP and BGS without regulation is evident from Fig.2 below. The BGS supply is represented by the yellow curve, while the PPP supply is orange. The BGS supply is stable according to the assumption of 100% reliable operation; on the contrary, the PPP supply fluctuates considerably, both in the slow changes (daily cycles) and the rapid changes (cloud amount change). There are changes in the range from 0 to 850kWe within the long-term/daily changes; short-term changes are in the range from 125 to 750kW. The total power supplied is represented by the green curve, with the mean supplied power to the DG being ca. 1289kW with a minimum of 998kW and a maximum of 1929kW. [2,3]



Fig. 2. Theoretical course of total active power from both sources to one DS point



Fig. 3. Theoretical course of total active power from both sources to one DS point

7.2 CGU regulation by supply from PPP

Diagram on Fig. 3 shows the output to the DG with the CGU regulation. Dynamic regulation was selected to control the CGU output, with the aim of achieving the most balanced power supply to the DG in a given period of time. The result of this regulation is the CGU production limitation during the PPP power supply and then its re-increase outside the PPP operating time. As stated above, the CGUs were regulated in the range of 50-100% of nominal output.

The average value of the power supplied to the grid was approximately 1083kW with the regulation, and it fluctuated in the range from 1000 to 1377kW. The diagram also shows that there was a significant reduction in the rapid changes in the power supply to the DG, while also limiting the maximum peak power when changing the PPP supply. Specifically, the fluctuation of total power to the DG was reduced from ca. 931kW to ca. 377kW. The above simulation corresponds to the PPP operation in summer months when the contribution of the PPP production is the highest.

7.3 Preconditions for PP and BGS cooperation

In this case, it is possible to retrofit the BGS with another CGU which would ensure the consumption of surplus biogas, while providing additional optimization and regulation. This additional CGU would be switched on only in the case of the BGS operation

with surplus biogas produced, i.e. at the time when BGS output would be regulated. By adding another suitably large CGU, the regulatory output would be increased again, while consuming the surplus biogas.

8 Conclusion

Using the above-described analysis of the cooperation of PPP and BGS, we can conclude that cooperation between the two sources is theoretically possible with a clear benefit for the DG. There was a significant reduction in the size of output fluctuation, both for short-term and long-term changes, in our simulation at all times using smooth regulation. The knowledge gained through this article will be further extended and applied to the previously created virtual model of BGS and PPP. The precondition is to complement the existing BGS and PPP cooperation with other variables such as power fluctuations in CGU, change in biogas consumption in CGU load change and possible size of other, new CGUs, as well as the conversion of all values from the 0.4kV level to the 22kV level for greater versatility of the model. The outcome of this model should be specific information about the possible cooperation of the two selected sources, as well as the technical parameters and preconditions needed to modify the existing operation.

The present results were included in the following publications:

1. Ladislav Novosád, Zdeněk Hradílek: Model of electric output from biogas station, The 9th International Scientific Symposium ELEKTROENERGETIKA 2017, 12.-14.9.2017, Stará Lesná, Slovak Republic. 576-579, ISBN: 978-80-553-3195-9
2. Ladislav Novosád, Zdeněk Hradílek, Návrh virtuálního modelu elektrického výstupu z bioplynové stanice, Energetika, číslo 2, 2018, ročník 68, strana: 341-345, DOI: 10.1109/EPE.2015.7161098

Acknowledgement: This research was partially supported by the SGS grant from VSB - Technical University of Ostrava (No. SP2018/61) and by the project TUCENET (No. LO1404).

References

1. L. Freris, D. Infield, "Renewable energy in power systems", Chichester, U.K.: John Wiley, 2008, XIV, 284p., ISBN 978-047-0017-494
2. L. Novosád, Z. Hradílek: Model of electric output from biogas station, The 9th International Scientific Symposium ELEKTROENERGETIKA 2017, 12.-14.9.2017, Stará Lesná, Slovak Republic. 576-579, ISBN: 978-80-553-3195-9
3. L. Novosád, Z. Hradílek: Design virtual model of electricity supply from biogas station, Proceedings of the 2017 18th International Scientific Conference on Electric Power Engineering (EPE), IEEE 2017, May 17-19, 2017, Hotel Dlouhé Stráně, Kouty nad Desnou, Czech Republic, 246-249, ISBN 978-1-5090-6405-2
4. Biogas production statistics, In: [online]. [2018-01-10]. Available from: <http://www.czba.cz/mapa-bioplynovych-stanic/>
5. Department of ERÚ statistics, Annual report on the operation of ES CR 2016. In: [online]. Praha, 2017 [2018-01-12]. Available from: <http://www.eru.cz>

Reliability of the PV system operation influencing connection to the distribution network

Petr Seroiszka

Department of Electrical Power Engineering, FEECS,
VŠB – Technical University of Ostrava, 17. listopadu 15,
708 33 Ostrava – Poruba, Czech Republic
`petr.seroiszka.st@vsb.cz`

Abstract. This paper deals with the reliability of the PV system's connection to the distribution network. The first part defines the conditions for the PV system's connection to the distribution network, while the second part defines the factors influencing the reliability of the PV system's operation and connection to the distribution network. The paper contains production data describing the failure and subsequent analysis of the failure of central inverters of the PV system. In the conclusion there are recommendations for the use of methods to analyse faults and to determine system reliability using the multi-criteria method.

Keywords: reliability, insulation resistance, inspection, verification of the PV system, Metrel, Benning 1-1, measurement, solar I-V, multi-criteria, analysis, method

1 Introduction

Almost 29,000 PV systems with an output of 2,300 MW have been built in the Czech Republic up to 2018.[2] These include photovoltaic systems with an output between 2.1 kW and 10 kW installed on residential houses and industrial rooftop-mounted photovoltaic installations of 30 kWp and more and, in particular, photovoltaic power plants built on '*greenfield sites*'. In order to ensure reliable and safe operation of these temporary structures, usually designed for 25 years, they had to be inspected in the first place. There are many inspections and verifications used for this purpose that are capable of revealing both the condition and reliability of PV installation in order for the maximum reliability of the PV plant as a system to be achieved. By doing so, the operational yield of the PV system will be maximized and the problems with connection to the distribution network will be minimized.

2 Inspections and verifications

Primarily, the PV system is subject to the input inspection and verification. This inspection is made to compare the design documentation with the actual state, i.e.

to find whether the design and applicable standards were complied with during the construction and whether the plant can be operated safely and reliably. Without this report the final inspection of the built structure cannot be made and the respective permit to operate the same cannot be obtained, i.e. the permit allowing generation of power based on the electric energy producer's licence. In the event that a photovoltaic system has been operating for several years, a repeated inspection is made to verify the PV system parameters according to the documentation and previous verification report. When a repeated failure occurs or a nonconforming operating parameter is found, extraordinary checks and inspections are made, the outcome of which is a recommendation on the removal of the failure and the method thereof.

3 Reliability of the PV system's connection to the distribution network

The reliable day-to-day connection of the PV system to the distribution network can be influenced by several factors that are subject to the aforesaid inspections. The factors influencing reliability can be defined:

- Low insulation state of the system when the insulation monitoring device of the solar PV system does not allow connection to a central or a local inverter to the network. If the system reports such fault, we have to assess how to detect it effectively. The most frequent cause of decreased reliability is either defective or inappropriate DC cabling that is not suited for placing in water and burying in the ground. The state of insulation is also affected by defective or inappropriate connectors that may cause secondary discharging in the earthed structure. When using any connectors whatsoever, the minimum cable bending angle specified by the cable manufacturer must be maintained in the proximity of the connector to avoid any risk of moisture penetration through the rubber sealing gland and subsequent contact oxidation. Sometimes, it is the panel itself that is defective, and the current discharges from the intermediate layer directly in the panel frame. Modern central inverters with an output from 350 kW to 1,000 kW are equipped with an automatic device monitoring the temperature, condition of the distribution network and state of insulation of the DC side being connected.[3] Where there is any suspicion of a fault in this automatic monitoring device of the state of insulation, the device must only be verified and calibrated by the manufacturer. When analysing the state of insulation, we perform the check step by step from the main DC cables to the DC cables of series-connected strings.

- Mechanical wear of power parts and servo drives – this needs to be taken into account and included in the maintenance plan.

- Data transfer fault – a fault due to failure to pass the data from the combiner of series-connected panel strings to the central inverter, or between the central inverter and the data logger. This results from a suspended data flow due to a voltage peak induced in the LV and communication cabling in the form of capacitive and inductive

energy. In such a case the only help consists in switching off the data and switching it on again. The fault is usually caused by failure to observe the distance between the HV, LV and communication cabling during the construction of the PV system.

- Shielding of photovoltaic panels will result in a short-term reduction in the output and reliability of the PV system. This fault occurs in the morning hours when the inverter is running and the sun is still so low that the tops of one row are shading the direct sun rays at the bottom of the next row. It has no significant influence on the specific yield (kWh/kWp) or performance ratio (in %) that also takes account the intensity of light exposure of the panels.

4 Instruments to measure the PV system reliability

For measuring the insulation state, METREL Eurotest XC and METREL Eurotest XE meters designed for inspection engineers and Metrel Eurotest XP meters specifically designed for photovoltaics are used. Last but not least, BENNING 1-1 meters specifically designed for photovoltaics are used for maintenance and fault detection. These meters enable performing the whole measurement faster. In one measurement cycle, the insulation states between the +pole of the panel and the earthed structure as well as between the -pole of the panel and the earthed structure are measured at one time. For measuring the reliability of individual series-connected strings and panels, as applicable, SOLAR 400 or SOLAR I-V meters are used. They contain a database of several hundreds of panel manufactures and of panels themselves so that we do not need to laboriously enter the values from catalogue sheets, but only to select the panel type and quantity. Subsequently, we can directly measure the panel or entire series-connected string. We compare the output and current-voltage curves of the panel to the manufacturer's curves. The difference is shown as a percentage. The manufacturer guarantees that the output will not drop below 85% during a period of 25 years. In practice, if any panel showing an output difference with a standard deviation higher than 5% is found, we try to replace it. When measuring I-V curves and output curves of photovoltaic panels, it is necessary at first to set the panel type and quantity. For the meter, it is important to determine the light exposure properly and select either monocrystalline or polycrystalline panel type. The best results are obtained when the sun's rays fall perpendicularly to the photovoltaic panel. To check the measurements, we use a device that is placed on the measured photovoltaic panel at a real inclination and works on the principle of a sundial. The shadow cast by the meter mandrel must be located in the respective permissible annulus region. In practice, it can be said that the optimum measurement is made between 11 am and 2 pm. For the connection, refer to Figure 1.

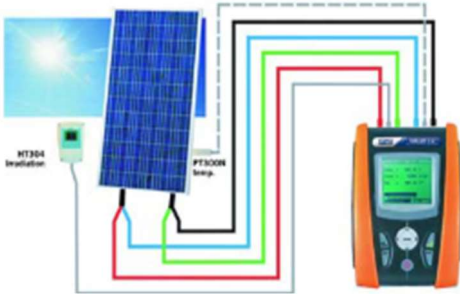


Fig. 1 [6]

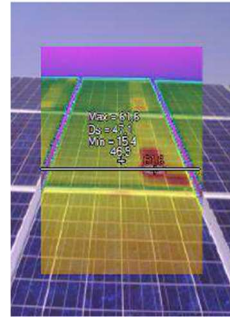


Fig. 2

Each year within the preventive maintenance, measurements are made using a FLUKE TiR125-1705114 thermal imaging camera. This measurement precedes the above-mentioned measurements because it is capable of revealing a defective cell in the photovoltaic panel at first, i.e. hotspot, which is a cell having a temperature considerably higher than the other cells. Only then is the panel reliability measured, i.e. the panel output reduction as a percentage. Subsequently, the panel insulation resistance is measured for preventive reasons. This issue is related not only with the effectiveness of power generation but also with a potential cause of fire. Therefore, thermal imaging is performed each year as a preventive measure. An example of a thermal image with a defective cell is shown in Fig. 2.

5 Reliability, and evaluation of faults

When assessing reliability and evaluating faults and defects, we need to collect data for a certain time period. Monthly power generation can be used as an example.

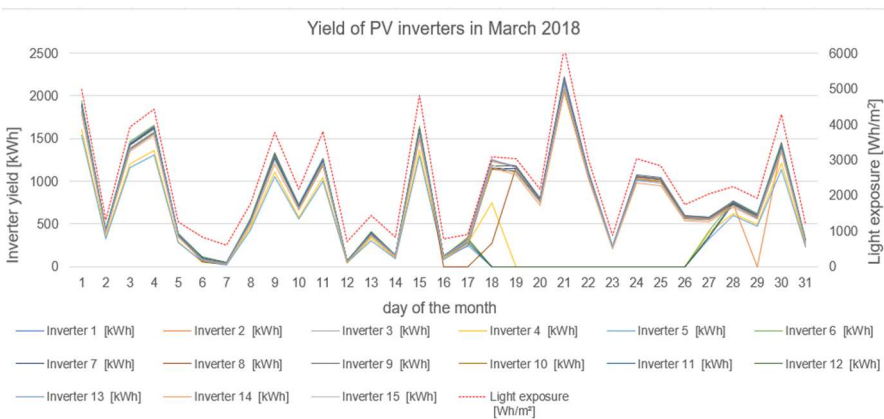


Chart 1[4]

supplied DC power from the photovoltaic panels and did not begin to supply any AC power to the distribution network.

Causes:

Potential causes have already been described above. In this case a fault was detected in the DC power switch CD 10; so, this was a mechanical fault – a fault caused by worn power parts of the system. In particular, this was a fault in the servo spring tension of the power switch. This problem was found in all five inverters; as a result, the PV system yield was reduced by one third of the production.

Measure:

These defective CD switches are not common spare parts and had to be ordered from Germany. The replacement has to be made by an authorized German guarantee contract partner. Once a Czech service company is trained, the repair, as well as shutdown times, will be shortened.

7 Conclusion

In conclusion, we can recommend that the PV system has a well-established maintenance and inspection plan and a sufficient number of spare parts available to maintain the reliability of generation. By doing so, losses in the PV system yield will be considerably reduced. To evaluate the alternatives of causes of failure rate of the PV system, it is recommended using MCA methods [1], particularly the ‘weighted sum approach’ (WSA) based on the principle of utility maximization and the ‘ideal points analysis’ (IPA) which is similar to the first method, but is best for options with the lowest utility, or the TOPSIS method (Technique for Order Preference by Similarity to Ideal Solution) based on the concept of minimization of the distance from the ideal option.

References

- [1] Hradílek, Z.: Elektroenergetika distribučních a průmyslových zařízení, VŠB-TU Ostrava, 2008, ISBN 987-80-7225-291-6
- [2] <http://www.silekro.cz/solarni-elektrarny/reseni/solarni-elektrarny>
- [3] <http://files.sma.de/dl/7796/SC4-63HE-BE-BCZ103280.pdf>
- [4] <https://portalsma.com>
- [5] Machů, Hradílek: Alternative Energy Sources Comparison for Heating a Residential House, ELNET 2017, pp. 1–9, ISBN 978–80–248–4154–0. VSB – Technical University of Ostrava, FEECS, 2017.
- [6] <http://www.manualsdir.com/manuals/367524/ht-instruments-solar-i-v-i-v400.html?page=41>

An Implementation of the DTC Method with Direct Calculation of Voltage Vector

Jakub Bača

Department of Electronics, FEECS,
VŠB – Technical University of Ostrava, 17. listopadu 15,
708 33 Ostrava – Poruba, Czech Republic
jakub.baca@vsb.cz

Abstract. Direct torque control is a modern way of controlling AC machines. This paper deals with the method of direct torque control of induction motor with direct calculation of voltage vector. The algorithm of the method was programmed into a control system with the TMS320F28335 digital signal controller, and a user application was created in LabVIEW to operate the system. The first section is dedicated to the theoretical description of the implemented method. The second section briefly describes the hardware used and courses of the most important quantities demonstrating the functionality of the implemented algorithm. The experimental results were obtained by measuring a real drive in laboratory conditions.

Keywords: Direct Torque Control, DTC, Induction Motor, TMS320F28335.

1 Introduction

There are currently three basic ways of controlling AC machines: scalar control, vector control and direct torque control. The scalar control is used only for dynamically non-problematic drives that work mainly in the steady state. For more demanding applications, vector control or direct torque control is used. These two methods are characterized by very high dynamics and the accuracy of the quantities in both steady states and transient states.

The aim of vector control and direct torque control is to achieve AC drive characteristics comparable to DC drives. The basic idea of these two methods is, therefore, to allow the independent control of the torque and excitation (flux) of a machine. For the vector control, these two variables are indirectly controlled by two mutually perpendicular components of the stator current vector, the so-called flux-generating and torque-generating current. The direct torque control of induction motor is based on the control of the electromagnetic torque and stator flux in the required tolerance band; the end-point of the stator flux vector moves along the specified curve (ideally a circle in steady state). The torque is given by the rotation speed of the stator flux vector and the magnetization of an induction motor is given by the modulus of the vector. [1, 2]

The method of direct torque control with direct calculation of voltage vector was developed in the 1990s at the Department of Electronics of VSB – TU of Ostrava. The computational algorithm was designed to provide directly, for each position of the stator flux vector, the inverter output voltage vector to be switched without the need to divide the α - β plane into sectors and create a switching table. [2, 3, 4]

The algorithm of this method was implemented using a modern control system which is based on the TMS320F28335 digital signal controller from Texas Instruments. The result is a functional laboratory application that can be further utilized within the lessons of the subject Electrical Controlled Drives III, or in other research activities and projects of the Department of Electronics.

2 Description of the control method

In Fig. 1, we can see vectors \mathbf{g}_1 and \mathbf{g}_2 plotted in the stator coordinate system $[\alpha, \beta]$. The vector \mathbf{g}_1 always has the same direction as the stator flux vector, while \mathbf{g}_2 is always perpendicular to the flux vector. By the vector sum of these two vectors, the resultant vector \mathbf{g} is given. If it is true that:

$$\Delta\Psi_1 = \Psi_{\text{ref}} - |\Psi_1^S| \quad (1)$$

$$\Delta T = T_{\text{ref}} - T \quad (2)$$

$$|\mathbf{g}_1| = k_1 \Delta\Psi_1 \quad (3)$$

$$|\mathbf{g}_2| = k_2 \Delta T \quad (4)$$

then the vector \mathbf{g} determines the direction of the voltage vector that should be switched. The constants k_1 and k_2 are weighting coefficients. If a voltage vector whose direction is identical to the vector \mathbf{g} is applied at the inverter output, then the size of vector \mathbf{g}_1 determines the degree of the motor excitation change and the size of vector \mathbf{g}_2 determines the degree of the rotation speed of the stator flux vector and thereby torque size. Since two-level voltage inverter has only eight voltage vectors – see Fig. 1, two of which are zero, it is necessary to select the vector that is in the direction closest to the desired vector \mathbf{g} . This can simply be done by determining in which sector from I to VI the vector \mathbf{g} is found and by assignment of the voltage vector which lies in the same sector. (e.g., III. $\Rightarrow \mathbf{u}_2$).

Fig. 2 shows a block diagram of the control structure. The phase currents i_{1a} and i_{1b} and the DC link voltage u_d are measured. The voltage at the motor terminals (stator voltage) is estimated from the u_d value and the switching combination. The actual torque and magnetic flux values are obtained by calculation using the values of the measured quantities and a mathematical model of an induction motor.

The key part of the control structure is the BSPC block. The output of this block is the switching combination of the voltage vector to be applied at the inverter output. In the block, the coordinates of the vector \mathbf{g} expressed in the stator coordinate system $[\alpha, \beta]$ are calculated first, they are marked as variables dx and dy in the algorithm. Then another calculations are performed to select a voltage vector (\mathbf{u}_1 to \mathbf{u}_6). In the case where

a torque reduction is requested, and a reversal is not being performed, a zero-voltage vector (\mathbf{u}_0 or \mathbf{u}_7) is preferred before the active voltage vector. Using the zero vectors to decrease the motor torque, the torque ripple, stator voltage distortion, harmonic losses and switching losses are reduced [3]. The zero vector should be selected according to the previous active vector to minimize the switching losses. The switching combination of such zero vector differs from the previous only in one phase of the inverter.

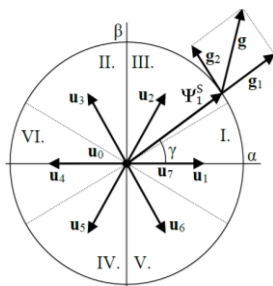


Fig. 1. Trajectory of the end-point of the stator flux vector

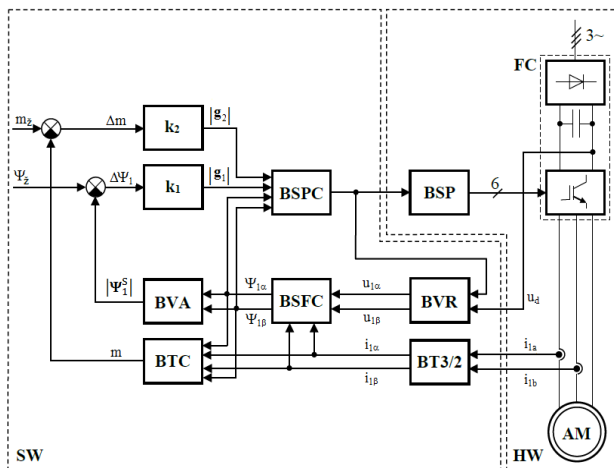


Fig. 2. Control structure of the DVC-DTC method

Meaning of blocks: **SW** – software; **HW** – hardware; **AM** – induction motor; **BT3/2** – 3/2 coordinate transformation (Clarke's transformation); **BVR** – voltage reconstruction; **BSFC** – stator flux calculation (voltage model); **BVA** – vector analyzer (modulus calculation); **BTC** – torque calculation (equation for electromagnetic torque); **BSPC** – switching pulses calculation; **BSP** – switching pulses creation.

3 Implementation

The control system used was developed at the Department of Electronics and is adapted for the control applications from the field of electric drives and power electronics. The key element of this control system is the TMS320F28335 digital signal controller from Texas Instruments which belongs to the C2000 family of microcontrollers. These microcontrollers have been designed to efficiently control embedded real-time systems, including electric drives. A common feature of the real-time systems is a large number of mathematical operations, which must be executed almost immediately.

The Digital Signal Controller (DSC) is essentially a single-chip microcomputer whose core is a Digital Signal Processor (DSP). In addition to the DSP core, the high computing power is provided by specialized hardware units. One of such units is, for example, the ePWM module which is intended to generate PWM signals controlling switching of transistors in the inverter. Using of peripherals saves the CPU time and

therefore speeds up the response of the control loop. Here is an overview of the selected parameters and peripherals of the DSC TMS320F28335:

- clock frequency up to 150 MHz (6.67 ns)
- 32-bit processor (floating point arithmetic, modified Harvard architecture, pipelining)
- ePWM (6 modules for generating PWM signals with wide setting options)
- eQEP (peripheral used to process the output signals from an incremental encoder)
- 12-bit A/D converter (0 ± 3 V, 16 channels, 80 ns conversion time per channel)
- communication peripherals: CAN, SCI(UART), SPI a I2C
- the JTAG debug interface

The source code for the controller was written in C, in the Code Composer Studio development environment, which is a part of Texas Instruments software support. The control system can be operated using an application created in LabVIEW – Fig. 3.

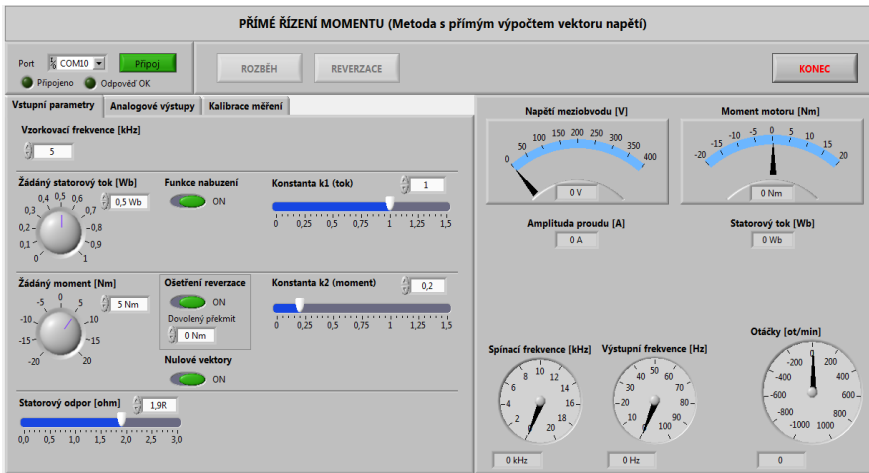


Fig. 3. User interface – main window

4 Experimental results

The following figures show the time courses of quantities obtained by measuring on a laboratory drive which consisted of an induction motor, a loading mechanism (separately excited DC motor), a frequency converter with a DC link and a control system. The internal variables were being written to the analogue output of the control system (4-channel D/A converter) and displayed on the *LeCroy Wave Surfer 424* oscilloscope. The DC link voltage was set to $U_{DC} = 200$ V. The values of the weighting coefficients were experimentally determined as follows: $k_1 = 1$ and $k_2 = 0.1$.

Rated parameters of the induction motor: $P_n = 2.7$ kW; $n_n = 1360$ min⁻¹; $T_n = 19$ Nm; $|\Psi_1|_n = 0.877$ Wb; $U_{1n} = 380/220$ V; $I_{1n} = 7.51$ A; $f_n = 50$ Hz.

Fig. 4 shows the start-up of the drive at a step change of the torque setpoint from 0 to 5 Nm. After an initiation of the start-up request, the motor excitation was performed

first. When the absolute value of the stator flux vector had reached the setpoint of 0.5 Wb, the direct torque control algorithm was launched. Then the flux vector began to rotate, a rotating magnetic field arose, and the motor torque was rising to the setpoint of 5 Nm very steeply. The movement of the flux vector during start-up is captured in the Fig. 5. Without previous motor excitation, an undesirable current overshoot would occur.

A steady state is captured in Fig. 6. The motor had to be loaded enough to prevent reaching a state where the rotor speed is too high, so it is impossible to develop the magnetic field frequency that is necessary to generate the desired torque. If the state is reached, the stator current and flux are being deformed and the motor torque is decreasing. The maximum speed depends on the DC link voltage and motor excitation.

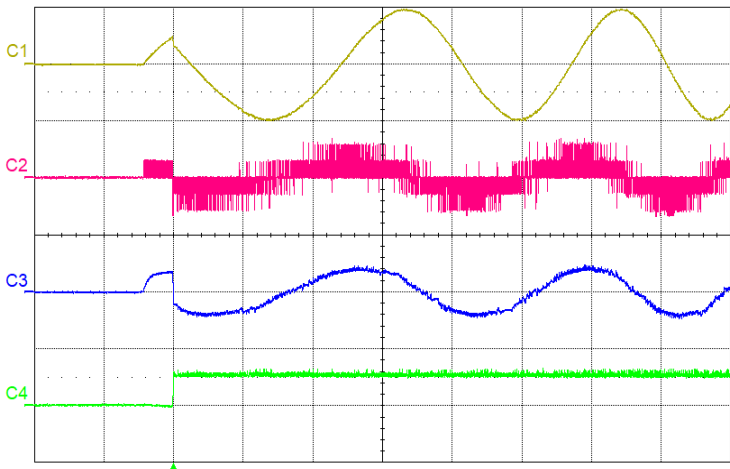


Fig. 4. Start-up of the drive ($T_{ref} = 0/5$ Nm; $\Psi_{ref} = 0.5$ Wb; $f_{sa} = 10$ kHz). (t : 50 ms/d; C1: $\Psi_{1\alpha} = f(t)$, 0.5 Wb/d; C2: $u_{1\alpha} = f(t)$, 200 V/d; C3: $i_{1\alpha} = f(t)$, 10 A/d; C4: $T = f(t)$, 10 Nm/d)

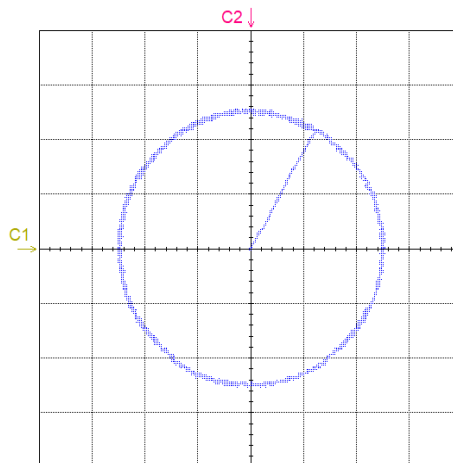


Fig. 5. Trajectory of the stator flux vector at start-up ($T_{ref} = 0/5$ Nm; $\Psi_{ref} = 0.5$ Wb; $f_{sa} = 10$ kHz). (t : 50 ms/d; C1: $\Psi_{1\alpha}$, 0.2 Wb/d; C2: $\Psi_{1\beta}$, 0.2 Wb/d)

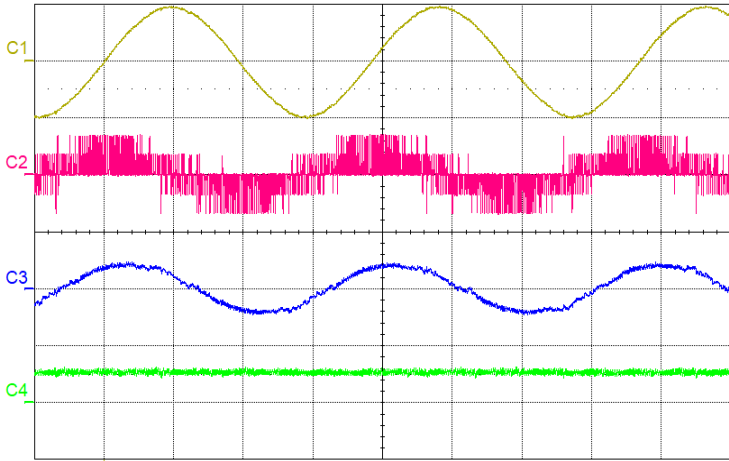


Fig. 6. The drive in a steady state ($T_{\text{ref}} = 5 \text{ Nm}$; $\Psi_{\text{ref}} = 0.5 \text{ Wb}$; $f_{\text{sa}} = 10 \text{ kHz}$). (t : 20 ms/d; **C1**: $\Psi_{1\alpha} = f(t)$, 0.5 Wb/d; **C2**: $u_{1\alpha} = f(t)$, 200 V/d; **C3**: $i_{1\alpha} = f(t)$, 10 A/d; **C4**: $T = f(t)$, 10 Nm/d)

5 Conclusion

The experimental results confirmed the functionality of the realized algorithm of direct torque control. As can be seen from the pictures, with the correct adjustment of the weighting coefficients, it was possible to achieve sinusoidal courses of the stator currents and flux, and the trajectory of the stator flux vector approximated a circle quite well. It turned out, however, that the optimal setting of k_1 and k_2 may depend on the actual operating state of a drive. These dependencies could be examined and the software enhanced with a function of weighting coefficients adaptation.

Acknowledgement

This paper was supported by the project No. SP2018/162 funded by the Student Grant Competition of VSB – Technical University of Ostrava.

References

1. VAS, Peter. *Sensorless vector and direct torque control*. New York: Oxford University Press, 1998. ISBN 0198564651.
2. BRANDSTETTER, Pavel. *A.C. Control Drives – Modern Control Methods*. Ostrava: VSB-Technical University, 1999. ISBN 80-7078-668-x.
3. HRDINA, Libor. *Direct Torque Control Methods of Induction Motors*. Ostrava, 2008. PhD thesis. VSB-Technical University of Ostrava.
4. BRANDSTETTER, P., P. CHLEBIS a P. PALACKY. Direct Torque Control of Induction Motor with Direct Calculation of Voltage Vector. *Advances in Electrical and Computer Engineering* [online]. 2010, **10**(4), 17-22 [cit. 2018-06-21]. DOI: 10.4316/aece.2010.04003.

Sensorless Induction Motor Drive Based on CB-MRAS Observer

Jakub Bača, Petr Chamrád, and Daniel Kouřil

Department of Electronics, FEECS,
VŠB – Technical University of Ostrava, 17. listopadu 15,
708 33 Ostrava – Poruba, Czech Republic
{jakub.baca, petr.chamrad, daniel.kouril}@vsb.cz

Abstract. This article deals the simulation of sensorless vector control of an induction motor using a CB-MRAS observer. In the introduction, the description is focused on basic problems of vector control of induction motor, followed by mathematical description of the CB-MRAS observer and the possibility of obtaining variables such as angular velocity and orientation angle. Based on the theoretical analysis, verification of the functionality of the control structure in the Matlab - Simulink is performed. The results are presented in the conclusion of the article.

Keywords: Induction motor, Sensorless vector control, CB-MRAS observer, Estimated angular speed, Estimated orientation angle.

1 Introduction

The most used type of engine in the industry is an induction motor. Its features include low price, robust construction and low need of maintenance. The disadvantage of this type of drive is a difficult manner of driving. Induction motors are powered by frequency inverter controlled by microcomputer with implemented control algorithm. In many cases, vector control excels in its robustness and dynamic properties and it is used to control AC motors.

The vector control is similar to the DC motor. For the correct separation of stator current, it is necessary to know the position of the rotor shaft measured by the incremental sensor. This is a mechanical device whose failure can lead to a malfunction of the drive. There are currently so-called observer and estimator algorithms, which to a certain extent can represent the function of the position sensor and thus increase the robustness of the drive.

2 Principle of vector control induction motor

The graphical distribution of the spatial vectors of the variables is shown in Fig. 1. The spatial vector of the stator current i_s^s is turned in the orientated orthogonal

coordinate system (OSS) with axes $[x, y]$ for easier realization. According to the spatial vector of the coupled magnetic flux of the rotor Ψ_R^O , which is initiated by the magnetization current through the main inductance of the motor, the \mathbf{i}_S^S stator current vector is decomposed into two components of stator current designated i_{Sx} and i_{Sy} . In the direction with the real axis x , there is a flux component of stator current vector and with the imaginary axis y the torque component of the stator current vector.

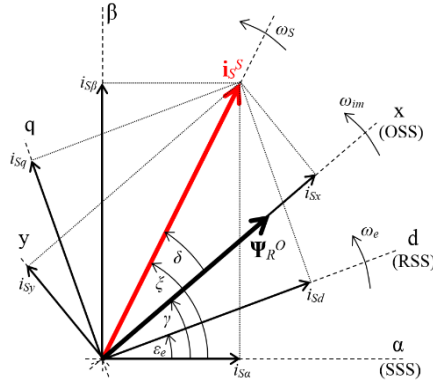


Fig. 1. Distribution of space vectors of individual variables and space distribution of orthogonal systems of induction motor

2.1 Mathematical model of induction motor

To obtain an idea of the behavior of an asynchronous motor in transient and steady states, the mathematical model of a general-purpose AC machine is used. The mathematical model is described by a set of differential equations. The moment on the shaft of the motor M_e is given by the following relation (4). Equation (3) represents the expression of the magnetizing current \mathbf{i}_m^S turned to the stator variables. Equations (6), (7) represent the final form of relations describing the behavior of an asynchronous machine.

$$\mathbf{u}_S^S = R_S \mathbf{i}_S^S + L_S \frac{d\mathbf{i}_S^S}{dt} + L_m \frac{d(\mathbf{i}_R^R e^{j\varepsilon})}{dt} \quad (1)$$

$$\mathbf{u}_R^R = R_R \mathbf{i}_R^R + L_R \frac{d\mathbf{i}_R^R}{dt} + L_m \frac{d(\mathbf{i}_S^S e^{-j\varepsilon})}{dt} = 0 \quad (2)$$

$$\mathbf{i}_m^S = \frac{\Psi_R^R e^{j\varepsilon}}{L_m} = \mathbf{i}_S^S + (1 + \sigma_R) \mathbf{i}_R^R e^{j\varepsilon} \quad (3)$$

$$M_e = \frac{3}{2} p_p L_m \text{Im}[\mathbf{i}_S^S (\mathbf{i}_R^R e^{j\varepsilon})^*] \quad (4)$$

$$L_S = (1 + \sigma_S) L_m \quad L_R = (1 + \sigma_R) L_m \quad \sigma = 1 - \frac{L_m^2}{L_S L_R} = \frac{1}{(1 + \sigma_S)(1 + \sigma_R)} \quad (5)$$

$$\mathbf{u}_S^S = R_S \mathbf{i}_S^S + \sigma L_S \frac{d\mathbf{i}_S^S}{dt} + (1 - \sigma) L_S \frac{d\mathbf{i}_m^S}{dt} \quad (6)$$

$$\mathbf{u}_R^R = R_R \mathbf{i}_R^R + L_m (\mathbf{i}_m^S e^{-j\varepsilon}) = 0 \quad (7)$$

2.2 Regulatory structure of vector control with CB-MRAS observer

The block diagram of the vector control structure with induction motor is shown in Fig. 2. The red block represents CB-MRAS observer, which determines the $\sin\gamma_{est}$, $\cos\gamma_{est}$ and mechanical angular velocity Ω_{mest} based on machine parameters and measured stator voltage and phase current. The phase current i_a and i_b is measured by a pair of current sensors and fed to the T3/2 transform block. Its outputs are currents called $i_{S\alpha}$ and $i_{S\beta}$ in the SSS with axes $[\alpha, \beta]$. The components of the stator current $i_{S\alpha}$, $i_{S\beta}$ and the estimated $\sin\gamma_{est}$ and $\cos\gamma_{est}$ are processed by the BVN block. The result of the conversion is the i_{Sx} flux component of stator current and the torque component of stator current i_{Sy} in the OSS. Measured currents i_{Sx} and i_{Sy} are fed to the flux controller of stator current (R_{iSx}) and the torque controller of stator currents (R_{iSy}) couple with desired values of stator currents $*i_{Sx}$ and $*i_{Sy}$. The outputs of controllers are the control voltages u_{Sx} and u_{Sy} to which a error signal from the BZV is added. Block BVN^{-1} with oriented angle ensures rotation from OSS to SSS. The control voltage $u_{S\alpha}$ and $u_{S\beta}$ are converted (T2/3) to three-phase voltages u_a , u_b and u_c for the PWM of the inverter. Angular speed controller R_Ω is override to torque controller of stator current R_{iSy} .

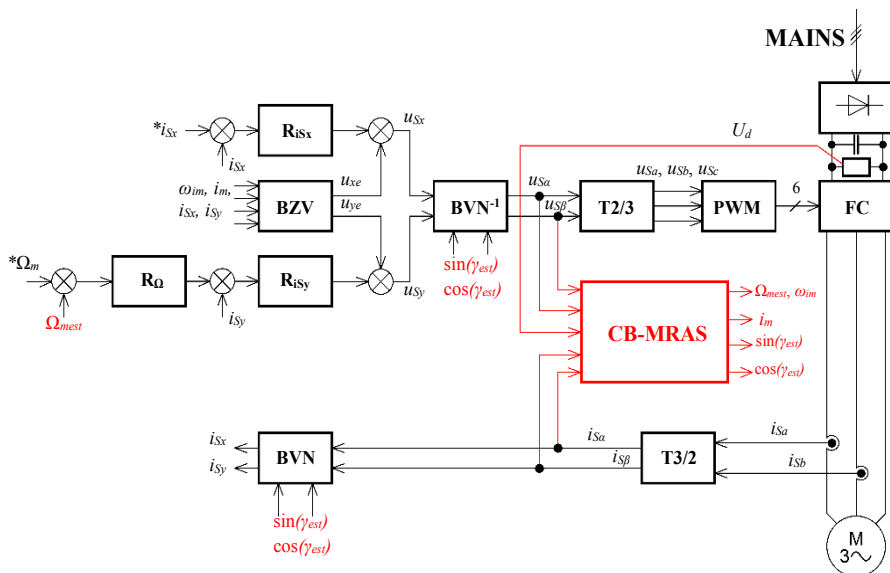


Fig. 2. Block structure of sensorless vector control of induction motor with CB-MRAS observer

By the vector rotation of relationship (6) from the SSS to the OSS, we modify the equation to form (8) and (9) respectively. This gives us an idea of the induction

motor behavior in vector control. Equations (10) and (11) are obtained by separation vectors into the real and imaginary part.

$$\mathbf{u}_S^0 = u_{sx} + ju_{sy} = R_S \mathbf{i}_S^0 + \sigma L_S \frac{di_S^0}{dt} + j\omega_{im} \sigma L_S \mathbf{i}_S^0 + (1 - \sigma) L_S \frac{di_S^0}{dt} + j\omega_{im} (1 - \sigma) L_S \mathbf{i}_S^0 \quad (8)$$

$$\mathbf{i}_S^0 = T_R \frac{di_m^0}{dt} + j\omega_{im} T_R \mathbf{i}_m^0 + (1 - j\omega_e T_R) \mathbf{i}_m^0 = i_{sx} + ji_{sy} \quad (9)$$

$$\sigma T_S \frac{di_{sx}}{dt} + i_{sx} = \frac{u_{sx}}{R_S} + \omega_{im} \sigma T_S i_{sy} - (1 - \sigma) T_S \frac{di_m}{dt} = \frac{u_{sx}}{R_S} + u_{xe} \quad (10)$$

$$\sigma T_S \frac{di_{sy}}{dt} + i_{sy} = \frac{u_{sy}}{R_S} + \omega_{im} \sigma T_S i_{sx} - (1 - \sigma) \omega_{im} T_S i_m = \frac{u_{sy}}{R_S} + u_{ye} \quad (11)$$

$$T_R \frac{di_m}{dt} + i_m = i_{sx} \quad (12)$$

$$\begin{aligned} \omega_{im} &= \frac{d\gamma}{dt} & \omega_e &= \frac{d\varepsilon_e}{dt} \\ T_S &= \frac{L_S}{R_S} & T_R &= \frac{L_R}{R_R} \end{aligned} \quad (13)$$

2.3 CB-MRAS observer

Mathematical equations describing the CB-MRAS observer are listed below. The oriented variables $\sin\gamma_{est}$ and $\cos\gamma_{est}$ is obtained by the equation (20).

$$\Psi_{Rest}^S = \int \left[(j\omega_{eest} - \frac{1}{T_R}) \Psi_{Rest}^S + \frac{1}{T_R} L_m \mathbf{i}_S^S \right] = \Psi_{Raest} + j\Psi_{R\beta est} \quad (14)$$

$$\mathbf{i}_{Sest}^S = \frac{1}{\tau_i} \int (k_1 \mathbf{u}_S^S + k_2 \Psi_{Rest}^S - j\omega_{eest} k_3 \Psi_{Rest}^S - \mathbf{i}_{Sest}^S) dt = i_{saest} + ji_{s\beta est} \quad (15)$$

$$\Phi(e) = (\mathbf{i}_S^S - \mathbf{i}_{Sest}^S) \times \Psi_{Rest}^S = (i_{s\alpha} - i_{saest}) \Psi_{R\beta est} - (i_{s\beta} - i_{s\beta est}) \Psi_{Raest} \quad (16)$$

$$\omega_{eest} = K_p \Phi(e) + K_I \int_0^{t_v} \Phi(e) dt \quad (17)$$

$$\Omega_{mest} = \frac{\omega_{eest}}{p_p} \quad (18)$$

$$k_1 = \frac{\frac{L_R}{L_m}}{\frac{L_R R_S + L_m}{L_m} + \frac{L_m}{T_R}} \quad k_2 = \frac{L_m}{T_R L_R R_S + L_m^2} \quad (19)$$

$$k_3 = \frac{1}{\frac{L_R R_S + L_m}{L_m} + \frac{L_m}{T_R}} \quad \tau_i = \frac{\frac{L_S L_R - L_m^2}{L_m}}{\frac{L_R R_S + L_m}{L_m} + \frac{L_m}{T_R}}$$

$$\sin(\gamma_{est}) = \left(\frac{\Psi_{R\beta est}}{\sqrt{\Psi_{Raest}^2 + \Psi_{R\beta est}^2}} \right) \quad \cos(\gamma_{est}) = \left(\frac{\Psi_{Raest}}{\sqrt{\Psi_{Raest}^2 + \Psi_{R\beta est}^2}} \right) \quad (20)$$

The block diagram of the CB-MRAS observer is shown in Fig. 3. It consists of two estimators, one of which is called the current model (reference model) and the other is the current estimator (adaptive model). The observer includes an adaptation

algorithm and a PI controller. Output is the estimated angular speed of the rotor ω_{est} . In addition, using the CB-MRAS observer, it is possible to determine orienting variables such as the oriented angle γ_{est} .

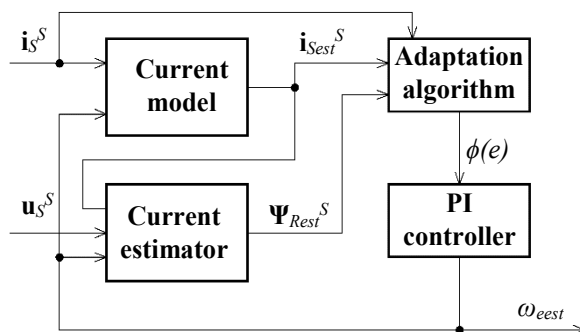


Fig. 3. CB-MRAS observer block diagram

3 Simulation of sensorless vector control IM with CB-MRAS observer

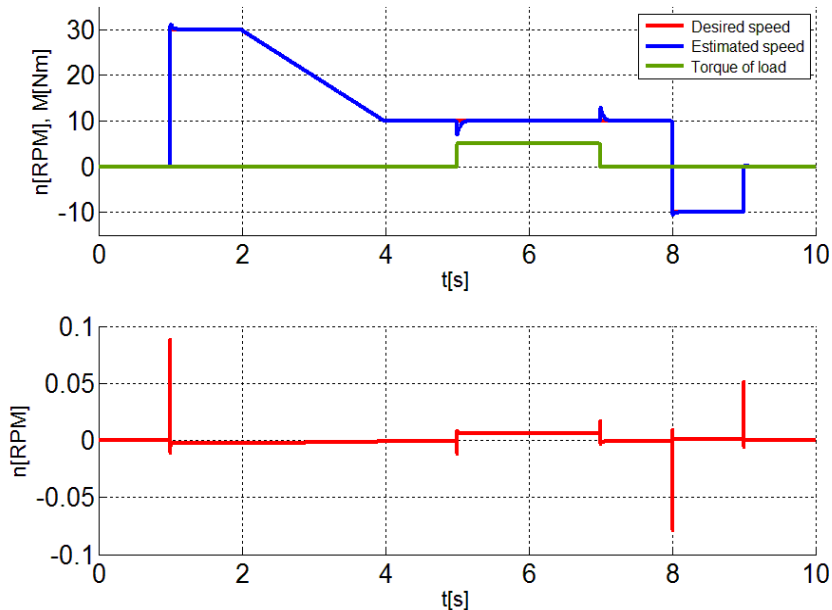


Fig. 4. The results of simulation of sensorless vector control of an induction motor with a CB-MRAS observer (top speed, estimated speed and torque load, bottom difference between actual and estimated speed)

The control structure of Fig. 2 was implemented to Matlab-Simulink. For the induction motor model, the P112M04 (MEZ Frenštát) type was used, which is used for laboratory purposes. Verification of control with the CB-MRAS observer has been simulated in various working areas of motor operating speed. The simulation was accomplished in the working area of very low motor speeds. The engine was first started at 30RPM, then slowed to 10RPM and loaded at 5Nm. Then the motor was relieved and set in at -10RPM. The results of the speed (including the difference between the actual and the estimated speed) are shown in Fig. 4.

4 Conclusion

This article describes one of many types of closed-loop MRAS observers. Based on the theoretical analysis (above), a control structure of sensorless vector control of an asynchronous motor with a CB-MRAS observer was created in the Matlab-Simulink. The results are shown in Fig. 4. The algorithm of the sensorless vector control of the asynchronous motor with the CB-MRAS observer was implemented in the microcomputer control system with the DSP TMS320F28335 and tested in the laboratory with good results. The device is currently used for educational and study purposes.

References

1. Pavel Brandštetter.: *Elektrické regulované pohony III*. Ostrava: VŠB – TU Ostrava, 2012.
2. Mateusz Dybkowski, Teresa Orłowska-Kowalska.: Low-speed Performance of the Stator Current-based MRAS Estimator with FL Controller in the Sensorless Induction Motor Drive. Wrocław University of Technology, Poland.
3. Peter Vas.: *Sensorless Vector and Direct Torque Control*. Oxford University Press, 1998.
4. Mateusz Dybkowski, Teresa Orłowska-Kowalska.: *Self-Tuning Adaptive Sensorless, Induction Motor Drive with the Stator Current-Based MRAS Speed Estimator*. Wrocław University of Technology, Institute of Electrical Machines, Drives and Measurements, Poland, 2009.

Acknowledgement

In the paper there are the results of the project SP2018/162 which was supported by Student Grant Competition of VSB – TU Ostrava.

Malfunction Simulation for Combustion Engines Powermanagement Systems

Tomáš Harach

Department of Electronics, FEECS,
VŠB – Technical University of Ostrava, 17. listopadu 15,
708 33 Ostrava – Poruba, Czech Republic
tomas.harach@vsb.cz

Abstract. This paper deals with the proposition of a reliable way of simulation of internal combustion engines powermanagement system faults for testing purposes.

Keywords: engine management system · compression ignition engine · engine ECU · engine control and regulation processes · engine flash memory modifications · engine · powermanagement · EGR system · injection system · boost system.

1 Introduction

Engine management systems are very complex nowadays and their testing requires a high-level skillset. In some cases, it can be required for an engine management system to operate with a dysfunction. An example, in which could be needed for the engine management to operate with a certain dysfunction is to measure the impact of this dysfunction on the exhaust gas composition.

The composition of exhaust gas can be described mathematically as a result from many variables interfering with the combustion quality and effectivity process. The closed loop regulation processes present in the modern engine management systems adjust their settings to achieve maximum performance, while maintaining the goals of the emission standard, into which the vehicle belongs.

This paper presents a repetitive and reliable way of a engine management modifications with a goal of engine management dysfunction simulation.

2 A Brief Common Engine Management Analysis ATD Engine Code, VW Group

This engine is managed by BOSCH EDC 15P engine control unit. It is equipped with a proportional control valve for the EGR system, proportional control valve for the geometry of the turbocharger, and a Unit Injector System.

2.1 Boost Control System

This system is characterized by the maximum absolute boost pressure which it is configured to achieve. The boost pressure (mbar) is regulated according to the engine speed (min⁻¹) and the injected fuel quantity (mg/stroke). There are several corrections that are present in the form of correction maps for the value of the absolute boost pressure.

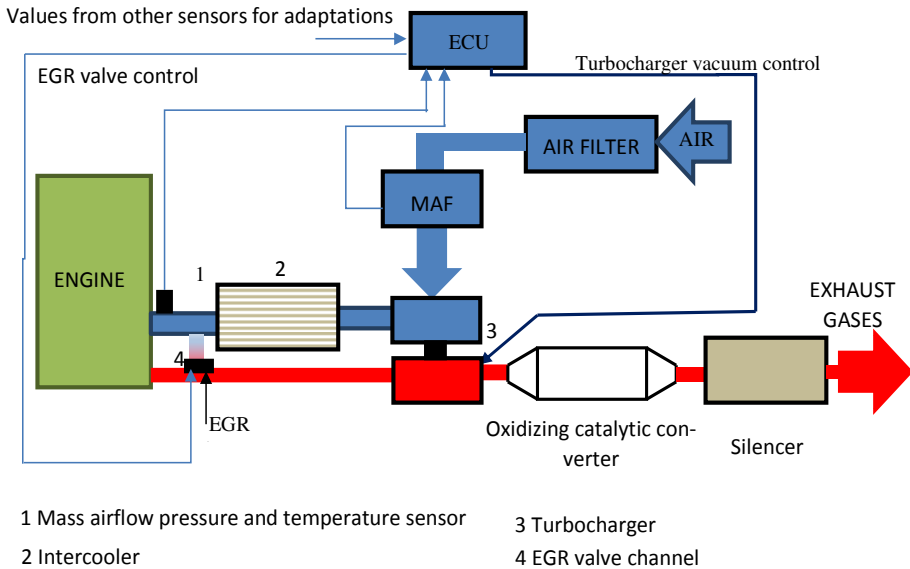


Fig. 1. ATD boost control system.

The Single Value Boost Limiter is used in function of the boost system fault detecting element. If exceeded, the engine management is set to limp home mode to not damage the boost system and the engine unit. The Boost limit map is used to correct values of absolute boost pressure (mbar) according to the current atmospheric pressure (mbar) and the engine speed (min⁻¹). The atmospheric pressure (mbar) value is measured by the pressure sensor integrated directly in the ECU. This map is also known as the altitude correction map.

2.2 EGR Control System

The EGR system is used to reduce NO_X emissions in the exhaust gases. The growth of NO_X emissions is caused by high temperatures of combustion mixture in combustion chamber. Using a controlled valve in the intake tract of the engine, part of the exhaust gas is brought back to the intake manifold of the

engine, which in turn reduces the combustion temperature. This phenomenon occurs because of the relatively high ability of the exhaust gases to absorb heat and by reducing the proportion of oxygen in the intake air [2].

The addition of exhaust gases to the air supply can degrade drivability by causing combustion effectiveness, especially at idle or low engine speeds and with a cold engine. Typically, the engine coolant temperature threshold is required before EGR is activated. Under acceleration and at idle the EGR is not activated.

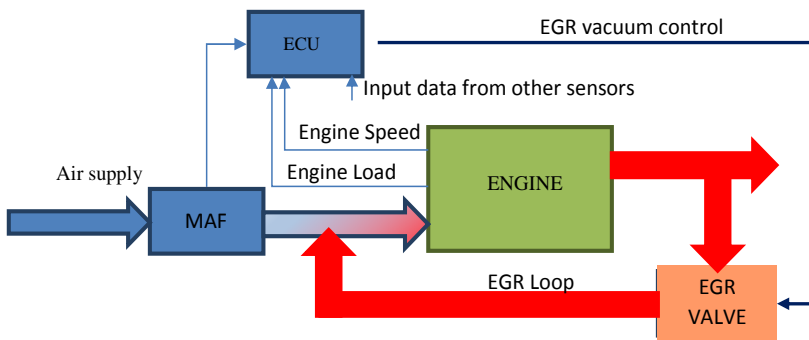


Fig. 2. EGR control loop [1].

Increasing the proportion of exhaust gases above a certain threshold leads to incomplete combustion of fuel and therefore increased presence of Hydrocarbons (HC) and Carbon Monoxide (CO) in the exhaust gases.

The amount of exhaust gases that are brought back to the combustion process through the EGR valve is measured indirectly as a difference between the theoretical value of air mass and the measured value at the mass airflow sensor. The duty cycle of controlling signal of the EGR vacuum valve is preprogrammed in the field of constant values and it is dependent on the engine speed and signal from MAF sensor [2].

2.3 Injection System

The ATD engine unit is equipped with PD injection system, in which the main injection pressure is achieved by the rotation of camshaft which presses onto the pump piston and as a result pressurizes the fuel that is injected directly into the combustion chamber through the injector nozzle. The amount of injected fuel is controlled by the high-pressure solenoid valve, as well as the precise timing of

fuel injection.

The injection system is the most important system in the engine management system. The fuel must be injected into the combustion chamber at the correct quantity, with the right timing and at a right pressure in order to form a good air/fuel mixture. Even minimal abnormalities in this system lead to higher levels of emission compounds or a bad fuel economy [1].

The fuel injection in PD injection system, which is controlled by electromagnetic valves, is separated into the pre injection cycle, and the main injection cycle.

Before the main combustion process a small amount of fuel is injected into the cylinder in order to raise the temperature and pressure in the combustion chamber. The purpose of the pre-injection cycle is to make the combustion process smoother, speed up the ignition of the main injection fuel amount and to lower the emissions of nitrogen oxides [4].

The injected fuel amount is set to the ECU by the request of the driver by monitoring the signal from the accelerator pedal and the engine speed. There are several corrections that change the injected fuel amount according to prescribed limits.

Injection duration is the period of time during which fuel enters the combustion chamber through the injector. It is essentially the difference between the Start of Injection (SOI) and End of Injection (EOI) and is expressed in degrees, which are related to the rotational movement of crankshaft.

The SOI value for any given engine condition is related to engine speed, injected fuel amount, the engine temperature correction, ambient barometric pressure and others. It is usually expressed degrees with respect to the rotational movement of crankshaft [2].

3 The Example of the Dysfunction Simulation - ATD Engine Maximum Power Enhancement

A non-conventional dysfunction was chosen to be executed specifically on this type of engine unit ECU remap. By performing engine unit software modifications, engine power was increased.

Hardware modifications can be executed to gain additional power output from the engine unit, most common being just software modifications. This dysfunction was performed by changing values that are stored in the FLASH memory of the ECU. This memory can be electrically erased and transformed

using specialized equipment.

n min-1	Driver wish(Pedal position,Rpm)/mg/str							
	1	4	10	23	45	65	85	100
0	Edited maximum requested injected fuel volume according to engine speed and accelerator pedal position (mg/stroke)				44,40	51,20	60,00	66,00
399					35,00	51,20	60,00	62,00
609					30,80	51,20	60,00	60,00
900					27,00	51,20	60,00	60,00
1008	0,00	2,70	0,10	10,90	25,16	51,20	60,00	60,00
1491	0,00	1,40	3,50	10,90	20,40	47,77	56,57	60,00
1995	0,00	0,00	2,50	8,50	18,00	42,91	51,71	60,00
2499	0,00	0,00	2,00	7,50	17,00	39,57	48,37	60,00
3003	0,00	0,00	1,50	7,00	16,30	36,51	45,31	60,00
3990	0,00	0,00	0,60	6,00	15,40	30,09	38,89	60,00
4998	0,00	0,00	0,00	5,00	13,60	28,00	34,75	60,00

Fig. 3. Edited injected fuel volume (mg/stroke).

Corrections were made to the field of constant values to increase the fuel amount entering the engine during the main injection cycle Fig. 3 and the required boost pressure was edited. Other corrections to values of requested absolute intake manifold pressure and injected fuel quantity had to be performed to the field constant values in order to increase the power production.

All these values had to be modified to suit new requested values for injected fuel volume and the raised boost pressure.

Additional corrected values include values for:

- smoke limiter,
- boost limiter,
- torque limiter,
- injection duration.

The key principal of the ECU remap of turbocharged compression ignition engines is basically supplying more fuel quantity and additional pressurized air to the process of combustion and therefore increasing the effective power of the engine unit.

The effective power can be calculated as using formula:

$$P_e = i \cdot V_c \cdot p_{eC} \cdot \frac{n}{\tau}, \tag{1}$$

where: P_e - effective power, i - number of cylinders of the engine unit, V_c - displacement of one cylinder, p_{eC} - mean effective pressure on the piston, n - engine speed, τ - number of engine cycles.

The displacement of the engine unit is represented by:

$$V_a = V_c \cdot i, \quad (2)$$

where: V_a [dm³] - displacement of an engine.

As shown distinctly from formula 1, the effective engine power can be increased by increasing the mean effective pressure on the piston. The mean effective pressure can be increased by introducing more fuel to the combustion process. To effectively burn the enlarged amount of fuel, larger quantity of air mass has to be supplied to the combustion process [5]. The mean effective pressure is represented by:

$$p_{eC} = \frac{CV}{\lambda_r \cdot \sigma_t} \cdot \sigma_{in} \cdot \eta_{vol} \cdot \eta_i \cdot \eta_m, \quad (3)$$

where: CV - calorific value of fuel, λ_r - combustion coefficient air ratio, σ_t - theoretical air/fuel mixing ratio, η_{vol} - volumetric efficiency, σ_{in} - density of intake air, η_i - indicated engine efficiency, η_m - mechanical engine efficiency [5].

4 Conclusion

As the paper presents, a reliable way of modifying powermanagement systems to simulate a dysfunction is to adjust the values stored in the engines ECU flash memory. By adjusting these values, many dysfunctions can be executed without the need of engine powermanagement hardware modifications. This proposed methodology can serve as a repetitive and reliable way of modifying engine powermanagement for testing purposes.

This proposed methodology requires some specialized equipment and high-level knowledge of the engine management systems. By the optimization of the values stored in the ECUs flash memory faulty sensors, actuators and also faulty engine components can be simulated to some extent.

Acknowledgement

This paper presents the results from the project reg. no. SP2018/167 funded by the Student Grant Competition of VSB–Technical University of Ostrava. This research was supervised by Ing. Petr Simonik, Ph.D.

References

1. RIBBENS, B. W. *Understanding Automotive Electronics*. Sixth Edition. USA: Elsevier Science, 2003. ISBN 0-7506-7599-3.
2. BOSCH, R. *Electronic diesel control EDC*. 1st edition. Stuttgart, 2001. ISBN 80-903132-4-8.
3. BOSCH, R. *Common rail injection system*. 1st edition. Stuttgart, 2004. ISBN 80-903132-7-2.
4. Delphi Worldwide Emission Standards, Passenger cars and light duty vehicles. 2016.
5. HEISLER, H. *Advanced engine technology*. 1st edition. Oxford, 2002. ISBN 1-56901-734-2.

The Control and Regulation Processes of Electronic Diesel Control Systems

Tomáš Klein

Department of Electronics, FEECS,
VŠB – Technical University of Ostrava, 17. listopadu 15,
708 33 Ostrava – Poruba, Czech Republic
tomas.klein@vsb.cz

Abstract. This article deals with an analysis of an engine control systems application software. In the introduction, an analysis of all EDC generations is performed, followed by an analysis of a specific application software. The next section deals with editing/optimalization of Electronic Control Unit data. This article also includes an experimental verification of results.

Keywords: Bosch EDC · EGR valve · exhaust gas emissions · OBD · OLS300 control and regulation · WinOLS.

1 Introduction

For modern diesel engines, exhaust emissions are reduced by optimized control and regulation algorithms that are indirectly controlling the combustion process. The Electronic Diesel Control (EDC) adjusts the injected fuel quantity according to load and engine speed and further adjusts this value based on actual temperature, atmospheric pressure, etc.

For the further research of the control and regulation processes Bosch control unit (type EDC15P) was used. This unit was modified and then supplemented with an OLS300 module which works with the WinOLS software. The modified control unit provides readings of the currently read values and allows real-time change of important data while the engine is running.

2 The Generation of EDC Engine Control Units

Bosch EDC (Electronic Diesel Control) is an electronic control system for modern diesel engines. It controls all the parameters that make the combustion process efficient, with low emission production. These control units are used by a wide range of car manufacturers such as BMW, VW AG, Opel and many others.

This article focuses on the EDC15P control units, which are mounted in VW AG vehicles with the TDI-PD engine.

2.1 EDC15

The base of the control unit is a multilayer circuit board, on which all important components are located. The main components include microcontroller, FLASH memory, voltage stabilized power supply, low and high power drive circuits, EEPROM and I/O circuits.

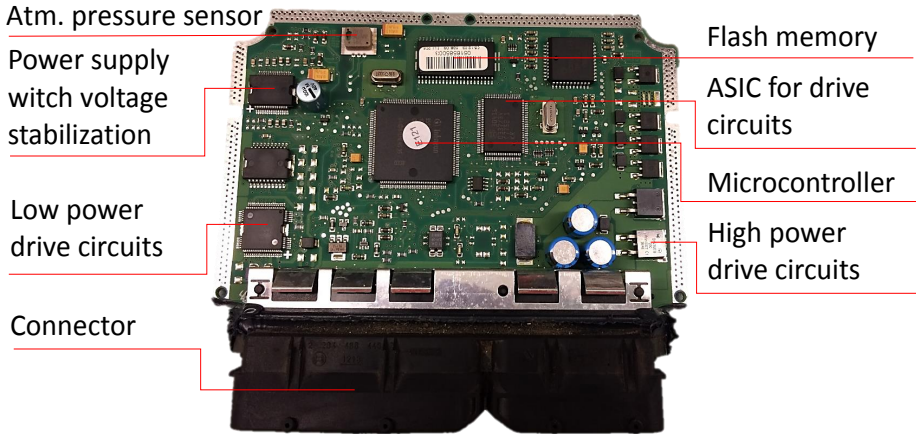


Fig. 1. Design EDC15 control unit.

The microcontroller of the control unit is a 16-bit Siemens C167CR. The FLASH memory is also a 16-bit, 512 kb, designated 29F-400BT, in the SOP 44 case. This memory stores application software from which the microcontroller reads all the data for motor control. The memory is divided into several areas depending on the type of control unit. These areas are created for different versions of the car's engine configuration. The vehicle may be equipped with a manual, automatic gearbox or all-wheel drive.

2.2 EDC16

The Bosch EDC16 is the first torque-controlled diesel engine control unit. This has a lot advantage when communicating with other controllers that require a change in actual operating variables such as automatic gearbox, ESP or air conditioning system. The control unit is used for pump-nozzle injection systems or Common Rail systems.

2.3 EDC17

In 2006, Bosch developed the new generation of EDC17 diesel control unit, which is still the most modern and most advanced control unit. Thanks to its large

computing power, it can be used in all automotive segments. The control unit enables accurate fuel injection control, exhaust gas recirculation control, supports a number of other functions such as controlling processes related to the correct operation of particulate filters or nitrogen oxide reduction systems.

The EDC17 control unit defines the injection parameters for each engine cylinder, and specifically adjusts these parameters based on certain measured values. This system not only improves the accuracy of injection but also leads to a reduction of emission compounds that are required by the strict emission classes such as EURO VI.

3 Control and Regulation

The EDC control unit is actually a "control and regulation unit". The concept of "control unit" has been greatly enforced even though it contains a lot of regulation process.

Control is a purposeful action of the control unit on the actuator to achieve the desired value. The control is divided into regulation with or without feedback.

Regulation without Feedback. The output control signals for the actuators are generated in the control unit from the data from the input signals from sensors, fields of constants, and various calculations. The position or status of the actuator is not controlled - open loop. This principle is used, for example, to control glow plugs.

Regulation with Feedback. The basis of this regulation is a closed loop, which consists of a regulators, actuators and sensors. The actual value is compared to the desired value. When the control deviation is non-zero, the regulator contained in the control unit will change the output value for the actuator. For example, this type of regulation is used for idle control.

4 Regulation of an EGR Valve

The exhaust gas recirculation means that some part of the exhaust gas is brought back in the intake manifold. Because the exhaust gas contains lower proportion of oxygen than ambient air, the EGR valve partially controls the proportion of oxygen entering the combustion process. This reduces the combustion temperature of the fuel / air mixture, thus reducing the formation of nitrogen oxides (NO_x). The amount of recirculated exhaust gases depends on engine speed, amount of injected fuel, intake air mass, and engine temperature.

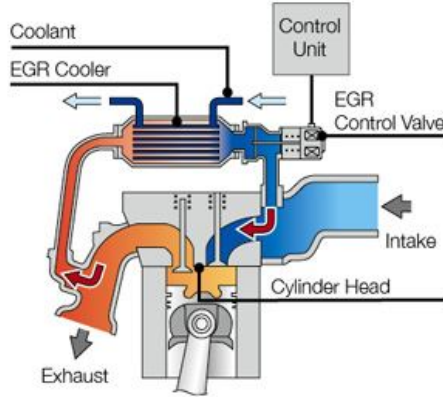


Fig. 2. Schematic representation of EGR system

The exhaust gas recirculation control is performed indirectly by monitoring the actual intake air mass. This actual value is compared with the theoretical (prescribed) air mass in application software engine control unit. Theoretical air mass is shown in Fig. 3).

g/str min ⁻¹	Egr(Amount of fuel,Rpm)/mg/str													
	0,0	3,0	7,4	10,0	12,4	15,0	17,4	20,0	22,4	25,0	29,0	33,0	51,0	
0	850,0	850,0	850,0	850,0	850,0	850,0	850,0	850,0	850,0	850,0	850,0	850,0	850,0	850,0
760	850,0	850,0	850,0	850,0	850,0	850,0	850,0	850,0	850,0	850,0	850,0	850,0	850,0	850,0
780	250,0	250,0	270,0	290,0	380,0	450,0	515,0	545,0	585,0	850,0	850,0	850,0	850,0	850,0
903	250,0	250,0	270,0	290,0	380,0	450,0	515,0	545,0	585,0	850,0	850,0	850,0	850,0	850,0
1000	250,0	250,0	270,0	290,0	380,0	450,0	515,0	545,0	585,0	650,0	850,0	850,0	850,0	850,0
1239	250,0	250,0	270,0	310,0	395,0	450,0	515,0	545,0	585,0	615,0	850,0	850,0	850,0	850,0
1386	250,0	250,0	270,0	310,0	395,0	450,0	500,0	540,0	575,0	605,0	655,0	850,0	850,0	850,0
1491	250,0	250,0	270,0	310,0	390,0	440,0	490,0	530,0	565,0	600,0	630,0	850,0	850,0	850,0
1596	250,0	250,0	270,0	310,0	380,0	430,0	480,0	520,0	555,0	590,0	620,0	850,0	850,0	850,0
1743	250,0	250,0	270,0	310,0	370,0	425,0	475,0	515,0	555,0	585,0	615,0	850,0	850,0	850,0
1995	250,0	250,0	270,0	310,0	370,0	425,0	475,0	515,0	555,0	585,0	615,0	850,0	850,0	850,0
2247	250,0	250,0	270,0	310,0	370,0	425,0	475,0	515,0	555,0	585,0	615,0	850,0	850,0	850,0
2600	260,0	270,0	290,0	325,0	385,0	445,0	495,0	540,0	580,0	610,0	640,0	850,0	850,0	850,0
3423	348,3	406,7	430,0	480,0	535,0	600,0	650,0	690,0	727,0	760,0	788,0	850,0	850,0	850,0
3612	850,0	850,0	850,0	850,0	850,0	850,0	850,0	850,0	850,0	850,0	850,0	850,0	850,0	850,0

Fig. 3. Map of required air mass for EGR control.

The X axis gives the required amount of injected fuel [mg/str], the Y axis describes the current engine speed [rpm]. The actual intake air mass is measured by an intake air mass sensor which is important for the EGR valve control. The electrical signal from the output circuits of the control unit is further converted to the vacuum value by valve N18 which mechanically opens and closes the flow of exhaust gas to the engine intake manifold. The control is provided by the PI controller implemented in the control unit, which works with three individual settings for the controller.

Settings of PI controller in the engine control unit:

- large positive control deviation,

- large negative control deviation,
- small control deviation.

The small control deviation is directly defined by the constant intake air flow rate - 40.8 mg/str. In addition, the minimum (0 mg/str) and maximum (850 mg/str) values of the intake air mass values are set.

Table 1. Settings of PI controller EGR valve

	Proportional gain [K_p]	Integral gain [τ_i]
large positive control deviation	0,112109	0,610352
large negative control deviation	0,045996	0,351868
small control deviation	0,045996	0,351868

5 Optimization EGR control

The required amount of intake air mass was adjusted for the range of 1491 rpm to 2600 rpm. By lowering these values, the PI controller secures a more open state EGR valve. Optimization is shown in Fig. 4.

g/str min-1	Egr(Amount of fuel,Rpm)/mg/str													
	0,0	3,0	7,4	10,0	12,4	15,0	17,4	20,0	22,4	25,0	29,0	33,0	51,0	
0	850,0	850,0	850,0	850,0	850,0	850,0	850,0	850,0	850,0	850,0	850,0	850,0	850,0	850,0
760	850,0	850,0	850,0	850,0	850,0	850,0	850,0	850,0	850,0	850,0	850,0	850,0	850,0	850,0
780	250,0	250,0	270,0	290,0	380,0	450,0	515,0	545,0	585,0	850,0	850,0	850,0	850,0	850,0
903	250,0	250,0	270,0	290,0	380,0	450,0	515,0	545,0	585,0	850,0	850,0	850,0	850,0	850,0
1000	250,0	250,0	270,0	290,0	380,0	450,0	515,0	545,0	585,0	650,0	850,0	850,0	850,0	850,0
1239	250,0	250,0	270,0	310,0	395,0	450,0	515,0	545,0	585,0	615,0	850,0	850,0	850,0	850,0
1386	250,0	250,0	270,0	310,0	395,0	450,0	500,0	540,0	575,0	605,0	655,0	850,0	850,0	850,0
1491	250,0	250,0	248,4	285,2	358,8	404,8	450,8	498,2	553,5	588,0	623,7	850,0	850,0	850,0
1596	250,0	250,0	248,4	285,2	349,6	395,6	441,6	488,8	543,7	578,2	613,8	850,0	850,0	850,0
1743	250,0	250,0	248,4	285,2	340,4	390,6	436,5	483,8	543,7	573,1	608,8	850,0	850,0	850,0
1995	250,0	250,0	248,4	285,2	340,4	390,6	436,6	483,8	543,7	573,1	608,8	850,0	850,0	850,0
2247	250,0	250,0	248,4	285,2	340,4	390,6	436,6	483,8	543,7	573,1	608,8	850,0	850,0	850,0
2600	260,0	270,0	266,8	298,5	353,7	409,0	455,0	507,6	568,4	597,8	633,6	850,0	850,0	850,0
3423	348,3	406,7	430,0	480,0	535,0	600,0	650,0	690,0	727,0	760,0	788,0	850,0	850,0	850,0
3612	850,0	850,0	850,0	850,0	850,0	850,0	850,0	850,0	850,0	850,0	850,0	850,0	850,0	850,0
Percentage reduction of:					8%			6%		2%		1%		

Fig. 4. Optimization EGR control.

Table 2 shows the comparison of the nitrogen oxide values (NO_x) between the stock software and the optimization. The optimization was most apparent for the 25 % and 40 % accelerator pedal position. Nitrogen oxides were down 20,1 % and 16,9 %.

A more open status EGR valve will cause a larger proportion of exhaust gas to be transferred into the engine intake (less oxygen). This results in a lower

combustion temperature. By adjusting the valve it reduces the nitrogen oxide, but on the contrary to this fact it will increase the production particulate matter.

Table 2. Comparison NO_x before and after optimization.

Accelerator pedal position [%]	NO_x [ppmvol] stock	NO_x [ppmvol] optimization	Reduction NO_x [ppmvol]	Reduction NO_x [%]
25	137 ± 7	99 ± 5	26	-20,1
30	177 ± 9	149 ± 7	12	-7,0
35	265 ± 13	216 ± 11	25	-9,9
40	625 ± 31	470 ± 24	100	-16,9
45	743 ± 37	621 ± 35	0	0,0
100	1917 ± 96	1917 ± 96	0	0,0

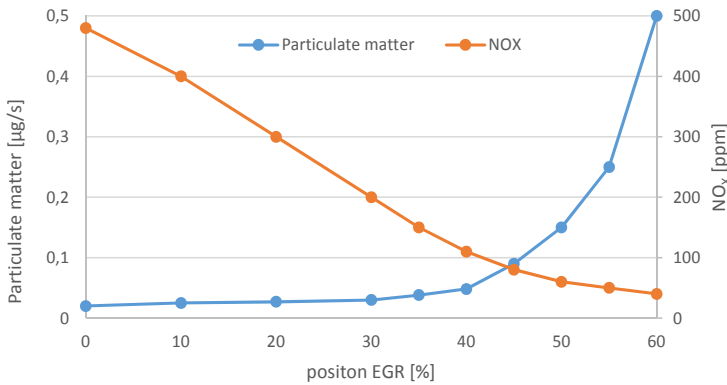


Fig. 5. Influence of EGR valve on engine emissions.

Acknowledgement

This paper presents the results from the project reg. no. SP2018/167 funded by the Student Grant Competition of VSB–Technical University of Ostrava. This research was supervised by Ing. Petr Simonik, Ph.D.

References

1. BOSCH R. *Electronic Diesel Control EDC*. Bentley Publishers, 2003. ISBN 978-0-83-761088-7.
2. BOSCH R. *Diesel Fuel-Injection Systems Unit Injector System/Unit Pump System: Bosch Technical Instruction*. Bentley Publishers, 2000. ISBN 978-0-83-760615-6.
3. STOSS, M. *Spalovací motory I*. Brno: VUT, 1992. ISBN 978-8-02-140417-5.

System architecture of experimental electric vehicle

Martin Kořený

Department of Electronics, FEECS,
VŠB – Technical University of Ostrava, 17. listopadu 15,
708 33 Ostrava – Poruba, Czech Republic
martin.koreny@vsb.cz

Abstract. This article describes the E/E system architecture of the university experimental electric vehicle code named Democar. The vehicle architecture consists of several ECUs which are connected together via CAN bus. Each ECU is responsible for controlling mechatronic and electrical system like steering control, power train, battery management, breaking system etc. Due to the fact that Democar is evolving since 2014 by individual implementations of each system during diploma thesis, primary focus was payed to provide functional solutions on component level. Due to the time constraints, currently limited implementations are present with regards of well-established automotive standards like A-SPICE or ISO26262 specially on system level. Current system architecture including all physical and functional interfaces has to be well defined and understood for further optimization and functionality enhancement steps.

Keywords: A-SPICE, ISO26262, ECU, system architecture; interface, electric vehicle.

1 Introduction

Democar is unmanned remotely driven full electrical experimental vehicle where main control units are developed directly by students. Basis for the vehicle is serial produced off road quad bike. After many changes to the mechanical parts of the original design and steering philosophy from manned to unmanned homologation is no longer valid therefore the vehicle as status quo is not allowed to enter public roads. To implement certain features readily available off the shelf parts were reused but all control units described in following chapters is own university design. Future plans are to further enhance functionality, reliability and safety. Latest status with all assembled parts and their control ecosystem can be seen in Fig.1.

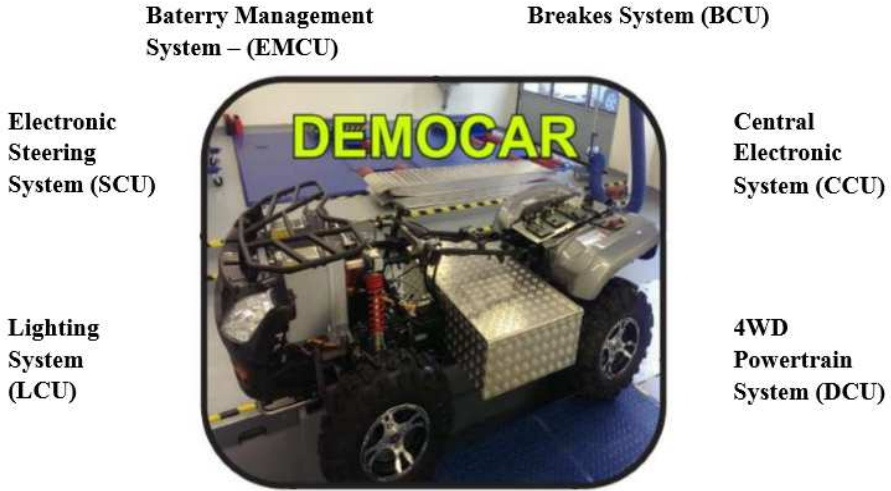


Fig. 1. Democar latest look [2]

2 Democar control system

Electrical system is divided to six subsystems as shown in Fig.2. Each subsystem has its own ECU. Each ECU is connected to the CAN bus. The vehicle is remotely operated via 16 channels remote control Jeti – Duplex DC-16 EX, 2.4GHz. Several values like vehicle speed (acceleration, breaking), vehicle direction (turn, forwards, backwards) or headlights functionality is implemented to be controlled remotely.

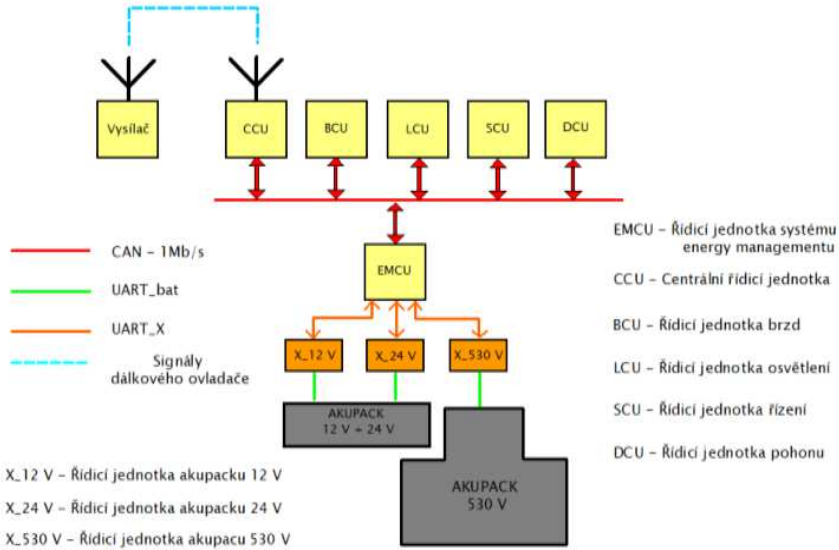


Fig. 2. System architecture (missing actuators)[2]

2.1 Central Control Unit (CCU)

This unit is responsible for data harvesting and evaluation from all other units. It acts also as a gateway between remote control and vehicle private CAN. Without this ECU driving of the vehicle is impossible. Driving Democar is similar like driving RC car with the exception of the size and weights. Power supply to CCU is ensured via 12V battery pack. Supervision and monitoring over following subsystems is implemented:

- energy management
- steering servo
- breaking system
- headlights

Future plan is to implement also more functionalities e.g. LIDAR system to support autonomous driving.

2.2 Energy Management Control Unit (EMCU)

Energy management is handling energy transfers, storage and charging. The target was to design the system as efficient as possible with considering self-power consumption as well, take in mind environmentally friendly design and secure uninterruptible energy with exception of failure states. The only source of energy of the Democar are three battery packs build from LiFePO₄ cells. Hi voltage battery pack 540V/20Ah use for power the motors, 24V/40Ah for frequency drives and 12V/80Ah for ECUs and steering servo unit. Monitoring of each cell is provided via intelligent balancers mounted on top of each cell. Balancers are connected in series via private UART bus. To be able to collect data od all balancers and be able to measure current so-called Module X is needed for each battery pack. Balancers and Module X are off the shelf parts. Recent diploma thesis [6] solved the issue with too long data stream from 164 balancers used in 540V battery pack by implementation of data switch.

If the power is interrupted the vehicle is considered as uncontrollable and therefore very dangerous to its near surrounding. Those aspects were taken into the design consideration so the system secure following features:

- Full control over energy from and to battery packs
- Adaptive charging,
- Real time monitoring of battery values (SOC, temperature, voltage, current, balancing)
- Switching off at failure states like insufficient isolation value, overtemperature, overcurrent, short circuit etc.).

CCU basically controls EMCU only in case of power on/off states for the complete vehicle electrical system.

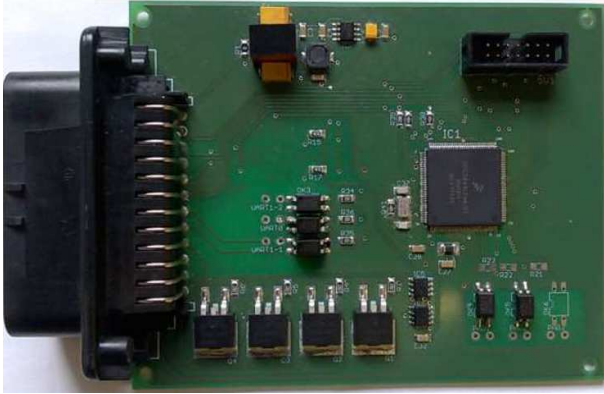


Fig. 3. EMCU, all other ECUs have same format, connectors and uC [6]

2.3 Steering Control Unit (SCU)

Because the vehicle is unmanned it was necessary to implement steer-by-air functionality. Air represents here wireless real time connection between remote control and steering mechanism with the stepper motor. The system was in past intensively tested and results lead to the decision to integrate off the shelf steering servo unit MOBIS MPS0002A AA670 565 HMEA1 2L563-98000 2L563-98010 4FDL0805 FFDK0803 to increase steering dynamics and reduce power of the stepper motor. Steering servo unit is supplied from 12V battery pack and due to high power consumption battery pack has currently relatively high capacity 80Ah.

2.4 Drive Control Unit (DCU)

Powertrain consists of four synchronous motors with permanent magnets Baumuller DSC100-S64U with power of 4.2kW each. Each motor is driven by its own frequency drive of the same brand bmaXX 4423-ST0-01200-03. The system has a capability of torque distribution to individual wheel so thanks to that, advanced functionality like electronic differential gear is also implemented. Currently the system testing was performed with active 2WD but the vehicle is capable of 4WD as well. Motors are connected to gear drives with perpendicular shafts with transfer ratio of 1:1. For better utilization of torque spectrum there is the plan to change the ratio to 4:1 or more.

The challenge with the drive system is to ensure synchronization of break and drive system. In situation when emergency breaking of the vehicle is requested for example to avoid crash it is essential to ensure maximal breaking effect so breaking and propelling moment has to be well aligned. Communication between frequency drives and DCU is realized over CAN Open protocol.

The power is provided by mechanically biggest and heaviest battery pack assembled in vehicle of nominal voltage 530V and capacity of 20Ah. This pack is exclusively connected to frequency drives resp. to theirs DC buses. Frequency drives requires also 24V for supplying internal electronics. DCU itself requires 12V.

2.5 Break Control Unit (BCU)

The BCU communicates with ABS/ASR/ESP module ESP 9.7.2 from Hyundai i20 over private CAN bus. BCU is driven from CCU over system CAN bus. First generation of breaking system was designed only for front axle but latest design utilizes breaks on all wheels supported by emergency break (only feasibility study) and more sophisticated hydraulic system.

From energy consumption perspective the break system is rather power demanding and battery capacity has to reflect this. Main factor is here pressure accumulator, which is needed to ensure breaking in case of electrical power outage.

2.6 Light Control Unit (LCU)

This ECU is used to control following light functions:

- Low beam
- High beam
- Turn indicator
- Day Running Light
- Position light
- Break light
- Reverse light
- Vehicle status light
- Error light

All functions are implemented utilizing homologated of the shelf parts.

3 References

1. JAHN, O.: Návrh a realizace osvětlovací soustavy demonstračního vozidla s elektrickým pohonem. Ostrava, 2014, Diplomová práce. Vysoká škola báňská – Technická univerzita Ostrava. Vedoucí práce Ing. Petr Šimoník, Ph.D.
2. JAROLIM, A.: Návrh a praktická realizace koncepce managementu napájení vozidla s elektrickým pohonem Democar. Ostrava, 2016, Diplomová práce. Vysoká škola báňská – Technická univerzita Ostrava. Vedoucí práce Ing. Petr Šimoník, Ph.D.
3. DULANSKÝ, D.: Sestavení funkční koncepce a vývoj aplikačního software elektronického systému servořízení elektromobilu Democar. Ostrava, 2016, Diplomová práce. Vysoká škola báňská – Technická univerzita Ostrava. Vedoucí práce Ing. Petr Šimoník, Ph.D.
4. WOLF, O.: Sestavení funkční koncepce a vývoj aplikačního software elektronického systému pohonu 4x4 elektromobilu Democar. Ostrava, 2016, Diplomová práce. Vysoká škola báňská – Technická univerzita Ostrava. Vedoucí práce Ing. Petr Šimoník, Ph.D.
5. PRZECEK, S.: Sestavení funkční koncepce a vývoj aplikačního software elektrohydraulického systému brzd elektromobilu Democar. Ostrava, 2016, Diplomová práce. Vysoká škola báňská – Technická univerzita Ostrava. Vedoucí práce Ing. Petr Šimoník, Ph.D.
6. OBRUSNIK, S.: Návrh a realizace energy managementu demonstračního vozítka s elektrickým pohonem. Ostrava, 2018, Diplomová práce. Vysoká škola báňská – Technická univerzita Ostrava. Vedoucí práce Ing. Petr Šimoník, Ph.D.

Development of the Application Software for Electrohydraulic Brakes System of the Electric Vehicle Democar

Samuel Przewczek

Department of Electronics, FEECS,
VŠB – Technical University of Ostrava, 17. listopadu 15,
708 33 Ostrava – Poruba, Czech Republic
samuel.przewczek@vsb.cz

Abstract. The main aim of this article is the design and practical realization of the second concept of the electrohydraulic brake system for demonstration vehicle Democar. The design is implemented with respect to the requirement to provide a braking effect in case of vehicle failure. This functionality is realized by electrohydraulic subsystem of emergency brake. The practical implementation is focused on the design of the overall concept of the braking system, including the emergency brake. This concept includes development of the control unit and application software.

Keywords: ABS Module, Brake System, CAN, Democar, Quad bike, Electromobil, MCU, Pressure Modulator, MQX, Emergency Brake, Controller, Software

1 Introduction

The continuous development of automotive systems implements increasing demand requirements of the market and government regulations. These requirements may be:

- increase safety,
- increasing the economy,
- increased ride comfort,
- improving the environment.

To ensure these requirements are developed specific systems. These may be hydraulic or pneumatic systems. The potential for the subsequent development and improvement of these systems is not because of technological saturation compared to electronic systems. In recent years there has been an extreme boom in electronic systems, for example in the field of vehicle propulsion, where conventional combustion units are replaced by hybrid or purely electronic systems. However, systems must be designed and developed to meet the requirements for proper operation of the electric motor itself, in this case its correct regulation, i.e. control. Another example of the boom of

electronic systems is, for example, the development of autonomous control where the complexity of the whole system exceeds recently developed systems.

2 Concept of Electrohydraulic Brakes

The braking system is among the systems that require increased demands on the quality of the design concept and the components used. The failure of individual parts of the braking system may lead to the consequences that are, in the best case, fatal to the vehicle, worse for road users.

The main parts of the electro-hydraulic braking system are:

- brakes,
- hydraulic hoses,
- pressure modulator,
- control unit (HW, SW),
- emergency brake circuit.

The main requirement for the braking system is slowing or stopping the vehicle. Requirements for brake system:

- all-wheel braking (hydraulic branch to each wheel),
- stopping a quad in cause of fault,
- communication with cooperating electronic systems,
- controlled pressure of modulation system. (operational and emergency brakes).

3 Emergency brake circuit

The emergency brake circuit forms another hydraulic circuit of the braking system. This hydraulic-electric part covers braking demand in case of power loss and pressure modulator failure. Emergency brake circuit consists of:

- 3/2 switch with solenoid actuator,
- throttle and safety valve,
- one-way valve,
- a pressure accumulator,
- P/I pressure sensor.

Pressure from the modulator opens a one-way valve and the pressure fluid compresses the diaphragm in the pressure accumulator. The one-way valve separates the emergency brake circuit from the service circuit. The pressure sensor provides feedback to the control unit about the system pressure value. By means of a pressure modulator pump, it controls the pressure in the emergency brake circuit. The accumulator serves as a supply of pressure energy in case of an emergency brake application. In the case of a fault detection on a co-operating electronic system or a power failure of a quadricycle, a solenoid of the switchgear controlling the position of the switchboard is

controlled via the control unit. This controls the pressure energy from the rear axle wheel brake cylinder.

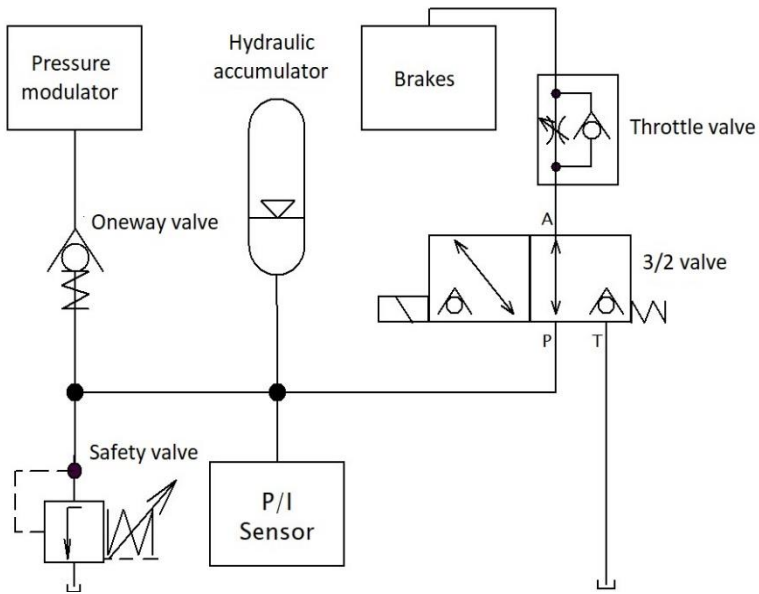


Fig. 1. Emergency brake circuit

The switchgear, throttle and safety valve are designed as a "sandwich plate" type from Bosch Rexroth. Inputs and outputs of the segments are directly seated. All three segments are stacked on each other.



Fig. 2. Hardware of EBC

4 Application Software

At the beginning of the design SW design, the requirements brake and the general requirements of the software function at the level of the electronic system were defined.

Requirements for emergency braking:

- monitoring fluid pressure in the accumulator,
- Emergency brake release after initialization,
- Emergency brake application in the event of failure of the pressure modulator and power supply,
- turning on the brake light at the moment of braking,

Requirements for the service brake function:

- braking based on user-defined intensity (remote control lever position),
- turning on the brake light at the moment of braking

Parking brake requirements:

- Activating / deactivating the parking brake via the remote-control lever.

General function requirements:

- read error messages of cooperating electronic systems (DCU, SCU, CCU, LCU) using CAN_CONTROL (1Mbit/s),
- sending emergency brake pressure and pressure modulator error messages with CAN_ABS (500kbit/s),
- communication with pressure sensor via analogue input and digital input via AD converter and I/O Link Interface,
- deactivating the drive in the event of braking.

When the program starts initialization occurs generally. Subsequently, the DCU, SCU, CCU states must be read, such as error messages, vehicle speed, remote control position segments. The first requirement for the quadricycle is to press the emergency brake. In the current testing phase, the minimum pressure threshold is set to 100 bar. In the case of less pressure, the pressurization process occurs. The control variable counts the loops through the loop. If, for whatever reason, the emergency brake accumulator is not pressurized by three loops through the loop, the emergency brake pressure error information is sent.

Another condition for operation is to check the condition of the modulator. In case of a received error message the pressure modulator fails, then to enter the loop. The variable mod signifies through the loop. Subsequently, the emergency brake is triggered. If the number of passes is greater than three, returns to the main branch. Thus, the mod variable also acts as a guard against the program overdrive.

The control of the DCU, SCU systems consists in checking the variables in which the reading of the frame byte obtained from the CAN bus. In the event of a fault on one of the systems, it enters the loop where the quad bikes are stopped by the service brake. Otherwise, the condition is met, and the execution of the program moves to the next condition. With the control variable, the loops are again signaled by the loop and thus it works against obstruction.

The request for starting the parking brake (emergency brakes) is set by the lever on the remote control. If the park brake request is active, the park variable is set = 1 and starting the parking brake at zero quad speed. If the zero speed is not met, program execution returns to the main branch and the park is set = 0, which is outside the service braking condition.

To activate the braking operation, the last evaluation block in the main branch is required. Control variables are used here. In the event of non-compliance with the condition, a global fault state is transmitted to the bus, which can handle, for example, a DCU to stop the drive. The park condition = 0 prevents the service brake from starting when the parking brake is applied.

5 References

1. BOSCH, R.: Bezpečnostní a komfortní systémy. Robert Bosch GmbH, 56 s., 1998. ISBN 80-902585-9-X.
2. O. JAHN, Diplomová práce, Návrh a realizace osvětlovací soustavy demonstračního vozidla s elektrickým pohonem, Ostrava: VŠB – Technická univerzita Ostrava 2014
3. PRZECZEK, S., Diplomová práce, Sestavení funkční koncepce a vývoj aplikačního softwaru elektrohydraulického systému brzd elektromobilu DemoCar. Ostrava: VŠB – Technická univerzita Ostrava, 2016
4. VLK, F, Elektronické systémy motorových vozidel[online] [cit. 2018.05.20]
URL: < <http://www.sinz.cz/archiv/docs/si-2005-04-193-212.pdf>>

Acknowledgement

In the paper, there are the results of the project reg. no. SP2018/167 funded by the Student Grant Competition of VSB-Technical University of Ostrava. This research was supervised by Ing. Petr Simonik, Ph.D.

Supported from the Moravian-Silesian Region budget under the program "Support for Science and Research in the Moravian-Silesian Region 2017" (RRC/10/2017).

AC Link Converters

Jan Strossa and Petr Chlebiš

Department of Electronics, FEECS,
VŠB – Technical University of Ostrava, 17. listopadu 15,
708 33 Ostrava – Poruba, Czech Republic
`jan.strossa.st@vsb.cz`

Abstract. This article deals with AC link power converters within the context of contemporary concepts issues, especially in terms of advantages of using AC links and its aspects of commercial expansion. The first part describes the benefits of AC links and explains which situations the using of these ones is beneficial in. The second part contains an examples of AC link concepts with the references to its possible uses and circuit diagrams. Subsequently, the figures of the electrical physical values, which were obtained from the AC link converter model realized at Department of Electronics, FEECS, are shown.

Keywords: AC link, converter, galvanic isolation, high frequency transformer.

1 Introduce

At present, the using of a DC link is relatively usual in an indirect frequency converters, especially in the areas of electric drives, where the voltage/current from the power AC supply is rectified - in the appliance of motor mode - and subsequently alternated to the required output size and frequency. Conversely, converters using AC links concepts are not so commonplace and its occurrence is rather uncommon in the industry. A portfolio of these types of converters constitutes only a very small fraction of the commercial products offered, and these are - excepting some specific applications, for example active filters, see [5] - mainly subjects of scientific researches.

However, with reference to an actual progress, it can be assumed that this situation will be changed, because, especially with regard to the development of electromobility, where AC link converters are suitable for charging, see [4] - and secondary, for example, with the development of solar power plants, the emergence of a new demand of galvanic isolation inverters within the current requirement for a low size and low weight isolation transformer can be expected. Just the requirements for minimizing the transformer that performs the galvanic isolation will cause that the ordinary concepts - consisting of the converter without galvanic isolation combined with a conventional transformer operating at a low 50 Hz frequency of the connected network - will not be usable. With reference to the principle of transformer operation for function of these ordinary concepts a large magnetic circuit due to the operation at a relatively low frequency is needed.

2 Reasons of using AC link

In general, a semiconductor converter is a device that transforms one type of electrical energy into another one, these changes can be reflected in values of voltages, currents, frequencies, mutual conversions of AC and DC quantities, or combinations of the changes stated above. From that point of view, we generally divide the converters into direct and indirect units. The indirect converters differ from the direct unit by the fact that they transform the input electric values firstly into some other type, which doesn't correspondent with required output, but these type's values are in the link, where the other parts of the converter transform them from to the output. In the case of more complicated converters, there can be more than one link between input and output.

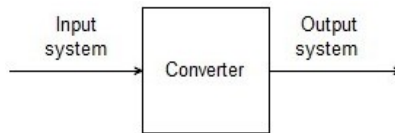


Fig. 1. Block diagram of direct converter

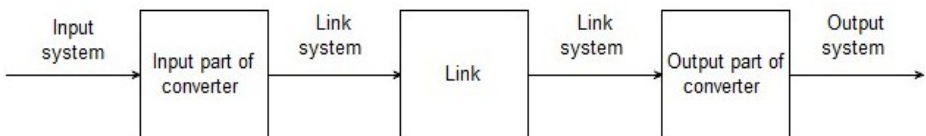


Fig. 2. Block diagram of indirect converter

At first sight, the indirect converter block system shown in Fig. 2 seems to be more complicated and there has to be a reason for its prioritization in front of the direct one illustrated in Fig. 1. This reason has to be reflected in the better functional properties of the resulting product, or at least, in the sphere of the commercial in some other benefits to the end user – e.g. in the form of lower price, lower operational requirements, higher reliability etc.

The logical necessity of existing a reason, or reasons, as stated above caused that indirect converters have found industrial applications primarily as frequency converters using a DC link. In this case, where the device consists of a rectifier, a DC link and an output inverter, there are more benefits of using concept of indirect converters. For example, it can be seen as a two separated cascaded converters - rectifier and inverter – that brings the possibility of certain independence and thus simplifying of controlling both the parts, additionally the semiconductor switching synchronization of the converter, where a DC voltage is on the one of the connected systems, is easier than in the case, where two AC systems are connected.

Taking a look at reasons for creating/advantages of using an AC link converter, we can find three ones basically. The first and crucial one is the possibility of transmit-

ting AC energy across the transformer, this may be useful if a request for galvanic isolation of the connected systems by the converter is required.

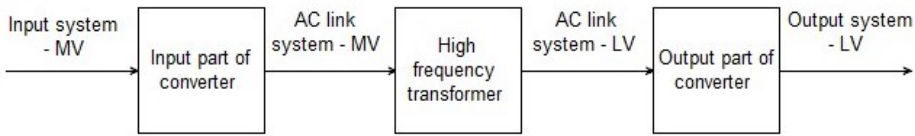


Fig. 3. Block diagram of indirect AC link converter with a step down transformer within the link, MV – medium voltage; LV – low voltage – regarding to [1]

Within the general concept shown in Fig. 3, it is possible to transmit energy across the transformer also by DC voltage - respectively current - pulses too. This has been used by the step-down and back-boost DC-DC converters, but DC pulses employ only $\frac{1}{2}$ of the available magnetic circuit of the transformer, which is not then used efficiently. There is a technical requirement for a larger size and weight of the transformer when transmitting DC pulses than in the case of AC converter with the same transmitted power. The concept with an AC link stated above is being currently applied to DC-DC converters, where the systems identified as input and output in Fig. 3 are both DC. In case where at least one of the connected power systems is AC, the isolation transformer is usually located outside the inverter just in that AC system.

The second advantage of using an AC link, which follows from the first one, is the possibility of using the link transformer for changing the voltage. When two electric systems of different voltage levels are connected, the risk of permanent interconnecting the medium voltage field with low voltage output in the event of failure of a semiconductor switcher or a failure of the control system is eliminated.

The third advantage of using an AC link, also based on the first one, is possibility of working the transformer at a high frequency. If the transformer is not located at the link, but it is between the converter and one of the connected systems of AC type, it usually works on 50 or 60 Hz, when working in the link, it can be used with frequency of tens to hundreds kHz. This is very important fact regarding to a size and weight of transformer, which decrease with increasing the working frequency.

3 AC link converters concepts

3.1 Intermediate AC link rectifier

This type of converter could be functionally replaced by the simplified form of the converter discussed in Chapter 3.2, but it does not contain a matrix part that is substituted by a conventional indirect frequency inverter in one-phase version and there is an ordinary uncontrolled rectifier. Using this circuit diagram combined with filters and a DC link may decrease the requirements for control system, especially in the context of ensuring sufficient dynamics. This concept can be also seen as ordinary indirect DC link frequency converter cascaded with an AC link and rectifier.

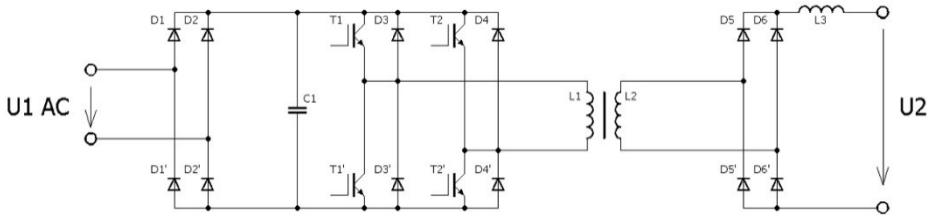


Fig. 4. Potential circuit diagram of intermediate AC link rectifier

This concept is been already used in so-called welding inverters, which, in comparison with conventional electric welders, allows DC welding. This means a possibility of better welding arc holding and realizing as a compact light and low-dimensional designs with relatively high welding power.

3.2 Indirect AC link AC – AC converter

This concept can be understood as derivate of an indirect AC - AC DC link converter but it is different by changing the link polarity. To be able to change that polarity the input and output parts of converter, which consist of two rectifying/inverting bridges at the ordinary DC link converter, has to be realized by semiconductor structure with a possibility of flowing and blocking a currents at all the directions. In fact, this is a pair of cascaded matrix converters, where the high frequency link transformer is located between. This converter is shown in Fig. 5, where the version with soft switching is.

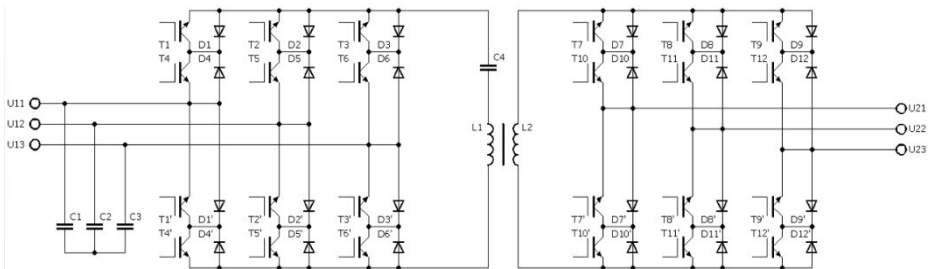


Fig. 5. Potential circuit diagram of indirect AC link AC – AC converter

4 Obtained results

In the framework of scientific research at Department of Electronics, FEECS, VŠB – Technical University of Ostrava, AC link DC-DC converter has been realized. The obtained results are shown below.



Fig. 6. Waveforms of primary AC link transformer winding voltage (blue curve, V) – and secondary AC link transformer winding voltage (violet curve, V), obtained from AC link DC-DC converter realized model, taken from [3]

5 Conclusions

In terms of use of AC link converters, it can be said that they are not currently commercially expanded - excepted some special types as a DC - DC converters with galvanic isolation and Active filters, see [5], welding inverters, etc. For converters operating with AC currents / voltages, galvanic isolation can be easily realized within out of the converter, and using of the AC link is meaningful in that case, when there are requirements for small size and low weight of the isolating transformer. The transformer operates at a higher frequency in the link than within out the converter, so it is less magnetically filled and the requirements for the dimensions of the magnetic circuit are lower. However, these requirements are not usual, so the AC-link converters are not very commercially expanded. According to [2], AC link concepts could be used in a railway technology in the future, where actual low-frequency transformers contribute significantly to hitting the weight limit of traction vehicles.

In the near future, a new demand for converters with a galvanic isolation integrated in the link, for example, in the case of high performance electric cars charging stations, see [4], can be expected. Charging with a high power of hundred kilowatts could be economically more expensive when using 50 Hz transformers – in the future – than using more complicated converters including smaller high frequency transformers.

6 Acknowledgement

This paper was supported by the projects: Center for Intelligent Drives and Advanced Machine Control (CIDAM) project, Reg. No. TE02000103 funded by the

Technology Agency of the Czech Republic and Project Research and Development of Electronic Systems for Vehicles with Autonomous Control II (SP2018/167) Reg. No. SP2018/167 funded by the Student Grant Competition of VSB – Technical University of Ostrava.

7 References

1. IEC 60038:2009. IEC standard voltages. Ed. 7.0. Geneva, Switzerland: International Electrotechnical Commission, 2009
2. PITTERMANN, Martin. Redukce hmotnosti trakční výzbroje vozidel pro střídavou trakční soustavu. Plzeň, 2016. Habilitation work. West Bohemian University in Pilsen.
3. STROSSA, Jan. Indirect AC link Frequency Converter. Ostrava, 2018, Diploma thesis. VSB-Technical University of Ostrava, FE ECS.
4. SIMONIK, Petr, HAVEL, Aleš, HROMJAK, Michal, CHLEBIS, Petr. Active Charging Stations for Electric Vehicles Charging. PROCEEDINGS OF PROGRESS IN ELECTROMAGNETICS RESEARCH SYMPOSIUM (PIERS 2012) Kuala Lumpur, MALAYSIA, 2012, pp. 1559-9450, ISBN: 978-1-934142-20-2
5. BRANDSTETTER, Pavel, CHLEBIS, Petr., SIMONIK, Petr., PALACKY, Petr. An Unconventional Soft Switched Parallel Active Power Filter. PROCEEDINGS OF THE 10TH INTERNATIONAL SCIENTIFIC CONFERENCE ELECTRIC POWER ENGINEERING 2009, Kouty nad Desnou, VSB-Technical University of Ostrava, FE ECS, 2009, pp. 347–351, ISBN 978-80-248-1947

A Fuzzy Evaluation of Quality of Color Vision Testing

Monika Borová and Michal Prauzek

Department of Cybernetics and Biomedical Engineering, FEECS,
VŠB – Technical University of Ostrava, 17. listopadu 15,
708 33 Ostrava – Poruba, Czech Republic
monika.borova@vsb.cz

Abstract. The determination of quality is important aspect in color vision testing, because testing under the right conditions is an essential part of correct results. The main task of the software is to replace the standard form of the Farnsworth-Munsell 100 hue test with a software form, and then the proposed fuzzy system evaluates the quality of this testing. Visual disorder, error score and condition of testing influence the quality of software based testing alike the manual testing. System is based on CCD model (conjunction-conjunction-disjunction) and the defuzzification uses method of Center of Gravity.

Keywords: Farnsworth-Munsell, Color Vision Disorders, Fuzzy Expert System, Quality of Testing

1 Introduction

As well as diagnostics of color vision disorders, it is also important to determine the quality of the performed examination. The vision is one of the most important sense, and early diagnosis of any of its disorders can help prevent serious illness such as diabetes, cataract, glaucoma or Parkinsons disease.

The software that deals with this article is able to provide testing and subsequent evaluation of color vision disorders based on the same principle as standard test forms of Farnsworth-Munsell 100 Hue Test and Farnsworth D15 test. In this article the proposed fuzzy expert system evaluates the quality of testing software based and standard based method, with input variables being the patient's visual disorder, error score, and conditions of testing.

2 Background

The main symptoms of illnesses such as diabetes, cataract, glaucoma or Parkinsons disease can be early diagnosed through examination of color vision disorders. During routine medical examination the most commons examination methods are the pseudoisochromatic plate and the Farnsworth D15 Test, described by [6]. The most reliable type of examination is The Farnsworth-Munsell 100 Hue Test, but this test is very time-consuming [2].

2.1 The Farnsworth-Munsell 100 Hue Test and Farnsworth D15 Test

The Farnsworth-Munsell 100 Hue Test is considered to be an international standard in ophthalmology, because it provides detailed diagnostics of inborn or acquired color vision disorders. This test consists of 93 caps divided into four boxes, where the first and last cap are fixed. The task of the patient is to arrange the caps between them with the smallest difference in hue of adjacent caps. Each cap has a specific number written on the back, which serves for evaluation of the test, see [9, 4]. The Farnsworth D15 Test is not time-consuming as the Farnsworth-Munsell 100 Hue Test and therefore it is more used in clinical practice described in [6]. The Farnsworth D15 Test is used to diagnose medium and strong defects of color vision. It consists of 16 caps, 15 for testing and one cap as a reference. The caps with special hues have to be arranged in the correct order. The resulting graph is created by the sequence of the patient's arrangement, see [6].

2.2 Fuzzy logic

The origins of system modeling and control based on using of fuzzy set theory as a mathematical background can be traced back to 1975, when the first rule-based controller powered by a fuzzy inference mechanism was introduced by Mamdani and Assilian [1].

Thanks to the fuzzy expert system, it is possible to emulate the reasoning process of a human expert or provide in an expert manner in a domain for which no human expert exists [3]. Due to the linguistically formulated fuzzy IF-THEN rules (1), conclusions on the basis of imprecise descriptions can be deduced:

$$IF X1 \text{ is } A1 \text{ AND } X2 \text{ is } A2 \text{ THEN } Y \text{ is } B \quad (1)$$

where $A1$, $A2$ and B are certain predicates characterizing the variables $X1$, $X2$ and Y . All types of variables are specified linguistically. Each variable is characterized by name, upper and lower bound and discretization of the universe. Upper and lower bounds specify the interval in which fuzzy sets interpret the linguistic expressions. Discretization of the universe specifies the number of points on the universe in which the membership functions are computed [5].

For the explication of fuzzy IF-THEN rules, it can be used several types of approximate reasoning methods such as logical deduction, fuzzy approximation with conjunctions or fuzzy approximation with implications. The method applied for the proposal system is fuzzy approximation with conjunctions, known as the Mamdani-Assilian method. The body of knowledge of the expert system is composed of Mamdani rules connected by a fuzzy logic operator OR, fuzzy logic operators between partial fuzzy statements of antecedents of rules AND and fuzzy implications THEN between antecedents and consequents (CCD model - conjunction-conjunction-disjunction) [3, 5].

As well as fuzzification, also defuzzification works with more available methods. For example, the Mean of Maxima Method, Defuzzification of Evaluating Expressions

or Center of Gravity Method [8]. The last of these methods was applied as a method of defuzzification of the proposal system. It consists of finding the centroid of the area bounded by the controller output membership function and it is expressed by the crisp controlling value.

3 Methods and Applications

3.1 Hospital Information System Architecture

The software can be used in hospital as a part of diagnostics color vision disorders, where fulfils the task of staff, because allows automatic plotting of score graph. But also this software can be used as a part of HomeCare system, enabling testing in the comfort of home. This kind of testing is very important for prevention and for following treatment.

3.2 Hue Test Testing Application

The software for color vision testing is based on classic methods of testing color blindness, mainly the Farnsworth-Munsell 100 Hue Test and the Farnsworth D15 Test. Compared to the classic methods, this software is able to plot graphs automatically from obtained results and save this results into database.

The modul for color vision testing creates the main part of the software. It provides testing by the Farnsworth-Munsell 100 Hue Test, the Farnsworth D15 Test and manual mode. The manual mode is particularly useful in case that the patient is tested by the standard methods and doctor or other medical staff want to show score graph and save results into database. The main advantages of this software are speed and reliability of evaluation, as the medical staff can make mistakes during manual plotting.

The software version of Farnsworth-Munsell 100 Hue Test is based on the same principle as standard method. The colors, which are used in this application come from Munsell Color system [7]. For testing, it is absolutely necessary to keep the same brightness all of color, because people with color vision disorders orientate according to them.

3.3 Proposal of Fuzzy Expert System

The aim of the proposal of fuzzy expert system is to determine the quality of color vision testing using a standardized method with respect to the patient's *visual disorders*, their *error score* when they are tested by the software based or standard based method and *examination conditions*. The proposed fuzzy system consists of three input variables with three linguistic variables and one output linguistic variable with five output variables (Table 1). Based on input and output variables, 27 decision rules were created for the fuzzy system. The proposed system was developed in the LFLC 2000 program. The input variables have been chosen to reflect as much as possible about the quality of color vision testing. The

input variable *visual disorder* refers to the visual difficulties the patient suffers from (short or long-sighted, astigmatism, etc.). The *error score* is based on data that can be measured. Patients without defect have error score at very low levels. *Testing conditions* may include, for example, the quality of the illumination or whether the patient performs the examination according to a standardized procedure, which is often not observed in practice.

Table 1. Input variable: Visual disorder

Input variable	Linguistic variables	Points of triangular function
Visual disorder	Healthy	(0, 0, 0.5)
	With mild difficulties	(0, 0.5, 1)
	With serious difficulties	(0.5, 1, 1)
Error score	Without defect	(0,0,10)
	Middle defect	(0, 10, 30)
	Serious defect	(30, 100, 100)
Conditions of testing	Ideal	(0,0,0.5)
	Sufficient	(0, 0.5, 1)
	Inconvenient	(0.5, 1, 1)
Output variable		
Quality of Color Vision Testing	Unacceptable	(0,0,0.25)
	Unfavourable	(0, 0.25, 0.5)
	Average	(0.25, 0.5, 0.75)
	Sufficient	(0.5, 0.75, 1)
	Excellent	(0.75, 1, 1)

4 Testing and Results

4.1 Testing Group

As to compare the proposal software reliability with the standard manual method, it had to be tested in the Eye clinic at University Hospital Ostrava. The testing group was consisted of 30 people at the age of 12 – 70 and with various disorders (myopia, hyperopia, cataract, tumor, diabetes).

4.2 Testing of proposal Fuzzy Expert System

For testing of quality model values were randomly selected for individual input variables (Table 2). In the LFLC 2000 program, the fuzzy approximation with conjunctions was selected as an interference method and center of gravity was selected as the defuzzification method.

The graphs below show results. Graphs with a) represent the resulting fuzzy set for a given combination of input variables, and the graphs with the label

Table 2. Testing values of linguistic variables

	Visual disorder	Error score	Conditions of testing	Value of Center of Gravity
Test 1	0.34	21.65	0.21	0.63
Test 2	0.68	14.95	0.87	0.31

b) represent the resulting values for the input variable *Visual disorder*. The combination (Figure (1)) of values of 0.34 for visual disorder which means mild difficulties, 21.65 for error score which means middle defect and ideal conditions with value 0.21 the fuzzy system evaluates as average to sufficient (value of center of gravity 0.63).

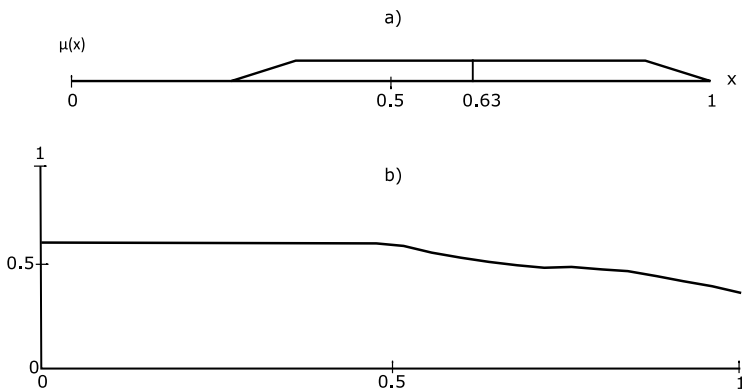


Fig. 1. a) Test 1 - Fuzzy set with 0.63 value of Center of Gravity b)Representation of variable *Visual disorder*

The second test (Figure (2)) for value 0.68 of mild difficulties, 14.95 for error score and 0.87 for conditions the fuzzy system evaluates as average to unfavorable with value 0.31 for center of gravity.

5 Conclusion and Future Work

This paper proposes a fuzzy evaluation of quality of testing color vision disorders. The principle of this evaluation je classic version of Mamdani model. Fuzzy system is composed of three input variables with three linguistic variables. The quality of testing depends on value of visual disorders, error score and on conditions of testing. The linguistic output value is defuzzificate with method of Center of Gravity.

It's important to consider the quality of results, because some visual disorders can influence the results alike the conditions of testing. In case of using software

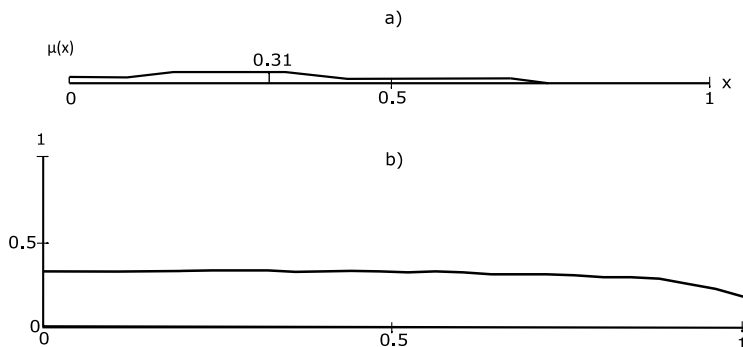


Fig. 2. a) Test 2 - Fuzzy set with 0.31 value of Center of Gravity b) Representation of variable *Visual disorder*

based testing, the conditions are always ideal, because the monitor is calibrated, but in case of manual testing, the quality of lighting can be poor. The software we are talking about in the article is based on standard tests such as the Farnsworth-Munsell 100 Hue Test and the Farnsworth D15 Test. This software allows quick automatic plotting of score graph and reliable evaluation.

References

1. Duțu, L.C., Mauris, G., Bolon, P.: A fast and accurate rule-base generation method for mamdani fuzzy systems. *IEEE Transactions on Fuzzy Systems* 26(2), 715–733 (2018)
2. Hidajat, R.R., Hidayat, J.R., McLay, J.L., Elder, M.J., Goode, D.H., Pointon, R.C.: A fast system for reporting the farnsworth-munsell 100-hue colour vision test. *Documenta Ophthalmologica* 109(2), 109 – 114 (2004)
3. Kandel, A.: *Fuzzy expert systems*. CRC press (1991)
4. Mntyjrvi, M.: Normal test scores in the farnsworth-munsell 100 hue test. *Documenta Ophthalmologica* 102(1), 73 – 80 (2001)
5. Novak, V., Perfilieva, I., Mockor, J.: *Mathematical principles of fuzzy logic*, vol. 517. Springer Science & Business Media (2012)
6. Roy, M., Gunkel, R., Rodgers, G., Schechter, A.: Lanthony desaturated panel d15 test in sickle cell patients. *Graefe's Archive for Clinical and Experimental Ophthalmology* 226(4) (1988)
7. Roy Choudhury, A.K.: Colorimetric study of scotdic colour specifier. *Coloration Technology* 124(5), 273 – 284 (2008)
8. Saade, J.J., Diab, H.B.: *Defuzzification methods and new techniques for fuzzy controllers* (2004)
9. Taylor, W.O.: Clinical experience of electronic calculation and automatic plotting of farnsworth's 100-hue test. *Modern problems in ophthalmology* 19, 150 – 154 (1978)

Design of fuzzy controller for simple inverted pendulum

Tomáš Dočekal and Štěpán Ožana

Department of Cybernetics and Biomedical Engineering, FEECS,
VŠB – Technical University of Ostrava, 17. listopadu 15,
708 33 Ostrava – Poruba, Czech Republic
{tomas.docekal, stepan.ozana}@vsb.cz

Abstract. This paper deals with design of fuzzy controller for stabilization of simple inverted pendulum in upper equilibrium. The Mamdani type fuzzy logic controller was used for this purpose. Two different control structures are presented and one is used for the design. Choice of scale factors for normalized fuzzy controller is also important part. The functionality of controllers was verified in offline simulation and compared with LQR controller.

Keywords: Fuzzy Controller, Simple Inverted Pendulum, Mamdani Model.

1 Introduction

The problem of inverted pendulum control is one of the most popular in the field of technical cybernetics. It has been known for a long time and is still being used in laboratory conditions due to its complexity, especially in education of control theory (see [1] or [2]). These properties predetermine it to be an appropriate subject for testing various new approaches and methods regarding modern control theory. At the same time, this problem is very attractive both for the lay public and experts.

Regarding the description of laboratory setup, it is usually composed of a cart that can move along a certain form of linear guidance, and a pendulum arm that is connected to the cart via a free joint to be able to rotate. The system is equipped with a single actuator capable of moving the cart. At the same time, this movement also influences the pendulum arm (its angle). Since the system has two degrees of freedom (linear movement of the cart and rotary movement of the pendulum arm), but the only one actuator, it belongs to the category of so called underactuated systems.

Fuzzy control was firstly used to control the inverted pendulum by Takeshim Yamakawa in 1987 [3]. Together with his coworkers they created a special hardware to implement the fuzzy controller. Only 7 rules out of 49 possible (both input variables had 7 fuzzy sets) were used to control, and only the pendulum angle was stabilized, not the cart position. Due to the popularity of the inverted pendulum control, subsequent papers on the use of fuzzy control for this system were created a long time ago [4], [5] and also recently [6], [7]. The presented article already focuses on the use of fuzzy control to stabilize the inverted pendulum arm and also the cart position.

2 Model of inverted pendulum

Various publications state that the design of the fuzzy controller does not require knowledge of the mathematical description of the system to be controlled. The entire design is based on the experience of an expert who knows the system and is able to interpret necessary relationships between its input and output variables. The goal is how to determine how the manipulated value that enters to the systems should change in the course of time depending on the measured values.

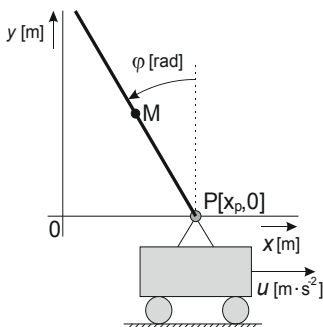


Fig. 1. Situation scheme for analytical identification

However, the model of the pendulum was used during the simulations that served to assess the proposed control mechanism and to verify its functionality. Analytical method of identification was used to construct the model, considering a cart acceleration to be an input of the system. In reality, this variable can be applied to the system via a speed loop including the actuator. The pendulum arm is for the sake of simplicity replaced by the mass point located at the center of gravity of the arm (M). The situation is illustrated in Fig. 1. The movement of the pendulum can be described by the differential equation (1).

$$l \cdot \varphi'' - g \cdot \sin \varphi + b \cdot \varphi' - u \cdot \cos \varphi = 0 \tag{1}$$

where

l	(m)	pendulum length to the mass center MP
φ	(rad)	pendulum angle
g	($m \cdot s^{-2}$)	gravity acceleration
b	($m \cdot s^{-1}$)	damping coefficient
u	($m \cdot s^{-2}$)	cart acceleration

This equation can then be extended to a state description (2), (3), (4) and (5) that considers the position and speed of the cart besides the angle and angular speed of the pendulum.

$$x_1' = x_2 \tag{2}$$

$$x_2' = \frac{g}{l} \cdot \sin \varphi + \frac{u}{l} \cdot \cos \varphi - b \cdot \varphi' \tag{3}$$

$$x_3' = x_4 \quad (4)$$

$$x_4' = u \quad (5)$$

where

x_1	(rad)	pendulum angle
x_2	(rad·s ⁻¹)	pendulum angular speed
x_3	(m)	cart position
x_4	(m·s ⁻¹)	cart acceleration

3 Control mechanism in the upright position

There are more variants of how the structure of the control circuit for stabilizing the inverted pendulum might look like. The basis is the regulation of the arm angle and its angular speed, but it is also necessary to consider the control of the cart (and its speed). Without this consideration the entire system would only be usable in simulation, as the cart would move uncontrollably with no respect to the real constraints (for example limited available length of the linear guidance).

Based on these requirements, one of the two control structures can be applied – either a single controller with four inputs and one output, or a structure with two controllers, each having two inputs and one output. To implement the upright position control, a solution using two fuzzy controllers of the PD type was chosen. The second variant of the control system arrangement should achieve the same results; however, having control variables regarding the cart separated from the ones that regard the pendulum arm makes the tuning and adjustments of control algorithms easier. The partial difference between these two structures is also in generation of resulting manipulated variable, which is used to affect the inverted pendulum. In case of two controllers their outputs are summed up, whereas when one controller is used, the individual terms are reassembled within the fuzzy model inference, and then defuzzification and obtaining a crisp number are performed. Therefore, the outputs might be different for the same inputs.

3.1 Fuzzy controller

The individual controllers are based on the Mamdani model and they use the standard form of input (see Fig. 2) and output (see Fig. 3) linguistic variables with fuzzy sets. For detail description, see [1] or [8]. Their range is therefore defined at -1 to 1, respectively -1.5 to 1.5 to ensure that the defuzzification for the output variable is limited to a range of -1 to 1.

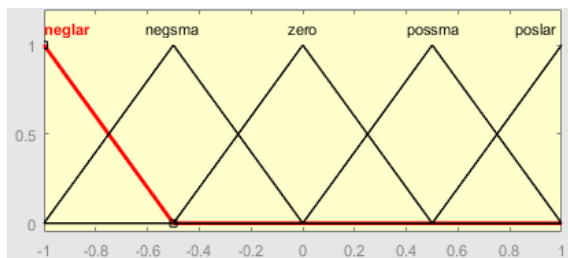


Fig. 2. Membership functions for fuzzy controller’s input linguistic variables

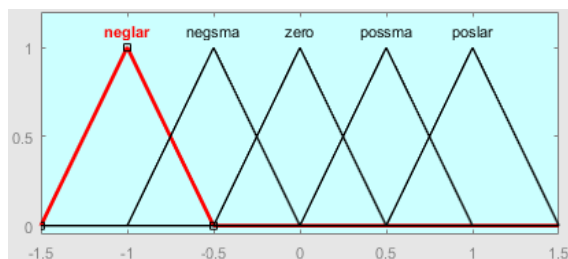


Fig. 3. Membership functions for fuzzy controller’s output linguistic variable

The fuzzy controller rules are introduced in the following Table 1. For the sake of clarity, substitute notation of individual fuzzy sets is used: neglar = -2, negsma = -1, zero = 0, possma = 1 and poslar = 2. In total, 25 rules are used.

Table 1. List of the fuzzy controller’s rules

Assessment for control signal u		Derivative of control error de				
		-2	-1	0	1	2
Control error e	-2	2	2	2	1	0
	-1	2	2	1	0	-1
	0	2	1	0	-1	-2
	1	1	0	-1	-2	-2
	2	0	-1	-2	-2	-2

Instead of control error e , the pendulum angle or the position of the cart may be used, and instead of the derivative of control error de the angular speed of the arm or the speed of the cart may be used. Fig. 4 shows in which direction the value is positive or negative. For example, if the pendulum angle deflection is positive ($x_1 > 0$) and its angular speed is zero ($x_2 = 0$), it means that the pendulum is tilted to the left, and therefore it is required that the cart also moves to the left to stabilize the arm. The situation can be verified according to the rules in Table 1, where the positive deflection of e and the zero deflection of de correspond to the negative value of the acceleration u , which causes the required movement shift to the left side.

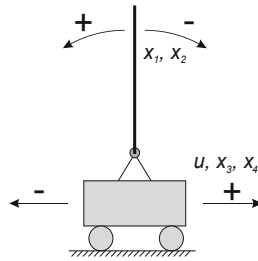


Fig. 4. Relation between the signs of the signals and sense of the movement

3.2 Scale factors

Since controllers with standard universes of all variables are used, it is necessary to add gains for each input and output to adjust the range of the given variable. In this way, a universally prepared fuzzy controller can be used for different systems, or for example, for a pendulum for two pairs of different variables. The entire scheme is shown in Fig. 5. If the gain terms are not intended to use, it is necessary to take into account the ranges of individual variables already when designing the controller and then to modify its universe. These data should be based on the knowledge of the regulated system, its possibilities and limitations. An example could be a DC motor where the speed must be controlled and the motor is agitated via an 8-bit PWM signal. The controller output will be defined on the universe ranging from -255 to 255. The input range will be derived from the maximum speed the motor can achieve.

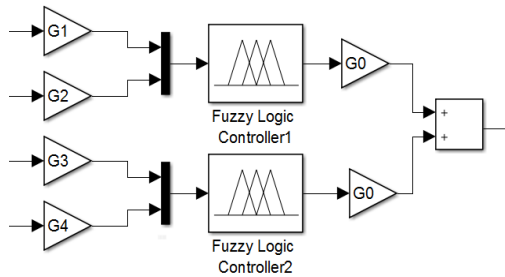


Fig. 5. Two-controllers scheme with scale factors

Gain terms for individual variables can be designed in different ways. In this paper, the derivation from the LQR controller was used. It is assumed that the constant K_i depends on G_i and G_0 . In simple terms it is possible to introduce the relationship (6).

$$K_i = G_0 \cdot G_i \tag{6}$$

A system of equations with $i + 1$ variables is achieved, so it is necessary to proceed with the choice of one constant. The selection can be done randomly and the value can be modified based on the simulation, or done according to the following rule. First, the variable that influences the controlled system (for example, the controlled

variable, which in our case is the angle of the arm) is chosen and the extent to which the control is to be performed is determined. Therefore, if the angle interval is -0.8 to 0.8 rad, the gain value of the input variable is selected as $1 / 0.8 = 1.25$ to convert this range to the standard range of the universe of the linguistic variable of the controller.

4 Implementation and verification

The first step is linearization of state-space of pendulum in an operating point corresponding to the upright position (7).

$$A = \begin{bmatrix} 0 & 1 & 0 & 0 \\ \frac{10}{0.15} & -\frac{0.0225}{0.15} & 0 & 0 \\ 0 & 0 & 0 & 1 \\ 0 & 0 & 0 & 0 \end{bmatrix}; B = \begin{bmatrix} 0 \\ 1 \\ 0 \\ 1 \end{bmatrix}; C = |1 \ 0 \ 0 \ 0|; D = |0| \quad (7)$$

The second step is calculation of the time invariant LQR controller for selected operating point. The entire process can be implemented in the Matlab environment using the `lqr` command. In addition to matrices A and B, it is also necessary to specify weight matrix Q for states and R for control signal (8). Their choice is made by an expert based on his experience and importance of each state value.

$$Q = \begin{bmatrix} 10 & 0 & 0 & 0 \\ 0 & 5 & 0 & 0 \\ 0 & 0 & 50 & 0 \\ 0 & 0 & 0 & 180 \end{bmatrix} \quad R = |1| \quad (8)$$

As mentioned above, the result of the design is the controller in the form of a matrix of constant coefficients K. After the calculation, the matrix (9) was obtained.

$$K = |58.8071 \ 7.4698 \ -7.0711 \ -15.7805| \quad (9)$$

The final step of the design is conversion between LQR controller constants to the gain values for the fuzzy controller. This is based on equation (6). Because the number of unknown variables is bigger than the number of equations, it is necessary to choose one of the gain values. This will be the G_1 value at the fuzzy controller input regarding the arm angle value. The regulation should operate at maximum of $\pm 45^\circ$, which is approximately ± 0.8 rad. It is worth noting that such large deflections are quite exaggerated and should not be achieved if tested on a real setup. Value of G_1 will be obtained as follows:

$$G_1 = \frac{1}{0.8} = 1.25 \quad (10)$$

The other constants can be calculated according equation (6).

$$G_0 = \frac{K_1}{G_1} = 47.0457 \quad (11)$$

$$G_2 = \frac{K_2}{G_0} = 0.1588 \quad (12)$$

$$G_3 = \frac{K_3}{G_0} = -0.1503 \quad (13)$$

$$G_4 = \frac{K_4}{G_0} = -0.3354 \quad (14)$$

The obtained values from (10)-(14) were applied to the structure shown in Fig. 5. The proposed controller was then tested in offline simulation. In order to assess its functionality, at the beginning of the simulation, the pendulum arm was shifted from the upright position via the initial condition in the pendulum integrator. Signals obtained from the simulation were compared the one that uses LQR controller designed during the previous calculations.

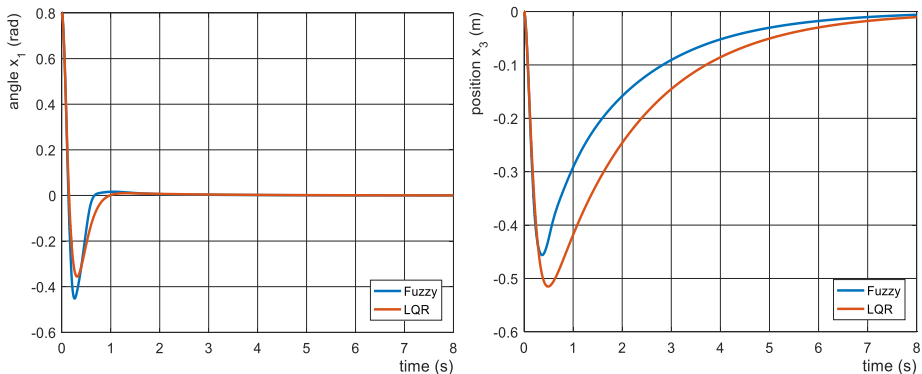


Fig. 6. Signal x_1 and x_3 over the time for simulation with initial pendulum angle deflection

5 Conclusion

The inverted pendulum can be stabilized in an upright unstable position in various ways. Typically, conventional methods are used, either the classic PID controller or a controller based on modern control theory. As an alternative, a pair of fuzzy controller based on the Mamdani model was used. The proposed paper outlined the other structure using a single controller. Several procedures have also been introduced, showing how to apply a standard fuzzy controller to a particular system. One of them was chosen and used to design pendulum stabilizing controller. Their functionality has been verified in simulation and compared to the LQR controller. Taking a look at this comparison in Fig. 6, it is necessary to realize that the fuzzy controllers are similar to the PD type and could be compared with a classical PD controller. Comparison with LQR has been chosen for its use in design process of fuzzy controllers.

The comparison in Fig. 6 shows a situation where, at the beginning of the simulation, the pendulum was deflected by 0.8 rad, i.e. approximately 45° . In both cases, the controllers managed to deal with this displacement even though they are designed for a linearized pendulum model in the upright position and the given displacement is quite far from that working point. This shows the robustness of both methods. When comparing the pendulum arm angle over time, it can be seen that when fuzzy control-

lers are used, there is a larger overshoot, but the settling time is smaller than in case of the LQR controller. Analysis of the cart position over the time, it is obvious that the system controlled by the fuzzy controllers shows a smaller deflection from the zero position and the settling time is smaller. However, in practice it corresponds to a few of centimeters only.

The paper introduced detailed control design for the inverted pendulum stabilization based on fuzzy controllers. It has also been verified in a pendulum simulation model corresponding to the real system, where the proposed strategy is supposed to be implemented. The simulation have shown that fuzzy control strategy is very robust and should therefore be able to deal with possible inaccuracies in the pendulum model compared to the real model and various disturbance variables. Control algorithm could be modified by changing the shape of each fuzzy set. However, it is already visible on the curves that the control is nonlinear.

References

1. Reznik, Leon.: Fuzzy controllers handbook: how to design them, how they work. Elsevier, 1997.
2. Ozana, Stepan, and Tomas Docekal.: The concept of virtual laboratory and PIL modeling with REX control system. Process Control (PC), 2017 21st International Conference on. IEEE, 2017.
3. Yamakawa, Takeshi: Stabilization of an inverted pendulum by a high-speed fuzzy logic controller hardware system. Fuzzy sets and Systems 32.2 (1989): 161-180..
4. Hong-yu, Luo, and Fang Jian.: An inverted pendulum fuzzy controller design and simulation. Computer, Consumer and Control (IS3C), 2014 International Symposium on. IEEE, 2014.
5. Yasunobu, Seiji, and Munehito Mori.: Swing up fuzzy controller for inverted pendulum based on a human control strategy. Fuzzy Systems, 1997. Proceedings of the Sixth IEEE International Conference on. Vol. 3. IEEE, 1997.
6. Oltean, Stelian-Emilian.: Swing-up and stabilization of the rotational inverted pendulum using PD and fuzzy-PD controllers. Procedia Technology 12 (2014): 57-64.
7. Radhamohan, Singh Vivekkumar, M. O. N. A. Subramaniam, and M. J. Nigam.: Fuzzy swing-up and stabilization of real inverted pendulum using single rulebase. Journal of Theoretical and Applied Information Technology 14.1/2 (2010): 43-49.
8. Mann, George KI, Bao-Gang Hu, and Raymond G. Gosine.: Analysis of direct action fuzzy PID controller structures. IEEE Transactions on Systems, Man, and Cybernetics, Part B (Cybernetics) 29.3 (1999): 371-388.
9. Reznik L. and Little A.: Fuzzy Controller Design From a Practitioner's Point of View – The Review of Methodologies. Australian Journal of Intelligent Information Processing Systems, 2 (4), 1995, pp. 1–9

Evaluation platform for quadcopter control design

Matěj Golembiovský

Department of Cybernetics and Biomedical Engineering, FEECS,
VŠB – Technical University of Ostrava, 17. listopadu 15,
708 33 Ostrava – Poruba, Czech Republic
matej.golembiovsky@vsb.cz

Abstract. This article is describing development of platform that can be used for easy testing control algorithms developed with Matlab and Simulink on the real quadcopter. It goes throughout basic information about choosing individual components of the system and integrating them together. Then different approaches about building the platform are discuss. Finally best solution that is capable of performing control loop in 3ms period is chosen. Whole platform is therefore capable of performing task for with it was designed.

Keywords: Quadcopter, Control, Matlab, Simulink, Rexygen

1 Introduction

Quadcopters are typical representation of the dynamic system that is really complex and difficult to control. For easier development and education of control systems for quadcopters, simple, known and graphical programing platform is essential. In the field of control design Matlab and Simulink is in fact sort of a standard.

Insomuch as Matlab and Simulink provide excellent capability for dynamic system identification and simulation, it is typically software to go for controller design. In order to rapidly verify designed controllers, there is need for testing platform that can provide connection between simulation and real-world system. Although Matlab and Simulink is really powerful software it lacks real-time capability for controlling target device. The main reason for this behavior is non-deterministic nature of the operating systems under witch it runs. To solve this problem control software compatible with Simulink called REXYGEN[3] [4] was chosen. This solution allow to take minimal effort in order to transfer designed controller from simulation to the real-world quadcopter.

The easiest and cheapest way to construct quadcopter these days is to use of the shelf components intended for the RC controlled models. With this in mind Navio2 control board was chosen. It integrates array of sensors[9] [10] that are suitable for positional feedback of the quadcopter and number of standard RC servo outputs for the control over the actuators. Another benefit of this board is that it is designed to work with Raspberry Pi minicomputer. This computer is

also supported by the Rexygen core. In combination with Linux core complicated with real-time extension whole system should perform deterministically in real-time tasks such as dynamic system control.

Whole Platform as described in this article can be seen in the figure1.

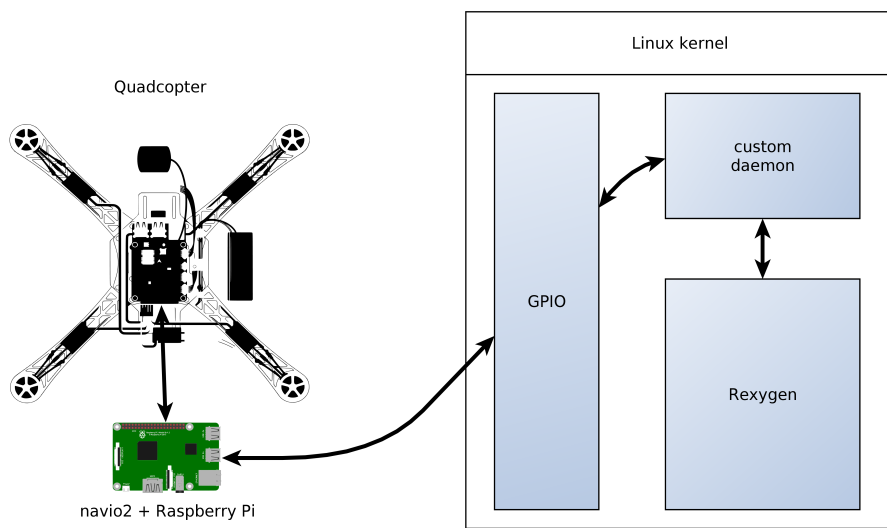


Fig. 1. Block diagram of the system.

2 Building the platform

In the introduction selected components and platforms was described. Although theoretically, all selected parts of the whole system, are really capable in performing tasks for witch they are designed, joining them together present some challenges. Both Rexygen and Navio2 comes with some ability to incorporate custom functions, but neither one of them are open-source so there is some serious limitations in doing so.

For a start Navio2 comes with examples of interfacing sensors and outputs with custom application. These examples are written for C++ and Python programming language. This allows to easy development of simple control application, or in our case some interface layer for Rexygen to gain access to the Navio2s peripherals. Biggest drawback in using Navio2 as a control board is that there is no available hardware schematic or firmware source code. That means that if there is some behavior not in favor of intended application, no easy fix is available and some workaround or compromise must be implemented. For example throughout development was found that update of the output servo RC signal happens only every 3ms and procedure for doing so is hard-coded in firmware of

the Navio2 and Linux kernel drivers. So compromise of limiting control period to minimum 3ms, from the 1ms target, had to be made.

As for the Rexygen available options for interfacing with Navio2 was described in[1]. Just for the recapitulation. There are three possible methods for interfacing external programs or adding new functions.

- SILO (Save input value, load output value)[6] - It is a block which allows to read and save (if need be) information into a file. This mechanism can be used in combination with external script which then exchanges information with Rexygen system using this file. In each file it is possible to transport only one variable which complicates systems with large amount of inputs/outputs. In case of use in control, this option can be very demanding in terms of hard disk use and its excessive wearing-out. For this reason it is advantageous to save transferred files to a part of file-system which is mapped in RAM-disc. Resulting regulation loop is therefore not burdened with access time and reading/entry speed of the hard drive.
- EPC (External program call)[7] - This option also uses the file saved in hard disk, or more precisely in RAM-disc for transferring information. However, it allows for more variables to be transferred in one structured file which makes it a lot easier to develop applications which have a large amount of inputs/outputs, or to be more precise, transferred information between Rexygen and external script.
- REXLANG[8] - As part of Rexygen system is also a Rexlang block which is basically an encapsulation of user code. This block is compiled together with a scheme and is as such an integral part of the resulting application, specifically the control loop. This significantly simplifies transfer of input and output variables, as it is no longer necessary to deal with transfer through files. Block uses its own scripting language derived from C language. Unlike language C, however, it is simplified to some extent and thus does not include all data types and operators. Experience also showed problem with declaration of variables in certain parts of the program. However, the biggest drawback is the inability to debug code and so this block is suitable for only the very basic applications.

In the process of development several strategies was tested out. First of all Rexlang block with code directly communicating with sensors on the Navio2 board was proposed. But practically intermediately after coding began it was clear that language for the Rexlang block is not up to the task. Finished code would be inefficient, hard to read and maintain.

As the next step utilization of the block EPC was tested. In this case Rexygen was writing control variables into the file located in RAM-disc. After that program written in C++ was called reading these variables and transferring them onto RC servo signals on the output pins of the Navio2 board. Then this program read all data from the sensors located on the Navio2 board, write them into another file on the RAM-disc and switch context to the Rexygen after terminating itself. Last step of this process is reading sensors data from the file by Rexygen and using them to calculate another control variable. This completed

control loop. This solution is pretty simplistic and solve some problems with synchronization of the REXYGEN and external program because REXYGEN starts external program and then waits until the program finishes. Sadly enough there is some significant drawbacks in the form of operating system overhead when new process is started. This overhead is so large that minimal period of control loop that was achieved was in the range of 100ms. And that was with the copy of external program located in RAM-disc to minimize latency due to loading speed from hard-drive.

Final solution is based on the combination of REXLANG block and external program running as daemon. External program fulfill similar role as the one in previous example. But communication between the daemon and REXYGEN is different. It utilizes TCP socket for data transfer between them(fig.2). Synchronization of the two programs is also completely different, daemon waits until REXYGEN connects to the socket and then restart internal counter of control loop period. After that point both program derive its control loop period from the system counter, therefore synchronization is guaranteed. Theoretically REXYGEN core and daemon could in this scenario run on the different computers exchanging data over LAN, but low latency[5] connection and different synchronization strategy must be implemented to ensure that whole system will maintain its deterministic behavior. With this model control loop with period 1ms was tested without a problem. But with limitation in the RC servo signal update rate resulting from issue mentioned above, periods of the control loop smaller than 3ms dos not make sense.

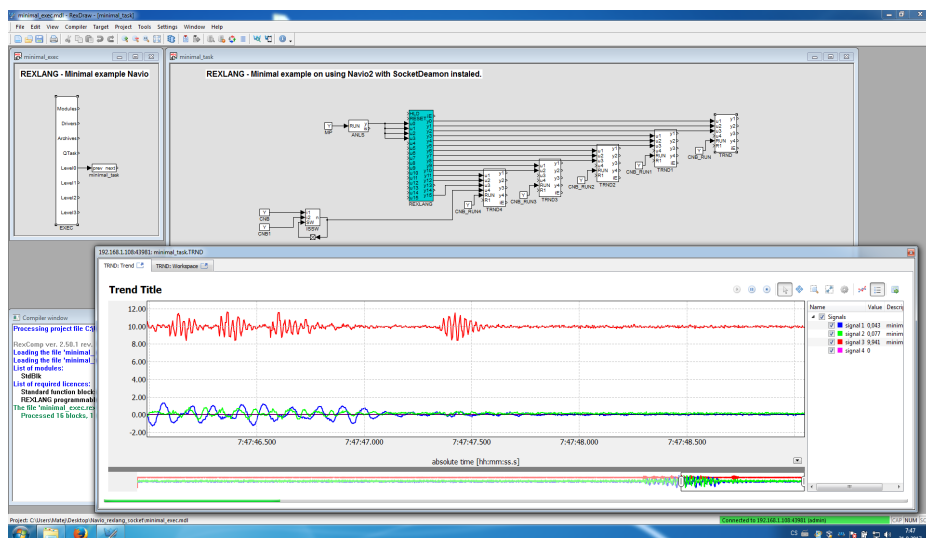


Fig. 2. Sensor data visualisation in REXYGEN.

As the last part, computationally intensive task of fusing data from sensors AHRS (Attitude Heading Reference System)[2] was implemented as part of the daemon. This system compute orientation of the quadcopter. Because of utilization 2 cores from the processor on the Raspberry Pi minicomputer. One for REXYGEN and one for daemon. It is advantageous to shift some processor intensive task to the daemon side to save more processor time for the control algorithm running under REXYGEN.

3 Conclusion

In this article platform for easy control algorithm of quadcopters was described. Platform is complex solution that can be used with various quadcopters constructed from of the shelf RC models parts. The size and lifting capability of the quadcopter is therefore scalable. For the control part of the system powerful enough single board computer Raspberry Pi in combination with matching control board for RC projects Navio2 was used. From the software point of view there is combination of REXYGEN control software, real-time Linux and custom written daemon. This system together deliver compatibility with Simulink models, real-time deterministic behavior and enough power to perform 3ms control loop.

As future improvement 1ms control loop would be nice achievement. But for this goal some custom hardware with high speed connection to the single board computer is probably necessary. In the case of development such a hardware capability of using DMA for data transfer between REXYGEN and it, for cut down daemon overhead, should be considered. And as last part of the chain standard RC motor controllers are probably not so fast to benefit from the shorter period of the control loop, so some custom solution of the controllers is probably option too.

Even though main goal of meeting 1ms control loop period was not achieved given limitations presented by chosen hardware solution. Robustness of presented solution and achieved 3ms control loop period put it in the category of successful evaluation platform for quadcopter control design.

4 Acknowledgment

This work was supported by the project SP2018/160, Development of algorithms and systems for control, measurement and safety applications IV” of Student Grant System, VSB-TU Ostrava.

References

1. Golembiovsky, M., J. Dedek, and S. Ozana. Multicopter Control with Navio using REX Control System, vol. 1836, 2017. doi:10.1063/1.4982002.

2. Madgwick, S. O. H., A. J. L. Harrison, and R. Vaidyanathan. Estimation of IMU and MARG Orientation using a Gradient Descent Algorithm, 2011. doi:10.1109/ICORR.2011.5975346.
3. S. Ozana, M. Pies, and T. Docekal, Case studies on design, simulation and visualization of control and measurement applications using rex control system, AIP Conference Proceedings, Vol. 1738 (2016).
4. Ozana, S., Pies, M., Slanina, Z., and Hajovsky, R., "Design and implementation of LQR controller for inverted pendulum by use of REX control system", 12th International Conference on Control, Automation and Systems (ICCAS), 343-347 (2012).
5. J. . Stauffert, F. Niebling, and M. E. Latoschik, Reducing application-stage latencies of interprocess communication techniques for real-time interactive systems, in Proceedings - IEEE Virtual Reality, Vol. 2016-July (2016), pp. 287288.
6. SILO Save input value, load output value <https://www.rexygen.com/doc/ENGLISH/MANUALS/BRef/SILO.html#x198-19700012>
7. EPC External program call <https://www.rexygen.com/doc/ENGLISH/MANUALS/BRef/EPC.html#x257-25600015>
8. REXLANG User programmable block <https://www.rexygen.com/doc/ENGLISH/MANUALS/BRef/REXLANG.html#x262-26100015>
9. Otahalova, T., Slanina, Z., and Vala, D., "Embedded sensors system for real time biomedical data acquisition and analysis", IFAC Proceedings Volumes (IFAC-PapersOnline) 11(part 1), 261-264 (2012).
10. Slanina Z., and Docekal, T., "Energy monitoring and managing for electromobility purposes", Proc. SPIE 10031, Photonics Applications in Astronomy, Communications, Industry, and High-Energy Physics Experiments 2016, 100311P (2016).

Chaotic properties of human gait

Radek Halfar

Department of Cybernetics and Biomedical Engineering, FEECS,
VŠB – Technical University of Ostrava, 17. listopadu 15,
708 33 Ostrava – Poruba, Czech Republic
radek.halfar@vsb.cz

Abstract. Human gait is one of the main attributes which ensures a good quality of life. It is basic way of travel and way to create a healthy lifestyle without cardiovascular system diseases. This article investigates dynamical properties of human gait represented as stride times intervals recorded from gait of ten healthy young man. For this purpose, the 0-1 test for chaos and Fourier spectra were applied.

Keywords: Gait, Chaos, 0-1 test for chaos, Fourier spectra

1 Introduction

Human gait is result of complex process which includes coordination of large amount of muscles. This process can be represented by number of different ways e.g. foot acceleration, angular velocity or ground reaction forces. In this paper, gait is represented by stride time intervals.

Since exists many methods of nonlinear analyses suitable for gait analysis, many studies can be found, that are dealing with this problem. For example, in study [1] researchers using Lyapunov exponents and fractal dimensions found, that human gait exhibit chaotic dynamics. In paper [2] authors focused on determination of the influence of gait speed on the value of Largest Lyapunov exponent. Since a large amount of data is needed to test dynamic parameters, chaotic properties of human gait are also explored using mathematical models. Example of model exhibiting chaotic properties can be seen in paper [3].

In this work investigation of stride time intervals is introduced using Fourier spectra and the 0-1 test for chaos. This new mathematical method for exploration of dynamical properties never been used for this purpose before in any study known to author.

2 Material and Methods

2.1 The 0-1 test for chaos

This test, introduced in [4] (see also [5]), is used to distinguish regular and chaotic dynamics. The resulting value of this test can only be 0 (regular behavior) or 1 (chaos). For a given set of observations $\phi(j)$ for $j \in \{1, 2, \dots, N\}$ are computed translation variables for suitable choice of $b \in (0, 2\pi)$.

$$p_b(n) = \sum_{j=1}^N \phi(j) \cos(jb) = 1,$$

$$q_b(n) = \sum_{j=1}^N \phi(j) \sin(jb) = 1,$$

then the mean square displacement is computed using the following equation

$$M_b(n) = \lim_{N \rightarrow \infty} \frac{1}{N} \sum_{j=1}^N [p_b(j+n) - p_b(j)]^2 + [q_b(j+n) - q_b(j)]^2$$

Here $n < n_{\text{cut}}$ where $n_{\text{cut}} \ll N$. Then, the estimate of the modified mean square displacement is computed using the next equation

$$D_b(n) = M_b(n) - \left(\lim_{N \rightarrow \infty} \frac{1}{N} \sum_{j=1}^N \phi(j) \right)^2 \frac{1 - \cos(nb)}{1 - \cos(b)}.$$

Finally, the output of the 0-1 test is obtained as correlation coefficient of ξ and Δ for fixed parameter b

$$K_b = \text{corr}(\xi, \Delta)$$

where $\xi = (1, 2, \dots, n_{\text{cut}})$ and $\Delta = (D_b(1), D_b(2), \dots, D_b(n_{\text{cut}}))$. To get K as the output of the 0-1 test, as limiting value of all K_b , the result value is taken as

$$K = \text{median}(K_b).$$

2.2 Dataset

The data used in this study was obtained using PhysioNet web site [6]. This dataset contains stride time intervals of ten young, healthy men. Participants had no history of any neuromuscular, respiratory or cardiovascular disorders, and were taking no medications. Mean age was 21.7 years (range: 18-29 years). Height was 1.77 ± 0.08 meters (mean \pm S.D.) and weight was 71.8 ± 10.7 kg.

Subjects walked continuously on level ground around an obstacle free, long (either 225 or 400 meters), approximately oval path and the stride interval was measured using ultra-thin, force sensitive switches taped inside one shoe. From this data stride intervals were extracted. More details about dataset can be found in [7].

3 Main results

Since the 0-1 test for chaos needs for proper work at least 3000 samples. Only data from normal walk and fast walk were evaluated. Results of these tests can be seen in Fig. 1. From these results can be seen, that stride time intervals exhibit chaotic behaviour, since all resulting values are close to one.

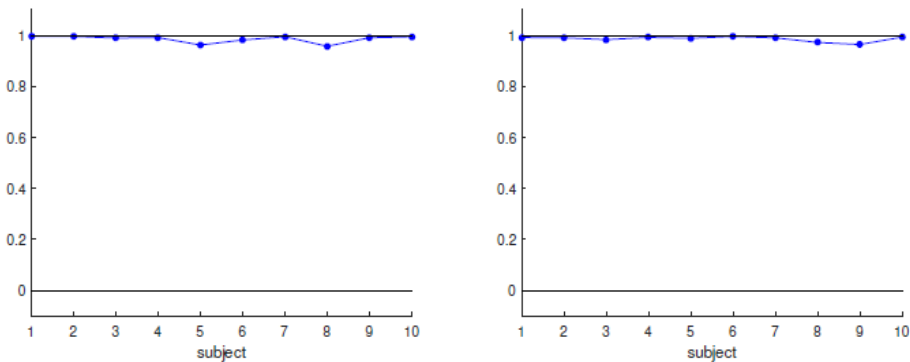


Fig. 1. Results of 0-1 test for chaos for stride interval - fast walk (left) and normal walk (right).

Next, Fourier spectra were plotted to confirm chaotic dynamic of investigated time series (see Fig. 2).

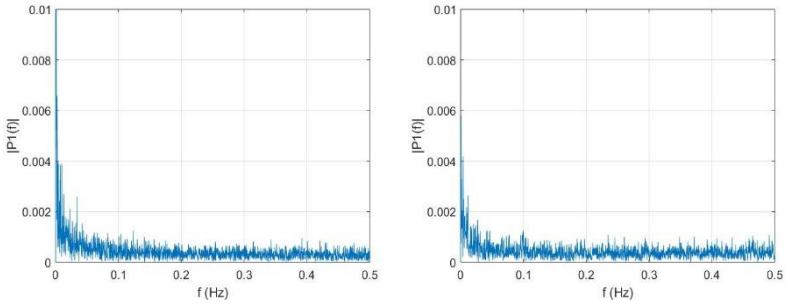


Fig. 2. Fourier spectrum of stride interval - fast walk (left) and normal walk (right).

In this case, the Fourier spectra is formed by a number of harmonic components having the basic, super-harmonic, sub-harmonic, and combination frequencies on which there are superposed further motions with frequencies forming the sided bands of the dominant frequencies. Their mutual ratio indicates the irregularity of the motion.

4 Conclusions

In this paper, dynamical properties of stride time intervals were investigated using the 0-1 test for chaos and Fourier spectra. From the results can be seen that this data showing chaotic dynamic.

References

1. S. Iqbal, X. Zang, Y. Zhu, H. M. A. A. Saad and J. Zhao, "Nonlinear time-series analysis of different human walking gaits," 2015 IEEE International Conference on Electro/Information Technology (EIT), Dekalb, IL, 2015, pp. 025-030. doi: 10.1109/EIT.2015.7293419.
2. Josiński, Henryk & Michalczuk, Agnieszka & Świtoński, Adam & Mucha, Romualda & Wojciechowski, Konrad. (2015). Quantifying Chaotic Behavior in Treadmill Walking. 317-326. 10.1007/978-3-319-15705-4_31.
3. Montazeri, Saeed & Sadeghi, Maryam & Niaty, Ali & Towhidkhal, Farzad & Jafari, Sajad. (2018). The simple chaotic model of passive dynamic walking. *Nonlinear Dynamics*. 10.1007/s11071-018-4252-8.
4. Gottwald A, Melbourne I. A new test for chaos in deterministic systems. *Proc. R. Soc. London A*. 2004;460:603–611.
5. Gottwald A, Melbourne I. On the implementation of the 0-1 test for chaos. *SIAM J. Appl. Dyn.*. 2009;8:129–145.

6. PhysioNet. Unconstrained and metronomic walking. <https://physionet.org/physiobank/database/umwdb/>, 2001. [Online; accessed 10-July-2018].
7. Hausdorff JM et al. Fractal dynamics of human gait: stability of long-range correlations in stride interval fluctuations. *J Appl Physiol* 80:1448-1457, 1996.

A Priority Driven Embedded Device

Karolína Janošová and Michal Prauzek

Department of Cybernetics and Biomedical Engineering, FEECS,
VŠB – Technical University of Ostrava, 17. listopadu 15,
708 33 Ostrava – Poruba, Czech Republic
karolina.janosova@vsb.cz

Abstract. The aim of this research article is find methods how to markedly decrease a power consumption of a low-power embedded system. Maintaining all system's features is desirable for a power management. Improving a power management is very important especially in battery operated embedded systems without any possibility of energy harvesting, that rely solely on a battery power.

This contribution propose a fuzzy rule-based classifier for a simulation of the priority of the operation and the battery voltage. The aim is to achieve a best possible efficiency of a whole system. Our paper offers a proposal of arrangements for a fuzzy expert system. Variables was chosen for proposal of a fuzzy expert system. These variables have a most significant impact on a extension of a systems operating time.

Keywords: Low-Power Embedded System, Fuzzy expert system, Battery management system

1 Introduction

Portable devices, like cellular phones, tablets, GPS trackers, watches, laptops etc. is possible to find in the all everyday technical areas. The practical examples are described in [5], [2] or in [6]. The energy harvesting system, which will be also one of the future use of this system, is introduced in [3].

A large amount of methods based on the hardware or the software solution were designed for the prolonging operating time of portable devices. The aim of this study is to come up with one universal method for reducing system's power consumption using the fuzzy expert system. Many of software-based methods are characterized in that they apply e.g. advanced data analytics from acquired measurements. The neural network or fuzzy expert system methods, etc. can be included among other methods. Furthermore, the study proposes a set of arrangements which could be applicable in many simple low-power embedded devices followed by the simulation of usable operating modes using the fuzzy method. As described in this paper, one of the topics is to focus on the hardware (re)configuration and finding sources of the most significant power draw. The aim of this study is to come up with one universal method for reducing system's power consumption using the fuzzy expert system.

Section Background briefly discusses general characteristics of battery management system and fuzzy methods. Parts of the designed measurement apparatus along with methods used for the Fuzzy control system are described in System Structure and Methods. Testing and Results section solves experiments of proposed fuzzy' expert system. Finally, major findings and outlines of our future work are summarized in the Conclusion.

2 Background

The issue of the energy consumption is one of the biggest concerns of current embedded systems. One of the general aims of the power management for portable devices, described in [7], is to balance power consumption to maximize device's operating time while maintaining required functionalities that are needed for the respective application under given conditions.

2.1 Fuzzy model

Artificial intelligence tools, such as expert system, fuzzy logic, and neural network are some of methods used in power electronics for the energy battery management system. The fuzzy expert system is a computer software that emulate the reasoning process of a human expert or provide in an expert manner in domain for which no human expert exists [1].

The language model is an expression that formalizes the relationship between input and output language values of the system. It is used to describe the non-numeric behavior of complex systems and defines the language model as an expression. In this expression occur language variables, their names, the names of their language values, the logical clutches and truth values. The standard form of the expression of this relationship is conditional IF-THEN rules. This rule is called the Mamdani type rule and it is a very effective form of expressing human knowledge in fuzzy systems. Fuzzy methods enable to deduce conclusions based on the imprecise description of the given situation thanks linguistically formulated fuzzy rules:

$$IF X1 \text{ is } A1 \text{ AND } X2 \text{ is } A2 \text{ THEN } Y \text{ is } B \quad (1)$$

where $A1$, $A2$ and B are certain predicates characterizing the variables $X1$, $X2$ and Y . They are specified linguistically. The software enables to work with specific kind of linguistic expressions, or the user may specify his own ones. There exist approximate reasoning methods (type of inference) for explication fuzzy IF-THEN rules. Logical deduction, Fuzzy approximation with conjunctions or Fuzzy approximation with implications [4] can be included among these methods. For this system the Fuzzy approximation with conjunction was chosen. The aim of this method is to approximate the function hidden inside the fuzzy relation. The Center of Gravity method (CoG) is one of the way how to achieve the functional fuzzy approximation for defuzzification. In this article the Center of Gravity method was chosen.

3 System Structure and Methods

3.1 Measuring Apparatus

The measuring apparatus features a microcontroller Freescale FRDM-KL25Z (MCU). The MCU is connected via I/O pins to multi-sensor board FRDM FXS MULT2-B. The accelerometer from FXS MULT2-B board was used as a load during the system testing. The system further comprises a „gas gauge” battery monitoring circuit LTC 2941, connected to the MCU via I²C communication. The designed measuring system comprises one rechargeable Li-ion battery 6SP652535 as a power supply having capacity 400 mAh.

3.2 Proposal of the Fuzzy Expert System

The aim of this proposal is simulate the lifetime of the designed device. The proposal is realized in the LFLC2000 software and presumes two input linguistic variables with five linguistic values and one output variable with five linguistic values. Based on created input and output variables follow by creation of 25 decision rules of the fuzzy expert system. This section defines input and output language variables and their parameters of the language values. Input linguistic variables include battery Voltage (Table 1). The output linguistic variable is the Mode of the entire device and has five linguistic values (Table 2). The experiments will be realized after proposing the system.

Table 1. Input variable Voltage. The following variable includes five input linguistic variables.

Voltage		Priority	
Linguistic variables	Points of triangular function	Linguistic variables	Points of triangular function
Lowest	(3, 3, 3.25)	Lowest	(0, 0, 25)
Low	(3.15, 13.33, 3.55)	Low	(0, 25, 50)
Average	(3.42, 3.59, 3.77)	Middle	(25, 50, 75)
High	(3.7, 3.85, 4.05)	High	(50, 75, 100)
Highest	(3.9, 4.18, 4.18)	Highest	(70, 100, 100)

The input variable Priority specifies the priority claim for the required operation or the process. This means that it determines the order of operations required by the system according to their importance (e.g. data processing or data transfer). Determining the Priority is therefore dependent on the amount of the battery voltage (its viability). An example may be when the battery voltage level is at a very low level e.g. 25 % and Priority is high e.g. 75 %. In this case, a less energy-intensive mode will be determined (e.g. mode with reduced frequency of data transmission or MCU frequency reduced, etc.), to achieve longer system operation.

Table 2. Output variable Mode. The following variable includes five output linguistic variables.

Linguistic variables	Points of triangular function
Mode 1	(0, 0, 1.25)
Mode 2	(0, 1.25, 2.5)
Mode 3	(1.25, 2.5, 3.75)
Mode 4	(2.5, 3.75, 5)
Mode 5	(3.75, 5, 5)

4 Fuzzy Expert System Design Testing

The settings of the individual mode is in the (Table 3).

Table 3. Arrangements for the individual modes of the the system's energy consumption. In the case of the individual mode was gradually reduces the MCU frequency and disconnected the unnecessary peripheries according to the system needs and priority of the user.

Mode	Settings of the mode
Mode 1	default
Mode 2	48 MHz, disconnect periph. and OpenSDA
Mode 3	8 MHz, disconnect periph. and OpenSDA, lower sampl. freq.
Mode 4	4 MHz, low sampling freq.
Mode 5	4 MHz, lower sampling freq., no processing

To verify the functionality of the proposed system, a simulation function verification was performed. Based on the model, values were randomly selected for individual input variables (Table 4). In the LFLC 2000 program, the fuzzy approximation with conjunctions as an interference method and as the defuzzification method the Center of gravity were chosen.

Table 4. Testing values of linguistic variables

	Test1	Test2
Voltage	3.80	3.94
Priority	87.11	64.43
Mode	4	2

The simulation tests were performed for input language variables and its parameters of language competence functions to test and display the result for

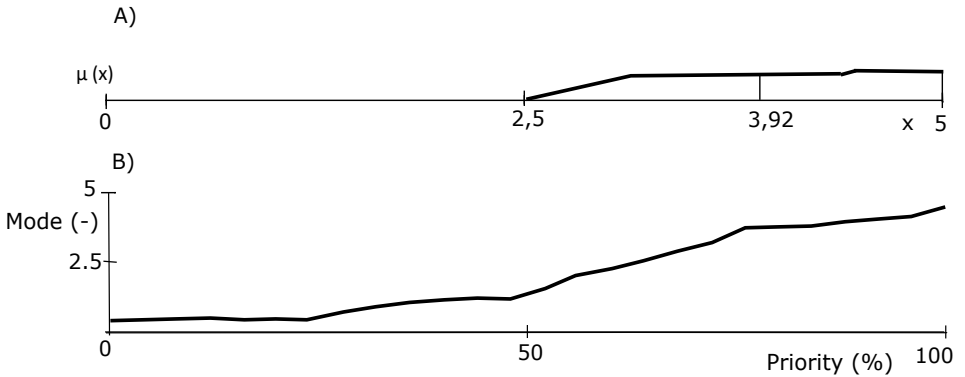


Fig. 1. The graphs illustrate the result from the Test 1 in (Table 4). In the section A) is possible to see the result after defuzzification and in the section B) Representation of variable Priority.

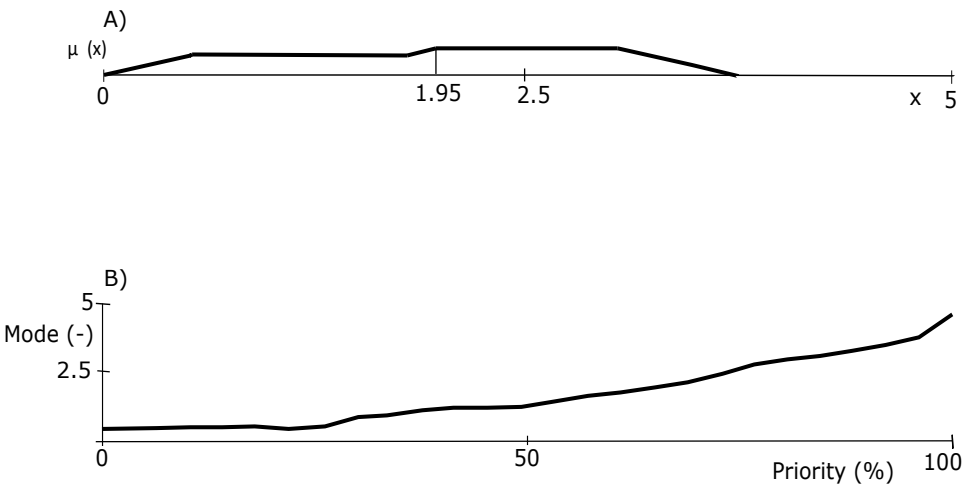


Fig. 2. The graphs illustrate the result from the Test 2 in (Table 4). In the section A) is possible to see the result after defuzzification and in the section B) Representation of variable Priority.

following values. The first test was provided for battery voltage 3.80 V and Priority 87.11 %. The best result is Mode (see in (Figure 1)). The second test was provided for higher battery voltage 3.94 V and lower Priority 64.43 %. The best result is Mode 2 (see in the (Figure 2)).

5 Conclusion

The aim of this research was to propose a functional fuzzy rule-based model for the evaluation of the operating mode, to enable the longest lifetime of the system. The system is composed from two input linguistic variables: Priority of the operations and Voltage of the battery. The output linguistic variable was the Mode. The Mamdani's Fuzzy Approach model was used for the design. Thereafter, as the method of the defuzzification, the Center of gravity was chosen.

The reason of our research was to create a functional model of the device. The device operates in a low energy mode and can be used to power a wide range of portable devices.

Our future work will be directed to the investigation of other ways leading to lower consumption, so as to make the battery management more efficient. Enhanced equipment can then be used for real-life testing, environmental testing, medical sensors or portable devices.

References

1. Kandel, A.: Fuzzy expert systems. CRC press (1991)
2. Kromer, P., Prauzek, M., Musilek, P.: Harvesting-aware control of wireless sensor nodes using fuzzy logic and differential evolution. In: 2014 11th Annual IEEE International Conference on Sensing, Communication, and Networking Workshops, SECON Workshops 2014. pp. 51–56 (2014)
3. Musilek, P., Prauzek, M., Kromer, P., Rodway, J., Barton, T.: Intelligent Energy Management for Environmental Monitoring Systems (12 2017)
4. Novak, V., Perfilieva, I., Mockor, J.: Mathematical principles of fuzzy logic, vol. 517. Springer Science & Business Media (2012)
5. Prabhakar, T., Devasenapathy, S., Jamadagni, H., Prasad, R.: Smart applications for energy harvested wsns. 2010 2nd International Conference on COMMunication Systems and NETworks, COMSNETS 2010 (2010)
6. Prauzek, M., Konecny, J., Hamel, A., Hlavica, J.: Fuzzy energy management of autonomous weather station. IFAC-PapersOnLine **28**(4), 226–229 (2015)
7. Stankovic, J.A., He, T.: Energy management in sensor networks. Philos Trans A Math Phys Eng Sci **370**(1958), 52–67 (Jan 2012)

Use of Independent Component Analysis for Fetal ECG Processing

René Jaroš and Radek Martinek

Department of Cybernetics and Biomedical Engineering, FEECS,
VŠB – Technical University of Ostrava, 17. listopadu 15,
708 33 Ostrava – Poruba, Czech Republic
{rene.jaros, radek.martinek}@vsb.cz

Abstract. This work deals with fetal electrocardiography (fECG) processing by Independent Component Analysis (ICA). Testing is performed on 7 synthetic records with different level of Signal-to-Noise Ratio (SNR) and the evaluation is performed on calculation of improvement SNR. The experiment was based on testing multiple algorithms based on the ICA method, such as the algorithm using the kurtosis value, the algorithm using the negentropy value and the algorithm using the maximum value of kurtosis. The results showed that all ICA based algorithms a lot improve SNR, but the lowest accuracy was achieved by the algorithm using the maximum value of kurtosis.

Keywords: ECG extraction; fetal Electrocardiogram; Independent Component Analysis; non-adaptive filtration; Signal to Noise Ratio

1 Introduction

Fetal electrocardiography (fECG) is very important tool for monitoring of fetal well being. From this signal is possible to determine fetal Heart Rate (fHR), which gives very important information about fetal hypoxia, and fECG contains information that cannot be obtained by ultrasound-based methods. Fetal ECG can be measured by invasive technique, but it is dangerous for mother and fetal health, because its invasive nature and because electrode is attached directly to the fetus. Non-invasive technique, which is measured by attaching electrodes to the maternal abdomen, is not too harmful method. Measured abdominal ECG signal (aECG) contains both maternal and fetal component and noises. Equation (1) shows composition of aECG signal [1, 2].

$$x_{\text{aECG}}(n) = x_{\text{mECG}}(n)x_{\text{fECG}}(n) + n(n) \quad (1)$$

The value of Signal-to-Noise Ratio (SNR) of aECG signal depends on position of fetus, week of pregnancy and also on placement of electrodes. For evaluation is important to know, that normal fHR is in range from 120 to 160 beats per minute (bpm) and that amplitude of fECG signal is 10 to 30 times weaker then amplitude of maternal ECG (mECG) [3, 4].

Required fECG signal is obtained by using the adaptive and non-adaptive methods. Adaptive methods uses for extraction of fECG signal one aECG signal and one mECG signal, which is recorded on the maternal thorax and does not contains fetal component. Non-adaptive methods use only aECG signal as input for their algorithms. The most widely used non-adaptive methods are methods based on blind source separation (BSS), where belongs the most commonly used method for fECG extraction called independent component analysis (ICA) [3].

This work deals with use of different ICA based algorithms for fECG extraction. Section 2 describes used material and methods. Section 3 focuses on the results of the experiment, and Section 4 includes discussion.

2 Materials and methods

2.1 Independent component analysis

Independent Component Analysis is looking for a non-Gaussian data with independent components, which are statistically independent. Basically, ICA projects the input data into higher dimension space. This method is very quick and requires at least two input aECG signals for estimation of fECG signal. Two electrodes placed on maternal abdomen provide two signals $x_1(t)$ and $x_2(t)$, where x_1 and x_2 are amplitudes, and t is the time. All signals are sum of heart signals and marked as $s_1(t)$ and $s_2(t)$. Equations (2) and (3) show principle of ICA, where a_{11} , a_{12} , a_{21} , and a_{22} are parameters that depend on distance of a maternal and fetal heart from an electrode. Equation (4) shows vector-matrix notation, where \mathbf{A}_{mix} is mixing matrix. Equation (5) shows, that from inverse matrix \mathbf{W} can be achieved matrix \mathbf{A}_{mix} [5, 6].

$$x_1(t) = a_{11}s_1 + a_{12}s_2 \quad (2)$$

$$x_2(t) = a_{21}s_1 + a_{22}s_2 \quad (3)$$

$$\mathbf{x} = \mathbf{A}_{\text{mix}}\mathbf{s} \quad (4)$$

$$\mathbf{s} = \mathbf{W}\mathbf{x} \quad (5)$$

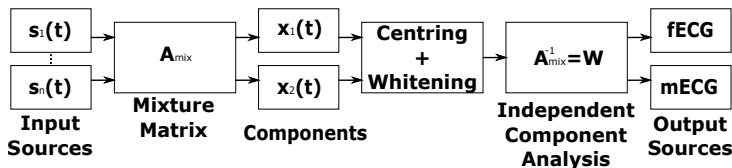


Fig. 1: Block scheme of independent component analysis.

Algorithm of ICA method contains its own pre-processing of signal by centering, which creates a vector with zero mean value, and whitening, which creates a vector which is white, its components are uncorrelated and their variances equal unity. Figure 1 shows function of ICA algorithm on a block diagram [1, 3].

2.2 Dataset

Synthetic data were created by the signal generator created by Martinek et al. in 2016 [7]. This generator is a multi-channel generator, which provides a reference fECG and mECG for the selected electrodes. Can be set value of fHR and maternal Heart Rate (mHR), pregnancy week from 20th to 42nd week of pregnancy can be selected, and noise could be added. By this generator, three electrodes was chosen, which contains fECG with 130 bpm and mECG with 75 bpm and sampling frequency was set on 1 kHz. This three aECG signals was generated with 7 different SNR levels from approximately 5 to -30 decibels (dB). The levels varied by 5 dB are marked with Roman numerals from I to VII. Reference fECG signals were also generated for all chosen levels of input SNR. Figure 2 shows the generated aECG signal, where fetal R peaks are marked with letter *f* and maternal R peaks are marked with letter *m*.

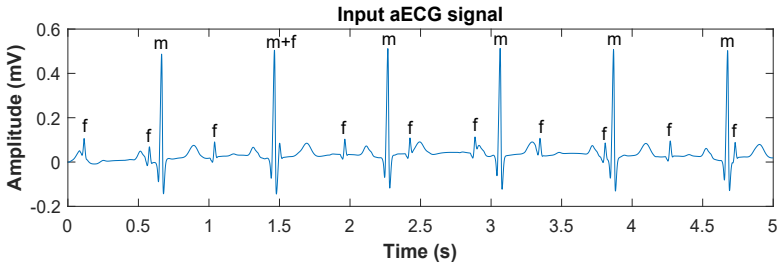


Fig. 2: Input aECG signal with SNR=-16.7584 dB, which belongs into level V.

2.3 Evaluation Parameter

For this article, objective evaluation is more relevant and SNR was chosen for it. Signal-to-Noise Ratio define the relationship between the required signal and the noise. The resulting SNR is calculated by subtracting input SNR from output SNR. Equation (6) shows calculation of SNR , where $fECG_{ideal}$ is generated fECG by generator and $fECG_{signal}$ is input aECG (calculation of input SNR) or extracted fECG by proposed algorithm (calculation of output SNR) [8].

$$SNR = 10 \log_{10} \frac{\sum_{n=1}^{N-1} (fECG_{ideal})^2}{\sum_{n=1}^{N-1} (fECG_{signal} - fECG_{ideal})^2} \quad (6)$$

3 Results

This section shows results of experiments made on synthetic data by three different ICA based algorithms, such as the algorithm using the kurtosis value (Kurtosis algorithm), the algorithm using the negentropy value (Negentropy algorithm) and the algorithm using the maximum value of kurtosis (Max algorithm). First, all ICA-based algorithms was implemented in program MATLAB and then these algorithms were used on all 7 synthetic data. Table 1, which summarize filtration efficiency, was created. It can be seen, that Kurtosis algorithm and Negentropy algorithm achieved practically same performance and that Max algorithm does not achieved the same high efficiency. At level of input aECG signals VII (approximately -28 dB), Kurtosis algorithm had output SNR -1.6522 dB, Negentropy algorithm -1.6699 dB and Max algorithm -1.5786 dB, that show that all three algorithms stoped working and we didn't tested them on input aECG signals with lowest SNR.

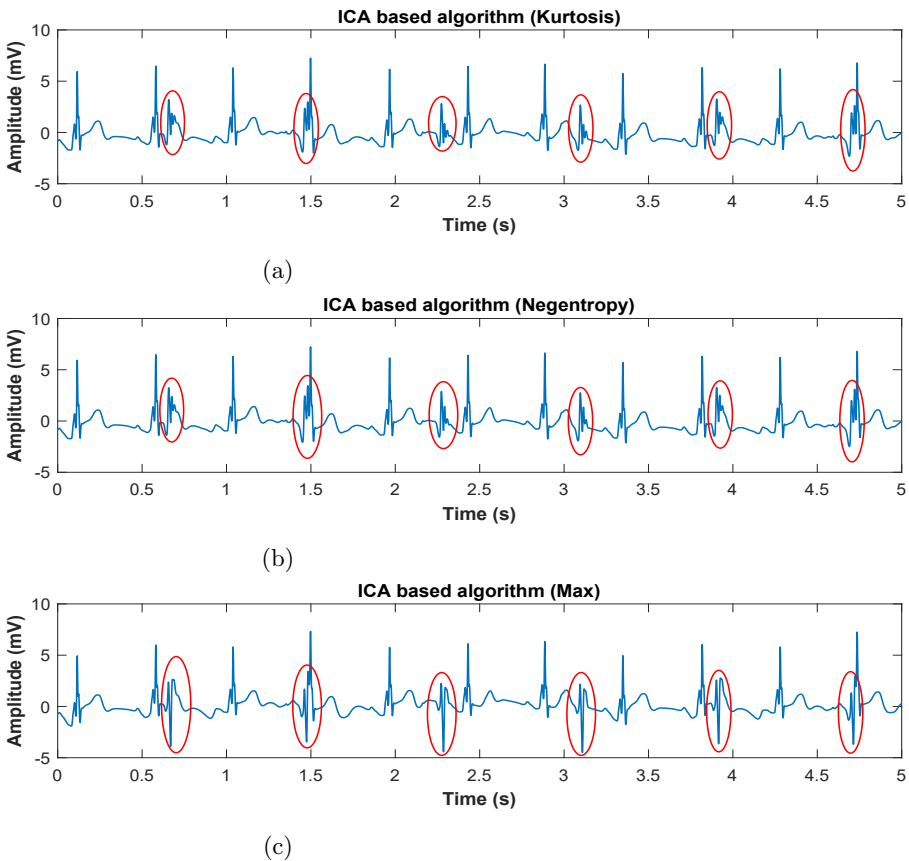


Fig. 3: Outputs of ICA based algorithms for fECG estimation.

Table 1: Table of calculated values of improvement SNR after using individual ICA based algorithms.

Level	Kurtosis	Negentropy	Max
I	-2.3773	-2.2151	0.3491
II	6.6729	5.7022	4.5971
III	9.2076	8.8729	3.7994
IV	13.8068	13.9592	7.4349
V	16.3069	16.7261	13.8369
VI	20.3542	20.2281	18.6271
VII	26.3907	26.3729	26.4643

Figure 3 shows example of output signals from all three algorithms achieved from synthetic data with SNR level V. From this figure can be seen, that ICA algorithm changes amplitude of output extracted signals. Red circles demonstrate deformations of fECG signals by maternal QRS complexes, but these deformations are not very critical to determining fHR.

4 Conclusion

In this paper, we have tested ICA based algorithms, such as the algorithm using the kurtosis value, the algorithm using the negentropy value and the algorithm using the maximum value of kurtosis. All three tested algorithms achieved good results, but Max algorithm does not achieved the same accuracy as other two algorithms. Minor negative of these algorithms is that they change amplitude of extracted components and that output fECG signals are deformed by maternal QRS complexes, but it's basically ICA problem. Evaluation by calculation of improvement SNR showed that ICA based algorithms stop working if input signals have SNR lowest then -30 dB. Kurtosis and Negentropy algorithms improved SNR by up to 25 dB, so these algorithms are very accurate and effective for fECG estimation.

Acknowledgment

This article was supported by the Ministry of Education of the Czech Republic (Project No. SP2018/170). This work was supported by the European Regional Development Fund in the Research Centre of Advanced Mechatronic Systems project, project number CZ.02.1.01/0.0/0.0/16_019/0000867 within the Operational Programme Research, Development and Education.

References

- [1] Martinek R., Kahankova R., Jezewski J., Jaros R., Mohylova J., Fajkus M., Nedoma J., Janku P., and Nazeran H. Comparative effectiveness of ica and pca in extraction of fetal ecg from abdominal signals: Toward non-invasive fetal monitoring. *Frontiers in physiology*, 9, 2018. ISSN 1664-042X. doi: 10.3389/fphys.2018.00648. URL <https://www.frontiersin.org/article/10.3389/fphys.2018.00648/full>.
- [2] Clifford R., Sameni G. D. A review of fetal ecg signal processing; issues and promising directions. *The open pacing, electrophysiology & therapy journal*, 3:4, 2010. ISSN 1876536X. doi: 10.2174/1876536X01003010004. URL <http://benthamopen.com/ABSTRACT/TOPEJ-3-4>.
- [3] Kahankova R., Jaros R., Martinek R., Jezewski J., He W., Jezewski M., and Kawala-Janik A. Non-adaptive methods of fetal ecg signal processing. *Advances in Electrical and Electronic Engineering*, 15(3):476, 2017. ISSN 1804-3119. doi: 10.15598/aeec.v15i3.2196. URL <http://advances.utc.sk/index.php/AEEE/article/view/2196>.
- [4] Jagannath D. J. and Selvakumar A. I. Issues and research on foetal electrocardiogram signal elicitation. *Biomedical signal processing and control*, 10:224–244, 2014. ISSN 17468094. doi: 10.1016/j.bspc.2013.11.001. URL <http://linkinghub.elsevier.com/retrieve/pii/S1746809413001560>.
- [5] Hyvärinen A. and Oja E. Independent component analysis: algorithms and applications. *Neural networks*, 13(4-5):411–430, 2000. ISSN 08936080. doi: 10.1016/S0893-6080(00)00026-5. URL <http://linkinghub.elsevier.com/retrieve/pii/S0893608000000265>.
- [6] Raj C. G., Harsha V. S., Gowthami B. S., and Sunitha R. Virtual instrumentation based fetal ecg extraction. *Procedia Computer Science*, 70: 289–295, 2015. ISSN 18770509. doi: 10.1016/j.procs.2015.10.093. URL <http://linkinghub.elsevier.com/retrieve/pii/S1877050915032573>.
- [7] Martinek R., Kelnar M., Koudelka P., Vanus J., Bilik P., Janku P., Nazeran H., and Zidek J. A novel labview-based multi-channel non-invasive abdominal maternal-fetal electrocardiogram signal generator. *Physiological measurement*, 37(2):238, 2016. ISSN 0967-3334. doi: 10.1088/0967-3334/37/2/238. URL <http://stacks.iop.org/0967-3334/37/i=2/a=238?key=crossref.b5fbd21e3809d22c39c7c527446f4fb>.
- [8] Martinez M., Calpe J., Soria E., Guerrero J. F., Camps G., and Gómez L. Methods to evaluate the performance of fetal electrocardiogram extraction algorithms. In *Computers in Cardiology 2001*, pages 253–256. IEEE, 2001. ISBN 0-7803-7266-2. doi: 10.1109/CIC.2001.977640. URL <http://ieeexplore.ieee.org/document/977640/>.

Comparison of Effectiveness of Image Processing on Different HW Platforms

Jakub Kolařík, Radek Martinek, Jakub Štefanský and Petr Bilík

Department of Cybernetics and Biomedical Engineering, FEECS,
VŠB – Technical University of Ostrava, 17. listopadu 15,
708 33 Ostrava – Poruba, Czech Republic
{jakub.kolarikk, radek.martinek, jakub.stefansky, petr.bilik}@vsb.cz

Abstract. The work describes evaluation of available platforms in relation to a defined task for comparison of the effectiveness of their use. The beginning of the work contains a summary of the facts, a description of the individual platforms and their hardware equipment. In this particular case, this is conducted by changing the resolution of the input image in which the edges are detected using the Canny edge detection algorithm. The result of this work is the relative comparison of the platforms, even with the increase in the volume of data processed by the algorithm.

Keywords: Image processing, LabVIEW, FPGA, cRIO

1 Introduction

This work deals with evaluation of hardware equipment that can be used for fast data processing. Two industrial platforms and three variants of personal computer use were selected for this experiment. The industrial devices used exploit the FPGA technology, but have different performance parameters. However, the FPGA interface and the processor, whose data throughput may limit the performance of the entire device, can become a weak point for these devices.

2 Description of Industrial Controllers

The hardware parameters used in the experiments are listed in the table below (see Table 1). The actual description of the industrial platforms is included in the subchapters. Thanks to this table, it is possible to compare the ability of the individual platforms to effectively use their hardware.

However, we cannot convert these parameters to a ratio that expresses the effectiveness of use of the available devices per memory unit by means of indirect proportion (time/memory size). The contribution of the FPGA chip to the time complexity of the operation and clocking cannot be taken into account in this coefficient.

Table 1. Description of Platforms

Platform	NI myRIO 1900	IC - 3173	Dell Vostro 5568
Processor	Dual-core ARM Cortex-A9 MPCore	Dual-core Intel i7 2,2GHz	Intel Core i5-7200U
Non-volatile memory	512MB	64 GB	256 GB SSD
Operation memory	256MB 533MHz	8 GB	8 GB
FPGA chip	Xilinx Artix-7	Xilinx Kintex-7 XC7K160T	-
USB interface	2x USB 2.0 Hi-Speed	2x USB 3.0	3x USB 3.0
OS system	RTOS	Windows Embedded Standard 7 NI Linux Real-Time	Windows 10 Pro

2.1 NI myRIO

This is a built-in device manufactured by NI. This device is primarily designed for academic purposes and is an industrial solution to the compactRIO device.

The device has a configurable IO and can be connected to a host device via USB or 802.11b wireless protocol.

The essence of the NI myRIO consists of a programmable system on the Zynq-7010 SoC chip, which includes the ARM Cortex-A9 dual-core processor and the Xilinx Artix-7 programmable gate array. The real-time operating system runs on the processor side.

2.2 NI Industrial Controller

Industrial controllers are also interesting NI products. They offer high levels of processing power and connectivity for automated image processing, data acquisition, and control applications in extreme environments. Industrial Controllers (IC) are high-performance, fanless controllers that provide connectivity for communication and synchronization to automation equipment. You can use LabVIEW system design software to create, debug, and deploy logic to both the onboard FPGA and the processor.

3 Description of the Algorithms Application

This chapter includes a description of the algorithm used to compare HW platforms. The individual parts are described according to the complexity of the mathematical and logical operations they use. IC are high-performance, fanless controllers that provide connectivity for communication and synchronization to EtherCAT and Ethernet

CompactRIO chassis, EtherCAT motion drives, GigE Vision and USB3 Vision cameras, and other automation equipment. Controllers also have onboard isolated, transistor-transistor logic (TTL), and differential digital I/O. You can use LabVIEW system design software to create, debug, and deploy logic to both the onboard FPGA and the processor. LabVIEW contains over 950 signal processing, analysis, control, and mathematics functions to accelerate development.

3.1 Transformation to a colour model

One of the first and most frequently used colour models is RGB. Each pixel in the image of this model is composed of three values that correspond to the representation of red, green and blue. CMY is an alternative model to RGB. Another way of writing a colour is, for example, the HSV model, which indicates colour using colour tone, saturation, and brightness. However, it is necessary to convert the image to a grayscale model for edge detection. According to formula (3.1), the brightness level for the grayscale model is calculated. The weight coefficients are set according to the sensitivity of the human eye.

$$Y = 0,299 \cdot R + 0,587 \cdot G + 0,114 \cdot B \quad (3.1)$$

3.2 Filtration

Filtration is conducted for the purpose of noise reduction, smoothing, highlighting and edge detection. Convolution describes the image passage through a linear filter, which is the basis for image function filtering. The image is processed as a product of the mask coefficients with the values of the input image with the surroundings O ; this procedure is performed sequentially for each pixel of the image.

$$g_b(u, v) = \sum_{s=-a}^a \sum_{t=-b}^b h(s, t) \cdot f_b(u + s, v + t) \quad (3.2)$$

Formula 3.2 is a mathematical description of the discrete convolution used for filter application. The output image is $g_b(u, v)$. The convolutional mask is h with a size equalling to $m \times n$ where $m = 2 \cdot a + 1$ and $n = 2 \cdot b + 1$, $a, b \in N$. The mask dimensions are odd so that the pixel calculated could be in the middle of the mask. The most commonly used mask is a square mask where $a = b$.

3.3 Gaussian Filter

This type of filter is called Gaussian smoothing that uses a convolution mask. Where the pixels closer to the centre have a higher weight than the marginal ones. The weight distribution follows from the Gaussian curve. The filtration rate is based on parameter σ , which indicates the slope of the Gaussian curve. Figure 1 shows a Gaussian curve for a 1D signal.

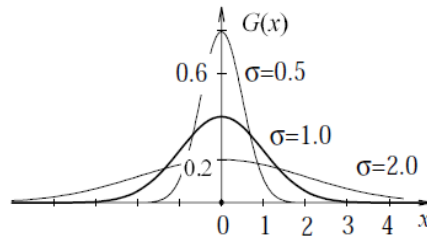


Fig. 1. Gaussian function

3.4 Edge detection – Sobel operator

Edge detection is performed by the Sobel operator using a 3x3 convolution mask. For edge detection, one vertical edge mask G_y and one horizontal edge mask G_x are used.

$$G_y = \begin{pmatrix} 1 & 2 & 1 \\ 0 & 0 & 0 \\ -1 & -2 & -1 \end{pmatrix}, G_x = \begin{pmatrix} -1 & 0 & 1 \\ -2 & 0 & 2 \\ -1 & 0 & 1 \end{pmatrix} \quad (3.3)$$

3.5 Canny Edge detection

Detection according to this algorithm consists of several steps [1]. At the beginning of the algorithm, significant edges are found to avoid omission or duplicate detection. Depending on the localization criterion, the actual and found edge position is then assessed, and such a deviation must be minimal. The last step is the requirement for one response, which is focused on shaded and particularly non-smooth edges not covered by the first requirement.

4 Image processing on FPGA

NI offers ready-made libraries and tools for working with the FPGA. These functions are divided into several categories according to their specific focus in the chain of processes that comprise image processing [3].

5 Test Implementation

The test contains the use of the Canny Edge Detection algorithm to determine the time complexity of this algorithm for each of the aforementioned platforms. This test was chosen because of its high demands on computing performance, which may result in platform deficiencies. The input data will be in three different resolutions in order to compare the results when increasing task complexity and to analyse the trends [2].

On the myRIO and IC platforms, there are two SW parts, one program runs on the RT processor and the other on the FPGA. Completely identical programs, except for minor differences in frequency and reference settings, will run on both platforms.

5.1 Real Time application

At the beginning, the program will initialize the camera for continuous scanning, image resolution and configuration of other parameters. The next step is uploading the FPGA application to the chip and running it. Based on the reference made to the FPGA application, two memories are initialized. The first memory is the DMA FIFO that is set to make the Host to Target transmission, representing the transfer from the RT processor to the FPGA chip. The second memory with the Target to Host transmission type transfers the data from the FPGA chip to the RT processor. The size of both memories corresponds to the number of pixels of the image scanned.

5.2 FPGA application

The FPGA application used the Single-Cycle Time (SCTL) main loop to optimize the codes for the FPGA platform. The content of this loop is then performed according to the specified clocking frequency. Due to the use of this loop, it was not possible to work with a decimal floating-point.

6 Evaluation of Performance Tests

The results of the tests enabled a comparison of the platforms according to the effectiveness of their hardware in the standardized image processing task. The graph (see Fig. 1 Fig. 2) shows the time complexity of the entire test. In the case of non-PC platforms, the next time stamp (see Fig. 3) was measured. This represents the time complexity of the detection algorithm without a delay caused by data transformation before and after the algorithm execution. This delay consists in converting a 2D field to a 1D field, and a reverse transformation after performing the Canny edge detector.

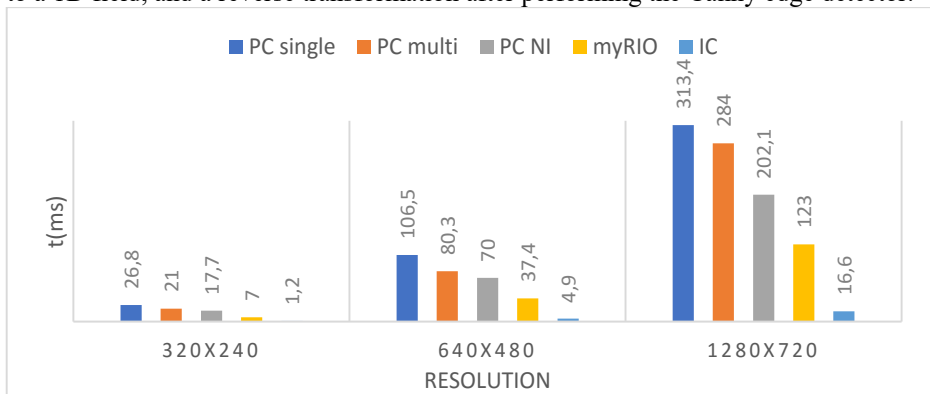


Fig. 2. Time complexity of Canny edge detection algorithm including array operations

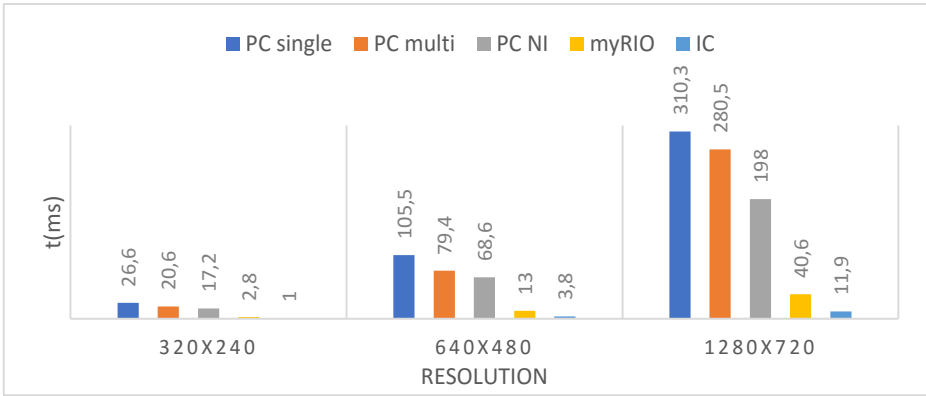


Fig. 3. Time complexity of Canny edge detection algorithm

To compare and highlight the effectiveness of HW platforms [4], the relative determination of time complexity according to the worst outcome (PC - single processor) was used. The Table 2 shows that, in the case of IC, the relative time complexity is maintained.

Table 2. Relative time delay of each platform compared to single processor PC

Platform		Relative time complexity [%]					
		Detection algorithm			Array manipulation included		
		320x240	640x480	1280x720	320x240	640x480	1280x720
PC	Single	-	-	-	-	-	-
	Multi	77,4	75,3	90,4	78,4	75,4	90,6
	NI	64,7	65,0	63,8	66,0	65,7	64,5
myRIO		10,5	12,3	13,1	66,0	65,7	64,5
IC		3,8	3,6	3,8	4,5	4,6	5,3

*Single - Single core processor; Multi – Dual core processor; NI – LabView Library function

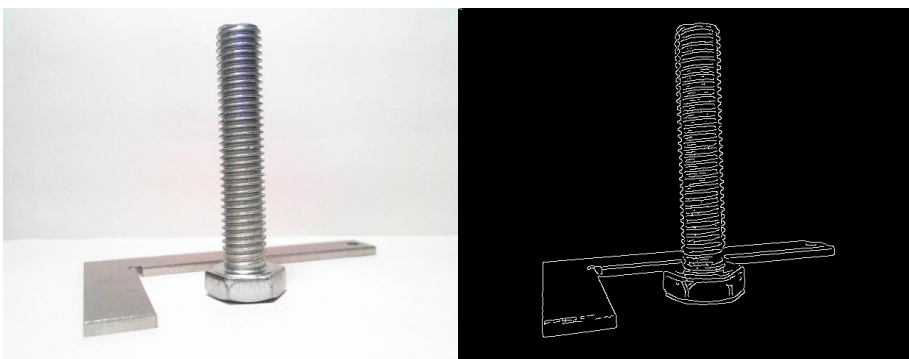


Fig. 4. Source image (left) and the result of Canny detection algorithm

7 Conclusion

Based on the results, it is obvious that the results of the industrial system using the FPGA chip come out significantly better than in the case of using a personal computer. However, these results may not be so disadvantageous for a personal computer due to a possible inefficient interpretation of the detection algorithm. When using the NI libraries, up to a 50% time saving was achieved compared to using the actual algorithm implementation on a single processor core.

When comparing the times measured, the IC overhead on the processor side is less than 2ms, while the time overhead from the process side of the much less powerful myRIO is less than 24ms. These data show that, in the case of myRIO, the processing time is most affected by the performance of the RT processor used other hardware components running under the processor.

Another limitation may be the transfer method, where the IC uses the PCIe between the processor and the FPGA, and myRIO uses transmission via the High performance AXI protocol.

Acknowledgment

This article was supported by the Ministry of Education of the Czech Republic (Project No. SP2018/170). This work was supported by the European Regional Development Fund in the Research Centre of Advanced Mechatronic Systems project, project number CZ.02.1.01/0.0/0.0/16_019/0000867 within the Operational Programme Research, Development and Education.

References

1. Kabade, A. L., & Sangam, D. V. (2016). Canny edge detection algorithm. *International Journal of Advanced Research in Electronics and Communication Engineering (IJARECE)*, 5(5), 1292-1295.
2. Maini, R., & Aggarwal, H. (2009). Study and comparison of various image edge detection techniques. *International journal of image processing (IJIP)*, 3(1), 1-11.
3. Xu, Q., Varadarajan, S., Chakrabarti, C., & Karam, L. J. (2014). A distributed canny edge detector: algorithm and FPGA implementation. *IEEE Transactions on Image Processing*, 23(7), 2944-2960.
4. Owens, J. D., Luebke, D., Govindaraju, N., Harris, M., Krüger, J., Lefohn, A. E., & Purcell, T. J. (2007, March). A survey of general-purpose computation on graphics hardware. In *Computer graphics forum* (Vol. 26, No. 1, pp. 80-113). Oxford, UK: Blackwell Publishing Ltd.
5. PXI FPGA Module for FlexRIO. National Instruments, <http://www.ni.com/cs-cz/shop/select/pxi-fpga-module-for-flexrio>

Model for autonomous classification of stage of heel bone fracture treatment using fixator based on X-ray images and Time iteration segmentation model

David Oczka

Department of Cybernetics and Biomedical Engineering, FEECS,
VŠB – Technical University of Ostrava, 17. listopadu 15,
708 33 Ostrava – Poruba, Czech Republic
david.oczka@vsb.cz

Abstract. In conventional procedures, reparation period of heel bone fracture is conventionally determined subjectively by clinician. Correct determination of treatment stage is very important in clinical traumatology, but human factor in such process can product in subjective mistakes. Autonomous classification of respective stage using mathematical model can be positive contribution to traumatology clinical practice. Because of periosteal callus is considered as main feature for stage of heel bone fracture determination in clinical practice, time deformation segmentation model based on fitting Gaussian energy for detection of periosteal callus was proposed.

Keywords: Heel bone fracture, fixator, autonomous classification, periosteal callus

1 Introduction

During healing period of heel bone, there are many factors, which could be observed to determine healing stage, such as thrombotic parameters, blood cells migration, oxygenation or forming of periosteal callus. Majority of such parameters are badly observable. The periosteal callus is structure formed in secondary period of healing of heel bone fracture and ensures stabilization of fracture fragments. It can be easily observable using X-ray.

2 Periosteal callus extraction

Geometrical parameters, such as diameter and size, of periosteal callus are tracked and processed. By clinical assumptions, such parameters can predict healing process.

3 Design and implementation

In cooperation with University hospital of Ostrava X-ray and CT clinical image data was used. CT images have significantly better contrast than X-ray images, but they are affected by certain artifacts. Therefore X-ray images were used for periosteal callus tracking. Developed segmentation model is fully autonomous. Only initial curve must be specified.

Periosteal callus is relatively homogenous environment without significant fluctuations of image intensity. Therefore, modeling based on Gaussian distribution was used. Then time deformation segmentation model using Gaussian energy minimization is used for relevant model of periosteal callus. Model works with predefined number of iterations to approximate area of periosteal callus. Based on energy map active contour is formed. Finally, binary model representing periosteal callus area is formed.

4 Results

Proposed segmentation model take advantage of well propagation of segmentation curve in analyzed environment without fast intensity changes, which means nearly focused intensity spectrum. Rapid changes of intensity as interface bone-periosteal callus terminates segmentation curve and determines segmentation model. In first iteration circle with smaller diameter than periosteal callus is set as segmentation curve. During each iteration, segmentation curve is changed to fit and approximate better shape of periosteal callus. After some experiments optimal setting was found as 500 iterations for iterative segmentation model. Segmentation curve of three X-ray images of same patient taken in third, sixth and ninth week after surgery is shown at Fig. 1.

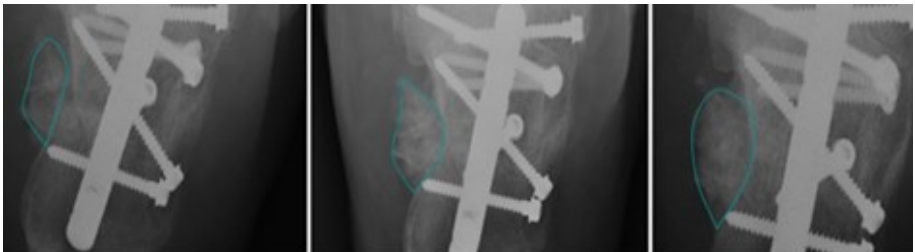


Fig. 1. Segmentation curve, indicated blue, for periosteal callus: 3 weeks (left), 6 weeks (middle) and 9 weeks after surgery.

In next step, classification of periosteal callus area inside of segmentation curve is done. Energy map is then created for active contour. With spreading of active contour, its energy is formed. Negative energy is inside of active contour curve and positive energy outside of curve. Using simple energy thresholding periosteal callus is formed.



Fig. 2. Binary segmentation model overlapped with the native X-ray images of periosteal callus for period: 3 weeks (left), 6 weeks (middle) and 9 weeks after surgery.



Fig. 3. Binary segmentation model of periosteal callus for period: 3 weeks (left), 6 weeks (middle) and 9 weeks after surgery.

5 Quantitative comparison

Lastly the comparative analysis of proposed segmentation model was done. Comparison was done with K-means, Region growing, FCM clustering and Otsu multi regional segmentation. Each result of individual method was compared with periosteal callus tracked manually by clinician.

Average results for 50 X-ray images are shown in Table 4, best results are highlighted. Parameters used for objective comparison are Rand Index, Variation of Information, Linear correlation and Mean squared error.

Rand Index defines similarity level between two regions. Rand Index is a normalized parameter where 0 indicates no similarity, and 1 stands for completely same.

Variation of Information defines distance between two regions regarding their conditional entropy. With lower variation values similarity is higher.

Linear correlation defines level of linear dependency between two vectors. Pearson correlation coefficient in a normalized range is used in our analysis. Linear independence is defined as 0, complete linear dependence is defined as 1.

Mean Square Error defines average quadratic difference between two regions. With higher dissimilarity mean squared error is higher.

Table 1. Quantitative comparison for the proposed model and alternative segmentations against the gold standard

	<i>Proposed model</i>	<i>K-means</i>	<i>Region growing</i>	<i>Otsu</i>	<i>FCM</i>
<i>Rand index</i>	0.96	0.74	0.86	0.88	0.91
<i>Variation of information</i>	3.12	4.54	4.21	3.92	3.11
<i>Linear correlation</i>	0.94	0.65	0.45	0.91	0.88
<i>Mean square error</i>	33.12	36.85	44.15	35.15	33.95

6 Conclusion

This paper presents segmentation model for autonomous tracking and modeling of periosteal callus. Results of model can offer possible prediction of heel bone fracture healing process what is very important benefit for clinical practice. Periosteal callus area is iteratively approximated using segmentation model based on Gaussian energy distribution. Finally, comparative analysis of model efficiency with other segmentation methods was done. Results of comparative analysis are shown in Table 1.

Similarly as different image processing methods, there can be limitations depending on image quality, noise presence or bone density changes depending on age.

7 Publication

1. OCZKA, David, Jan GREPL, Vladimír KAŠÍK, Marek PENHAKER, Lukáš KNYBEL a Jakub CVEK. Patient's respiratory curve synchronization by visual feedback application. *Lékař a technika - Clinician and Technology*. 2018, **48**(1), 17-21. ISSN 0301-5491.
2. OCZKA, David, Marek PENHAKER, Lukáš KNYBEL a Jan KUBÍČEK. Evaluation Application for Tracking and Statistical Analysis of Patient Data from Hospital Real Time Location System. LHOTSKA, Lenka, Lucie SUKUPOVA, Igor LACKOVIĆ a Geoffrey S. IBBOTT, ed. *World Congress on Medical Physics and Biomedical Engineering 2018* [online]. Singapore: Springer Singapore, 2019, 2019-05-30, s. 805-808. IFMBE Proceedings. DOI: 10.1007/978-981-10-9023-3_146. ISBN 978-981-10-9022-6.
3. KUTALEK, Frantisek, Radka PUSTKOVA, David OCZKA, Marek PENHAKER a Jan KUBICEK. Visualization of transient characteristics of warming with thermal cameras. In: *2018 IEEE 16th World Symposium on Applied Machine Intelligence and Informatics (SAMI)* [online]. IEEE, 2018, 2018, s. 000037-000042. DOI: 10.1109/SAMI.2018.8323983. ISBN 978-1-5386-4772-1.
4. KASIK, Vladimir, Radana KAHANKOVA, Zuzana CHVOSTKOVA, Jan KUBICEK, Marek PENHAKER a David OCZKA. Real-time analysis of semiconductor memories under the influence of ionizing radiation. In: *2018 IEEE 16th World Symposium on Applied Machine Intelligence and Informatics (SAMI)* [online]. IEEE, 2018, 2018, s. 000081-000084. DOI: 10.1109/SAMI.2018.8323990. ISBN 978-1-5386-4772-1.

5. KUBICEK, Jan, Marek PENHAKER, Martin AUGUSTYNEK, Martin CERNY, David OCZKA a Petra MARESOVA. Detection and Dynamical Tracking of Temperature Facial Distribution Caused by Alcohol Intoxication with Using of Modified OTSU Regional Segmentation. NGUYEN, Ngoc Thanh, Duong Hung HOANG, Tzung-Pei HONG, Hoang PHAM a Bogdan TRAWIŃSKI, ed. Intelligent Information and Database Systems [online]. Cham: Springer International Publishing, 2018, 2018-02-14, s. 357-366. Lecture Notes in Computer Science. DOI: 10.1007/978-3-319-75420-8_34. ISBN 978-3-319-75419-2.
6. KUBICEK, Jan, Marek PENHAKER, David OCZKA, Martin AUGUSTYNEK, Martin CERNY a Petra MARESOVA. Analysis and Modelling of Heel Bone Fracture with Using of Active Contour Driven by Gaussian Energy and Features Extraction. NGUYEN, Ngoc Thanh, Duong Hung HOANG, Tzung-Pei HONG, Hoang PHAM a Bogdan TRAWIŃSKI, ed. Intelligent Information and Database Systems [online]. Cham: Springer International Publishing, 2018, 2018-02-14, s. 405-414. Lecture Notes in Computer Science. DOI: 10.1007/978-3-319-75420-8_39. ISBN 978-3-319-75419-2.
7. KUBICEK, Jan, Marek PENHAKER, Martin AUGUSTYNEK, Martin CERNY a David OCZKA. Multiregional Soft Segmentation Driven by Modified ABC Algorithm and Completed by Spatial Aggregation: Volumetric, Spatial Modelling and Features Extraction of Articular Cartilage Early Loss. NGUYEN, Ngoc Thanh, Duong Hung HOANG, Tzung-Pei HONG, Hoang PHAM a Bogdan TRAWIŃSKI, ed. Intelligent Information and Database Systems [online]. Cham: Springer International Publishing, 2018, 2018-02-14, s. 385-394. Lecture Notes in Computer Science. DOI: 10.1007/978-3-319-75420-8_37. ISBN 978-3-319-75419-2.
8. KUBICEK, Jan, Martin AUGUSTYNEK, Marek PENHAKER, Martin CERNY a David OCZKA. Analysis and modeling of alcohol intoxication from IR images based on multiregional image segmentation and correlation with breath analysis. In: 2017 IEEE Conference on Big Data and Analytics (ICBDA) [online]. IEEE, 2017, 2017, s. 49-54. DOI: 10.1109/ICBDAA.2017.8284106. ISBN 978-1-5386-0790-9.
9. KUBICEK, Jan, Martin AUGUSTYNEK, Andrea VODAKOVA, Marek PENHAKER, Martin CERNY a David OCZKA. Segmentation and modeling of scattered RTG irradiation on quality of skiagraphy images in clinical conditions. In: 2017 IEEE Conference on Big Data and Analytics (ICBDA) [online]. IEEE, 2017, 2017, s. 105-110. DOI: 10.1109/ICBDAA.2017.8284115. ISBN 978-1-5386-0790-9.
10. OCZKA, David, Marek PENHAKER, Lukas KNYBEL, Jan KUBICEK a Ali SELAMAT. Design and Implementation of an Algorithm for System of Exposure Limit in Radiology. KRÓL, Dariusz, Lech MADEYSKI a Ngoc Thanh NGUYEN, ed. Recent Developments in Intelligent Information and Database Systems [online]. Cham: Springer International Publishing, 2016, 2016-02-27, s. 433-443. Studies in Computational Intelligence. DOI: 10.1007/978-3-319-31277-4_38. ISBN 978-3-319-31276-7.

Skin pigment evaluation using image processing

Tomáš Ondraczka

Department of Cybernetics and Biomedical Engineering, FEECS,
VŠB – Technical University of Ostrava, 17. listopadu 15,
708 33 Ostrava – Poruba, Czech Republic
tomas.ondraczka@vsb.cz

Abstract. This paper deals with developing the algorithm for skin pigment detection and evaluation its parameters based on ABCD rule. Images are provided by web camera. Skin pigment is detected by edge detection method followed by methods of mathematical morphology. Skin pigment parameters are measured using specially designed methods. Algorithm for parameters evaluation is based on conditions (If Then rules). The software is designed for public as online software. The user can evaluate skin pigment from home using only web camera. Main goal of this software is to decrease the number of patients on dermatological ambulances and provide time for examination of the serious cases.

Keywords: Image, Image Processing, Image Segmentation, Edge detection, Mathematical morphology, Skin pigment, ABCD rule.

1 Introduction

The essence of this work is to design the software for detection of skin pigment and evaluate if it is necessary to proceed to another examination. The software is designed for public use as online software. A public user can easily evaluate the skin pigment by using only computer and web camera. Then the public user can decide if he will follow the recommendation of the software to visit a doctor or not.

This software evaluates skin pigment by ABCD rule. It is the first examination of skin pigment used by doctors. For another examination, the special equipment must be used. The web camera is unusable for that examination.

For edge detection in image the Sobel type edge detector is used. Sobel detector will find local edges in the image. After edge detection, the local edges must be connected into global edges. For this problem, the methods of the mathematical morphology are applied. Next algorithm calculates parameters by ABCD rule. For the final analysis, three parameters are calculated.

The first parameter is the skin pigment total size. Size, in this case, means the longest distance between two points in the skin pigment.

The second parameter is the skin pigment margins regularity. The algorithm is based on total size and circle diameter comparison. Algorithm presumes the detected skin pigment has a circular shape.

The third parameter is the skin pigment colour. The algorithm is based on calculating the mean value of all nonzero pixels of the RGB image.

Algorithm for final evaluation is based on conditions method. The conditions are determined heuristically.

The software is suitable for preventive examination of the skin pigment for public use. This will help to decrease the number of the patients on dermatological ambulances.

2 Algorithm methodology used for creating the software

The software is designed to solve the algorithm as quickly as possible. Therefore, it is based on solutions that lead to shorter time needed to perform a given function. In practice, it is necessary to choose a less precise method to reduce the processing time as much as possible.

There are five parts of the algorithm (Fig. 1):

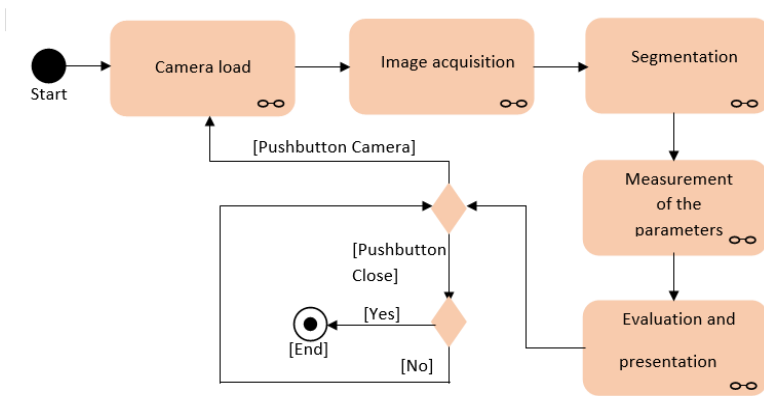


Fig. 1. The software flow chart.

For easy control of the software, the GUI (Fig. 2) is designed.

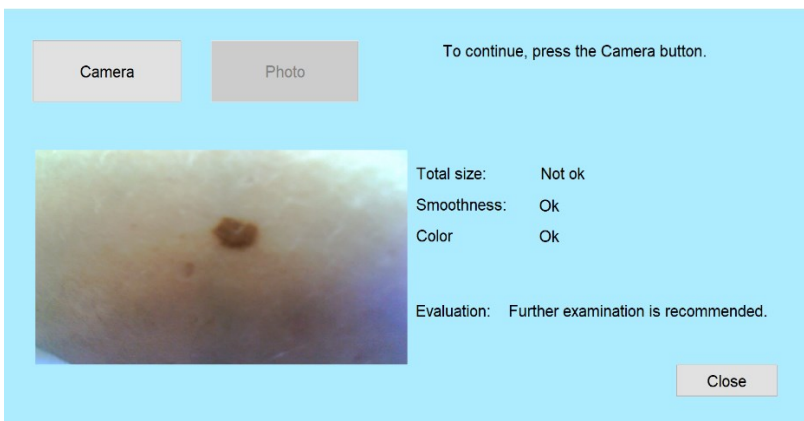


Fig. 2. GUI of the software for skin pigment evaluation.

3 Methods used in the software

To make an object detectable in an RGB image, the format must be changed from RGB to grayscale. If the image was in RGB format, it would not be possible to use the Sobel edge detector. The detector works with a two-dimensional matrix.

3.1 Sobel edge detector

Application of Sobel edge detector allows finding the local edges of objects in the image. The suitability of the detector is in its speed and, in this case, in search efficiency. Skin image is highly specific [2].

Objects in the image have a distinctly different colour, so their gradient difference from the background gradient is high. Therefore, these objects will be easily found by the detector (Fig. 3) [3].

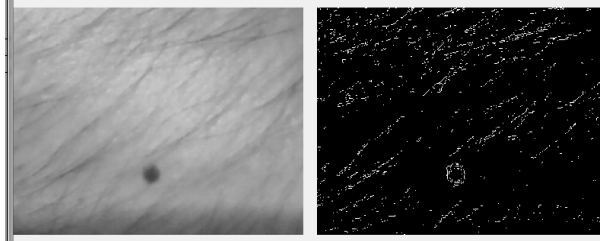


Fig. 3. Input (left) and output (right) of the edge detection.

3.2 Methods of mathematical morphology

Morphological methods (dilation, erosion ...) are very effective for processing binary data [1].

Dilation.

To connect the local edges found by the edge detector to the global edges, the dilation of the objects in the input image is used. The input of this method is the edge detection output. The output of the dilation is a binary matrix of the same size (Fig. 4). Dilation extends objects using a morphological structural element. For this application, a diamond shaped structural element is used.

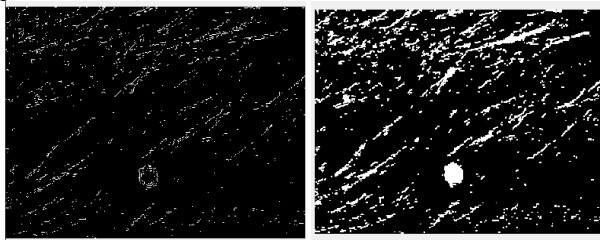


Fig. 4. Input (left) and output (right) of the dilation method.

Erosion.

To smooth out objects while removing smaller objects from the image, one of the main functions of mathematical morphology must be applied. This function is called erosion. For better extermination and removal results, double erosion (erosion followed by erosion) is used [3, 4].

The input of the function is a binary image and the output is a binary image of the same size (Fig. 5). Erosion reduces objects using a morphological structural element of diamond shape.



Fig. 5. Input (left) and output (right) of the erosion method.

4 Methods for the calculation of parameters used in the software

The input of this part of the algorithm is the object detection output, that is the binary matrix with the detected skin pigment. The three parameters are the total size (the longest distance in the skin pigment), the margins regularity, and the skin pigment colour.

4.1 Total Size

To measure the total distance, the longest distance the skin pigment contains, the cycle command is used, which finds the longest distance from all possible measured distances between the pixels. The image must be adjusted from filled object to perimeter object (Fig. 6).



Fig. 6. Input (left) and output (right) of the border method.

The value of the distance is in pixels, so it is necessary to convert distance into millimetres by calibration so that this value can be presented to the user. Calibration is defined by the calibration constant.

The calibration constant is calculated as measured real distance in millimetres divided by the same distance measured by the program in pixels. This result is multiplied by the distance in pixels, which will convert the value to millimetres.

4.2 Margins Regularity

The exact determination of the second parameter (regularity of the margins) is very problematic. From a few possible methods, the method of comparing the diameter of the assumed shape of the object (circle) with the value of the total distance was finally chosen.

4.3 Colour Determination

To determine the colour, we need to apply a binary mask with the object (object detection output) to the original image in RGB format. An RGB image is created, where only the skin pigment is. (Fig. 7).



Fig. 7. The result of the algorithm of using the binary mask on the original image (left - original image, middle - binary mask, right - the result of the binary mask application).

The first part of the algorithm is to divide the three-dimensional RGB image into three colour components (red, green, blue). The algorithm calculates the mean value of the pixel size in each RGB format components.

5 Methods for parameters evaluation

Each parameter is evaluated separately, except for an overall evaluation that compares all parameters at once.

The first condition is to verify the total size. If the condition is met and the parameter meets the required value, this information is displayed to the user as a positive message. If the condition is not met, the information is displayed as a negative message.

The second condition verifies the regularity of the margins. The value resulting from the difference of the diameter of the predicted circle and the total size is verified. If this

value is too large, the edges are irregular, and the program displays this as a negative message. Otherwise, a positive message is displayed.

The third condition is to meet the colour. The pixel mean values in individual RGB components are used as the input values for the condition. These values are verified separately. If any of these values do not match the colour range, a negative message is displayed. Otherwise, a positive message is displayed.

The last condition is to verify all the measured parameters at one time. The result is displayed as the recommendation for the next step. Provided that all the ranges defined in the condition are met, a positive recommendation is displayed. Otherwise, the negative recommendation is displayed.

6 Conclusion

The paper deals with the design and realization of an autonomous system for the detection and evaluation of skin pigment by a camera.

It describes methods for object detection in an image. It also describes methods for measuring certain parameters of a skin pigment and comparing them with theoretical values. Finally, the system functionality and the implemented algorithm are verified.

Developments in the field of using webcams with software to detect and evaluate skin pigment in dermatological ambulances, or to provide preventive testing for public users by providing software to the public, is in the beginning. This research area and application of image processing methods in this area have great potential.

7 Acknowledgement

This work was supported by the project SP2018/160, „Development of algorithms and systems for control, measurement and safety applications IV" of Student Grant System, VSB-TU Ostrava.

8 References

1. Haska, J., Pies, M. and Machacek, Z. (2014). Image signal processing, analysis and detection for robotic system. *14th International Conference on Control, Automation and Systems*, 1060-1063.
2. Klepaczko, A., Szczypinski P., Deistung A., Reichenbach J. R. and Materka A. (2016). Simulation of MR angiography imaging for validation of cerebral arteries segmentation algorithms. *Computer Methods and Programs in Biomedicine*, 137, 293-309.
3. Kubicek, J., Penhaker, M., Bryjova, I. and Augustynek, M. (2016). Classification Method for Macular Lesions Using Fuzzy Thresholding Method. *XIV Mediterranean Conference on Medical and Biological Engineering and Computing 2016*, 239-244.
4. Kubicek, J., Bryjova, I., Penhaker, M., Kodaj, M. and Augustynek, M. (2016). Surface of Articular Cartilage Extraction Using Fuzzy C-means Segmentation. *Recent Developments in Intelligent Information and Database Systems*, 209-219.

Use of the IQRF and Node-RED technology

Jiří Škovránek

Department of Cybernetics and Biomedical Engineering, FEECS,
VŠB – Technical University of Ostrava, 17. listopadu 15,
708 33 Ostrava – Poruba, Czech Republic
jiri.skovranek@vsb.cz

Abstract. This article describes the implementation of wireless communication between the control unit and remote device with using IQRF technology. Together with the Node-RED programming tool, it creates a robust, efficient and reliable platform for the Internet of Things. This paper shows implementation of IQRF and Node-RED for home monitoring (embedded device for detection of entry). The result is a design of event base control system with using IQMESH network and MQTT protocol.

Keywords: Gateway, IQRF, IQMESH network, Internet of Things, MQTT, Node-RED, Raspberry Pi, Visualization, Wireless communication, Detection of entry

1 Introduction

At present, the world is particularly interested in customized comprehensive wireless measurement or monitoring system, whether in the automation of production, smart homes (home-security), cities, agriculture or in other industries. [1]. Systems are created the way that it is striving to be flexible with a simple user interface. The trend of storing data on cloud storage and subsequent data processing and visualization is widespread. Requirements are on long distance transmission, low power consumption, fast response time, and service costs. This article describes the fast implementation of a wireless network for detection of entry at home (door, window). Module programming (transmitting/receiving, peripheral control) can be done using Direct Peripheral Access (DPA), a unique protocol that simplifies the work with modules and the network. After uploading a hardware profile (HWP), we gain the ability to communicate with a higher layer (DPA framework) over the operating system of a given IQRF module that allows the peripheral control over the data stream, where control and data management is defined in the Custom Handler layer (Fig. 1). After downloading the HWP, the IQRF module can receive and send DPA messages or create the IQMESH network using the IQMESH Network Manager tool in the development environment. [2]

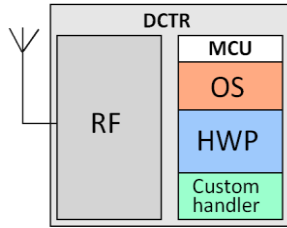


Fig. 1. Three-layer IQRF architecture

2 Description of technology

2.1 IQRF technology

The IQRF technology is suitable for fast and simple implementation of wireless network. Ideal choice for transmission a few amount of data (max. 64B/packet). IQRF technology offers a module of series TR-2x (green series), TR-5x (blue series), TR-6x (purple series) and actual TR-7x (red series). It is depends on hardware specification and variant of board. (SIM – The module is inserted to the socket as SIM card, or SMT – The module is inserted directly to the board). Communication between IQRF module and master device use SPI bus. Module can be connected to the Raspberry PI using SPI adapter. The modules can be offered a wide range of modification and possibility of use. The main advantages include:

DPA programming

Direct Peripheral Access (DPA framework). It is an unique protocol for simplify of work for wireless communication. The IQRF module peripherals can be controlled by a DPA request which makes the required peripheral change after the sending. DPA protocol has a byte format of data and sequential order by little-endian. Sequence of message is composed from request, confirmation and response packet.

IQMESH network

MESH network is a type of topology which is not expected any organization of network node. It is different from star, linear and another topology. If the receiver module is out of coverage, packet can be delivered over the another elements of network (router). The network is created and set in IQMESH network managery tool in the development of the program IQRF IDE. MESH network is consisted at least of one coordinator (C – control of network) and node (N – end point device of network for using of sensors). For simplify of connection to the network there must be uploaded the hardware profile (HWP) and source code (CustomDPAhandler) to each module for using the peripheral operation. [3]

2.2 Node-RED

Node-RED is a programming tool for wiring together hardware devices, APIs and online services in new and interesting ways [4]. It provides a browser-based editor. The engine of tool is running on Java Script code. Node-RED was developed by IBM in 2013. The main reason for programming tool was a faster hardware connection and subsequently of visualization. Node-RED programming tool works on the principle of merging blocks. Blocks have a defined function as hardware, graphic, mathematical, or online services. A library allows you to save useful function and simplify of work with visualization and communication. The data are transmission between bloks using buffer (msg.payload).

3 Introduction a solution

The Raspberry PI with inserted SPI adapter (KON-RASP-01) and IQRF module (coordinator) creates the control unit for sending and receiving the data from IQMESH network. For node of network there was created a device with function for detection of entry. (open, close, remove states).

For reliable wireless communication is important connection of module to IQMESH network. In the IQMESH network managery there is connection one of coordinator (C) and four of node (N1, N2, N3, N4). The device for detection of entry was fixed at position above the door. The structure of network depends on the power of signal and distance from coordinator (Fig. 2).

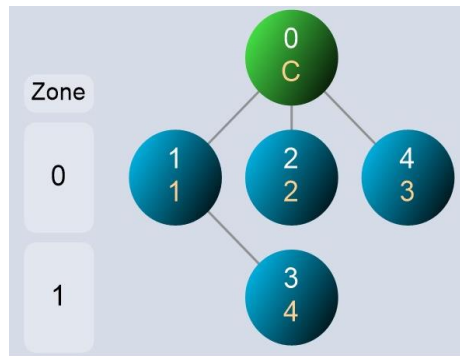


Fig. 2. Structure of IQMESH network

3.1 Software resources

After the installation of the software resources into the Raspberry PI becomes the IQRF Gateway. The Gateway is configured through the interface at address {<http://localhost:1880>}. But into the Raspberry PI there must be implemented software support as IQRF gateway daemon, IQRF web-app, Node-RED, Node.js and MQTT broker (Mosquitto).

3.2 An example of use platform

Inside Raspberry PI is installed an IQRF daemon that handles of MQTT communication between Node-RED and IQRF daemon (gets data from coordinator). To verify the correct functionality of the platform (wireless of system) there is created application for monitoring of actual door states. (open, close and remove from the wall). The picture (Fig. 3) shows the structure of complex design system for detection of door states in terms hardware and software requirements.

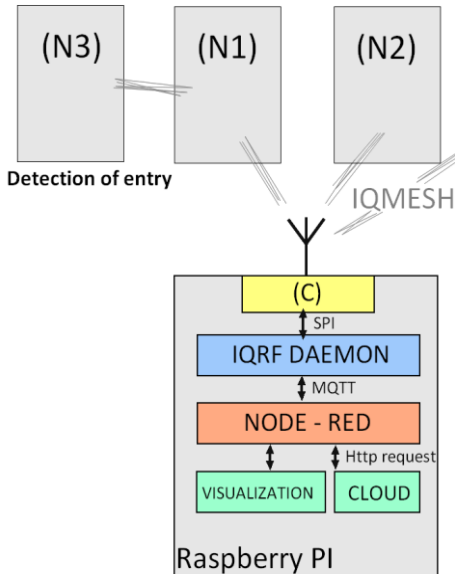


Fig. 3. Implementation of IQRF technology and Node-RED

4 Design of devices for detection of entry

4.1 Hardware and software

The device (Fig. 4) has a protection against unauthorized manipulation (removing the cover) and detection changes using a magnetic sensor located on the doors or windows. There are also battery power supplies of circuit which can be charged directly from USB. The model is powered by the LI-ION battery (1050mA) with emphasis at the consumption.

The program sends asynchronous message (DPA request) to the IQMESH network or receives message. The node is inserted into the SIM socket on the board. In the initial state the device that works in sleep mode (saves energy). If the door is opened, it wakes up and sends an asynchronous message to the coordinator. Inside the Raspberry PI runs a MQTT broker which waits for incoming messages. New message is processed in Node-RED.

Software of module is designed as event base control for transmission of data. When there is change of state as opening the door, the device wakes up at the moment from sleep mode and sends a message (DPA packet) and then the device goes to the sleep mode again.

The consumption:

- Module sleep mode: 61µA
- After sending the data the value of current peak will be increment at 12mA and then goes to the sleep mode during 60ms.



Fig. 4. The wireless devices for detection of entry

5 Program and visualization

The program was created and deployed in the Node-RED from web browser editor at address {localhost: 1880} and visualization is default at address {localhost: 1880/ui}. The created program below (Fig. 5) makes a modification of received data from IQRF module (gets data from coordinator) and subsequently this data will be visualized (Fig. 6).

The block (MQTT response) is waiting for incoming data. When MQTT broker (installed in Raspberry PI) receives the data (DPA confirmation and DPA response from coordinator), DPA response packet is edited in JavaScript and it is sorted by number of node (block IQRFtoJSON). Edited data are visualized using library Node-RED Dashboard.

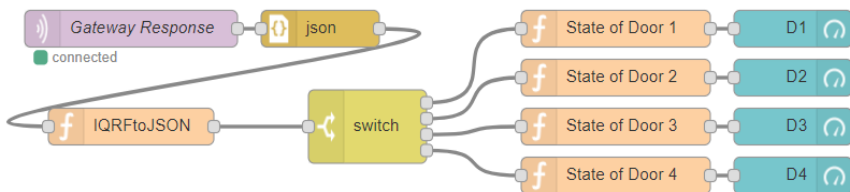


Fig. 5. The program from Node-RED

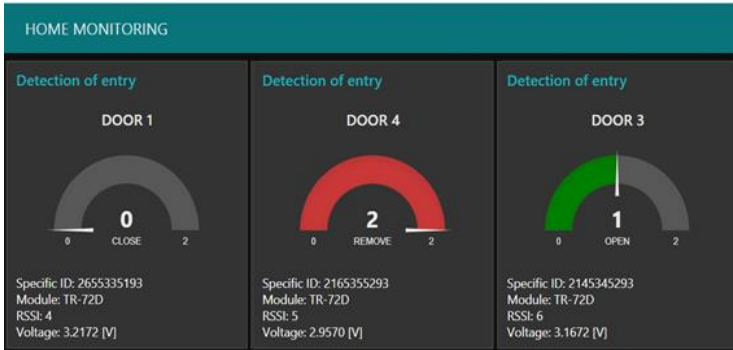


Fig. 6. Visualization from Node-RED

6 Conclusion and future work

This paper addresses the use of the IQRF technology in combination with Raspberry PI and the programming tool Node-RED. The chosen platform is suitable for fast deployment of wireless communication with visualization capabilities. This paper describes how to connect each device to the IQMESH network, settings and software requirements to create the IQRF Gateway from Raspberry PI.

The result is an application that visualizes data from created new device for detection of entry. This end point of network is focused on low consumption. In default states it has a reaction only on the events triggered by the environment. In default state the device has consumption only $61\mu\text{A}$ (sleep mode). The platform has features like fast implementation, simple modification of program and clarity of code. Future work will focus on Node-RED communication over the (UDP) protocol and visualization with own schematics for a web application with data transfer over a web socket channel. The future belongs to small devices. The used IQRF and Raspberry PI platform allow quick and efficient wireless measurement, control and visualization of various processes.

7 References

1. Z. Slanina and T. Docekal. Energy meter for smart home purposes. In V. Tarassov, A. Abraham, S. Kovalev, A. Sukhanov, V. Snasel, and M. Vasileva, editors, *Advances in Intelligent Systems and Computing*, volume 680, pages 57-66. Springer Verlag, 2018. doi: 10.1007/978-3-319-68324-9_7.
2. IQRF Tech s.r.o. IQRF - technology for wireless, 2018. URL <https://www.IQRF.org/>.
3. R. Hajovsky and M. Pies. Use of IQRF technology for large monitoring systems. In A. Milik, editor, *IFAC-PapersOnLine*, volume 28, pages 486,491, 2015. doi: 10.1016/j.ifacol.2015.07.082.
4. Node-RED, A project of the JS Foundation, Flow-based programming for the Internet of Things, 2018. URL <https://www.nodered.org/>.

Emergency Record Digitalization Using NFC Tags

Tomáš Urbanczyk

Department of Cybernetics and Biomedical Engineering, FEECS,
VŠB – Technical University of Ostrava, 17. listopadu 15,
708 33 Ostrava – Poruba, Czech Republic
tomas.urbanczyk@vsb.cz

Abstract. This paper deals with digitalization of the Emergency service data of the Moravian-Silesian region in the Czech Republic. For digitalization, Near Field Communication (NFC) based on RFID technology is utilized. Documents with NFC tag allow finding the data needed quickly. The electronic record created by the assistant in the notebook is stored in duplicate. Subsequently, this mark is attached to the printed version of the record, which is delivered to the hospital where the patient is transported to. This hospital needs to be equipped by NFC reader and registration system that is adapted for patient registration using NFC tag. This makes the registration process significantly faster which is necessary for solving critical situations (mass catastrophes, etc.).

Keywords: Emergency medical services, Analysis, Time, Near Field Communication

1 Introduction

Emergency medical services (EMS) during their response to an accident they are obliged to create a record of pre-hospital care, which is defined by the Decree of the Czech Republic Act. No. 98 / 2012Sb. about medical documentation. [2] The document provider of emergency medical services consists of document files and audio recordings related to the particular patient. The document is created electronically at this time. [5] The hospital to which the patient is transported receives the report in printed form, along with the verbal understanding of the rescuer about the course of the patient's medical condition. The document serves to ensure the continuity of health care during further patient care and as a legal basis in the case of court proceedings. The hospital must store it for 5 years. [7]

At present, there is the possibility of online transmission of pre-hospital care records to the appropriate hospital, which has a hospital-based information system (NIS) adapted to that effect and can continuously establish its internal health records on the electronic record of rapid rescue services. This is not the case anywhere in the Czech Republic. [8] The article focuses on the use of NFC technology to optimize patient registration and linking pre-hospital documentation to internal hospital documentation. Hospitals with which the NIS will not allow access to a system for sharing, transferring and sharing patient information is an appropriate and inexpensive alternative to documenting, including pre-hospital care.

Near Field Communication (NFC) is a non-contact communication technology based on RFID with a communication frequency of 13.56 MHz. NFC communication works at a very close distance (4cm) to eliminate third-party interception. [9] The communication takes place via a modulated electromagnetic field with the communication protocol ISO 14443A. MIFARE tags are used to store text data. Mostly low-passive and passive (without power supply) tags with memory capacity 1K or higher. [10] Tagging is done through a multi-protocol RFID reader / recorder SL500F with a USB interface.

The article discusses the low-cost possibilities of extending the medical documentation on pre-hospital care. It completes the record and generates an overview of the health operations in the timeline. The first part of the article mentions the used tags, which are used to store the electronic record together with the chosen technology. We also describe the current solutions and optimization capabilities through the implementation of NFC technology. Part of the solution is also the design of a filing cabinet for archiving sheet documents. The output of the article points to a simple pairing of pre-hospital data with the hospital system.

2 Technical background

In this work, RFID technology operating at a frequency of 13.56MHz, which falls under High Frequency, was used. The final rescue folder's final record is stored in the NFC tag using RFID recorders. For this work, Mifray NFC tags with a memory capacity of 2 Kb were used for writing and reading. The big advantage of these tags is that they do not depend on power. A description of the NFC tag functionality is explained below. The ISO14443A standard and NDEF messages with index are used to write and read in memory. The format of the NDEF message is set to TNF WELL KNOWN, and RTD TEXT NFC is set to define the textmime type. [11] You can see the NFC tag in Figure 1. Most of the tag surface occupies an antenna that receives electromagnetic waves.

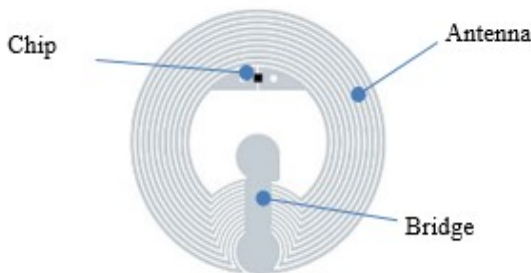


Fig. 1. Passive NFC tag mifray. [8]

An antenna reader sends periodically on its carrier frequency electromagnetic wave (radio wave) to the surroundings. If a suitable distance from the marker antenna appears, which is designed to the same frequency, this wave is received by the antenna. The induced voltage on the tag antenna causes the alternating current to be transferred

and charges the capacitor in the tag. The stored energy is used to power the logic and radio circuits of the tag. If the capacitor voltage reaches the minimum required level, starts the control circuits inside the tag and it begins to send a response to the reader. Tag transmission is typically performed using a two-state ASK (Amplitude Shifting Key) modulation, which is implemented by changing the termination impedance of the antenna. The transponder antenna is either matched or short-circuited. Modulation represents a thorough influence of three signal parameters, namely the height, frequency, and amplitude phase. You can write to the tag using wave modulation sent from the reader (if possible). [3] By analyzing these waves anywhere within the reader's range, we can reconstruct the received wave message - demodulation. Reflections generated by the antenna impedance change are detected by the reader and interpreted as logical levels 1 and 0. Sufficient energy for transponder capacitor charge and the ability to detect received transponder reader are the major hardware operating conditions of the RFID system. As the distance between the reader and the transponder increases, the quality of the RFID signal decreases. Increasing the noise in the base signal leads to the impossibility of successfully detecting the received message. [5]

2.1 Czech Communications Standard DASTA

The data standard for data transfer between healthcare information systems was created in 1997 and since 2002 it has been widely used in all Czech health information systems. DASTA is an equivalent to the world-wide HL7 communication standard. It covers clinical, laboratory, statistical and administrative areas. Currently, the most up-to-date version of DS4, which opens with the most up-to-date dials that are over three hundred. [13] The most important dials are the NZIS dial lists and the block of dial for the laboratory complex, the most extensive and most significant part of which is the National Laboratory Codebook (NLCL). Thanks to this standard, data can be stored under index. They contain a header that defines the patient's basic information, and then records the rescued components along with the valid dials of the individual exercises. [12]

3 Implementation of new solution

In the territory of the Czech Republic, an emergency is currently dealt with as an "Integrated Rescue System" (hereinafter referred to as an IRS). Components of the IRS, procedures at the place of occurrence, duties and powers are defined by the Integrated Rescue System Act of 28 June 2000 (Act No. 239/2000 Sb.). Medical rescue service is addressed by the Medical Emergency Service, which is one of the three basic components of the IRS. Keeping medical records is an obligatory part of each trip. The exit record is defined by Decree 98 / 2012Sb, which sets out the minimum range of information that a document must contain.

- Date and time (time to report an emergency, Response time and delivery time a patient in the hospital catchment area)

- Serial number of the Emergency Response
- Personal data of the patient
- A brief description of the patient's clinical status
- Work diagnosis
- Description of provided medical care (drug administration, name of medicine, dose, treatment, performance)
- Used material
- Personal information and signature of the lead manager
- The hospital the patient is transported to

The rescue component record may contain additional studies (e.g. Ischemic brain disease). In the Czech Republic there are no uniform forms of record keeping on rescue items.

At present, the medical rescue service uses an electronically managed record that is clearly structured so that crew intervention is as fast as possible, expert with the support of available hospital data, and then the necessary administrative work is done only once and all information is subsequently shared. The system allows the electronic exchange of crew data in the field with the dispatching information system and the information systems of the hospital the patient is transported to. However, the final record of the rescue files is transmitted only in printed form to the treating physician of the hospital the patient is transported to.



Fig. 2. Scheme of information transfer between the EMS and the hospital the patient is transported to.

In figure two, we see several ways of sharing a rescue folder record with a catchment hospital. Now, there are two ways that are often paralleling. During the exit, the rescuer makes an exit report electronically on his computer. During the transfer of the patient, the rescuer prints the record (c) of the exit and at the same time sends the message to the cloud (a). Our solution enables a third way to upload an electronic message to the NFC tag (e). The NFC tag sticks to the paper record and passes to the registration nurse. The rescuers inform the patient of the patient's state verbally. Many

hospitals do not allow a communication route (b) and therefore do not have an electronic record. The hospital must therefore take the document physically in paper form (d) and often duplicate the information into the NIS. Our system enables very fast retrieval of the electronic record to the NIS. Thanks to the RFID reader, the registration nurse reads the NFC tag (f) and transfers it to the NIS instantly. [4] The nurse only visually checks the accuracy of the data and establishes internal documentation. This system eliminates the introduction of a human factor error by duplicating the rewriting of data and clearly speeds up the patient's registration process. [6]

4 Conclusion

In the past year 2017, the Czech Republic's Medical Emergency Service escalated to approximately 750 thousand Emergency Responders. Every way by law must have a final record of the Emergency Response that needs to be kept for 5 years. Nowadays information technology helps rescuers with electronic documentation management. Especially rescuers cooperate with dispatching and catchment hospitals. By means of telecommunication networks, they get detailed information about the patient before they reach the scene. Using a data sentence, they can inform the gradient hospital about the condition of the patient. Some hospitals only work with information received over the phone.

The ability of the electronics to output record using the NFC helps speed up the patient's reception in the hospital without the hospital being forced to implement a new complex system. Our solution speeds up the registration of the patient in the hospital information system as it uses the electronic record of the rescue units and completes the hospital documentation on pre-hospital care. Information entered in the NFC tag is easily imported into the hospital system via the NFC reader, so there is no duplicate filling of the information only for the visual check of the record by the registry nurse in the hospital.

NFC tags also make it possible to locate a physical paper entry through the RFID card index, thus speeding up the search for archived documents.

References

1. KIM J. VICENTE. Cognitive work analysis toward safe, productive, and healthy computerbased work. Mahwah, N.J: Lawrence Erlbaum Associates, 1999. ISBN 1410603032.
2. VAVŘÍKOVÁ, Dana. Analýza a optimalizace vedení zdravotnické dokumentace na záchranné službě. Zlín, 2013. bakalářská práce (Bc.). Univerzita Tomáše Bati ve Zlíně. Fakulta humanitních studií
3. Tomala, K., Plucar, J., Dubec, P., Rapant, L., and Voznak, M. (2013). The data extraction using distributed crawler inside multi-agent system. *Advances in Electrical and Electronic Engineering*, 11(6), 455.
4. Mann, G. (2017). Improving Efficiencies with Real Time Locating Systems in Emergency Departments. *Prehospital and Disaster Medicine*, 32(S1), S37-S38. doi:10.1017/S1049023X17001157

5. XU, Boyi, et al. Ubiquitous data accessing method in IoT-based information system for emergency medical services. *IEEE Trans. Industrial Informatics*, 2014, 10.2: 1578-1586.
6. PRGOMET, Mirela; GEORGIU, Andrew; WESTBROOK, Johanna I. The impact of mobile handheld technology on hospital physicians' work practices and patient care: a systematic review. *Journal of the American Medical Informatics Association*, 2009, 16.6: 792-801.
7. REMEŠ, R, TRNOVSKÁ, S. *Praktická příručka přednemocniční urgentní medicíny*. 2013 Praha : Grada, 2013. ISBN 978-80-247-4530-5.
8. URBANCZYK, Tomas. *Design and Partial Implementation of e-version of Intensive Care Record*. Ostrava, 2015. Diplomová práce. Vysoká škola báňská - Technická univerzita Ostrava. Fakulta elektrotechniky a informatiky. Vedoucí práce Jindřich Černohorský.
9. R. Want, "Near Field Communication," in *IEEE Pervasive Computing*, vol. 10, no. , pp. 4-7, 2011. doi:10.1109/MPRV.2011.55
10. HALL, Steven; AWAD, Mohamed; TROST, Theodore. Optimization of NFC tag for different battery levels. U.S. Patent No 9,119,160, 2015.
11. SETHIA, Divyashikha, et al. NFC based secure mobile healthcare system. In: *Communication Systems and Networks (COMSNETS)*, 2014 Sixth International Conference on. IEEE, 2014. p. 1-6.
12. DOLIN, Robert H., et al. The HL7 clinical document architecture. *Journal of the American Medical Informatics Association*, 2001, 8.6: 552-569.
13. NAGY, M., et al. Semantic interoperability in Czech healthcare environment supported by HL7 version 3. *Methods of information in medicine*, 2010, 49.02: 186-195.

Simulation of Transactions Behavior in IOTA Network

Tomáš Janečko

Department of Computer Science, FEECS,
VŠB – Technical University of Ostrava, 17. listopadu 15,
708 33 Ostrava – Poruba, Czech Republic
tomas.janecko@vsb.cz

Abstract. This paper presents a simulation of transactions behavior in the IOTA network. Based on executed transactions in the testnet environment have been measured and observed different inclusion of final transactions into the graph. The main feature of the IOTA is the Tangle which is the name for the directed acyclic graph (DAG). This graph is highly responsible for persisting transactions in the network. The goal of this network is to provide peer-to-peer communication between machines, humans and as well for the Internet of Things (IoT) industry.

Keywords: IOTA, transactions, tangle, directed acyclic graph, IoT

1 Introduction

With the advent of the distributed ledger technologies, [1] we are now able to distribute and synchronize ledgers of data and money in secure, distributed, decentralized and permissionless environments.

In the increasing adoption of IoT technologies is necessary to provide any system which will be able to handle massive load of microtransactions and data integrity for machines. For that was created cryptocurrency called IOTA which is the main token in the network. To master this the [1] IOTA's distributed ledger does not consist of transactions grouped into blocks and stored in sequential chains, but as a stream of individual transactions entangled together.

2 The Tangle

The Tangle, which is the data structure behind IOTA, is a particular kind of directed graph, which holds transactions. Each [1] transaction is represented as a vertex in the graph. When a new transaction joins the tangle, it chooses two previous transactions to approve by adding two new edges to the graph. The example of the graph is presented in Fig. 1.

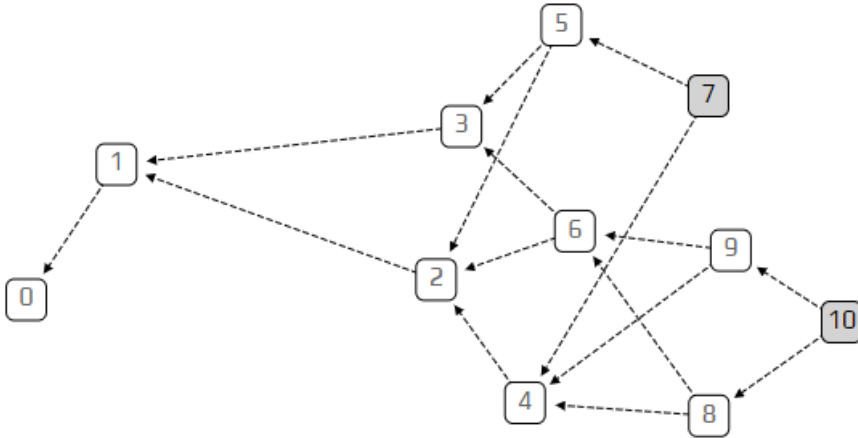


Fig. 1. The Tangle overview

In the example above transaction number 6 approves transactions number 2 and 3. The greyed out transactions number 7 and 10 are called *tips*. The tips are the unconfirmed transactions in the tangle graph because no one approved it yet. Each new incoming transaction needs to choose two tips to approve. The key point for the correct behavior of the network is to choose the correct algorithm for tips selection.

3 Tip Selection Algorithm

For the organic growth of the network exist next algorithms:

- Uniform random - Randomly select next transaction when observing new path
- Unweighted random walk - All next transactions have the same probability for path selection
- Weighted random walk - All next transactions have influenced probability by the cumulative weight

The cumulative weight is a very important metric for transactions on its way to network approval. A transaction with a larger cumulative weight is more important than a transaction with a smaller cumulative weight. Each new transaction added to the tangle increases the ancestors cumulative weight by the weight of that transaction. Older transactions grows in importance over time. The use of cumulative weights is to avoid spamming and other attack styles in the network. It is [6] assumed that no entity can generate an abundance of transactions with acceptable cumulative weights in a short period of time.

In that case we could ask whether we need any randomness or if we could use and select the walk direction strictly on the cumulative weight of the transactions. The real world use case shows us that in the network is created heavy channel which leads growth of the network and a lot of transactions are left behind the main channel and will never be confirmed. Those transactions became an orphans. The next Fig. 2 describes that behavior.

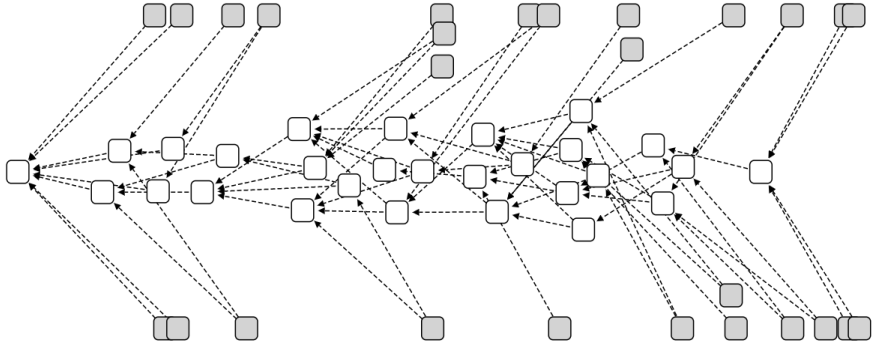


Fig. 2. The weighted walk which is heavily led by cumulative weight

The gray squares are tips, with zero approvers. While [1] it is normal to have some tips on the right end of the diagram, it is a problem to see so many of them spread out across the timeline.

4 Experiment Design

In our environment the transactions weren't provided into the tangle in the fixed rate but were parametrized. Because as we know from the real world scenarios it depends on the periods of the day. Some of them are busier and we can call them peeks. For simulation is crucial to take that into account. This randomness, [1] which makes the model more realistic is achieved by using a Poisson point process to model how transactions arrive.

The Poisson point process is one of the most studied and used point processes, in both the field of probability and in more applied disciplines concerning random phenomena, [3][4][5] due to its convenient properties as a mathematical model as well as being mathematically interesting.

4.1 Transaction Rate

For the simulation of randomness purposes we need to define a constant of transactions rate. In our experiment the constant was called λ . Depending on

the value set to the λ the behavior of the network was different. This variable means how many transactions can be processed in the particular time block.

If we set λ to a very small amount we get a chain. This happens because transactions are coming in so slowly that at any given time there is only a single tip to approve. In the other extreme, with huge λ , [1] all of the transactions arrive so fast that the only tip they see is the genesis. The examples of the outputs can be visible on the next Fig. 3 and Fig. 4.

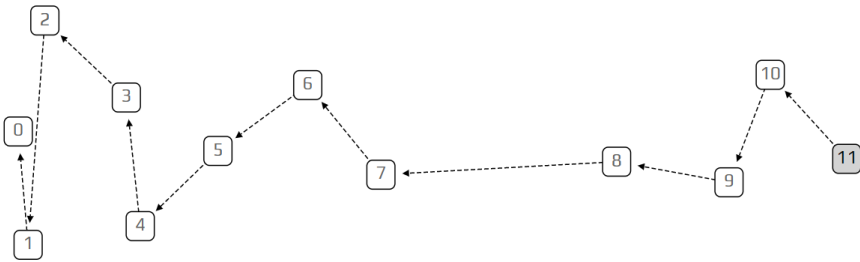


Fig. 3. With small amount of λ tangle produces chain

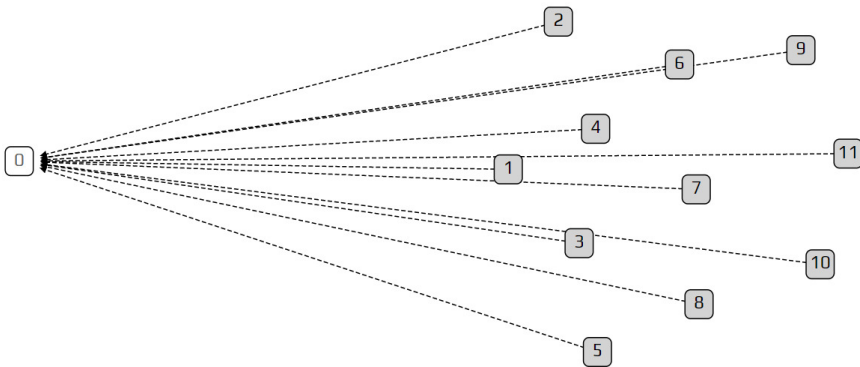


Fig. 4. With huge amount of λ is visible only single transaction

The delay for propagation transactions into tangle is very important for creation of correct graph and not only for simulation of real behavior.

4.2 Random Walk Monte Carlo

From the previous observing we need to introduce a new parameter α which will describe how important is the cumulative weight of the each transaction. This parameter provide us new variable to simulate probability during the random walk.

The goal of the Random Walk Monte Carlo algorithm is to generate fair samples from some difficult distribution. The Random Walk Monte Carlo (RWMC) [6] algorithm is used in two ways:

- To choose two other unconfirmed transactions (tips) when creating a transaction
- To determine if a transaction is confirmed

In a Markov chain [1] each step does not depend on the previous one, but follows from a rule that is decided in advance. The rules and probabilities can be influenced by the α . Together with the different combination of α and λ parameters we could simulate different behaviors of the transactions.

In the next table Tab. 1 are compared different outputs from the testnet environment for different variables and amount of transactions in the time period.

Table 1. Transaction distribution

Number of transactions	Transaction rate (α)	Cumulative weight importance (λ)	Tip orphans count
100	1.7	0.36	8
100	1.7	2	25
100	30	0.36	55
200	12	0.1	26

5 Results

To uncover the nature of the behavior in the network, it was necessary to analyze the differences between λ and α parameters and their variations.

Upon closer measurement, it was found that the nodes which are responsible for transactions propagation into the network are using different tip selection algorithm setups.

These differences in the node setups can lead into unbalanced organic growth which has big impact on the whole network.

We distinguish between two regimes, low load and high load. There are only a few tips in the low load regime. A tip [2] gets approved for the first time in $\theta(\lambda^{-1})$ time units, where λ is the rate of the incoming flow of transactions.

In the high load regime the typical number of tips depends on the tip approval strategy employed by the new transaction. If a transaction uses the strategy of approving two random tips, the typical number of tips is given by (1). It can be shown that this strategy is optimal with respect to the typical number of

tips. However, [2] it is not practical to adopt this strategy because it does not encourage approving tips.

More elaborate strategies are needed to handle attacks and other network issues. The typical time for a tip to be approved is $\theta(h)$ in the high load regime, where h is the average computation/propagation time for a node. However, [2] if the first approval does not occur in the above time interval, it is a good idea for the issuer and/or receiver to promote that transaction with an additional empty transaction.

6 Conclusion

In this paper, IOTA network was used for simulation of transactions behavior. From the above findings we came to the conclusion that the main problem in the tangle is that in current state the volume of transactions is very low. This causes that the IOTA ecosystem is vulnerable for various attacks and is necessary to have Cooperation nodes from IOTA foundation.

The wider adoption by the IoT industry will help to make the network more robust, but before that need to be solved the performance and throughput issues which were mentioned in the paper above.

For further research we would like to focus how to apply evolution algorithms which could help with more stable transactions distribution and propagation into the tangle. As a second option we would like to look at the whole network as a communication channel.

The results from these experiments will be published at 3rd International Scientific Conference "Intelligent Information Technologies for Industry".

Acknowledgement: The following grants are acknowledged for the financial support provided for this research by Grant of SGS No. 2018/177, VSB-Technical University of Ostrava and under the support of NAVY and MERLIN research lab.

References

1. IOTA Foundation: <https://www.iota.org>
2. Popov S.: The Tangle https://assets.ctfassets.net/r1dr6vzfxhev/2t4uxvsIqk0EUau6g2sw0g/45eae33637ca92f85dd9f4a3a218e1ec/iota1_4_3.pdf [Online; accessed 26-June-2018]
3. J. F. C. Kingman: Poisson Processes. ISBN: 978-0-19-159124-2.
4. Daley D. J., Vere-Jones D.: An Introduction to the Theory of Point Processes: Volume II: General Theory and Structure. Springer Science & Business Media. ISBN: 978-0-387-21337-8.
5. Snyder D. L., Miller M. I.: Random Point Processes in Time and Space. Springer Science & Business Media. ISBN: 978-1-4612-3166-0
6. Mobilefish: <https://www.mobilefish.com>
7. Tahmasebi P., Javadpour F.; Sahimi M.: Stochastic shale permeability matching: Three-dimensional characterization and modeling. International Journal of Coal Geology. doi:10.1016/j.coal.2016.08.024.

The Method of Vertical Cuts (MoVC) in Action Recognition

Radek Simkanič

Department of Computer Science, FEECS,
VŠB – Technical University of Ostrava, 17. listopadu 15,
708 33 Ostrava – Poruba, Czech Republic
`radek.simkanic.st@vsb.cz`

Abstract. The Method of Vertical Cuts (MoVC) is introduced in this work for description and recognition of human activity from the depth sequences. This method is invariant to different duration of activities; it is assumed that the beginning and the end are known. The different view to the depth data called vertical cutting is used, and subsequently the Gaussian smoothing is applied. Then HoG is applied on this data and used for the SVM classifier. This method is robust to noisy data, and it can be adjusted how much data is used for recognition. Implementation is relatively simple with good speed performance.

Keywords: human action recognition, depth map, 3D action feature representation, HoG

1 Introduction

With higher availability of low-cost RGBD sensors for the public, they can be used in the research of human activity recognition. These sensors provide new useful information that was difficult to obtain from the conventional cameras, especially the depth map. The approaches based on the depth maps achieve good results and simplify the implementation better than RGB approaches.

The Depth Motion Maps (DMM) introduced in [2] can be regarded as a frequently used method. This method has an easy implementation in which the sum of the differences between the consecutive depth maps are computed. DMM can be extended of approaches which use, for example, Histogram of Gradients (HoG)[12], Local Binary Patterns[1] and Convolution Neural Networks (CNN)[11]. The Convolutional Neural Network approaches are used in the works [9, 4]. The Space-Time Occupancy Pattern (STOP), which is introduced in [7], is a method based on the space-time probabilistic occupancy grid. The local descriptor based on Sparse Codint (SC) and Fisher Vector (FV), which encodes the shape and motion cues using the surface normals in 4D space of depth, is introduced in [5]. The representation based on the cloud points was applied to the 4D subvolumes sampled by a weighted sampling scheme in a random occupancy pattern (ROP) in [8].

This paper is organised as follows. In Section 2, the details of the new method are stated. The experimental results are reported in Section 3. The conclusion can be found in Section 4.

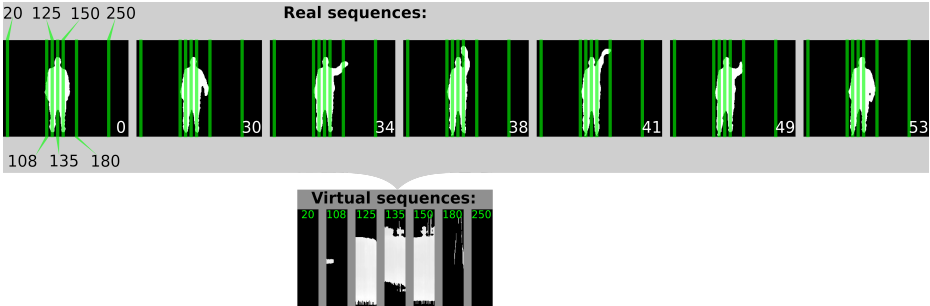


Fig. 1. The demonstration of the MoVC data rearrangement. The white numbers represent the frame number. The black numbers represent the column number which is corresponding to the green line. The green numbers represent the virtual frame number which is corresponding to the green line.

2 Proposed method

This section is focused on a detailed description of the novel method and alternative view of data called the Method of Vertical Cuts (MoVC). This method is developed for human action recognition and alternative representation of changes in the sequences of images in specific ranges. In this case, the sequences of the depth images are used. It is possible to choose the amount of data for the recognition of human activities and, thus, choose a required ratio between the recognition accuracy and performance speed.

The principle of the method is based on creating the sequences of virtual frames from the sequence of frames. Each virtual frame represents the history of a specific column in a defined interval of frames. The selection of columns for creating the virtual frames has to be done manually. The transformation from the classic sequence in a specific interval to the virtual sequences of selected columns is demonstrated in Figure 1. It can be observed in the certain virtual frames that some of them show that columns of frames do not change during the time of the activity. The columns which are not significant in all activities can be removed. It is also possible to remove adjacent the virtual frames, because there are high probabilities that there are small changes. This allows for a rapid decrease of the amount of data with minimal influence on the accuracy result of recognition.

Once the sequence of virtual frames is prepared, the width of all virtual frames should be normalized into the same size. In this work, the bilinear interpolation is used for normalizing the width. The normalization of width is

necessary to ensure for the same dimension of feature vector for each activities. The 48-pixels width is used for the experiments. In the virtual frames with the normalised size (width), the histogram of oriented gradients (HoG) can be applied to capture the vector of features. The vectors of features of each virtual frame are chained into one feature vector. The feature vector can be processed by using any algorithm for machine learning. In this case of our experiments, the SVM classifier with intersection and linear kernel is used.

2.1 Filtering

The filters mentioned in this section were used in experiments. In this work, only the Gaussian smoothing filters are used. First, the Gaussian filter with the kernel of size 5 is applied to the virtual frames in the time-direction before the normalization of width. This cause creating the ghosts because there is a partial imprinted history and future on each frames (this is demonstrated in Figure 2.). The next Gaussian filter with the kernel size of 5×5 is improving the results. It is applied on the virtual frames after the width normalization.



Fig. 2. The demonstration of the 30th frame of the first action stream from MSR Action3D Dataset where the Gaussian blurring is applied across the time. The ghosts of short history and future are seen here.

2.2 HoG Configurations

In this section, the HoG configurations are described that are used in experiments. The resolution of each virtual frame used in the experiments is 48×240 (width \times height). In the experiments, three HoG configurations are used simultaneously: (i) block size 24×32 , block stride 12×16 and cell size 12×32 ; (ii) block size 48×32 , block stride 48×16 and cell size 24×32 ; (iii) block size 12×32 , block stride 6×16 and cell size 6×32 . The number of bins is 9 and 64 levels with signed gradients without gamma correction. The vectors of all HoG features are chained to one HoG feature vector.

3 Experiments

In this section, the proposed method is evaluated by using two different datasets: (i) MSR Action3D Dataset [3], and (ii) UTKinect-Action3D dataset [10]. Two

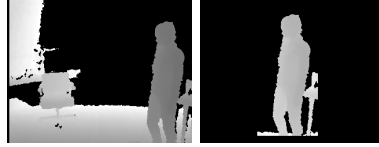


Fig. 3. Original but normalised first depth image (left) and normalised depth image without background (right).

techniques are used to demonstrate the accuracy of the new method: (i) ACC (accuracy) by the formula $ACC = \frac{TP+TN}{TP+TN+FP+FN}$, (ii) the harmonic mean of precision and sensitivity $F1 = \frac{2 \cdot TP}{2 \cdot TP+FP+FN}$.

MSR-Action3D dataset[3] was captured using a Microsoft Kinect-like depth sensor. This dataset contains 20 action types, each action is performed by 10 human subjects who repeat the same action 2 or 3 times. Altogether, there are 557 valid action sequences of depth maps (310×240) with a separated background. This is the challenging dataset because many sequences of actions in different classes are similar to each other.

UTKinect-Action3D dataset[10] was captured by using Microsoft Kinect sensor. It contains 10 action types, each action is performed by 10 human subjects again, every action is repeated twice. Altogether, there are 199 action sequences contained within 20 depth map video sequences (310×240). The action in this dataset contained high intra-class variations.

Table 1. The experimental results of the proposed method on the MSR-Action3D dataset via cross-subject decomposition. AS1 - AS3 is provided by Li. et al. [3] protocol and All is provided by Wang et al. [8] protocol.

Methods	AS1		AS2		AS3		All	
	F1 %	ACC %	F1 %	ACC %	F1 %	ACC %	F1 %	ACC %
Li e al. [3]	72.9	–	71.9	–	79.2	–	–	–
DMM	97.8	99.78	75	93.75	81.08	95.27	72.89	97.29
MoVC	82.86	95.71	79.46	94.87	95.5	98.87	82.78	98.28

MSR-Action3D dataset allows for several validation protocols which are summarised in [6]. Several protocols have been used in this article. The first used protocol is introduced in Li. et al. [3]. In this standard protocol, the dataset is divided into three action subsets AS1, AS2 and AS3 (8 action types per a subset), which may share some action types. The accuracy of the proposed method on the dataset is tested by cross-subject decomposition which is a challenge, because each person slightly differently performs the same activity than another person. One half of the samples of subjects is used for training, the other half is used for validation. The second used protocol is provided in Wang et al. [8]. This protocol is not divided into subsets AS1 - AS3, but the test is applied over all action types of the entire dataset. The evaluations by these protocols are shown in Table 1. It

can be observed that all subsets of cross-samples achieve high accuracy, precision and sensitivity. The proposed method (MoVC) has average accuracies of protocol Li. et al [3]: 96.48 % (F1 85.94 %) for cross-subject. The reference method DMM has average accuracies of protocol Li. et al [3]: 96.27 % (F1 84.63 %) for cross-subject. The MoVC is slightly better than DMM. The proposed method is comparable to the state-of-the-art methods.

The next experiment, the measuring of the F1 score if less virtual frames are used for recognition. The experiment is performed via MSR-Action3D dataset on the cross-subject with all classes of activities. The intersection and the linear SVM kernel are used. Sampling of virtual-frame sequence is performed so that the n th virtual frames are used. The type of sampling is depicted on the x-axis on the chart in Figure 4. The MoVC still works well if each twentieth virtual frame from sequence is used for recognition. This brings a huge reduction of used data.

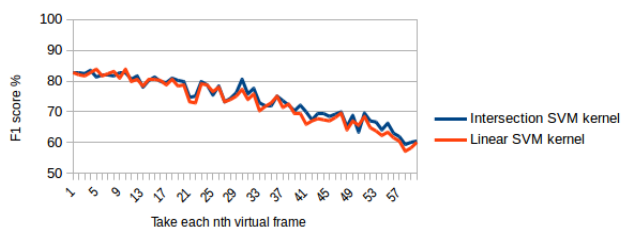


Fig. 4. Chart which shows, how F1 score is changed based on sampling.

The UTKinect-Action dataset contains the depth maps sequences without separation of a background. The background was removed by simple method based on the location of skeleton and thresholding. The depth maps without the background are aligned to the center by the position of human in the scene. Both the images are normalised to the interval 0 - 1 by the maximum value in frame. Example of the depth image with a background and without a background is shown in Figure 3. The new method is compared with one of the state-of-the-art methods, namely with the method called Depth Motion Maps (DMM) [2] which is also implemented for these experiments. The frames without background are used for these methods. In this case for this purpose, the intersection kernel of SVM is used for DMM. Frames without background are also used for our MoVC. Frames with background are experimentally used for MoVC to test the robustness of algorithm to these data. The cross-subject and cross-sample protocol are used for the UTKinect-Action dataset. The cross-subject protocol, half of the subjects is used for training while the other half is used for testing. The cross-samples protocol, first sample of each subject is used for training while the second is used for testing. The evaluations by these protocols are shown in Table 2. The proposed method is better than DMM on the data without the background.

Table 2. The experimental results of proposed method on the UTKinect-Action dataset.

Methods	cross-subject		cross-sample	
	F1 %	ACC %	F1 %	ACC %
DMM	69.7	93.9	72.7	94.5
MoVC (without background)	85.86	97.17	85.86	97.17
MoVC (with background)	68.69	93.74	75.76	95.15

4 Conclusion

The proposed method was developed and tested to robustness of noise. The robustness of noise was tested on the UTKinect dataset. In addition, less data can be used with this method which is presented on the chart in Figure 4. This method is easy to implement and does not need much performance. Therefore, it is suitable for real-time recognition. The selection of the columns for creating virtual frames is to be carried out manually, but in the future, we will focus on the developing the method for selection of columns.

References

1. Chen, C., Jafari, R., Kehtarnavaz, N.: Action recognition from depth sequences using depth motion maps-based local binary patterns. 2015 IEEE Winter Conference on Applications of Computer Vision (2015)
2. Chen, C., Liu, K., Kehtarnavaz, N.: Real-time human action recognition based on depth motion maps. *Journal of Real-Time Image Processing* vol. 12(issue 1), 155–163 (2016)
3. Li, W., Zhang, Z., Liu, Z.: Action recognition based on a bag of 3d points. In: 2010 IEEE Computer Society Conference on Computer Vision and Pattern Recognition - Workshops. pp. 9–14. IEEE (2010)
4. Liu, Z., Zhang, C., Tian, Y.: 3d-based deep convolutional neural network for action recognition with depth sequences. *Image and Vision Computing* 55, 93100 (2016)
5. Nguyen, X.S., Nguyen, T.P., Charpillet, F.: Improving surface normals based action recognition in depth images. 2016 13th IEEE International Conference on Advanced Video and Signal Based Surveillance (AVSS) (2016)
6. Padilla-López, J.R., Chaaraoui, A.A., Flórez-Revuelta, F.: A discussion on the validation tests employed to compare human action recognition methods using the MSR action3d dataset. CoRR abs/1407.7390 (2014), <http://arxiv.org/abs/1407.7390>
7. Vieira, A.W., Nascimento, E.R., Oliveira, G.L., Liu, Z., Campos, M.F.: On the improvement of human action recognition from depth map sequences using spacetime occupancy patterns. *Pattern Recognition Letters* vol. 36, 221–227 (2014)
8. Wang, J., Liu, Z., Chorowski, J., Chen, Z., Wu, Y.: Robust 3d action recognition with random occupancy patterns. In: *Computer Vision - ECCV 2012*, pp. 872–885. Springer, Berlin (2012)
9. Wang, P., Li, W., Gao, Z., Zhang, J., Tang, C., Ogunbona, P.: Deep convolutional neural networks for action recognition using depth map sequences. CoRR abs/1501.04686 (2015), <http://arxiv.org/abs/1501.04686>

10. Xia, L., Chen, C.C., Aggarwal, J.K.: View invariant human action recognition using histograms of 3d joints. In: 2012 IEEE Computer Society Conference on Computer Vision and Pattern Recognition Workshops. pp. 20–27. IEEE (2012)
11. Yang, R., Yang, R.: Dmm-pyramid based deep architectures for action recognition with depth cameras. *Computer Vision – ACCV 2014 Lecture Notes in Computer Science* p. 3749 (2015)
12. Yang, X., Zhang, C., Tian, Y.: Recognizing actions using depth motion maps-based histograms of oriented gradients. *Proceedings of the 20th ACM international conference on Multimedia - MM 12* (2012)

Crowd Sourcing as an Improvement of N-Grams Text Document Classification Algorithm

Petr Šaloun, David Andrešič, and Barbora Cigánková

Department of Computer Science, FEECS,
VŠB – Technical University of Ostrava, 17. listopadu 15,
708 33 Ostrava – Poruba, Czech Republic
{petr.saloun, david.andresic.st, barbora.cigankova.st}@vsb.cz

Abstract. A common task in natural language processing is text classification to some pre-defined classes, which is useful for e.g. spam filters, documents sorting, science articles categorization or plagiarism detection. This can still be done best by human, on the other hand, often we can accept certain error in the classification in exchange for classification speed. Here, natural language processing mechanism transforms the text in natural language to a form understandable by a classifier such as k-means neighbor, decision tree, neural network or support vector machine. We can also use this human element to help automated classification to improve its accuracy by means of crowdsourcing.

This work deals with classification of text documents and its improvement through crowdsourcing. Its goal is to design and implement text documents classifier prototype based on documents similarity and to design evaluation and improvements of classification using crowd-sourcing. For classification the N-grams algorithm has been chosen. In addition to data collection, the purpose of interface is to evaluate classification accuracy, which leads to extension of classifiers test data set, thus the categorization is more successful. We test our approach on two data sets with promising preliminary results even across different languages.

Keywords: Natural Language Processing, N-grams, Crowdsourcing, Statistics, Classification

1 Introduction

Despite the progress in text classification, humans are still more accurate, which opens a space for human-assisted classification such as collective intelligence of people called crowdsourcing. In this work, we describe our experience and preliminary results with documents written in (czech) natural language. We also offer a general overview of today algorithms for text classification, lemmatization and stemmatization focused on czech language. We tested the approach on two data sets (described in section 6) and compared with crowdsourcing approach.

2 Text Document Classification Overview

Its goal is to assign the text to some pre-defined class. In the area of text mining, it is also a process of automatic learning of categorization schemas[1]. Some approaches use different forms of document similarity metric. Before the classification, removing of stop words, tags and other pre-processing (see section 3) must be done as well as information extraction for the classifier (in vectors [1])

The classifier training using a labeled training data set follows. After this, classification of new documents can be performed. Today's classifiers use statistical approaches (e.g. Naive Bayes Classifier [1][2], TF-IDF [3], Latent Semantic Analysis [4][5]) or machine learning (e.g. Support Vector Machines [6][7]).

2.1 N-grams

N-gram is a tuple of N items that belongs to some sequence of e.g. words or letters. During the classification, sequence of letters is used. The beginning and the end of the word is marked by some special character such as underscore [8].

Since there is no need for text pre-processing such as stemming or lemmatization, N-grams are usually language-independent. They also tolerate some grammar errors and typos. On the other hand, a large number of generated N-grams can be considered as a drawback. This can be reduced by e.g. removing stop words or by using stemming or lemmatization (or some other text length reduction), but by doing this, we lose the advantage of language independency.

3 Processing of Texts Written in Natural Language

NLP software requires consistent knowledge base such as large dictionary, grammar rules, ontology and synonyms etc. [10]. After a pre-processing (including stemming [11] and lemmatization [12]), NLP process usually consists of several phases: [9][10]: morphological, syntax and semantic analysis.

Stemmers and Lemmers for Czech Language Czech language is a bit difficult for stemming and lemmatization due to its prefixes and more complex inflection. Due to this there are not many frameworks or software libraries. One solution offers Apache Lucene¹. This search engine offers czech analyzer with czech stop words, stemmer and extensible tokenizer. Absence of lemmatizer can be compensated by czech morphological analyzer called Majka².

4 Crowdsourcing

It is a concept also known as wisdom of crowd. Definition in [13] answers to 8 basic questions about crowdsourcing. A nice description of crowdsourcing pros can be found in [14]. The motivation of crowd is then nicely described in [15].

¹ <https://lucene.apache.org/>

² <https://www.muni.cz/vyzkum/publikace/935762>

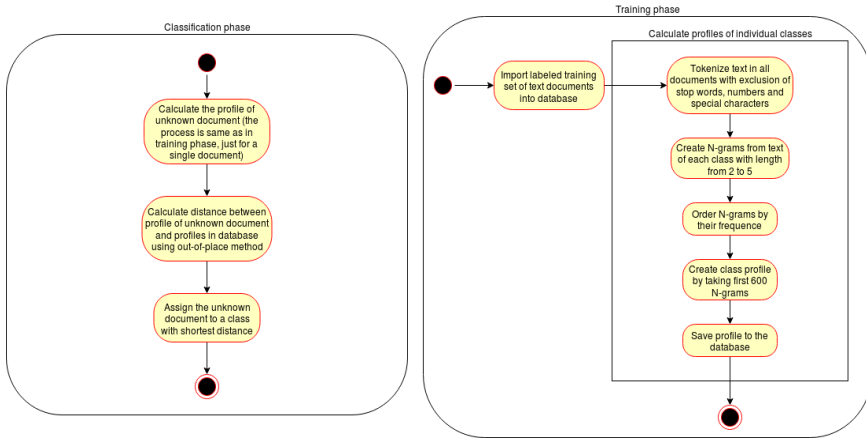


Fig. 1. Classifier training (right) and classification (left) phase.

5 Prototype Description

We eventually chose the N-grams algorithm for the easiness of its implementation but also for language independency. The implementation is based on [8] and consisting from two phases: training (see Fig. 1) and classification (see Fig. 1).

In oposite to [8] our classifier utilizes a reduction of words count in document by removing the stop words. Using this reduction, it is not necessary to start in the profile class at the position 300 (as sugested in [8]) but it is possible to start from the beginning of the list. Also, our classifier works with longer progiles, mostly because of planned classification of psychological text. Their classes have usually a very thin border so we can expect the need of more N-grams.

Our application also determines key words of each class. These key words will then be displayed to selected users with a kind request to use them in their contribution. By showing key words only to some users, we create two user groups that will serve as referential groups to confirm the following hypothesis: Classification will perform better if contributions for classification contain pre-defined key words. The calculation of key words is realized by TF-IDF algorithm modified (in respect to [16]) to class purpose. The calculation is done by:

$$TF_{ij} = \frac{n_{ij}}{\sum_k n_{kj}} \quad (1)$$

where n_{ij} is frequency of term i in documents of class j .

$$IDF_i = \log\left(\frac{|D|}{|d : t_i \in d|}\right) \quad (2)$$

where t_i is term and D is set of all classes.

TF_{ij} is quotient of term frequency n_{ij} to count of all word in documents of the given class. IDF_i is then logarithm of quotient of classes count to count of

classes containing term t_i . Five key words with greatest weight for each category from those obtained by this method are selected and stored to database.

6 Preliminary Results

Our classifier was tested on two datasets and then briefly with use of crowd-sourcing.

6.1 Language Data Set

The source of the data is DATAKON conference (from 2010 to 2014) with technical texts in czech, slovak and english. Each category contained 40 texts with 60 up to 20 words. Both training and test data set contained 20 random texts per class. Our classifier successfully classified all 60 test documents (see Table 1) which confirms the N-grams language independence. In future, we could add similar languages such as polish or russian.

<i>Class</i>	<i>Accuracy</i>
<i>English</i>	20/20
<i>Slovak</i>	20/20
<i>Czech</i>	20/20
<i>Sum</i>	100 %

Table 1. Classification accuracy for language data set.

6.2 Psychological Data Set

It contains not so balanced count of psychological texts. It's aim was to investigate how the classifier will perform with not so well structured data. They are sorted to classes with not so clear borders. These texts are often difficult to classify even by human. The expected accuracy of classification therefore was not high. The data set contains 87 documents in 3 classes: 63, 8 and 14 documents in each class. Training set contained 80% of randomly chosen documents.

Table 2 shows that in each class one document was misclassified. From profile distances we assumed that one error was caused by text length corresponding to the topic (introduction is about a different topic, which confuses the classifier that may not have enough of N-grams). The content of another misclassified documents is close to a border of two topics (small distance between document and class profile) and is again difficult to be correctly classified even by human. The last document is again a border one. Here, the correct class is the most distant one. A possible improvement could be a better structure of data set.

<i>Class</i>	<i>Accuracy</i>
<i>Personal issues, illness</i>	12/13
<i>Work, finances, school</i>	1/2
<i>Romantic, family and employment relationships</i>	2/3
<i>Sum</i>	69 %

Table 2. Classification accuracy for psychological data set.

Crowdsourcing The classifier accuracy was also tested by implemented crowdsourcing interface. Our crowd contained people from OSU³ and VŠB-TUO universities. Training set was provided by OSU and contained 180 one- or two-sentence texts in 4 classes. In case of error, correct class was assigned to the text.

Another aim of this work was also suggest an approach that will lead to increased classification quality using crowdsourcing. The suggested approach was to extended training set - mostly by incorrectly classified contributions.

So far 8 contributions were added (2 per class) by a single author, which means a similar dictionary. First, one contribution was added to each class which led to 0% accuracy probably due to a difference in text nature of contribution and training data. After data synchronization, second phase was done in the same way with accuracy of 50%. Although we can see an improvement, we cannot make any conclusions from such small amount of data.

7 Conclusion

The aim was to create a text document classifier based on document similarity with further use of crowdsourcing increasing classification accuracy. The accuracy was tested on two data sets and then by our crowdsourcing interface. With first data set classifier performed excellently proving its language independency. Second data set with psychological data also performed very good, because incorrect classifications would be difficult for a human as well. Eventually, accuracy was left to the user themself using crowdsourcing interface. In order to improve it, extending the training set (especially with misclassified texts) was suggested.

With respect to a small number of contributions it is not possible to make further conclusions about classifier accuracy. Nevertheless even with such small sample we can see a growing trend. These results shall not be generalized though because all contributions were made by a single author.

In this work, a hypothesis about increasing classification accuracy using key words from available data was mentioned. Nevertheless, in respect to a small number of available contributions, we cannot make any conclusions yet.

Acknowledgements The following grants are acknowledged for the financial support provided for this research: Grant Agency of the Czech Republic - GACR

³ <https://www.osu.cz/>

P103/15/06700S, Grant of SGS No. SGS 2017/134, VSB-Technical University of Ostrava. The Ministry of Education, Youth and Sports from the National Programme of Sustainability (NPU II) project IT4Innovations excellence in science - LQ1602.

References

1. KARMAN, S. Senthamarai; RAMARAJ, N. Similarity-Based Techniques for Text Document Classification. *Int. J. SoftComput*, 2008, 3.1: 58-62.
2. OPITKA, P.; ŠMAJSTRLA, V. PRAVDĚPODOBNOST A STATISTIKA, [In Czech] (Probability and statistics) 2013. [Online]. Available: <https://homen.vsb.cz/oti73/cdpast1/KAP02/PRAV2.HTM>. [Accessed on 4. 3. 2018].
3. Tf-idf :: A Single-Page Tutorial - Information Retrieval and Text Mining, [Online]. Available: <http://www.tfidf.com/>. [Accessed on 25. 12. 2017].
4. LANDAUER, Thomas K.; FOLTZ, Peter W.; LAHAM, Darrell. An introduction to latent semantic analysis. *Discourse processes*, 1998, 25.2-3: 259-284.
5. HÁJEK, Petr, et al. Možnosti využití přístupu indexování latentní sémantiky při předpovídání finančních krizí. *POLITICKÁ EKONOMIE*, [In Czech] (Possible use of indexed latent semantic approach for financial crisis prediction) 2009, 6: 755.
6. Support Vector Machines (SVM), TIBCO Software Inc, [Online]. Available: <http://www.statsoft.com/Textbook/Support-Vector-Machines>. [Accessed on 28. 12. 2017].
7. ŽIŽKA, J. Studijní materiály předmětu FI:PA034, [In Czech] (Study materials to FI:PA034) [Online]. Available: https://is.muni.cz/el/1433/podzim2006/PA034/09_SVM.pdf. [Accessed on 29. 12. 2017].
8. CAVNAR, William B., et al. N-gram-based text categorization. *Ann arbor mi*, 1994, 48113.2: 161-175.
9. HABROVSKÁ, P. Vybrané kapitoly z počítačového zpracování přirozeného jazyka, 2010. [In Czech] (Selected chapters from natural language processing) [Online]. Available: <http://www.inflow.cz/kratce-o-zpracovani-prirozeneho-jazyka>.
10. SCAGLIARINI, L.; VARONE, M. Natural language processing and text mining, 11 April 2016. [Online]. Available: <http://www.expertsystem.com/natural-language-processing-and-text-mining/>. [Accessed on 15. 12. 2017].
11. KODIMALA, Savitha. Study of stemming algorithms. 2010.
12. RISUENO, T. The difference between lemmatization and stemming, 28. 1. 2018. [Online]. Available: <https://blog.bitext.com/what-is-the-difference-between-stemming-and-lemmatization/>. [Accessed on 4. 3. 2018].
13. ESTELLÉS-AROLAS, Enrique; GONZÁLEZ-LADRÓN-DE-GUEVARA, Fernando. Towards an integrated crowdsourcing definition. *Journal of Information science*, 2012, 38.2: 189-200.
14. KALSI, M. Crowdsourcing through Knowledge Marketplace, 3. 3. 2009. [Online]. Available: http://blog.spinact.com/knowledge_as_a_service/2009/03/crowdsourcing-through-knowledge-marketplace.html. [Accessed on 2018 3. 4.].
15. KAUFMANN, Nicolas; SCHULZE, Thimo; VEIT, Daniel. More than fun and money. Worker Motivation in Crowdsourcing-A Study on Mechanical Turk. In: *AMCIS*. 2011. p. 1-11.
16. VRL, NICTA. An unsupervised approach to domain-specific term extraction. In: *Australasian Language Technology Association Workshop 2009*. 2009. p. 94.

The Comparison of Windows API Functions Usage between Malware and Legitimate Applications

Filip Zatloukal

Department of Computer Science, FEECS,
VŠB – Technical University of Ostrava, 17. listopadu 15,
708 33 Ostrava – Poruba, Czech Republic
vsb@zatloukal.net

Abstract. The goal of our research is to extend and improve the existing methods of malware detection or to create some new malware detection methods. This paper introduces the concepts of our newly proposed method that we will test and measure in near future. The focus of this paper is to prepare the theoretical foundation needed for the upcoming research.

Keywords: Malware, Windows API, PE header.

1 Introduction

The goal of our research is to extend and improve the existing methods of malware detection or to create some new malware detection methods. This paper introduces the concepts of our newly proposed method that we will test and measure in near future. The focus of this paper is to prepare the theoretical foundation needed for the upcoming research.

There is a number of malware detection methods and ways to analyse malware. Each has some advantages and disadvantages. Where some methods are successful, others may fail. Some methods are able to find new kinds of threads, some not. Some have very good performance, some are slower.

2 Malware analysis

2.1 Related methods

This chapter contains an overview of important and well-known malware analysis and detection methods.

Static analysis analyzing unknown software without need to execution. Several techniques like string signature, byte-sequence n-grams, syntactic library call, control flow graph and opcode frequency distribution and so on could be used for static analysis.

Dynamic analysis is analyzing the behavior of unknown software - how this software interacts with the system, which is separated from user's environment. This environment could be sandbox, virtual machine or another emulator with control capabilities [1].

The biggest disadvantage of this technique is time for execution and also there could be a problem, that analyzed software could behave differently in controlled environment than in another one (due to different date or time when program runs or another unpredictable dependency which make malicious code active - for example Logic Bombs [2]).

2.2 PE headers and Import/Export functions

In PE headers, there are besides two tables that are useful for the static analysis. Import functions and export functions [3]. Executables and libraries can use functions from other libraries and executables that are offered. Libraries offer their functions to be used in such programs. This kind of functions is called exported functions.

On the other hand, the imported functions are those functions that are included in software from exported functions. Imported functions are very common in executables (also in libraries), exported functions are common for libraries and rare for executables. However, it is possible to make exported functions in executables too [4].

It is important for the malware analysis that operating systems offer own libraries with exported functions to manipulate the system and make basic and advanced operations. Windows offers these functions in Windows API specification [5].

Since we have information about imported/exported functions in PE headers, we are able to extract them, including libraries, where the functions are presented. The finished analysis shows that it is common practice to include system libraries to malware and to use their functions.

3 Experiment

3.1 Method

Our training set of samples is divided into two categories: goodware and malware. Each category contains samples with different characteristics but all of these are either legit or malicious applications, both in valid Windows PE format.

We would like to propose a new method based on comparing the usage of Windows API function between goodware and malware. In the learning stage of the process, we iterate all samples from a training set and parsing list of import functions from PE header for each sample. Samples are inserted into our application, together with two counters (for each function). For every single function (from the import table) of each sample from the dataset a relevant counter is incremented. A "Good" counter is incremented if sample is from the

goodware category and a “Bad” counter for the malware category. At the end, “security” index for each function is calculated as a difference between “Good” and “Bad” counters. These indices will be used in future research for evaluating samples from the testing set.

3.2 Dataset

The dataset we are using is composed of 6 232 Windows programs in PE file format. 3 480 of them are malicious software and 2 752 user-friendly (clean) executable files or DLLs. User-friendly programs were collected from different sites as Studna [6], sourceforge [7], filehippo [8] and our local laboratory’s files. Within research, these files were downloaded manually to do not break license terms of selected servers. Applications included in Microsoft Windows 7 and some selected games were tested, too. Malicious software comes from: VirusShare [9], Malekal malware db [10] and from our private collection.

For this research, we only process valid 32-bit or 64-bit Windows executable or DLL files with valid PE headers. 16-bit DOS files or files with invalid PE headers are skipped. Most of the legitimate applications were downloaded in the format of installer or package. Scan of these installers would return unwanted results - it would return information about installers instead of information about applications. Therefore, it was needed to install (or unpack) all of these applications firstly and scan installed/unpacked application then.

4 Results

In this paper we would like to introduce first/initial results that are already measured. These results focus on the statistics from the dataset rather than on results from scanning and using the detection method itself. These measures are not finished yet and will be introduced later. All samples from the dataset are already included in the results. The following results show the differences between the usage of Windows API functions by legitimate applications and malware. The first column is the name of the function, the second is the name of the library from which the function is loaded. “Good” column keeps the number of legit applications (from the dataset) that include the function in their Import list. “Bad” column is the same, but for malware.

The safest functions:

As the safest function is considered the function for which the biggest difference between its usage by a legitimate and a malicious application is in favour of goodwill.

Table 1. The safest functions from whole database.

Function name	Library name	Good	Bad
InitializeCriticalSection	KERNEL32.dll	1543	1016
DeleteCriticalSection	KERNEL32.dll	1826	1368
DisableThreadLibraryCalls	KERNEL32.dll	539	81
strncmp	msvcrt.dll	459	50
abort	msvcrt.dll	451	49
_iob	msvcrt.dll	465	66
LeaveCriticalSection	KERNEL32.dll	1771	1381
vfprintf	msvcrt.dll	401	14
fwrite	msvcrt.dll	444	61
calloc	msvcrt.dll	440	61
QueryPerformanceCounter	KERNEL32.dll	1883	1511
EnterCriticalSection	KERNEL32.dll	1771	1403

The most dangerous functions:

As the most dangerous function is considered the function for which the biggest difference between its usage by a legitimate and a malicious application is in favour of malware.

Table 2. The most dangerous functions from whole database.

Function name	Library name	Good	Bad
ExitProcess	KERNEL32.dll	1307	2339
LoadLibrary	KERNEL32.dll	1673	2645
GetCommandLine	KERNEL32.dll	1145	2023
WriteFile	KERNEL32.dll	1357	2209
lstrlen	KERNEL32.dll	768	1574
GetModuleFileName	KERNEL32.dll	1478	2277
GetStartupInfo	KERNEL32.dll	1142	1935
CreateFile	KERNEL32.dll	1317	2109
RegOpenKey	advapi32.dll	946	1727
DeleteFile	KERNEL32.dll	819	1594
DispatchMessage	USER32.dll	705	1458
RegCloseKey	advapi32.dll	969	1719

The functions used mostly by legitimate applications:

The list of functions that are mostly used by legit application (without the comparison with malware).

Table 3. The functions that are used mostly by legitimate applications.

Function name	Library name	Good	Bad
GetCurrentThreadId	KERNEL32.dll	2156	1855
GetProcAddress	KERNEL32.dll	2093	2546
GetCurrentProcess	KERNEL32.dll	2016	2014
GetModuleHandle	KERNEL32.dll	1999	2636
GetLastError	KERNEL32.dll	1982	2377
GetCurrentProcessId	KERNEL32.dll	1961	1694
QueryPerformanceCounter	KERNEL32.dll	1883	1511
Sleep	KERNEL32.dll	1877	2214
GetTickCount	KERNEL32.dll	1848	1926
DeleteCriticalSection	KERNEL32.dll	1826	1368
TerminateProcess	KERNEL32.dll	1806	1611
GetSystemTimeAsFileTime	KERNEL32.dll	1799	1479

The functions used mostly by malicious applications:

The list of functions that are mostly used by malware (without the comparison with goodware).

Table 4. The functions that are used mostly by malicious applications.

Function name	Library name	Good	Bad
LoadLibrary	KERNEL32.dll	1673	2645
GetModuleHandle	KERNEL32.dll	1999	2636
GetProcAddress	KERNEL32.dll	2093	2546
GetLastError	KERNEL32.dll	1982	2377
ExitProcess	KERNEL32.dll	1307	2339
CloseHandle	KERNEL32.dll	1724	2329
GetModuleFileName	KERNEL32.dll	1478	2277
Sleep	KERNEL32.dll	1877	2214
WriteFile	KERNEL32.dll	1357	2209
CreateFile	KERNEL32.dll	1317	2109
GetCommandLine	KERNEL32.dll	1145	2023
GetCurrentProcess	KERNEL32.dll	2016	2014

5 Discussion

The results show functions from Windows API and their usage by good-ware and malware. According to the results, we can observe interesting facts that can be useful for malware analysis:

- Table 1. contains a multiple function for a thread-safe resources access. This may indicate that multi-threading is used mainly for legit applications and not for malware.

- In Table 2., there are functions used for run-time library loading. These functions are widely used by malware.
- Malware often treats files and Windows registers according to Table 2.
- Table 3. and Table 4. confirm the results from previous tables.

6 Conclusion and Future work

This paper describes a proposal of a new method for malware analysis. The method we are working on is based on the comparison of the usage of functions that are included in PE header of both – legit applications and malware. The main idea is to count security index for each function of Windows API and use these indices for relevant functions from the testing set. These methods supposed to be relatively fast and might be able to detect new threads as well. But the following research will show the potential and accuracy of the proposed method.

The goal of this paper was to provide first measurements and statistics from the training set. The following research will be focused on individual evaluated functions and their usage in the testing set.

Acknowledgement

The following grants are acknowledged for the financial support provided for this research: Grant of SGS No. SGS 2018/177, VSB-Technical University of Ostrava.

References

1. Ekta Gandotra, Divya Bansal, and Sanjeev Sofat. Malware analysis and classification: A survey. *Journal of Information Security*, 05(02):56–64, 2014.
2. Manuel Egele, Theodoor Scholte, Engin Kirda, and Christopher Kruegel. A survey on automated dynamic malware-analysis techniques and tools. *ACM Computing Surveys (CSUR)*, 44(2):1–42, Jan 2012.
3. Eldad Eilam and Elliot J. Chikofsky. *Reversing: secrets of reverse engineering*. John Wiley & Sons, 2011.
4. Michael Sikorski and Andrew Honig. *Practical malware analysis: the hands-on guide to dissecting malicious software*. No Starch Press, 2012.
5. Yanfang Ye, Dingding Wang, Tao Li, Dongyi Ye, and Qingshan Jiang. An intelligent pe-malware detection system based on association mining. *Journal in Computer Virology*, 4(4):323–334, May 2008.
6. Studna.cz. <http://www.studna.cz/>, 2018. Online; accessed 23 July.
7. Sourceforge - the complete open-source software platform. <https://sourceforge.net/>, 2018. Online; accessed 23 July.
8. Filehippo.com - download. <https://filehippo.com/>, 2018. Online; accessed 23 July.
9. Virusshare.com. <https://virusshare.com/>, 2018. Online; accessed 23 July.
10. Liste malware - malekal.com. <http://malwaredb.malekal.com/>, 2018. Online; accessed 23 July.

Quasilinear boundary problem with p-Laplacian

Michaela Bailová

Department of Applied Mathematics, FEECS,
VŠB – Technical University of Ostrava, 17. listopadu 15,
708 33 Ostrava – Poruba, Czech Republic
michaela.bailova@vsb.cz

Abstract. Many engineering problems lead to solving quasilinear boundary problems with p-Laplacian operator. The approach introduced here is based on the fact that, under certain assumptions, the weak solutions of such problems coincide with critical points of the corresponding functionals. In the paper, we introduce a specific type of boundary problem. Thanks to the geometry, we can use the Mountain Pass Theorem to prove the existence of critical points. Subsequently, a mountain pass algorithm is introduced and used for finding numerical solutions.

Keywords: p-Laplacian operator, quasilinear elliptic PDE, critical point, Mountain Pass Theorem, mountain pass algorithm

1 Introduction

In this paper, we study the quasilinear elliptic boundary problem

$$\begin{cases} -\Delta_p u = u^3 & \text{in } \Omega, \\ u = 0 & \text{on } \partial\Omega, \end{cases} \quad (1)$$

where

$$\Delta_p u = \operatorname{div}(|\nabla u|^{p-2} \nabla u),$$

Ω is a bounded domain in \mathbb{R}^2 with Lipschitz boundary and $p \in (\frac{4}{3}, 4)$.

Note 1. If we take $p = 2$, (1) turns into a classical Laplace operator Δ .

The solutions of (1) correspond to critical points of the following functional

$$J(u) = \frac{1}{p} \int_{\Omega} |\nabla u|^p dx - \frac{1}{4} \int_{\Omega} u^4 dx. \quad (2)$$

To prove the existence of critical points of J , we use the Mountain pass theorem. Consequently, a minimax algorithm is introduced and used to compute numerical solutions.

2 Analytical background

The Mountain pass theorem, introduced by Ambrosetti and Rabinowitz in 1973 (see [1], [2], [3]), is an important tool for proving the existence of critical points of the functionals $J \in C^1(X, \mathbb{R})$.

Theorem 1 ((Mountain pass theorem, 1973)). *Let*

- X be a Banach space,
- $J \in C^1(X, \mathbb{R})$,
- $r \in \mathbb{R}^+$, $e \in X$, $\|e\|_X > r$,
-

$$\inf_{\|u\|_X=r} J(u) > J(0) \geq J(e), \tag{3}$$

- J satisfy the Palais-Smale (PS) condition, i.e.

$$\left. \begin{array}{l} (u_n) \text{ is a sequence in } X \\ (J(u_n)) \text{ is bounded in } \mathbb{R} \\ J'(u_n) \rightarrow 0 \text{ in } X^* \end{array} \right\} \Rightarrow (u_n) \text{ has a convergent subsequence.} \tag{4}$$

Then

$$c := \inf_{\gamma \in \Gamma} \max_{t \in [0,1]} J(\gamma(t)),$$

where $\Gamma = \{\gamma \in C([0, 1], X) : \gamma(0) = 0, \gamma(1) = e\}$,
 is a **critical value** of J .

First, we show that $J'(u) \in (W_0^{1,p}(\Omega))^*$. We know that

$$\langle J'(u), v \rangle = \int_{\Omega} |\nabla u|^{p-2} \nabla u \nabla v \, dx - \int_{\Omega} u^3 v \, dx.$$

It is clear that $J'(u)$ is linear. Furthermore, using the Hölder’s inequality and the continuous embedding, we get

$$|\langle J'(u), v \rangle| \leq \|u\|_{1,p,0}^{p-1} \|v\|_{1,p,0} + \|u\|_{L^4}^3 \|v\|_{L^4} \leq k \|v\|_{1,p,0}.$$

It is known that $J \in C^1(X, \mathbb{R})$. Consequently, we have to prove that J has a mountain pass geometry (in other words, J satisfies the assumption (3)). The functional J can be written as follows

$$J(u) = \frac{1}{p} \|u\|_{1,p,0}^p - \frac{1}{4} \|u\|_{L^4}^4. \tag{5}$$

Let us consider $\Omega \subset \mathbb{R}^2$. For $p > 2$, we know that

$$W_0^{1,p}(\Omega) \hookrightarrow C(\bar{\Omega}) \hookrightarrow L^4(\Omega).$$

Hence, there exists a constant $k \in \mathbb{R}^+$ such that

$$J(u) = \frac{1}{p} \|u\|_{1,p,0}^p - \frac{1}{4} \|u\|_{L^4(\Omega)}^4 \geq \frac{1}{p} \|u\|_{1,p,0}^p - \frac{k}{4} \|u\|_{1,p,0}^4.$$

For all $2 < p < 4$, we get

$$J(u) \geq \|u\|_{1,p,0}^p \left(\frac{1}{p} - \frac{k}{4} \|u\|_{1,p,0}^{4-p} \right). \tag{6}$$

Let us now assume that $p \in (\frac{4}{3}, 2]$. Considering

$$W_0^{1,p}(\Omega) \hookrightarrow L^4(\Omega),$$

we also get the estimation (6). For this reason, for every $p \in (\frac{4}{3}, 4)$, there exists $r \in \mathbb{R}^+$ satisfying

$$\inf_{\|u\|=r} J(u) > J(0) = 0.$$

Let us now take

$$0 \neq u \in W_0^{1,p}(\Omega) \text{ and } t \in \mathbb{R}.$$

Then, for $p \in (\frac{4}{3}, 4)$,

$$J(tu) = \frac{1}{p} t^p \int_{\Omega} |\nabla u|^p \, dx - \frac{1}{4} t^4 \int_{\Omega} u^4 \, dx \rightarrow -\infty \text{ for } t \rightarrow +\infty.$$

Hence, there exists $e = tu \in W_0^{1,p}(\Omega)$ such that

$$\|e\| > r, \quad J(e) \leq 0 = J(0).$$

It remains to show that J satisfies the Palais-Smale condition. Let (u_n) be the Palais-Smale sequence in $W_0^{1,p}(\Omega)$, i.e. let us assume that

$$c := \sup\{|J(u_n)| : n \in \mathbb{N}\} \in \mathbb{R}, \tag{7}$$

$$J'(u_n) \rightarrow 0. \tag{8}$$

It follows from (7), (8) that, for $n \in \mathbb{N}$ large enough,

$$c + \frac{1}{4} \|u_n\|_{1,p,0} \geq J(u_n) - \frac{1}{4} \langle J'(u_n), u_n \rangle = \left(\frac{1}{p} - \frac{1}{4} \right) \|u_n\|_{1,p,0}^p.$$

For this reason, the sequence (u_n) is bounded. The space $W_0^{1,p}(\Omega)$ is a reflexive Banach space so there exists $u \in W_0^{1,p}(\Omega)$ and a subsequence of (u_n) (labeled the same way) such that

$$u_n \rightharpoonup u.$$

Since

$$0 \leftarrow \langle J'(u_n), u_n - u \rangle = \int_{\Omega} |\nabla u_n|^{p-2} \nabla u_n \nabla (u_n - u) \, dx - \int_{\Omega} u_n^3 (u_n - u) \, dx$$

and the second term approaches 0, we have

$$\int_{\Omega} |\nabla u_n|^{p-2} \nabla u_n \nabla (u_n - u) \, dx \rightarrow 0.$$

It follows from the Hölder’s inequality that

$$0 \leftarrow \int_{\Omega} (|\nabla u_n|^{p-2} \nabla u_n - |\nabla u|^{p-2} \nabla u) \nabla (u_n - u) \, dx \geq \tag{9}$$

$$\geq (\|u_n\|_{1,p,0}^{p-1} - \|u\|_{1,p,0}^{p-1})(\|u_n\|_{1,p,0} - \|u\|_{1,p,0}) \geq 0. \tag{10}$$

which implies

$$\|u_n\|_{1,p,0} \rightarrow \|u\|_{1,p,0}.$$

The uniform convexity of $W_0^{1,p}(\Omega)$ yields $u_n \rightarrow u$. We have shown that J satisfies all assumptions of the Mountain pass theorem. Hence, we have proved the existence of nontrivial solution of the problem (1).

2.1 Numerical experiments

The algorithm we use for the numerical computation is inspired by [4] and assumes J to have the mountain pass geometry. At first, p was chosen between $\frac{4}{3}$ and 2. In the tables 1, 2, we can see the results for the desired precision $\varepsilon = 10^{-2}$. The discretization step in the first table was, due to the limits of the computer, set to $h = \frac{1}{32}$.

Table 1. Results for various p

p	$\ \Delta_p u + u^3\ $	$J(u)$	it
$\frac{3}{2}$	0.070	7.72	712
$\frac{11}{6}$	0.052	20.04	1056
2	0.065	37.74	69
$\frac{7}{3}$	0.020	213.17	148
3	0.044	$3.89 \cdot 10^5$	330

Table 2. Results for various h

	$\ \Delta_p u + u^3\ $			
p	$h = \frac{1}{16}$	$h = \frac{1}{24}$	$h = \frac{1}{32}$	$h = \frac{1}{40}$
$\frac{3}{2}$	0.1165	0.0794	0.0704	0.0363
$\frac{11}{6}$	0.0760	0.0595	0.0529	0.0509
2	0.0597	0.0573	0.0569	0.0564
$\frac{7}{3}$	0.0780	0.0367	0.0216	0.0147
3	0.1126	0.0644	0.0445	0.0339

To approximate the value of $\Delta_p u(x_{ij})$, we use the following formulas:

$$\nabla u(x_{ij}) = \left(\frac{u(x_{(i+1)j}) - u(x_{(i-1)j})}{2h}, \frac{u(x_{i(j+1)}) - u(x_{i(j-1)})}{2h} \right) =: (g_1(x_{ij}), g_2(x_{ij})),$$

$$\Delta_p u(x_{ij}) = |\nabla u(x_{ij})|^{p-2} \left(\frac{g(x_{(i+1)j}) - g(x_{(i-1)j})}{2h} + \frac{g(x_{i(j+1)}) - g(x_{i(j-1)})}{2h} \right).$$

We compute the elements of a vector $\Delta_p u_{ij} + u_{ij}^3$ and we apply the Euclidean norm. The result of the algorithm can be seen in the figure 2.1.

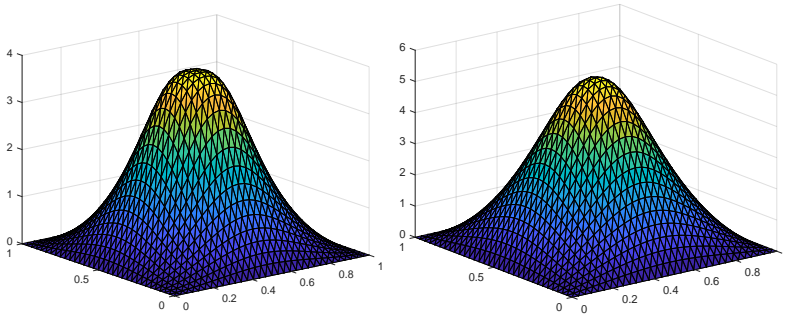


Fig. 1. Solution for $p = \frac{3}{2}$ and $p = \frac{11}{6}$.

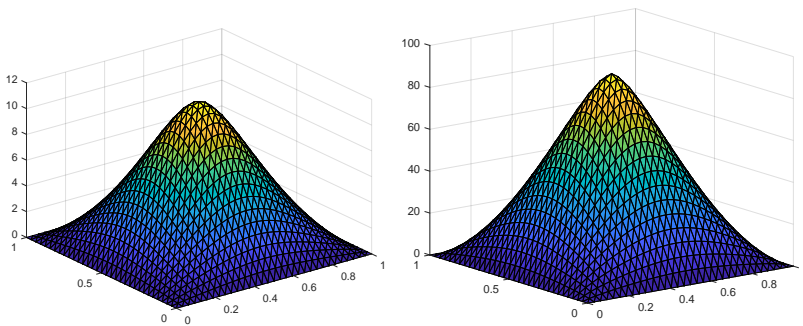


Fig. 2. Solution for $p = \frac{7}{3}$ and $p = 3$.

3 Conclusion

Our research can follow many directions. One possible way is to develop the theory and the algorithm presented in this paper and focus on more general problems with the mountain pass geometry

$$\begin{cases} -\Delta_p u = f(x, u(x)) & \text{in } \Omega, \\ +\text{boundary conditions on } \partial\Omega, \end{cases} \tag{11}$$

where $f : \mathbb{R}^2 \rightarrow \mathbb{R}$ is a function that is nonlinear with respect to u . Another space for research is the algorithm itself. There are many approaches that can be used and combined with respect to the problem. We will also deal with the theoretical background and analysis.

References

1. Y. Jabri, *The Mountain Pass Theorem: Variants, Generalizations and Some Applications*. Encyclopedia of Mathematics and its Applications, Cambridge University Press, 2003.
2. P. H. Rabinowitz, "Minimax methods in critical point theory with applications to differential equations," vol. 65, 01 1986.
3. B. Haim and N. Louis, "Remarks on finding critical points," *Communications on Pure and Applied Mathematics*, vol. 44, pp. 939–963.
4. Z. Ding, D. Costa, and G. Chen, "A high-linking algorithm for sign-changing solutions of semilinear elliptic equations," *Nonlinear Analysis: Theory, Methods and Applications*, vol. 38, no. 2, pp. 151 – 172, 1999.
5. A. Ambrosetti and P. H. Rabinowitz, "Dual variational methods in critical point theory and applications," *Journal of Functional Analysis*, vol. 14, no. 4, pp. 349 – 381, 1973.
6. J. Bisgard, "On mountain pass type algorithms," *Nonlinear Differential Equations and Applications NoDEA*, vol. 20, pp. 1499–1518, Aug 2013.
7. M. Willem, *Minimax theorems*. Boston: Birkhauser, 1996.

Classification problem with multinomial regression and random forests

Michal Běloch

Department of Applied Mathematics, FEECS,
VŠB – Technical University of Ostrava, 17. listopadu 15,
708 33 Ostrava – Poruba, Czech Republic
`michal.beloch@vsb.cz`

Abstract. Classification is the common problem in statistics and machine learning. There exists a variety of methods capable of producing satisfactory results, although usually with different outcome when applied on the same data. Therefore, it is desirable to apply various methods on the same problem and decide which approach is best in given context. Here, two models are confronted, multinomial logistic regression model and random forest model. Both are applied to real data from the Open University.

Keywords: Multinomial logistic regression · decision tree · random forests · classification.

1 Introduction

Prediction of the outcome variable based on the explaining variables can be divided into two groups. If the outcome variable is continuous, we talk about regression. If it is discrete, we perform classification. The underlying idea however, is the same. Based on the input, we want to accurately predict the output. The most problematic part is the model creation. There are lots of methods available, although many of them specialize on a given type of data and even then their acceptable performance is not guaranteed. It is always a good idea to build some number of models and then decide which one is the best to use. Of all the model building techniques, the two following methods continue to provide satisfactory results and also provide sufficient amount of customisation.

2 Multinomial logistic regression

Logistic regression is the member of the generalised linear model family and is performed when the outcome variable is binary. Independent variables can be either binary, or nominal, or continuous. The logit of the regression model is given in the form $g(x) = \beta_0 + \beta_1 x_1 + \dots + \beta_p x_p$ and the regression model is $P(Y = 1|x) = \pi(x) = \frac{e^{g(x)}}{1+e^{g(x)}}$. The unknown parameters $\beta_{0..p}$ are then found

as a minimisation of the likelihood function. More thorough description can be found in [1, 2].

Multinomial logistic regression is generalisation of the logistic regression and is used when the outcome variable is nominal. One level of the outcome variable is chosen as a pivot and then logistic regression is run $K - 1$ times against the pivot level, where K is the number of levels the outcome variable has. This will result in $K - 1$ pivot functions $g_{1..(K-1)}(x)$ and regression models $\pi_{1..(K-1)}(x)$. To obtain the value of the last model $\pi_K(x)$, we simply subtract from one the sum of the $K - 1$ models: $\pi_K(x) = 1 - \sum_{i=1}^{K-1} \pi_i(x)$. Further information can once again be found in [2].

3 Decision trees and random forests

Decision tree is simple and easy to understand method for both the regression and the classification problems. The nodes of the tree represent an attribute, links stand for decision rules and the leaves are outcomes. The tree is created with recursive binary splitting algorithm which chooses the nodes and splits so the cost of the wrong classification is minimal. Widely used is the Giny score: $\sum_i = 1^K p_i * (1 - p_i)$. Detailed description can be found in [3] and [4].

The problems of the decision trees are frequent over fitting and high variance. Possible approach to diminish these shortcomings is to generate a high number of trees and then combine them to obtain more precise results. This is the idea behind random forests. It uses the concept of bootstrap aggregation (or bagging), where random samples with replacement of the training set are selected and a tree is created for each of them.

For the classification purposes, each tree gives the chosen class and the answer of the model is based on a majority vote (or averages the outputs in the case of regression), since all the trees have equal weight. The number of trees in a forest is usually chosen between 100 and 500. All the trees are created from the randomly selected number of independent variables and recommended amount is the square root of the total number of predictors. The final numbers should be as always selected with data set in mind and further adjustment can be made after evaluation of the model. More thorough discussion can be found in [4].

4 Application on data

4.1 Data description

Data set was provided by the Open University, Walton Hall in Milton Keynes. It contains the demographic data and the results of the graded activities the students passed during their study. All the students undertook the same study programme in 2014.

The total number of students is 356. They were then randomly divided into two groups, training group, which contains 249 students, and testing group, which contains 107 students.

The independent variables in the data set are:

- Gender: How the students identify themselves. It has two levels, male, and female.
- Region: Where are the students from. It has 13 levels, East Anglian Region, East Midlands Region, Ireland, London Region, North Region, North Western Region, Scotland, South East Region, South Region, South West Region, Wales, West Midlands Region, and Yorkshire Region.
- Education: Highest attained education, it has 5 levels, no formal quals, lower than A level, A level or equivalent, HE qualification, and post graduate qualification.
- Age band: Age group the students fall into. It has 3 levels, less than 35, between 35 and 55, and more than 55.
- Number of previous attempts: How many times have students tried to complete this course before.
- Disability: Mental or physical shortcomings complicating the study process. Either yes or no.
- TMA1, TMA2, TMA3, TMA4: The results of the graded activities on a scale from 0 to 100.

The outcome or dependant variable is the final result. The students can either pass the course or fail to pass or pass it with honours or withdraw from it. In this particular dataset, none of the students withdrew.

All the models were generated in free statistical software R [5]. Regression model requires package [6], decision tree is from [7], and random forest uses [8].

4.2 Regression model

We start with the regression model. Since the outcome variable has three levels, there will be two logit functions in the form $g_i(x) = \beta_{0,i} + \beta_{1,i}Gender + \beta_{2,i}Region + \beta_{3,i}Education + \beta_{4,i}Age_band + \beta_{5,i}Prev_attempts + \beta_{6,i}Disability + \beta_{7,i}TMA1 + \beta_{8,i}TMA2 + \beta_{9,i}TMA3 + \beta_{10,i}TMA4$, $i \in \{1, 2\}$.

After the model was trained, its predictive capabilities were tested on the testing group and its performance is displayed in the confusion matrix (table 1).

Table 1. Confusion matrix for regression model.

	Predicted value		
Actual value	Failed	Passed	With honours
Failed	2	4	0
Passed	8	66	14
With honours	0	3	10

The misclassification error of this model is 27.1 %. Possible step to improve this model is to perform z-tests for each independent variable and see which one can be omitted. The z-tests were done with 95% confidence and they suggest

that variables gender, number of previous attempts, disability, and TMA2 do not provide statistically significant information to the model, and therefore new model is created without these variables and tested on the training data set. Its performance is shown in the following confusion matrix (table 2).

Table 2. Confusion matrix for refined regression model.

	Predicted value		
Actual value	Failed	Passed	With honours
Failed	2	4	0
Passed	4	70	14
With honours	0	4	9

The misclassification error for this model is 24.3 % making it slightly better than the previous model.

4.3 Tree and forest models

We first create a simple tree to see whether it provides sufficient model. The confusion matrix can be seen in table 3.

Table 3. Confusion matrix for classification tree.

	Predicted value		
Actual value	Failed	Passed	With honours
Failed	2	3	1
Passed	4	70	14
With honours	0	5	8

The misclassification error for this model is 24.4 %, which is basically same as the refined regression model. If we compare both confusion matrices, we can note little difference between them.

Next we create random forest model. This forest has 439 trees. Since it is computationally more demanding, it took few seconds to complete. Confusion matrix is in the table 4. The misclassification error for this model is 13.1 %,

Table 4. Confusion matrix for random forest.

	Predicted value		
Actual value	Failed	Passed	With honours
Failed	2	4	0
Passed	1	85	2
With honours	0	7	6

which is noticeable improvement to all previous models, making this model easily recommendable. But even this model is not without flaws. If we compare confusion matrix of the refined regression model with this one, we can see the random forest model has problems with classifying the group of students that completed the course with honours.

5 Conclusion

For the given dataset, the best performing model is the random forest one. The misclassification error of this model was 11.2 percentage points lower than that of the best regression model. Both the classification tree and regression models were performing similarly. However, indisputable advantage of these two models is that it is easier to describe for someone with little statistical and modelling background.

Acknowledgements.

The work was supported by Grant of SGS No. SP2018/68, VŠB - Technical University of Ostrava, Czech Republic.

References

1. Hosmer, D.W., Lemeshow, S. Applied logistic regression, Wiley (2000), ISBN 0-471-35632-8.
2. Briš, R., Litschmannová, M., STATISTIKA II., E-learningový prvek pro podporu výuky odborných a technických předmětů v rámci projektu CZ.O4.01.3/3.2.15.2/0326, VŠB-TUO, 2007, ISBN 978-80-248-1482-7.
3. Maimon, O., Rokach, L. Data mining and knowledge discovery handbook, Springer 2005, ISBN 978-0-387-24435-8.
4. Williams, G. Data mining with Rattle and R, Springer (2011), ISBN 978-1-4419-9889-7
5. R Core Team (2014). R: A language and environment for statistical computing. R Foundation for Statistical Computing, Vienna, Austria. URL <http://www.R-project.org/>.
6. Venables, W. N. & Ripley, B. D. (2002) Modern Applied Statistics with S. Fourth Edition. Springer, New York. ISBN 0-387-95457-0
7. Torsten Hothorn, Kurt Hornik and Achim Zeileis (2006) Unbiased Recursive Partitioning: A Conditional Inference Framework. *Journal of Computational and Graphical Statistics*, 15(3), 651–674.
8. Liaw, A. and Wiener, M. (2002) Classification and Regression by randomForest. *R News* 2(3), 18–22.

Parareal: From ODE to PDE

Ladislav Foltyn

Department of Applied Mathematics, FEECS,
VŠB – Technical University of Ostrava, 17. listopadu 15,
708 33 Ostrava – Poruba, Czech Republic
ladislav.foltyn@vsb.cz

Abstract. In a paper we present a review of the Parareal method which is used for parallel computing along the time. At first we will recall for a scheme of the Parareal method and after that we will show you some numerical examples, i.e. solving a linear ODE and solving a linear PDE in 1D so semi-discretization technique will be applied.

Keywords: semi-discretization, Parareal, parallel computing, time depended problems, ODE, PDE

1 Introduction

Solving space-time problems in an efficient way is a big challenge in nowadays. There exist a lot of papers, so much works, about solving some spatial problem using a domain decomposition method, for example non-overlapping method, e.g. [1], [2], or overlapping method, e.g. [3], but find an effective solver of time depended problems may be difficult.

In this contribution we will focus on a method called the Parareal. The Parareal method is based on predictor-corrector scheme which is quite simple and may be also used in combination with some domain decomposition method, overlapping one or non-overlapping.

Due to the length of the paper we will only introduce the scheme of the Parareal method as it is introduced in [4] and we will solve one linear ODE problem and one linear PDE problem in 1D. In both cases we will discuss its convergence rate.

2 Scheme of the Parareal method

As we said, the paper is based on the scientific work [4] and we will recall the Parareal scheme as it is presented in the mentioned work above, now.

Consider some linear ordinary differential equation

$$\begin{cases} \frac{dy(t)}{dt} = -a \cdot y(t) , t \in [0; T] , \\ y(0) = y_0 , \end{cases} \quad (1)$$

where a represent a constant, y_0 some initial condition and $T > 0$ is the end time. To solve the problem (1) (and other following problems) we will use an implicit Euler method.

At first we have to define approximate solution Y^n which we obtain by using the implicit Euler method with a coarse time step $\Delta T > 0$

$$\begin{cases} \frac{Y^{n+1} - Y^n}{\Delta T} + a \cdot Y^{n+1} = 0, \\ Y^0 = y_0. \end{cases} \quad (2)$$

Next, we will treat resulting solutions Y^n as an initial conditions for each time subinterval $[T^n; T^{n+1}]$, the length of the subinterval $[T^n; T^{n+1}]$ is correspond to the coarse step ΔT , so we can define n independent problems which we are able to solve in parallel

$$\begin{cases} \frac{dy^n(t)}{dt} = -a \cdot y^n(t), t \in [T^n; T^{n+1}], \\ y^n(T^n) = Y^n. \end{cases} \quad (3)$$

In this step of the algorithm we could use exact solution, if it is known, or we could use the implicit Euler method with a fine step $\delta t > 0$, $\delta t \ll \Delta T$.

In following, we define a loop of the method

1. Compute jumps (the difference between the fine and the coarse solution):

$$J_k^n = y_k^{n-1}(T^n) - Y_k^n.$$

2. Propagate jumps with the coarse step

$$\begin{cases} \frac{q_k^{n+1} - q_k^n}{\Delta T} + a \cdot q_k^{n+1} = \frac{J_k^n}{\Delta T}, \\ q_k^0 = 0. \end{cases} \quad (4)$$

3. Update coarse solution: $Y_{k+1}^n = y_k^{n-1}(T^n) + q_k^n$.

4. Solve problem (exact or with the fine step)

$$\begin{cases} \frac{dy_{k+1}^n(t)}{dt} = -a \cdot y_{k+1}^n(t), t \in [T^n; T^{n+1}], \\ y_{k+1}^n(T^n) = Y_{k+1}^n. \end{cases} \quad (5)$$

And that is all so the scheme of the Parareal method is already known for us and we can move to some numerical experiments.

3 Numerical experiment: ODE

Consider a following linear ODE problem

$$\begin{cases} \frac{dy(t)}{dt} = -y(t), t \in [0; 2], \\ y(0) = 1. \end{cases} \quad (6)$$

We will solve the problem (6) by the Parareal method in two ways. First one will be based on an exact solution because it is known and its expression is

$$y(t) = e^{-t} . \tag{7}$$

Second one will use the implicit Euler method with the fine step.

So what does it mean for us from the point of view of the Parareal scheme that the exact solution is known? We could use the exact solution to solve the problem of each subinterval, i.e. where we have to solve problems (3) and (5) to find values $y^{n-1}(T^n)$. Due to the known exact solution we are able to observe, by the best way, a behavior of the Parareal method. In a Table 1 below we can see a logarithm of an error (a difference of approximate solution to the exact one in euclidean norm) for different coarse steps. Empty cells represent the error equal to zero.

Table 1. Logarithm of the error for exact solution.

k	1	2	3	4	5	6
$\Delta T = 1$	–	–	–	–	–	–
$\Delta T = \frac{1}{2}$	-5.3418	-8.9334	–	–	–	–
$\Delta T = \frac{1}{4}$	-5.5462	-8.8871	-12.6473	-16.8665	-21.6380	-27.2265
$\Delta T = \frac{1}{8}$	-6.2041	-9.9317	-13.9357	-18.2011	-22.7142	-27.4666
$\Delta T = \frac{1}{16}$	-7.0591	-11.3457	-15.8624	-20.5891	-25.5058	-30.5996

Results from the Table 1 above are corresponding to a theoretic one from [4] and it says: There exists a constant $c_k > 0$ that

$$\forall n, 0 \leq n \leq N - 1 : |Y_k^n - y(T^n)| + \max_{t \in [T^n; T^{n+1}]} |y_k^n(t) - y(t)| \leq c_k \Delta T^k . \tag{8}$$

So if we are able to use as many processors as number of subintervals $[T^n; T^{n+1}]$ we will get the solution quite faster than by a sequential one. Keep on mind that the results mentioned above are satisfied only if we know the exact solution. The second approach with the fine step will be analysed, now.

The problems (3) and (5) will be replaced by the implicit Euler method with the fine step δt , $\delta t \ll \Delta T$. We choose, for example, $\delta t = \frac{\Delta T}{128}$. The same linear ODE problem (6) will be solved by this modified scheme.

In a following Table 2 the logarithm of the error of this approach for different coarse steps is shown. The error was computed as the difference of the approximate solution to the exact solution in euclidean norm as it was done in the previous example.

Table 2. Logarithm of the error for the fine step.

k	1	2	3	4	5	6
$\Delta T = 1$	-3.9506	-3.9506	-3.9506	-3.9506	-3.9506	-3.9506
$\Delta T = \frac{1}{2}$	-2.8005	-4.2235	-4.2960	-4.2960	-4.2960	-4.2960
$\Delta T = \frac{1}{4}$	-3.1771	-4.5210	-4.6443	-4.6420	-4.6420	-4.6420
$\Delta T = \frac{1}{8}$	-4.0044	-4.9264	-4.9893	-4.9883	-4.9883	-4.9883
$\Delta T = \frac{1}{16}$	-5.1340	-5.3131	-5.3349	-5.3347	-5.3347	-5.3347

As we could see in the Table 2 above, the convergence rate of this modification is quite fast, too, but don't forget that the resulting error depends on an error of the implicit Euler method for the fine step δt . So, if we need a more precise solution, we have to use smaller step δt . However, from the Table 2 we can also see that the Parareal method is fully functional if use only the approximate solution for each subinterval $[T^n; T^{n+1}]$ so we can move on to an another example in which the linear PDE will be solved.

4 Numerical experiment: PDE

In this section, the Parareal scheme is extended for a linear PDE problem.

Consider following linear PDE problem

$$\begin{cases} c_H \frac{\partial u}{\partial t}(x, t) - \frac{\partial^2 u}{\partial x^2}(x, t) = 0, & \text{for } x \in [0; 1], t \in [0; 2], \\ u(0, t) = u(1, t) = 0, & \text{for } t \in [0; 2], \\ u(x, 0) = u_0(x), & \text{for } x \in [0; 1], \end{cases} \tag{9}$$

where $c_H > 0$ is a given heat capacity constant (in our example $c_H = 100$), $u_0(x)$ represents initial condition and its expression is

$$u_0(x) = \begin{cases} 256x^2(1 - 4x)^2 & \text{for } x \in [0; \frac{1}{4}], \\ 0 & \text{for } x \in (\frac{1}{4}; 1]. \end{cases} \tag{10}$$

We note that the problem (9) is taken from [5]. An analytic solution of the problem (9) is in a form

$$u(x, t) = \sum_{k=1}^{\infty} u_k e^{-\frac{(k\pi)^2 t}{c_H}} \sin k\pi x, \tag{11}$$

$$u_k = 1024 \frac{(192 - k^2 \pi^2) (1 - \cos(\frac{k\pi}{4})) - 24k\pi \sin(\frac{k\pi}{4})}{k^5 \pi^5}$$

so we will be able to compare approximate solution with the analytic one.

To solve the problem (9) we had to derive its variational formulation to find $u(x, t) \in \mathcal{U}$ which satisfy

$$c_H \int_0^1 \frac{\partial u}{\partial t}(x, t)v(x) dx + \int_0^1 \frac{\partial u}{\partial x}(x, t) \frac{\partial v}{\partial x}(x) dx = 0 \quad \forall v(x) \in \mathcal{V}, \quad (12)$$

where \mathcal{U}, \mathcal{V} are appropriate spaces. Important is that we have integrated the problem (9) only over spatial variable so this approach will lead to the semi-discretization technique.

We assume that the approximate solution could be written as

$$u_h(x, t) = \sum_{j=1}^N u^j(t)\varphi_j(x), \quad (13)$$

where N is a dimension of the finite subspace $\mathcal{U}_h \subset \mathcal{U}$ and $\varphi_j(x)$ represents its basis function.

Due to this assumption we obtain a form

$$\sum_{j=1}^N c_H \frac{du^j}{dt}(t) \int_0^1 \varphi_j(x)\varphi_i(x) dx + u^j(t) \int_0^1 \varphi'_j(x)\varphi'_i(x) dx = 0 \quad \forall i = 1, \dots, N. \quad (14)$$

In a matrix form it represents an equation

$$M \cdot \frac{d\bar{u}}{dt} + A \cdot \bar{u} = 0 \quad (15)$$

which we modify for the use of the implicit Euler method

$$\begin{aligned} M \cdot \frac{\bar{u}_{n+1} - \bar{u}_n}{\Delta T} + A \cdot \bar{u}_{n+1} &= 0 \\ (M + \Delta T \cdot A) \cdot \bar{u}_{n+1} &= M \cdot \bar{u}_n. \end{aligned} \quad (16)$$

Table 3. Logarithm of the error of the PDE problem.

k	1	2	3	4	5	6	7	8
$\Delta T = 1$	-	-	-	-	-	-	-	-
$\Delta T = \frac{1}{2}$	0.6941	-1.3185	-	-	-	-	-	-
$\Delta T = \frac{1}{4}$	1.8738	1.0087	-0.2858	-1.9252	-4.1186	-6.8593	-	-
$\Delta T = \frac{1}{8}$	2.5416	2.2283	1.6936	1.0027	0.1338	-0.9079	-2.1333	-3.5492

In following numerical experiment we considered that a step h (spatial discretization) is fixed $h = \frac{1}{64}$. The fine step $\delta t = \frac{\Delta T}{128}$ so we only changed the coarse

step ΔT . In a Table 3 above, the logarithm of the error is shown again. The error was computed as the difference of approximate solution of the Parareal method to the approximate solution of the implicit Euler method in euclidean norm. We chose this difference to compute error due to a fact that the solution depends on the time step δt and also on spatial step h so comparison with the analytic one could be more difficult.

Empty cells of the Table 3 represent no error ($error = 0$). For $\Delta T = \frac{1}{8}$ algorithm stopped for $k = 14$ with the logarithm of the error -16.7501 . For next $k = 15$ was the error equal to zero so we can see that the Parareal scheme really ends with the k which is less than the number of subintervals $[T^n; T^{n+1}]$.

At last, we apologize to reader for a potential mistake in this experiment. Given results were not stable during testing for smaller steps. There was a hidden problem which we could not resolve to the deadline. Also our Parareal scheme for linear PDE doesn't have fast convergence rate as it could have so if you are skilled in this topic, we will be glad for every advice you have.

5 Outlooks

In the future work, we will combine the Parareal method with some domain decomposition method. Maybe a comparison of this approach with e.g. an approach using discontinuous Galerkin method will be done.

References

1. Bouchala, J., Lukáš, D., Malý, L., and Vodstrčil, P.: 2-Dimensional Primal Domain Decomposition Theory in Detail. *Application of Mathematics* (2015), vol. 60, nr. 3, pp. 265-283.
2. Bramble, J. H., Pasciak, J. E. and Schatz, A. H.: The construction of preconditioners for elliptic problems by substructuring. I. *Math. Comp.* **47** (1986), 103-134.
3. Farhat, C., Roux, F.X.: A method of finite element tearing and interconnecting and its parallel solution algorithm, *Internat. J. Numer. Methods Engrg.*, pp. 1205-1227, 32 (1991)
4. Lions, J.-L., Maday, Y. and Turinici, G.: Résolution d'EDP par un schéma en temps «pararéel», *Comptes Rendus de l'Académie des Sciences – Series I – Mathematics*, vol. 332, no. 7, pp. 661–668, Apr. 2001.
5. Steinbach, O.: *Space-time finite element methods for parabolic problems*. Institut für Numerische Mathematik, TU Graz, 2015.

Semi-smooth Newton Method for Solving the Stokes Problem with the Stick-slip Boundary Condition

Radek Kučera¹ and Jan Pacholek²

¹IT4Innovation, VŠB – Technical University of Ostrava, 17. listopadu 15,
708 33 Ostrava – Poruba, Czech Republic

²Department of Applied Mathematics, FEECS,
VŠB – Technical University of Ostrava, 17. listopadu 15,
708 33 Ostrava – Poruba, Czech Republic
jan.pacholek.st@vsb.cz

Abstract. The paper deals with the Stokes flow with the monotonously increasing threshold slip boundary condition. Using the P1-bubble/P1 finite element approximation of the velocity-pressure formulation we arrive at an algebraic variational inequality. This inequality is equivalent to a saddle-point problem whose optimality conditions are the starting point for the algorithm. The semi-smooth Newton method implementation of the algorithm is based on active/inactive sets. We improve on previously suggested options on how to create them. The algorithm is then tested in MATLAB environment. Experiments are done on the "L-shaped" domain, where we study the effects of the adhesive coefficient and preconditioning on the efficiency of computations.

1 Introduction

Let Ω be a bounded domain in \mathbb{R}^2 with a sufficiently smooth boundary $\partial\Omega$ that is split into three nonempty disjoint parts: $\partial\Omega = \bar{\gamma}_D \cup \bar{\gamma}_N \cup \bar{\gamma}_C$. We consider the model of a viscous incompressible Newtonian fluid modelled by the Stokes system with the Dirichlet and Neumann boundary conditions on γ_D and γ_N , respectively, and with the impermeability and the stick-slip boundary condition of the Navier-Tresca type on γ_C :

$$\left. \begin{aligned} -\nu\Delta\mathbf{u} + \nabla p &= \mathbf{f} && \text{in } \Omega, \\ \nabla \cdot \mathbf{u} &= 0 && \text{in } \Omega, \\ \mathbf{u} &= \mathbf{u}_D && \text{on } \gamma_D, \\ \boldsymbol{\sigma} &= \boldsymbol{\sigma}_N && \text{on } \gamma_N, \\ u_n &= 0 && \text{on } \gamma_C, \\ u_t = 0 \Rightarrow |\sigma_t| &\leq g && \text{on } \gamma_C, \\ \sigma_t u_t + g|u_t| + \kappa u_t^2 &= 0 && \text{on } \gamma_C. \end{aligned} \right\} \quad (1)$$

We are searching for a vector function representing the flow velocity field $\mathbf{u} : \bar{\Omega} \rightarrow \mathbb{R}^2$, $\mathbf{u} = (u_1, u_2)$ and a scalar function representing the pressure field $p : \bar{\Omega} \rightarrow \mathbb{R}$,

where $\nu > 0$ is the dynamic viscosity, $\mathbf{f} : \bar{\Omega} \rightarrow \mathbb{R}^2$ describes the forces acting on the fluid, $\mathbf{u}_D : \gamma_D \rightarrow \mathbb{R}^2$ and $\boldsymbol{\sigma}_N : \gamma_N \rightarrow \mathbb{R}^2$ are the Dirichlet and Neumann boundary data, respectively. Further \mathbf{n} and \mathbf{t} are the unit outward normal and tangential vectors on $\partial\Omega$ and we define the normal and tangential component of the velocity and the stress as

$$u_n = \mathbf{u} \cdot \mathbf{n}, u_t = \mathbf{u} \cdot \mathbf{t}, \sigma_n = \boldsymbol{\sigma} \cdot \mathbf{n}, \sigma_t = \boldsymbol{\sigma} \cdot \mathbf{t},$$

where

$$\boldsymbol{\sigma} = \nu \frac{\partial \mathbf{u}}{\partial \mathbf{n}} - p \mathbf{n}, \frac{\partial \mathbf{u}}{\partial \mathbf{n}} = \left(\frac{\partial u_1}{\partial \mathbf{n}}, \frac{\partial u_2}{\partial \mathbf{n}} \right) \quad \text{on } \partial\Omega$$

is the stress vector on $\partial\Omega$. On γ_C we consider the given slip bound $g : \gamma_C \rightarrow \mathbb{R}_+$ and the adhesive coefficient $\kappa : \gamma_C \rightarrow \mathbb{R}_+$ defining the stick-slip boundary condition. We get the classical Navier law for $g = 0$, while $\kappa = 0$ leads to the Tresca law.

The solution of (1) for $\kappa = 0$ has been discussed and solved in [3, 10, 1]. In texts [2] and [9] we can find solutions for $\kappa \neq 0$. Furthermore, in [2] and [7] the interior point method is introduced as one of the methods that may be used in either cases. The other method used to find solution of (1) for $\kappa \neq 0$ is the semi-smooth Newton method [5]. It has been described in [9] and in this text, we will introduce the given algorithm and modify it so that it accepts even $\kappa = 0$.

2 Weak Formulation and Algebraic Problems

The weak formulation of (1) leads to the following variational inequality problem:

$$\left. \begin{aligned} &\text{Find } (\mathbf{u}, p) \in V_{\mathbf{u}_D} \times L^2(\Omega) \text{ so that} \\ &a(\mathbf{u}, \mathbf{v} - \mathbf{u}) + b(p, \mathbf{v} - \mathbf{u}) + j(\mathbf{v}, \mathbf{u}) - j(\mathbf{u}, \mathbf{u}) \geq l(\mathbf{v} - \mathbf{u}) \quad \forall \mathbf{v} \in V_{\mathbf{u}_D} \\ &b(q, \mathbf{u}) = 0 \quad \forall q \in L^2(\Omega), \end{aligned} \right\} \quad (2)$$

where $V_{\mathbf{u}_D} = \{\mathbf{v} \in (H^1(\Omega))^2 : \mathbf{v} = \mathbf{u}_D \text{ on } \gamma_D, \nu_n = 0 \text{ on } \gamma_C\}$ is the velocity set and

$$\begin{aligned} a(\mathbf{w}, \mathbf{v}) &= \nu \int_{\Omega} \nabla \mathbf{w} : \nabla \mathbf{v} dx, & b(q, \mathbf{v}) &= - \int_{\Omega} q(\nabla \cdot \mathbf{v}) dx, \\ l(\mathbf{v}) &= \int_{\Omega} \mathbf{f} \cdot \mathbf{v} dx + \int_{\gamma_N} \boldsymbol{\sigma}_N \cdot \mathbf{v} ds, & j(\mathbf{v}, \mathbf{w}) &= \int_{\gamma_C} g|v_t| + \kappa w_t v_t ds \end{aligned}$$

for $\mathbf{v}, \mathbf{w} \in (H^1(\Omega))^2$ and $q \in L^2(\Omega)$. The solvability of (2) can be proven in a similar way as in [3] for $\kappa = 0$. The symbol \mathbf{u} denoting here the vector function will be used also in the subsequent parts for the algebraic vector representing its finite element counterpart.

We approximate (2) by the mixed finite element method based on the P1-bubble/P1 finite elements [8]. The resulting algebraic problem leads to the

saddle-point formulation which is equivalent to the following optimality conditions:

$$\left. \begin{aligned} &\text{Find } (\mathbf{u}, \mathbf{p}, \mathbf{s}_t, \boldsymbol{\lambda}_n) \in \mathbb{R}^{n_u} \times \mathbb{R}^n \times \mathbb{R}^{n_c} \times \mathbb{R}^{n_c} \text{ such that} \\ &\mathbf{A}\mathbf{u} - \mathbf{l} + \mathbf{T}^T \mathbf{s}_t + \mathbf{N}^T \boldsymbol{\lambda}_n + \mathbf{B}^T \mathbf{p} = \mathbf{0}, \\ &\mathbf{B}\mathbf{u} - \mathbf{E}\mathbf{p} - \mathbf{c} = \mathbf{0}, \\ &\mathbf{N}\mathbf{u} = \mathbf{0} \\ &\left. \begin{aligned} &(\mathbf{T}\mathbf{u})_i = 0 \Rightarrow |s_{ti}| \leq g_i, \\ &(\mathbf{T}\mathbf{u})_i > 0 \Rightarrow s_{ti} = g_i + \kappa_i(\mathbf{T}\mathbf{u})_i, \\ &(\mathbf{T}\mathbf{u})_i < 0 \Rightarrow s_{ti} = -g_i + \kappa_i(\mathbf{T}\mathbf{u})_i, \end{aligned} \right\} i \in \mathcal{N}, \end{aligned} \right\} \quad (3)$$

where $\mathbf{s}_t = \boldsymbol{\lambda}_t + \mathbf{D}(\boldsymbol{\kappa})\mathbf{T}\mathbf{u}$ and $\mathcal{N} = \{1, \dots, n_c\}$. Here, $\mathbf{A} \in \mathbb{R}^{n_u \times n_u}$ is the symmetric, positive definite stiffness matrix for the Laplace operator, $\mathbf{l} \in \mathbb{R}^{n_u}$, $\mathbf{B} \in \mathbb{R}^{n_c \times n_u}$ is the full row rank stiffness matrix for the divergence operator. $\mathbf{T}, \mathbf{N} \in \mathbb{R}^{n_c \times n_u}$ are full row rank matrices given by the normal and tangential vectors at the nodes $\mathbf{x}_i \in \bar{\gamma}_C n \bar{\gamma}_D$, respectively. Further, $\mathbf{D}(\boldsymbol{\kappa}) = \text{diag}(\boldsymbol{\kappa}) \in \mathbb{R}^{n_c \times n_c}$, where $\boldsymbol{\kappa} = (\kappa_1, \dots, \kappa_{n_c})^T \in \mathbb{R}^{n_c}$, $\kappa_i = h_i \kappa(\mathbf{x}_i)$, $g_i = h_i g(\mathbf{x}_i)$, and h_i is the length of the segment connecting \mathbf{x}_i and \mathbf{x}_{i+1} , $i \in \mathcal{N}$; n_u is the number of velocity components, n is the number of the finite elements nodes, and n_c is the number of the stick-slip nodes. The symmetric, positive semidefinite matrix $\mathbf{E} \in \mathbb{R}^{n_c \times n_c}$ and the vector $\mathbf{c} \in \mathbb{R}^{n_c}$ arise from the elimination of the bubble components. The unknowns \mathbf{u}, \mathbf{p} are the vectors of velocity and pressure components, respectively. Finally, $\boldsymbol{\lambda}_t, \boldsymbol{\lambda}_n$ are Lagrange multipliers regularizing the non-differentiability of j from (2) and releasing the impermeability condition, respectively. Note that $\mathbf{s}_t, \boldsymbol{\lambda}_n$ approximate $-\sigma_t, -\sigma_n$ on γ_C , respectively.

3 Application of Semi-smooth Newton Method

The stick-slip law in (3) given by the relation between $(\mathbf{T}\mathbf{u})_i$ and s_{ti} can be represented by piecewise linear function and by using the projection on the interval $[a, b]$ as follows:

$$P_{[a,b]}(x) = x - \max\{0, x - b\} + \max\{0, a - x\}, \quad x \in \mathbb{R}.$$

The stick-slip law in (3) can then be represented by

$$\left. \begin{aligned} &(\mathbf{T}\mathbf{u})_i = \max\{0, \kappa_i^{-1}(s_{ti} - g_i)\} - \max\{0, -\kappa_i^{-1}(s_{ti} + g_i)\}, \\ &\rho(\mathbf{T}\mathbf{u})_i = \max\{0, s_{ti} - g_i + \rho(\mathbf{T}\mathbf{u})_i\} - \max\{0, -s_{ti} - g_i - \rho(\mathbf{T}\mathbf{u})_i\}, \end{aligned} \right\} \quad (4)$$

where $\rho_i = \kappa_i > 0$ in the first equation and $\kappa_i = 0, \rho > 0$ in the second equation in (4).

Problem (3), with the stick-slip condition represented by (4), can be written as one equation:

$$\mathbf{G}(\mathbf{y}) = \mathbf{0} \quad (5)$$

for $\mathbf{G}(\mathbf{y}) = (\mathbf{G}_1^T(\mathbf{y}), \mathbf{G}_2^T(\mathbf{y}), \mathbf{G}_3^T(\mathbf{y}), \mathbf{G}_4^T(\mathbf{y}), \mathbf{G}_5^T(\mathbf{y}))^T$ and $\mathbf{y} = (\mathbf{u}^T, \mathbf{s}_t^T, \boldsymbol{\lambda}_n^T, \mathbf{p}^T)^T$, where $\mathbf{G}_1(\mathbf{y}) = \mathbf{A}\mathbf{u} - \mathbf{l} + \mathbf{T}_+^T \mathbf{s}_{t_+} + \mathbf{T}_0^T \mathbf{s}_{t_0} + \mathbf{N}^T \boldsymbol{\lambda}_n + \mathbf{B}^T \mathbf{p}$, $\mathbf{G}_2(\mathbf{y}) = \mathbf{T}_+ \mathbf{u} - \max\{\mathbf{0}, \mathbf{D}_{\kappa_+}^{-1}(\mathbf{s}_{t_+} - \mathbf{g}_+)\} + \max\{\mathbf{0}, -\mathbf{D}_{\kappa_+}^{-1}(\mathbf{s}_{t_+} + \mathbf{g}_+)\}$, $\mathbf{G}_3(\mathbf{y}) = \rho \mathbf{T}_0 \mathbf{u} - \max\{\mathbf{0}, \mathbf{s}_{t_0} - \mathbf{g}_0 + \rho \mathbf{T}_0 \mathbf{u}\} + \max\{\mathbf{0}, -\mathbf{s}_{t_0} - \mathbf{g}_0 - \rho \mathbf{T}_0 \mathbf{u}\}$, $\mathbf{G}_4(\mathbf{y}) = \mathbf{N}\mathbf{u}$, $\mathbf{G}_5(\mathbf{y}) = \mathbf{B}\mathbf{u} - \mathbf{E}\mathbf{p} - \mathbf{c}$, and $\mathcal{N}_+ = \{i \in \mathcal{N} : \kappa_i > 0\}$, $\mathcal{N}_0 = \{i \in \mathcal{N} : \kappa_i = 0\}$, $\mathbf{T}_+ := \mathbf{T}_{\mathcal{N}_+}$, $\mathbf{T}_0 := \mathbf{T}_{\mathcal{N}_0}$, $\mathbf{s}_{t_+} := \mathbf{s}_{t_{\mathcal{N}_+}}$, $\mathbf{s}_{t_0} := \mathbf{s}_{t_{\mathcal{N}_0}}$, $\mathbf{g}_+ := \mathbf{g}_{t_{\mathcal{N}_+}}$, $\mathbf{g}_0 := \mathbf{g}_{t_{\mathcal{N}_0}}$. We obtain equation (5) that can be solved by a Newton-type method. Due to the presence of max-functions, the Jacobian matrix to \mathbf{G} does not exist at all points so that the classical Newton method cannot be used. On the other hand, \mathbf{G} is semi-smooth in the sense of [5] and, therefore, the semi-smooth Newton method can be used as a solver.

The algorithm generates the sequence $\{\mathbf{y}^k\}$. For each \mathbf{y}^k we define the active/inactive sets:

$$\begin{aligned} \mathcal{I}_{t_+}^+ &= \{i \in \mathcal{N}_+ : s_{t_i}^k - g_i \geq 0\}, & \mathcal{I}_{t_+}^- &= \{i \in \mathcal{N}_+ : s_{t_i}^k + g_i \leq 0\}, \\ \mathcal{I}_{t_0}^+ &= \{i \in \mathcal{N}_0 : s_{t_i}^k - g_i + \rho(\mathbf{T}\mathbf{u})_i \geq 0\}, & \mathcal{I}_{t_0}^- &= \{i \in \mathcal{N}_+ : s_{t_i}^k + g_i + \rho(\mathbf{T}\mathbf{u})_i \leq 0\}, \\ \mathcal{A}_0 &= \mathcal{N}_0 \setminus (\mathcal{I}_{t_0}^+ \cup \mathcal{I}_{t_0}^-), \end{aligned}$$

and the indicator matrices $\mathbf{D}(\mathcal{I}_t^-)$, $\mathbf{D}(\mathcal{I}_t^+)$, respectively. The indicator matrix to $\mathcal{S} \subset \mathcal{N}$ is given by $\mathbf{D}(\mathcal{S}) = \text{diag}(s_1, \dots, s_{n_c}) \in \mathbb{R}^{n_c \times n_c}$ with $s_i = 1$ for $i \in \mathcal{S}$ and $s_i = 0$ if $i \notin \mathcal{S}$. The new iterate \mathbf{y}^{k+1} is computed by solving the following linear system:

$$\left(\begin{array}{c|ccc} \mathbf{A} & \mathbf{T}_+^T & \mathbf{T}_{\mathcal{A}_0}^T & \mathbf{N}^T & \mathbf{B}^T \\ \mathbf{T}_+ & -\mathbf{D}_{\kappa_+}^{-1} \mathbf{D}(\mathcal{I}_{t_+}^+ \cup \mathcal{I}_{t_+}^-) & \mathbf{0} & \mathbf{0} & \mathbf{0} \\ \mathbf{T}_{\mathcal{A}_0} & \mathbf{0} & \mathbf{0} & \mathbf{0} & \mathbf{0} \\ \mathbf{N} & \mathbf{0} & \mathbf{0} & \mathbf{0} & \mathbf{0} \\ \mathbf{B} & \mathbf{0} & \mathbf{0} & \mathbf{0} & -\mathbf{E} \end{array} \right) \begin{pmatrix} \mathbf{u}^{k+1} \\ \mathbf{s}_{t_+}^{k+1} \\ \mathbf{s}_{t_{\mathcal{A}_0}}^{k+1} \\ \boldsymbol{\lambda}_n^{k+1} \\ \mathbf{p}^{k+1} \end{pmatrix} = \begin{pmatrix} \tilde{\mathbf{b}} \\ \tilde{\mathbf{g}} \\ \mathbf{0} \\ \mathbf{0} \\ \mathbf{c} \end{pmatrix}, \quad (6)$$

where $\tilde{\mathbf{b}} = \mathbf{b} - \mathbf{T}_{\mathcal{I}_{t_0}^+}^T \mathbf{g}_{\mathcal{I}_{t_0}^+} + \mathbf{T}_{\mathcal{I}_{t_0}^-}^T \mathbf{g}_{\mathcal{I}_{t_0}^-}$ and $\tilde{\mathbf{g}} = \mathbf{D}_{\kappa_+}^{-1}(\mathbf{D}(\mathcal{I}_{t_+}^-) - \mathbf{D}(\mathcal{I}_{t_+}^+))\mathbf{g}_+$.

As it is unrealistic to find the exact solution of large linear algebraic systems, we use the Schur complement system to solve (6):

$$\mathbf{S}^k \mathbf{r}^{k+1} = \mathbf{C}\mathbf{A}^{-1}\tilde{\mathbf{b}} - \mathbf{h}^k,$$

with $\mathbf{S}^k = \mathbf{C}\mathbf{A}^{-1}\mathbf{C}^T + \mathbf{D}^k$, where

$$\mathbf{C} = (\mathbf{T}_+^T, \mathbf{T}_{\mathcal{A}_0}^T, \mathbf{N}^T, \mathbf{B}^T)^T, \quad \mathbf{D}^k = \text{diag}(\mathbf{D}_{\kappa_+}^{-1} \mathbf{D}(\mathcal{I}_{t_+}^+ \cup \mathcal{I}_{t_+}^-), \mathbf{0}, \mathbf{0}, \mathbf{E}).$$

and

$$\mathbf{r}^{k+1} = \begin{pmatrix} \mathbf{s}_{t_+}^{k+1} \\ \mathbf{s}_{t_{\mathcal{A}_0}}^{k+1} \\ \boldsymbol{\lambda}_n^{k+1} \\ \mathbf{p}^{k+1} \end{pmatrix}, \quad \mathbf{h}^k = \begin{pmatrix} \tilde{\mathbf{g}} \\ \mathbf{0} \\ \mathbf{0} \\ \mathbf{c} \end{pmatrix}.$$

We use the conjugate gradient method with an adaptive precision control and the diagonal preconditioner

$$\mathbf{P}^k = \text{diag } \mathbf{S}^k.$$

One can prove [9, 6] that the spectral condition number of $(\mathbf{P}^k)^{-1}\mathbf{S}^k$ does not depend on the block $\mathbf{D}(\boldsymbol{\kappa})^{-1}$, which is ill-conditioned if κ or h_i are too small.

4 Numerical experiments

We consider the L-shaped domain $\Omega = (0, 5) \times (0, 2) \setminus \bar{\mathcal{S}}$, $\mathcal{S} = (0, 1) \times (0, 1)$ with $\nu = 1$ and $\mathbf{f} = \mathbf{0}$; $\gamma_D = \gamma_{top} \cup \gamma_{left}$ with $\gamma_{top} = (0, 5) \times \{2\}$, $\gamma_{left} = \{0\} \times (1, 2)$, $\mathbf{u}_D|_{\gamma_{top}} = \mathbf{0}$, and $\mathbf{u}_D|_{\gamma_{left}} = (4(x_2 - 2)(1 - x_2), 0)$; $\gamma_N = \{5\} \times (0, 2)$ with $\boldsymbol{\sigma}_N = \mathbf{0}$; $\gamma_C = \partial\Omega \setminus (\gamma_D \cup \gamma_N)$ with $g = 1$. In tables below we present $iter/n_S$, where $iter$ is the number of the Newton iterations and n_S is the total number of the matrix-vector multiplications by the Schur complements. In other words, n_S determines the computational efficiency.

Table 1. The computational complexity for different $\kappa \geq 0$ without preconditioning.

$n_u/n_p/n_c$	$\kappa = 1$	$\kappa = 0.5$	$\kappa = 0.1$	$\kappa = 0.01$	$\kappa = 0.001$	$\kappa = 0$
344/206/32	9/1377	9/1467	10/2001	11/2770	11/2837	12/1054
1352/744/64	10/3698	10/4210	11/6850	11/7429	12/9523	12/1686
5366/2819/128	9/6305	10/9021	10/1161	11/16596	13/27768	15/3942
21386/10965/256	10/14848	10/16680	11/29878	12/38700	*	10/5386
85394/43241/512	10/21789	10/27256	11/41416	*	*	*

Table 2. The computational complexity for different $\kappa \geq 0$ with preconditioning

$n_u/n_p/n_c$	$\kappa = 1$	$\kappa = 0.5$	$\kappa = 0.1$	$\kappa = 0.01$	$\kappa = 0.001$	$\kappa = 0$
344/206/32	8/146	8/153	9/159	10/164	10/149	8/150
1352/744/64	8/199	9/222	10/256	10/205	11/223	8/168
5366/2819/128	9/269	10/319	10/298	11/304	12/326	8/207
21386/10965/256	9/342	8/247	10/340	11/398	12/404	8/290
85394/43241/512	9/353	9/346	9/349	11/522	12/509	9/477

Table 3. The computational complexity for different $\kappa \geq 0$ for interior point method

$n_u/n_p/n_c$	$\kappa = 1$	$\kappa = 0.5$	$\kappa = 0.1$	$\kappa = 0.01$	$\kappa = 0.001$	$\kappa = 0$
344/206/32	18/344	18/357	19/367	18/382	19/381	19/410
1352/744/64	20/491	20/455	20/480	20/492	20/471	20/483
5366/2819/128	18/454	19/505	19/473	19/487	19/483	19/507
21386/10965/256	19/581	20/625	19/561	19/579	19/560	19/561
85394/43241/512	19/733	19/733	19/769	19/743	19/691	19/677

It is easy to observe from Table 1 and Table 2 that n_S increases considerably for finer meshes and smaller κ , and that this effect is eliminated by the preconditioning. Table 3 is then displayed for the computational efficiency of interior point method, which, in comparison with the semi-smooth Newton method, requires more matrix-vector multiplications.

Conclusion

Summarizing and using the results from [9], we successfully modified the algorithm to accept $\kappa = 0$ as well, increasing its potential use. Furthermore, we have shown that the preconditioning has an important impact on the computational efficiency and that without it, it is impossible to solve larger linear systems.

References

1. M. Ayadi, L. Baffico, M. K. Gdoura, T. Sassi, *Error estimates for Stokes problem with Tresca friction conditions*, ESAIM: Mathematical Modelling and Numerical Analysis, **48**, 1413 - 1429 (2014).
2. J. K. Djoko, M. Mbehou, *Finite element analysis for Stokes and Navier Stokes equations driven by threshold slip boundary conditions*, Int. J. Numer. Anal. Model., Series B, **4**, 235-255 (2013).
3. H. Fujita, *A mathematical analysis of motions of viscous incompressible fluid under leak and slip boundary conditions*, RIMS Kokyuroku, **888**, 199-216 (1994).
4. J. Haslinger, R. Kučera, and V. Štek, *Stokes system with selection-dependant threshold slip boundary conditions: Analysis, approximation and implementation*, accepted in Mathematics and Mechanics of Solids (2017).
5. H. Hintermüller, K. Ito, K. Kunisch, *The primal-dual active set strategy as a semi-smooth Newton method*, SIAM J. Optim., **13**, 865-888 (2003).
6. R. Kučera, J. Machalov, H. Netuka, P. Ženčák, *An interior point algorithm for the minimization arising from 3d contact problems with friction*, Optimization Methods and Software **28**, 1195-1217 (2013).
7. R. Kučera, J. Haslinger, V. Štek, M. Jaroš, *Efficient methods for solving the Stokes problem with slip boundary conditions*, accepted in Mathematics and Computers in Simulation (2017), <https://doi.org/10.1016/j.matcom.2016.05.012>.
8. J. Koko, *Vectorized Matlab codes for the Stokes problem with P1-bubble/P1 finite element*, at: <https://www.isima.fr/~jkoko/Codes/StokesP1BubbleP1.pdf>.
9. J. Pacholek, *Semi-smooth Newton method for solving the Stokes equations with monotonously increasing slip condition*, Diploma thesis, VŠB-TU Ostrava (2017).
10. I. Rao, K. Rajagopal, *The effect of the slip boundary conditions on the flow of fluids in a channel*, Acta Mechanica **135**, 113-126 (1999).

Publications

Kučera, R., Pacholek J.: Semi-smooth Newton method for solving the Stokes problem with the stick slip boundary condition. In series: Modern Mathematical Methods in Engineering, Ostrava, 2018, VŠB-Technical University of Ostrava, 135-142

Parallel Runge-Kutta method in nonadiabatic molecular dynamics

Stanislav Paláček

Department of Applied Mathematics, FEECS,
VŠB – Technical University of Ostrava, 17. listopadu 15,
708 33 Ostrava – Poruba, Czech Republic
stanislav.palacek@vsb.cz

Abstract. Semiclassical nonadiabatic molecular dynamics have shown to be computationally very demanding for calculations of more complicated systems. Example of such a system is $CH_4 + O^+$. This reaction is significant in atmosphere of Saturn’s moon Titan as has been shown by Cassini-Huygens mission. Main computational difficulty is given by ab-initio calculations which are needed for obtaining gradients of potential energy surfaces (PES) which give forces acting between particles, transition dipole moments causing radiative transitions between states of system and nonadiabatic couplings causing nonradiative transitions. For semiclassical nonadiabatic molecular dynamics calculations have been developing a package of programs called lib4nodyn. Core program of this package which performs numerical integration of equations of motions is called MULTIDYN. For numerical integration of equations of motion several Runge-Kutta methods and several multistep methods have been implemented. For acceleration of calculations parallel implementations of fourth-order Runge-Kutta method have been proposed.

1 Equations of motion

Lets have a system of atoms. In this paper coordinates of electrons will be denoted by \mathbf{r} and coordinates of atomic nucleus by \mathbf{R} . The total quantum mechanical Hamiltonian of a system can be then written as [1]

$$\begin{aligned}\mathcal{H} &= -\frac{\hbar^2}{2} \sum_{\alpha} M_{\alpha}^{-1} \nabla_{R_{\alpha}}^2 - \frac{\hbar^2}{2} \sum_{\beta} m_{\beta}^{-1} \nabla_{r_{\beta}}^2 + V_{rR}(\mathbf{r}, \mathbf{R}) \\ &= -\frac{\hbar^2}{2} \sum_{\alpha} M_{\alpha}^{-1} \nabla_{R_{\alpha}}^2 + \mathcal{H}_r(\mathbf{r}, \mathbf{R}).\end{aligned}\tag{1}$$

M_{α} denotes mass of atomic nucleus α and m_{β} is mass of electron β . Term $V_{rR}(\mathbf{r}, \mathbf{R})$ is a potential energy and include all interparticle interactions, i. e. electron-electron repulsion, nucleus-nucleus repulsion, nucleus-electron attraction, spin-orbit interactions, etc. $\mathcal{H}_r(\mathbf{r}, \mathbf{R})$ is electronic Hamiltonian, i.e. Hamiltonian that governs the motion of electrons when nuclei are at fixed positions \mathbf{R} .

Separation of Hamiltonian into electronic and nucleus parts is called Born-Oppenheimer approximation. In semiclassical approximation atomic nuclei can

be treated classically and are described by a classical Hamilton equations of motion

$$\begin{aligned}\frac{d\mathbf{P}_\alpha}{dt} &= -\frac{\partial H_R}{\partial \mathbf{R}_\alpha} = \mathbf{F}_\alpha, \\ \frac{d\mathbf{R}_\alpha}{dt} &= \frac{\partial H_R}{\partial \mathbf{P}_\alpha} = \frac{\mathbf{P}_\alpha}{M_\alpha}.\end{aligned}\quad (2)$$

\mathbf{P}_α denotes momentum of atom (nucleus) α , H_R is Hamilton function for classical system of atoms, \mathbf{F}_α is force acting on atom α . Electrons are described by time dependent Schrödinger equation

$$\mathcal{H}_r(\mathbf{r}, \mathbf{R}(\mathbf{t}))\phi(\mathbf{r}, t) = i\hbar \frac{\partial}{\partial t} \phi(\mathbf{r}, t). \quad (3)$$

Where $\phi(\mathbf{r}, t)$ is electronic wave function. To solve equation (3) it is convenient to choose appropriate basis functions $\phi_j(\mathbf{r}, \mathbf{R})$. The most used functions are adiabatic and diabatic basis functions. In general, functions $\phi_j(\mathbf{r}, \mathbf{R})$ are orthonormal with respect to integration over coordinate space of electrons

$$\int \phi_i(\mathbf{r}, \mathbf{R})\phi_j(\mathbf{r}, \mathbf{R})d\mathbf{r} = \delta_{ij}, \quad (4)$$

where δ_{ij} is the Kronecker delta function. There are also defined the following matrix elements:

$$H_{ij} = \int \phi_i(\mathbf{r}, \mathbf{R})\mathcal{H}_r(\mathbf{r}, \mathbf{R})\phi_j(\mathbf{r}, \mathbf{R})d\mathbf{r} = H_{ji}(\mathbf{R}), \quad (5)$$

$$\mathbf{d}_{ij}^\alpha(\mathbf{R}) = \int \{\phi_i(\mathbf{r}, \mathbf{R})[\nabla_{R_\alpha} \phi_j(\mathbf{r}, \mathbf{R})]\}d\mathbf{r}, \quad (6)$$

$$D_{ij}^\alpha(\mathbf{R}) = - \int \{\phi_i(\mathbf{r}, \mathbf{R})[\nabla_{R_\alpha}^2 \phi_j(\mathbf{r}, \mathbf{R})]\}d\mathbf{r}. \quad (7)$$

Each of these matrix elements depends on the coordinates of atomic nuclei \mathbf{R} . $\mathbf{d}_{ij}(\mathbf{R})$ and $D_{ij}(\mathbf{R})$ are called nonadiabatic coupling vector and nonadiabatic coupling elements or first and second derivative couplings, respectively.

In this paper let $\phi_j(\mathbf{r}, \mathbf{R})$ denote adiabatic, sometimes called Born-Oppenheimer, basis functions. Electronic wave function can be then written as

$$\phi(\mathbf{r}, t) = \sum_j c_j(t)\phi_j(\mathbf{r}, \mathbf{R}). \quad (8)$$

Where c_j denotes adiabatic amplitude of state j and $|c_j|^2$ gives probability of finding system in adiabatic state j . The adiabatic wave functions are defined as eigenfunctions of $\mathcal{H}(\mathbf{r}, \mathbf{R})$ for given positions \mathbf{R} of nuclei

$$\mathcal{H}(\mathbf{r}, \mathbf{R})\phi_j(\mathbf{r}, \mathbf{R}) = \varepsilon_j(\mathbf{R})\phi_j(\mathbf{r}, \mathbf{R}), \quad (9)$$

where $\varepsilon_j(\mathbf{R})$ is a potential energy surface of adiabatic state j . This equation is also known as stationary Schrödinger equation.

If expansion 8 of electronic wave function is inserted into Schrödinger equation of motion for electrons 3, multiplied from left by $\phi_i(\mathbf{r}, \mathbf{R})$ and integrated over the space of electrons coordinates \mathbf{r} , the following equations is obtained

$$\dot{c}_j = -\frac{i}{\hbar}\varepsilon_j c_j - \sum_{i\alpha} c_i \dot{\mathbf{R}}_\alpha \mathbf{d}_{ji}^\alpha(\mathbf{R}). \quad (10)$$

Forces which act on atoms can be obtained using Hellmann-Feynman [2] theorem

$$\mathbf{F}_\alpha = -\langle \phi | \nabla_\alpha \mathcal{H}_r | \phi \rangle, \quad (11)$$

which gives

$$\mathbf{F}_\alpha = -\sum_i |c_i|^2 \nabla_\alpha \varepsilon_i + \sum_{i \neq j} c_i^* c_j (\varepsilon_j - \varepsilon_i) \mathbf{d}_{ji}^\alpha. \quad (12)$$

The first term in equation (12) is weighted average of forces of all adiabatic states and the second term takes into account quantum forces resulting from nonadiabatic transitions in the electronic subsystem.

2 Numerical solution of equations of motion

To calculate time evolution of atomic system it is needed to numerically integrate system of differential equations

$$\begin{aligned} \frac{d\mathbf{P}_\alpha}{dt} &= \mathbf{F}_\alpha, \\ \frac{d\mathbf{R}_\alpha}{dt} &= \frac{\mathbf{P}_\alpha}{M_\alpha}, \\ \dot{c}_i &= -\frac{i}{\hbar}\varepsilon_i c_i - \sum_j D_{ij} c_j, \\ \mathbf{F}_\alpha &= -\sum_i |c_i|^2 \nabla_\alpha \varepsilon_i + \sum_{i \neq j} c_i^* c_j (\varepsilon_j - \varepsilon_i) \mathbf{d}_{ji}^\alpha, \end{aligned} \quad (13)$$

with initial conditions giving geometric arrangements and momenta of atoms at the beginning. For every integration step regardless of the integration method used there is need to solve several times, in dependence on the order of used method, stationary Schrödinger equation (9) to obtain energy gradients and nonadiabatic couplings. These calculations are computationally very demanding. To minimize computational time it would be desirable to parallelize, for every integration step, these demanding calculations.

2.1 Parallel fourth-order Runge-Kutta method

Let's have ordinary differential equation with initial condition

$$\frac{d\mathbf{y}}{dt} = \mathbf{f}(t, \mathbf{y}); \quad \mathbf{y}(t_0) = \mathbf{y}_0 \quad (14)$$

This equation can be numerically solved by Runge-Kutta methods among which fourth order methods are most frequently used as a trade-off between computational demands and accuracy, [4,3]

$$\begin{aligned} \mathbf{y}_{n+1} &= \mathbf{y}_n + \frac{h}{6}(\mathbf{k}_1 + 2\mathbf{k}_2 + 2\mathbf{k}_3 + \mathbf{k}_4) \\ \mathbf{k}_1 &= \mathbf{f}(t_n, \mathbf{y}_n) \\ \mathbf{k}_2 &= \mathbf{f}\left(t_n + \frac{h}{2}, \mathbf{y}_n + \frac{h}{2}\mathbf{k}_1\right) \\ \mathbf{k}_3 &= \mathbf{f}\left(t_n + \frac{h}{2}, \mathbf{y}_n + \frac{h}{2}\mathbf{k}_2\right) \\ \mathbf{k}_4 &= \mathbf{f}(t_n + h, \mathbf{y}_n + h\mathbf{k}_3). \end{aligned} \quad (15)$$

To parallelize this method we need to calculate all the k 's at the same time. Prototype of such parallel method can be proposed so that new K 's are calculated from K 's calculated in previous step [3]

$$\begin{aligned} \mathbf{y}_{n+1} &= \mathbf{y}_n + \frac{1}{6}(\mathbf{K}_{1,n} + 2\mathbf{K}_{2,n} + 2\mathbf{K}_{3,n} + \mathbf{K}_{4,n}) \\ \mathbf{K}_{1,n} &= h\mathbf{f}(t_n, \mathbf{y}_n) \\ \mathbf{K}_{2,n} &= h\mathbf{f}\left(t_n + \frac{h}{2}, \mathbf{y}_n + \frac{1}{2} \sum_{j=1}^4 b_{2j}\mathbf{K}_{j,n-1}\right) \\ \mathbf{K}_{3,n} &= h\mathbf{f}\left(t_n + \frac{h}{2}, \mathbf{y}_n + \frac{1}{2} \sum_{j=1}^4 b_{3j}\mathbf{K}_{j,n-1}\right) \\ \mathbf{K}_{4,n} &= h\mathbf{f}\left(t_n + h, \mathbf{y}_n + \sum_{j=1}^4 b_{4j}\mathbf{K}_{j,n-1}\right). \end{aligned} \quad (16)$$

It can be shown, that if function \mathbf{f} is Lipschitz continuous with respect to \mathbf{y} , then also $\mathbf{K}_{i,n}$, $i = 1, 2, 3, 4$ are Lipschitz continuous. [3] Therefore the proposed method is convergent. Coefficients $\mathbf{K}_{i,n}$ can be written in the form

$$\mathbf{K}_i(t_n, h) = h\mathbf{f}(\mathbf{y}(t_n) + c_i \sum_{j=1}^4 b_{ij}\mathbf{K}_j(t_n - h, h)); \quad i = 1, 2, 3, \quad (17)$$

and can be expanded in Taylor series around $h = 0$:

$$\begin{aligned} \mathbf{K}_i(t_n, h) = & h\mathbf{y}^{(1)} + h^2 p_i \mathbf{y}^{(2)} + h^3 \left[q_i \mathbf{f}_y \mathbf{y}^{(2)} + \frac{1}{2} p_i^2 f_{yy}(\mathbf{y}^{(1)})^2 \right] + \\ & h^4 \left[\frac{1}{6} p_i^3 \mathbf{f}_{yyy}(\mathbf{y}^{(1)})^3 + p_i q_i \mathbf{f} \mathbf{f}_y \mathbf{y}^{(1)} + \left(\frac{1}{2} \sum_{j=1}^4 b_{ij} p_j^2 - q_i - \frac{1}{2} p_i \right) \mathbf{f}_y \mathbf{f}_{yy}(\mathbf{y}^{(1)})^2 + \right. \\ & \left. \left(\sum_{j=1}^4 b_{ij} q_j - q_i - \frac{1}{2} p_i \right) \mathbf{f}_y \mathbf{f}_y \mathbf{f}_y \mathbf{y}^{(1)} \right] + O(h^5) \end{aligned} \quad (18)$$

$$p_i = \begin{cases} \frac{1}{2} \sum_{j=1}^4 b_{ij}, & i = 2, 3 \\ \sum_{j=1}^4 b_{ij}, & i = 4 \end{cases}, q_i = \begin{cases} \frac{1}{2} \sum_{j=1}^4 b_{ij} (p_j - 1), & i = 2, 3 \\ \sum_{j=1}^4 b_{ij} (p_j - 1), & i = 4 \end{cases}$$

$$p_1 = q_1 = 0; b_{11} = b_{12} = b_{13} = b_{14} = 0$$

A Taylor expansion can be also performed for $\mathbf{y}(t_{n+1}) = \mathbf{y}(t_n + h)$:

$$\mathbf{y}(t_{n+1}) = \mathbf{y}(t_n) + h\mathbf{y}^{(1)} + \frac{h^2}{2}\mathbf{y}^{(2)} + \frac{h^3}{6}\mathbf{y}^{(3)} + \frac{h^4}{24}\mathbf{y}^{(4)} + O(h^5) \quad (19)$$

On the other hand

$$\mathbf{y}(t_{n+1}) = \mathbf{y}(t_n) + \frac{1}{6}[\mathbf{K}_1(t, h) + 2\mathbf{K}_2(t, h) + 2\mathbf{K}_3(t, h) + \mathbf{K}_4(t, h)] \quad (20)$$

By substitution of expansions for $\mathbf{K}_i(t, h)$ (18) into equation (20) and by equating terms of the same order in last two equations a complicated system of equations will be obtained for coefficients of parallel fourth order Runge-Kutta method. One of possible solutions gives the following parallel method:

$$\begin{aligned} \mathbf{y}_{n+1} = & \mathbf{y}_n + \frac{1}{6}(\mathbf{K}_{1,n} + 2\mathbf{K}_{2,n} + 2\mathbf{K}_{3,n} + \mathbf{K}_{4,n}) \\ \mathbf{K}_{1,n} = & hf(t_n, \mathbf{y}_n) \\ \mathbf{K}_{2,n} = & hf(t_n + \frac{h}{2}, \mathbf{y}_n - \frac{3}{4}\mathbf{K}_{1,n-1} + \frac{1}{2}\mathbf{K}_{2,n-1} + \frac{3}{4}\mathbf{K}_{4,n-1}) \\ \mathbf{K}_{3,n} = & hf(t_n + \frac{h}{2}, \mathbf{y}_n - \mathbf{K}_{1,n-1} + 2\mathbf{K}_{2,n-1} - \frac{1}{2}\mathbf{K}_{3,n-1}) \\ \mathbf{K}_{4,n} = & hf(t_n + h, \mathbf{y}_n + \frac{1}{2}\mathbf{K}_{1,n-1} + \frac{1}{2}\mathbf{K}_{4,n-1}) \end{aligned} \quad (21)$$

3 Results

For testing of parallel method several calculations of $CH_4 + He$ system were performed with same initial conditions. Calculations were run in adiabatic regime

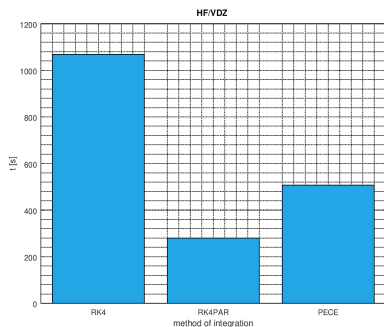


Fig. 1. Comparison calculation times of nonparallel fourth order Runge-Kutta, parallel fourth-order Runge-Kutta and multistep methods.

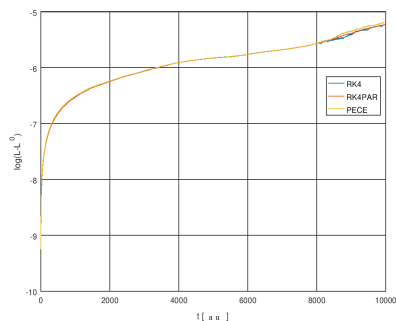


Fig. 2. Comparison conservation of angular momentum for nonparallel fourth order Runge-Kutta, parallel fourth-order Runge-Kutta and multistep methods.

in electronic ground state. For ab initio calculations program MOLPRO were used with Hartree-Fock method and AVDZ basis. Numerical integration was performed by classical fourth-order Runge-Kutta method, parallel fourth-order Runge-Kutta method and a linear multi-step method [4] of Adams type with a Crane-Klopfenstein predictor. This multistep method were used in prediction, evaluation, correction, evaluation (PECE) regime. Integration step was set to 2 atomic units with the total integration time equal to 10000 atomic units. In a figure 1 comparison of calculation times for those three integration methods can be seen, the parallel Runge-Kutta method requiring approximately one fourth of running time of the non-parallel Runge-Kutta method. For comparison of accuracy the logarithmic dependence of the difference of angular momentum in time t and angular momentum in time $t = 0$ on time is shown on figure 2. As we can see a deviation from conservation of angular momentum have for all three integration methods approximately same order.

References

1. *Modern Methods for multidimensional Dynamics Computations in Chemistry*, J.C. Tully, *Nonadiabatic Dynamics*, 1998, World Scientific
2. *Quantum Simulations of Complex Many-Body Systems: From Theory to Algorithms*, N.L. Doltsinis, *Nonadiabatic Dynamics: Mean-Field and Surface Hopping*, 2002, 1st ed. Jülich: NIC-Secretariat
3. Liu C., Wu H., Feng L., Yang A. (2011) Parallel Fourth-Order Runge-Kutta Method to Solve Differential Equations. In: Liu B., Chai C. (eds) *Information Computing and Applications*. ICICA 2011. Lecture Notes in Computer Science, vol 7030. Springer, Berlin, Heidelberg
4. E. Vitásek, *Numerické metody*, PRAHA 1987, SNTL
5. J. Formánek, *Úvod do kvantové teorie*, Academia, Praha 2004
6. J. Chem. Phys. 43 (1965) 3259, Karpulus et al.

New upper bounds for the orders of (k, g) -graphs

Tom Raiman

Department of Applied Mathematics, FEECS,
VŠB – Technical University of Ostrava, 17. listopadu 15,
708 33 Ostrava – Poruba, Czech Republic
`tom.raiman.st@vsb.cz`

Abstract. A (k, g) -graph is a graph with regularity k and girth g . We present new upper bounds for the orders of (k, g) -graphs, which were derived from conditions for adding vertices to the (k, g) -graphs, while preserving the degree and girth. We compare our bounds to the Sauer's bound. Sauer bound is currently the best known general upper bound for the orders (k, g) -graphs. This bound is constructive and it is known that there exists a (k, g) -graph of any admissible order greater than or equal to this bound.

Keywords: cage, k -regular graphs, girth, Sauer bound

1 Introduction

A (k, g) -graph is a k -regular graph of girth g . A (k, g) -cage is a smallest (k, g) -graph; its order is denoted by $n(k, g)$.

The question of existence of (k, g) -graphs for any pair k and g has been resolved in 1960's [4], [1]. However, the orders $n(k, g)$ of (k, g) -cages have been only determined for small sets of parameter pairs [2].

The Moore bound gives a natural lower bound for the orders of (k, g) -graphs (and therefore also for the order $n(k, g)$ of the (k, g) -cages).

$$n(k, g) \geq M(k, g) = \begin{cases} \frac{k(k-1)^{(g-1)/2}-2}{k-2}, & \text{if } g \text{ is odd,} \\ \frac{2(k-1)^{g/2}-2}{k-2}, & \text{if } g \text{ is even.} \end{cases} \quad (1)$$

It is known that the orders of the majority of cages exceed the value $M(k, g)$. Graphs for which $n(k, g) = M(k, g)$ are called Moore graphs. Full survey of the cage problem can be found in [2].

In the 1960's, Erdős and Sachs introduced an upper bound for the order of (k, g) -graphs. Their bound was later improved by Sauer. We will denote Sauer's bound by $S(k, g)$ [5], [2]:

$$n(3, g) \leq S(3, g) = \begin{cases} \frac{4}{3} + \frac{29}{12}2^{g-2}, & \text{if } g \text{ is odd,} \\ \frac{2}{3} + \frac{29}{12}2^{g-2}, & \text{if } g \text{ is even.} \end{cases} \quad (2)$$

For $k \geq 4$

$$n(k, g) \leq S(k, g) = \begin{cases} 2(k-1)^{g-2}, & \text{if } g \text{ is odd,} \\ 4(k-1)^{g-3}, & \text{if } g \text{ is even.} \end{cases} \tag{3}$$

We will call (k, g) -graphs of order at least $S(k, g)$ Sauer graphs. The significance of these bounds lies in the fact that from the bound onward there exists a (k, g) -graph of any order greater than or equal to the Sauer bound.

At the conclusion of paper [3] we stated that it would be interesting to find the lower bounds of the orders of (k, g) -graphs for the use of the theorems from [3]. In this paper, we will address this problem and find the number of edges sufficient for the use of the theorems from [3]. We will show this on the example of the Petersen graph. We proved that a $(3, 5)$ -graph of order n exists for every even order greater than or equal to 10. Fig. 1 illustrates the first steps of a series of recursive constructions of larger graphs from smaller graphs as described in [3].

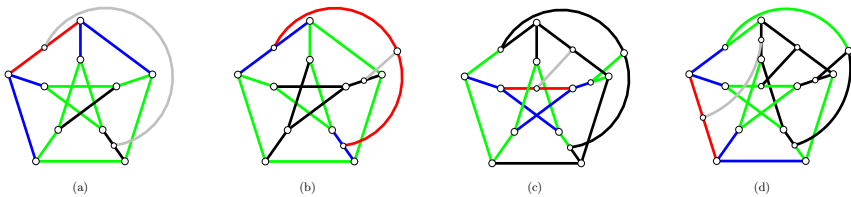


Fig. 1. Adding vertices to Petersen graph, where red edge is the initial edge, blue edges are edges at distance 0, green edges are at distance 1, black edges are at distance 2 and the grey edge is the added edge; (a) $(3, 5)$ -graph of order 12, (b) $(3, 5)$ -graph of order 14, (c) $(3, 5)$ -graph of order 16, (d) $(3, 5)$ -graph of order 18

In [3], it is also stated that the method described in Theorem 1 does not work for Heawood graph (the $(3, 6)$ -cage), because there are no required pair of edges at the distance 3. This leads us to the natural question: What is the lower bound of this recursive construction for the order of $(3, g)$ -graph which will guarantee the existence of a $(3, g)$ -graphs of higher orders. Another interesting question is, whether this bound is better than the Sauer bound.

2 New upper bounds for the orders of (k, g) -graphs

First, we recall the definition of edge distance. It is an essential part of all of the following theorems. Let e and f be two edges of a graph G . The edge distance between e and f is the length of the shortest path between a(ny) vertex of e and a(ny) vertex of f .

We begin by restating a theorem from [3]:

Theorem 1 ([3]). *Let Γ be a $(3, g)$ -graph of order n . If Γ has at least two edges of distance at least $g - 3$, then there exists a $(3, g)$ -graph Γ' of order $n + 2$.*

When we observe Fig. 1, we see that for $(3, 5)$ -graphs we are always able to find a pair of edges at the distance 2 and the natural question is why. We start with an edge e . We will count how long we get the desired distance from edge e . The size of a graph is its number of edges. Since all the vertices must be of degree 3 we will add two edges to both vertices, which are incident with edge e . Thus we have 4 new edges of distance 0 and we will denote these edges $e_{1,0}, e_{2,0}, e_{3,0}, e_{4,0}$ (the number after comma represents the distance at which is the edge from the edge e). Now we must add two edges to every vertex incident to $e_{1,0}, e_{2,0}, e_{3,0}, e_{4,0}$, but is not incident with the edge e . Thus we add 8 new edges $e_{1,1}, e_{2,1}, e_{3,1}, \dots, e_{8,1}$. These edges are at the distance 1. We would repeat this until we get to distance $g - 4$, at which point we have to add 2^{g-2} edges. This means that we need $4 + 8 + 16 + \dots + 2^{g-2}$ edges, but we must not forget about the edge e and we need one more edge at the distance $g - 3$. Thus the total count is $1 + 4 + 8 + 16 + \dots + 2^{g-2} + 1 = 2 + 4 + 8 + 16 + \dots + 2^{g-2} = \sum_{i=1}^{g-2} 2^i = 2^{g-1} - 2$. The above arguments provide us with a proof of the following theorem. Fig. 2 shows the above described argument.

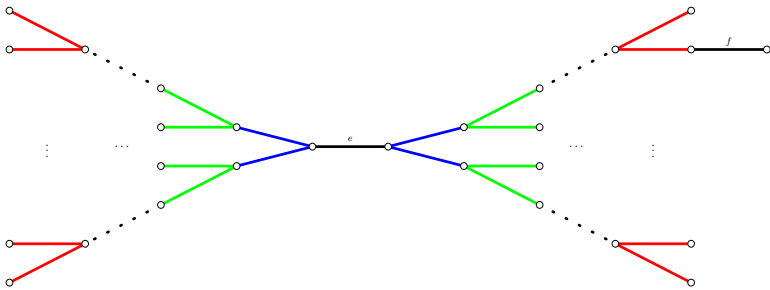


Fig. 2. Illustration of distance between edges e and f in $(3, g)$ -graph; blue edges are at distance 0, green are at distance 1, red are at distance $g - 4$

Theorem 2. *If Γ is a $(3, g)$ -graph of size at least $2^{g-1} - 2$, then Γ contains a pair of edges of distance $g - 3$ and thus admits a construction of Γ' .*

Theorem 1 gives an instruction, how to create graph Γ' from graph Γ . Because Γ' has certainly more than $2^{g-1} - 2$ edges, we can create from Γ' graph Γ'' and so on.

Now, from Theorem 2, we know what is the size that is sufficient to guarantee that we can apply the recursive construction of the $(3, g)$ -graphs. We can count from parity principal ($\sum_{v_i \in V(G)} \deg(v_i) = 2|E(G)|$), how many vertices are needed and thus determine the order of such a $(3, g)$ -graph. When we substitute in the equation of parity principal we get $3|V(G)| = 2|E(G)|$, and it follows that $|V(G)| = 2/3 \cdot |E(G)|$.

Theorem 3. *Let Γ be a $(3, g)$ -graph. If Γ is of order at least $\frac{1}{3}2^g - \frac{4}{3}$, then there exists a $(3, g)$ -graph of any greater even order (with the repeated use of Theorem 1).*

Now, we revisited the statement about the existence of a $(3, 5)$ graphs we gave in the introduction. We have to substitute $g = 5$ in Theorems 2 and 3. Thus we get that $(3, 5)$ -graph exists if there exists a $(3, 5)$ -graph with at least 14 edges and $28/3$ vertices (this number has to be ceiled). Such a $(3, 5)$ -graph exists and it is the Petersen graph.

Next, we compare our bound to the Sauer bound for $(3, g)$ -graphs. Since the difference of Sauer bound $S(3, g)$ is only in the constant we will take the smaller one of those two. Thus we will compare our bound from Theorem 3 to $2/3 + 29/12 \cdot 2^{g-2} = 2/3 + 5/12 \cdot 4 \cdot 2^{g-2} = 2/3 + 5/12 \cdot 2^g$. If we omit the constants from Theorem 3 and from Sauer bound we get the following inequality $1/3 \cdot 2^g < 5/12 \cdot 2^g$. Thus our bound is slightly better approximately by $1/12$. The advantage of Sauer bound is that those graphs certainly exists, we do not know if our graphs do exist.

If $g \geq 6$ than our bound is worse than the best known $(3, g)$ -cages or $(3, g)$ -records. In case of $g = 6$ the order of our graph is 19, that is worse than $(3, 6)$ -cage. If we compare our bound to the Sauer bound which is 39 than our bound is significantly better.

In paper [3] we also stated condition for even regular graphs.

Theorem 4 ([3]). *Let Γ be a $(2k, g)$ -graph of order n . If Γ has at least k edges with distance at least $g - 2$ between each other and if at least one pair of edges is at the distance exactly $g - 2$, then there exists a $(2k, g)$ -graph Γ' of order $n + 1$.*

For the purpose of this article we will consider only the 4-regular case. In the extended version of this paper we will consider the whole general even regular case. Reason we choose the 4-regular case is that it is similar to the 3-regular case, because we only need to consider distance between two edges.

We start with an edge e . Since all the vertices must be of degree 4 we will add three edges to both vertices, which are incident with edge e . Thus we have $6 = 2 \cdot 3$ new edges those are at the distance 0 and we will denote these edges $e_{1,0}, e_{2,0}, \dots, e_{6,0}$. Now we must add three edges to every vertex incident to $e_{1,0}, e_{2,0}, e_{3,0}, e_{4,0}$, but is not incident with the edge e . Thus we add $18 = 2 \cdot 9$ new edges $e_{1,1}, e_{2,1}, \dots, e_{18,1}$. These edges are at the distance 1. We would repeat this until we get to distance $g - 3$, at which point we have to add $2 \cdot 3^{g-3}$ edges. This means that we need $2 \cdot (3 + 9 + 27 + \dots + 3^{g-3})$ edges, but we must not forget about the edge e and we need one more edge at the distance $g - 2$. Thus the total count is $1 + 2 \cdot (3 + 9 + 27 + \dots + 3^{g-3}) + 1 = 2 + 2 \cdot (3 + 9 + 27 + \dots + 3^{g-3}) = 2 + 2 \sum_{i=1}^{g-3} 3^i = 1/2 \cdot 7^{g-2} - 3/2$. The above arguments provide us with a proof of the following theorem.

Theorem 5. *If Γ is a $(4, g)$ -graph of size at least $\frac{1}{2}7^{g-2} - \frac{3}{2}$, then Γ contains a pair of edges of distance $g - 3$ and thus admits a construction of Γ' .*

If we divide the size of Γ by 2 (parity principal) we get the minimal order of the $(4, g)$ -graph, for which the application of Theorem 4 is guaranteed.

Theorem 6. *Let Γ be a $(4, g)$ -graph. If Γ is of order at least $\frac{1}{4}7^{g-2} - \frac{3}{4}$, then there exists a $(4, g)$ -graph of any greater even order (with the repeated use of Theorem 4).*

Now, we compare our bound from Theorem 6 to the Sauer bound $S(4, g) = 2 \cdot 3^{g-2}$ if g is odd and $S(4, g) = 4 \cdot 3^{g-3}$ if g is even. Obviously, our bound is worse than the Sauer bound, so we know that our graphs always exist.

3 Conclusion

We presented two new upper bounds for the order of (k, g) -graphs and we compared them to the Sauer bound $S(k, g)$. In the case of $(3, g)$ -graphs we were able to show that our bound is better by approximately $1/12$ (Theorem 3). In the case of $(4, g)$ -graphs, where the condition for adding vertices given in Theorem 4 is similar to condition in Theorem 1, the Sauer bound is better.

The only unresolved question is if there exists a $(3, g)$ -graphs of order given by Theorem 3.

References

1. Erdős, P., Sachs, H.: Reguläre graphen gegebener tailenweite mit minimaler knotenzahl. *Wiss. Z. Martin-Luther-Univ. Halle-Wittenberg Math.-Natur. Reihe* 12, 251–257 (1963)
2. Exoo, G., Jajcay, R.: Dynamic cage survey. *Electron. J. Combin.* 15(16), 4 (2008)
3. Raiman, T.: Conditions for adding vertices in (k, g) -graphs. Paper in preparation (2018)
4. Sachs, H.: Regular graphs with given girth and restricted circuits. *Journal of the London Mathematical Society* 1(1), 423–429 (1963)
5. Sauer, N.: Extremaleigenschaften regularer graphen gegebener tailenweite, I and II. *Sitzungsberichte Osterreich. Acad. Wiss. Math. Natur. Kl* pp. 27–43 (1967)

Prediction models in medical data analysis: methodology overview

Adéla Vrtková

Department of Applied Mathematics, FEECS,
VŠB – Technical University of Ostrava, 17. listopadu 15,
708 33 Ostrava – Poruba, Czech Republic
adela.vrtkova@vsb.cz

Abstract. Medical data are very specific type of data which have many unique properties and their analysis can be characterized especially by the requirement for the interpretability of results. While building prediction models, the limitations of particular methods have to be considered. Flexible methods could have problem with desirable interpretability and might be characterized as "black box" methods. On the other hand, methods which provide easily interpretable results could have problem with modelling complex relationships. In this paper, we provide overview of several methods which are widely-used for the purpose of building prediction models in medical data analysis or in related fields.

Keywords: medical data, prediction, logistic regression, multilayer perceptron, random forests

1 Motivation

Smaller sample sizes, various types of variables or outliers - all these are typical features of medical data which have to be dealt with during the analysis. Therefore, when choosing suitable method for building prediction models, one has to review assumptions and limitations of considered methods. In this paper, we would like to provide an overview of three methods - logistic regression, multilayer perceptron and random forests which have already been examined in [12, 13]. Then, we aim to discuss limitations of these methods, and possibilities of application on medical data based on current scientific and research background.

Usually, in medical data analysis, the subject of interest is prediction of patient's condition after selected treatment, prediction of the probability of successful procedure or building a decision-support tool which is directly based on prediction models. Hence, the independent and dependent variables could be of different type and the selection of suitable method for prediction is truly challenging task, moreover, when the requirements on prediction models are certainly demanding - strong prediction ability and satisfactory interpretability.

2 Logistic regression

Generally, the logistic regression is a predictive analysis which is used to describe and explain the relationship between one dependent variable (binary, categorical, ordinal) and one or more independent variables which can be qualitative and quantitative.

2.1 Binary Logistic Regression

The method, described in [11], deals with situation when the dependent variable is binary while the independent variables can be qualitative or quantitative. The key in modelling a binary variable is in considering the probability of the related event rather than modelling the values (0 and 1) of the binary variable itself.

From the mathematical point of view, let us assume that Y is the binary dependent variable which takes value 1 with the probability $\pi = P(Y = 1)$. The probability π can take any value between 0 and 1, so the *odds* $\pi/(1 - \pi)$ can take any positive value. The *logit* function is defined as

$$\text{logit}(\pi) = \ln \frac{\pi}{1 - \pi}, \quad (1)$$

which ranges from minus infinity to infinity. Therefore, we obtained suitable transformation of the binary dependent variable which could be used within the meaning of the multiple linear regression as follows

$$\ln \frac{\pi}{1 - \pi} = \beta_0 + \beta_1 X_1 + \dots + \beta_p X_p, \quad (2)$$

where X_j , $j = 1, \dots, p$ are the independent variables and $\beta_0, \beta_1, \dots, \beta_p$ are the parameters. The relationship between the dependent variable Y and particular independent variable X_j can be described with the value e^{β_j} . The interpretation depends on the type of X_j , if it is qualitative or quantitative.

2.2 Ordinal Logistic Regression

The ordinal logistic regression, described in [11], is type of regression analysis which can work with an ordinal variable as the dependent variable. The crucial step from the binary logistic regression to the ordinal logistic regression is in a different definition of probabilities.

Let us assume the ordinal dependent variable Y with k categories. We define the *cumulative probability* as $\pi_i = P(Y \leq i)$, the *cumulative odds* is given by

$$\frac{\pi_i}{1 - \pi_i} = \frac{P(Y \leq i)}{1 - P(Y \leq i)} = \frac{P(Y \leq i)}{P(Y > i)}, \quad (3)$$

and again, the logit function is applied and we obtain so-called *cumulative logits*

$$\text{logit}(\pi_i) = \ln \frac{\pi_i}{1 - \pi_i}, \quad (4)$$

where $i = 1, \dots, k - 1$.

Now, we can define the model for the ordinal logistic regression which simultaneously uses all cumulative logits as

$$\ln \frac{\pi_i}{1 - \pi_i} = \beta_0^i + \beta_1 X_1 + \dots + \beta_p X_p, i = 1, \dots, k - 1. \quad (5)$$

It can be noticed that each cumulative logit has its own intercept β_0^i which increases with increasing i . However, the parameters β_1, \dots, β_p are the same. This model can be used only under the assumption of proportional odds. That's why the model (5) is also called the *proportional odds model*. It means that the effect of an independent variable should be uniform for all levels of the dependent variable. If the proportional odds assumption is violated, the generalized ordinal logistic regression can be used, for example the *partial proportional odds model*.

3 The multilayer perceptron

The multilayer perceptron (MLP) belongs to the class of supervised neural networks, derived from [3, 5]. It means that both input (exploratory) and output (target) variables are available. The algorithm iteratively makes predictions and those predictions are corrected by the known values of the output. The MLP doesn't require any assumptions on data distribution. It can also model non-linear functions, therefore, the algorithm could be good alternative to standard statistical approaches when their assumptions are not met.

Firstly, the information enters into the input layer which only passes the information to the hidden layers without any computation. Then, nodes in hidden layers perform computations (process called *activation*) and pass the information to the output layer. The result coming from the output layer can be perceived as a measure of belonging to a particular class provided that an appropriate activation function is used.

From the mathematical point of view, let us describe the process in one node in a hidden layer of the MLP. We denote x_1, x_2, \dots, x_p as the inputs and y_j as the output of j th node. Then, we denote w_{ji} as the connection weight between input x_i and neuron j , b_j as the bias, and $\varphi_j(\cdot)$ as the activation function of j th neuron. The whole process in neuron j is defined as

$$y_j = \varphi_j \left(\sum_{i=1}^p w_{ji} x_i + b_j \right). \quad (6)$$

The activation function φ is usually sigmoid (also called logistic) function which is generally defined as

$$\varphi(z) = \frac{1}{1 + e^{-z}}. \quad (7)$$

The advantages of using the sigmoid function is especially in interpretation of the results. Since its range is between 0 and 1, the outputs can be interpreted

as probabilities of belonging to classes. Moreover, the sigmoid function is easily differentiable which plays a vital role in training of the MLP.

The training of the MLP uses a method called the *backpropagation*. This method uses the gradient descent optimization algorithm for the purpose of minimizing error function (also called loss or cost function) while updating connection weights. The training starts with (pseudo)randomly generated weights. The computations according to (6) are performed. Then, the resulting output is compared to the target value (known from the data), the error is computed and it goes back through the network. The minimization of error function is performed with the gradient descent optimization algorithm with lastly used weights as initial values. With the minimization, we obtain new weights which minimize the error function and the process repeats. For detailed and accurate mathematical background of the backpropagation, let us refer to [3, 5].

4 The Random Forests Algorithm

The random forests algorithm belongs to the group of decision tree methods which are highly flexible, non-parametric methods design for dealing with regression or classification problems. The random forests algorithm is based on the classification tree model or the regression tree model. Our focus will be on the algorithm which is based on the classification tree models.

The classification tree model, described in [6] uses so-called recursive binary splitting process which begins in the root node (the top of the tree) and continues in the sense of making the best split in each node until reaching the terminal node. The best split is made with consideration of all exploratory variables which could be both quantitative and qualitative. Of course, the choice of the split naturally should be done in the sense of minimizing some suitable criteria which are available in [6]. The necessary step from the classification tree model to the random forests is combining large amount of the classification trees.

The first step in the random forests algorithm, described in [1, 2], is the selection of many bootstrap samples from the original dataset, where the number of bootstrap samples determines the number of trees. In the next step, the classification tree model is built for each bootstrap sample and at each node, certain number of exploratory variables is chosen randomly and they are used for making the best split. This step is repeated until the terminal node is reached and the prediction from each tree is obtained. In the end, the predictions from all trees are aggregated within the meaning of the vote for the most popular category.

Data, which are not used for building trees, are called *out-of-bag* observations (OOB) and predictions obtained from these observations are called OOB predictions. With these predictions, we are able to compute the OOB error estimation which is an accurate estimation of the error rate. Moreover, thanks to the nature of the algorithm and the OOB error, performing cross-validation is not necessary.

The alternative approach introduced in [9, 10] helps prevent biased variable importance measures when exploratory variables are of different type. The main

difference in the alternative approach is in using the conditional inference trees and the bootstrap sampling without replacement. During the selection of variables, the "standard" classification tree chooses the variables randomly, the conditional inference tree chooses from those predictors which have statistically significant relationship with the target variable.

5 Discussion

Firstly, let us discuss the above-described methods within the meaning of flexibility. Flexibility of the logistic regression clearly is not comparable with other two methods. The assumption of the independence of exploratory variables or the assumption for linear dependence between independent variables and the log-odds (1) suggest significant limitations in usage of this method. On the other hand, the MLP and the random forests can work with data with various non-linear relationships among variables. Moreover, the random forests algorithm doesn't require any normalization of variables (for the MLP, normalization is recommended) and can tackle such a problem as data with "small n , large p ", i.e. small sample size and large number of variables.

Then, of course, we are interested in the prediction accuracy. If the assumptions for the logistic regression are met, the performance of the model should be comparable with the MLP and the random forests. Naturally, it doesn't make any sense to consider using the logistic regression if the assumptions are violated and somehow compare it with other methods. The performance of the MLP and the random forests is entirely dependent on the particular dataset and the relationships we aim to model.

Finally, we are interested in the interpretability. From this point of view, the logistic regression has the most clear interpretation. The regression coefficients express the relationship between the corresponding independent variable and the dependent variable. The MLP and the random forests are truly within the meaning of interpretability "black boxes". However, the random forests algorithm can provide the variable importance score. Results of application of similar methods to particular medical dataset were published e.g. in [4], [8] or [14].

6 Conclusion and future work

This paper provided an overview of several methods which are applied in the field of medical data analysis with satisfactory results. Also, limitations and difficulties related to these methods were discussed.

For future work, we would like to examine other multivariate methods for further analysis of the structure of data, such as the multiple correspondence analysis or multidimensional scaling, etc. Also, the cooperation with the University Hospital Ostrava continues and the goal of building a decision-support tool for contributing to the ischemic stroke treatment is still of interest.

In 06/2018, in cooperation with the University Hospital Ostrava, a paper related to the topic of the analysis of ischemic stroke data was published in

the Medical Science Monitor [7]. Findings presented in this paper are the essential part of the research which leads to the above-mentioned desirable decision-support tool.

Acknowledgement

The author acknowledges the support of VŠB-Technical University of Ostrava (Project No. SP2018/68) and the support of the Moravian-Silesian Region (RRC/10/2017).

References

1. Breiman, L.: Random forests. *Machine learning* 45(1), 5–32 (2001)
2. Cutler, D.R., Edwards, T.C., Beard, K.H., Cutler, A., Hess, K.T., Gibson, J., Lawler, J.J.: Random forests for classification in ecology. *Ecology* 88(11), 2783–2792 (2007)
3. Efron, B., Hastie, T.: *Computer age statistical inference*, vol. 5. Cambridge University Press (2016)
4. Eftekhari, B., Mohammad, K., Ardebili, H.E., Ghodsi, M., Ketabchi, E.: Comparison of artificial neural network and logistic regression models for prediction of mortality in head trauma based on initial clinical data. *BMC Medical Informatics and Decision Making* 5(1), 3 (2005)
5. Haykin, S.S., Haykin, S.S., Haykin, S.S., Haykin, S.S.: *Neural networks and learning machines*, vol. 3. Pearson Upper Saddle River, NJ, USA: (2009)
6. James, G., Witten, D., Hastie, T., Tibshirani, R.: *An introduction to statistical learning*, vol. 6. Springer (2013)
7. Prochazka, V., Jonszta, T., Czerny, D., Krajca, J., Roubec, M., Macak, J., Kovar, P., Kovarova, P., Pulcer, M., Zoubkova, R., et al.: The role of von willebrand factor, adamts13, and cerebral artery thrombus composition in patient outcome following mechanical thrombectomy for acute ischemic stroke. *Medical Science Monitor* 24, 3929–3945 (2018)
8. Statnikov, A., Wang, L., Aliferis, C.F.: A comprehensive comparison of random forests and support vector machines for microarray-based cancer classification. *BMC bioinformatics* 9(1), 319 (2008)
9. Strobl, C., Boulesteix, A.L., Kneib, T., Augustin, T., Zeileis, A.: Conditional variable importance for random forests. *BMC bioinformatics* 9(1), 307 (2008)
10. Strobl, C., Boulesteix, A.L., Zeileis, A., Hothorn, T.: Bias in random forest variable importance measures: Illustrations, sources and a solution. *BMC bioinformatics* 8(1), 25 (2007)
11. Tutz, G.: *Regression for categorical data*, vol. 34. Cambridge University Press (2011)
12. Vrtková, A.: Predicting clinical status of patients after an acute ischemic stroke using random forests. In: *Information and Digital Technologies (IDT), 2017 International Conference on*. pp. 417–422. IEEE (2017)
13. Vrtková, A.: Using the random forests algorithm for medical data analysis. In: *WOFEX 2017*. pp. 366–370 (2017)
14. Yan, H., Jiang, Y., Zheng, J., Peng, C., Li, Q.: A multilayer perceptron-based medical decision support system for heart disease diagnosis. *Expert Systems with Applications* 30(2), 272–281 (2006)

Orientations of Almost Regular Graphs

Jakub Závada¹, Petr Kovář^{1,2}, Michal Kravčenko^{1,2}, Matěj Krbeček¹, Michael Kubesa^{1,2}, and Adam Silber¹

¹Department of Applied Mathematics, FEECS,
VŠB – Technical University of Ostrava, 17. listopadu 15,
708 33 Ostrava – Poruba, Czech Republic

²IT4Innovation, VŠB – Technical University of Ostrava, 17. listopadu 15,
708 33 Ostrava – Poruba, Czech Republic
jakub.zavada.st@vsb.cz

Abstract. An almost regular graph is a simple graph, in which the difference between maximum degree and minimum degree is at most 2. Our goal is to find an optimal orientation of such graph. Orientation of a graph is a digraph made from that graph by orienting every edge. Orientation is optimal if the maximum outdegree is minimized (there does not exist an orientation of our graph with lower maximum outdegree). It is quite easy to prove that if the difference between maximum and minimum degree is at most 1, then we can find an optimal orientation very quickly. But if the difference is 2, then we can find an optimal orientation using the same algorithm only if maximum degree is even or if there exists an induced subgraph H in graph G such that maximum degree of H is equal to maximum degree of G and the number of vertices of maximum degree in H is higher than the number of vertices of minimum degree in H (here we mean the minimum degree of G , not of H). There exists an induced subgraph H in graph G such that maximum degree of H is equal to maximum degree of G and the number of vertices of maximum degree in H is higher than the number of vertices of minimum degree in H (here we mean the minimum degree of G , not of H). We show that the optimal orientation can be found in $O(|E|)$ time using our algorithm if the difference between maximum and minimum degree is at most 1 or if at least one of the conditions mentioned above is satisfied. For all remaining almost regular graphs we can use a different algorithm, which finds the optimal orientation with the best possible time complexity.

Keywords: graph orientation, graph theory, maximum flow problem

1 Introduction

In general, orientation of a simple weighted graph $G = (V, E, w)$ is a NP-complete problem [1], but the problem of the orientation of unweighted graphs (or graphs with equal weights) can be solved in $O(|E|^2)$ time using the algorithm provided in [2]. This algorithm was slightly improved in [1], where it is shown, that the problem can be solved in $O(|E|^{\frac{3}{2}})$ time. An optimal orientation can be

found even faster for some special cases of graphs such as trees (with $O(|V|)$ time complexity) [1] or planar graphs (with $O(|E|)$ time complexity) [3].

Our goal is to solve the orientation problem optimally for another class of graphs, which we call almost regular graphs. We will provide two algorithms. First of them is faster ($O(|E|)$ time complexity), but the orientation found by this algorithm is for some of almost regular graphs not optimal. We show the conditions, which are necessary for finding an optimal orientation using the first algorithm. Then we show another algorithm, which is slightly slower, but can find an optimal orientation for every almost regular graph. In the following sections we consider only connected graphs. Optimal orientation problem for disconnected graphs can be solved by applying the same algorithm on each component of the graph separately.

2 First Algorithm

First (and faster) algorithm will always find an optimal orientation of graph G with the property $\Delta(G) - \delta(G) \leq 1$. If $\Delta(G) - \delta(G) = 2$, then the first algorithm finds an optimal orientation if $\Delta(G)$ is even or if there exists an induced subgraph H of G such that $\Delta(H) = \Delta(G)$ and the number of vertices of degree $\Delta(G)$ in H is higher than the number of vertices of degree $\delta(G)$ in H .

Theorem 1. *The optimal value of the maximum outdegree in an almost regular graph G , which satisfies*

- $\Delta(G) - \delta(G) \leq 1$ or
- $\Delta(G)$ is even or
- there exists an induced subgraph H of G such that $\Delta(H) = \Delta(G)$ and the number of vertices of degree $\Delta(G)$ in H is higher than the number of vertices of degree $\delta(G)$ in H ,

is always $\left\lceil \frac{\Delta(G)}{2} \right\rceil$.

Proof. First we find a lower bound for the maximum outdegree of optimal orientation of such graph G . Every edge will contribute 1 to the total outdegree of one vertex and to the total indegree of a different vertex. It means that the average outdegree in an arbitrary orientation of graph G is always equal to the half of the average degree in graph G . It is clear that the maximum outdegree can never be lower than the average outdegree, so we can use the ceiling of the average outdegree as a lower bound for the maximum outdegree. This value is equal to $\left\lceil \frac{\Delta(G)}{2} \right\rceil$ if $\Delta(G) - \delta(G) \leq 1$ and also if $\Delta(G)$ is even. In other almost regular graphs the ceiling of the average outdegree can be equal to $\left\lceil \frac{\Delta(G)}{2} \right\rceil$, but if there is an induced subgraph H with the properties given in the theorem, then the average outdegree of H should be used as a lower bound and this number is again equal to $\left\lceil \frac{\Delta(G)}{2} \right\rceil$.

It remains to prove that we can always achieve the lower bound. If the graph G is Eulerian, we can find an Eulerian circuit and orient edges of the graph along the circuit. This process returns an orientation with optimal maximum outdegree $\lceil \frac{\Delta(G)}{2} \rceil$. If the graph is not Eulerian, we can add one new vertex v to the graph, then connect this vertex with every vertex of odd degree by a single edge. Now we get an Eulerian graph and we can find an Eulerian circuit. Orientation along the circuit followed by removal of vertex v gives again an orientation with optimal maximum outdegree $\lceil \frac{\Delta(G)}{2} \rceil$.

We use Hierholzer’s algorithm [4] to find an Eulerian circuit. Then optimal orientation of G can be found using the algorithm described in the proof with $O(|E|)$ time complexity.

The algorithm described in this section will not find the optimal orientation in every almost regular graph. Actually, this algorithm can always (even for graphs which are not almost regular) find an orientation with maximum outdegree $\lceil \frac{\Delta(G)}{2} \rceil$, but if the optimum is lower than $\lceil \frac{\Delta(G)}{2} \rceil$, or if we do not know the optimum, then we have to use a different algorithm if we want to find the optimal orientation.

An example of almost regular graph, which optimal maximum outdegree is lower than $\lceil \frac{\Delta(G)}{2} \rceil$, is depicted in Fig. 1. Optimal maximum outdegree is 1, but our first algorithm would find only an orientation with optimal maximum outdegree 2.

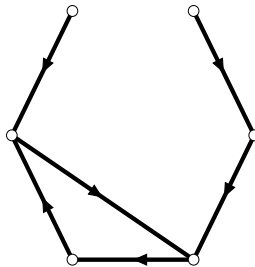


Fig. 1. Optimally oriented almost regular graph.

3 Second Algorithm

When $\Delta(G)$ is odd and the number of vertices of degree $\Delta(G)$ is less or equal to the number of vertices of degree $\delta(G)$, the optimal maximum outdegree can be $\lfloor \frac{\Delta(G)}{2} \rfloor$ or $\lceil \frac{\Delta(G)}{2} \rceil$. The value of the optimum depends on the existence of induced subgraph H of G such that $\Delta(H) = \Delta(G)$ and the number of vertices

of degree $\Delta(G)$ in H is higher than the number of vertices of degree $\delta(G)$ in H , but the time complexity of searching for such subgraph is more expensive than the time complexity of second algorithm, so in this case we will always use the second algorithm.

The second algorithm is based on finding the maximum flow. We add two vertices to the graph G . One of them, called supersource, will be connected by an edge with all vertices of degree $\delta(G)$. The other one, called supersink, will be connected by an edge with all vertices of degree $\Delta(G)$. The capacity of every edge we set equal to 1 and we search for the maximum flow from the supersource to the supersink.

If the value of the maximum flow is equal to the number of vertices of degree $\Delta(G)$, then there exists an orientation with maximum outdegree $\lfloor \frac{\Delta(G)}{2} \rfloor$. We can orient edges of the maximum flow along the flow from the supersource to the supersink. Then we will remove the supersource and the supersink. The subgraph without oriented edges, supersource and supersink is Eulerian (or the subgraph consists of several components and each of them is Eulerian) and we use the first (faster) algorithm to orient edges in this subgraph.

If the value of the maximum flow is not equal to the number of vertices, then it is not possible to find a sufficient number of paths from vertices of degree $\Delta(G)$ to the vertices of degree $\delta(G)$ and the optimal value of maximum outdegree is $\lfloor \frac{\Delta(G)}{2} \rfloor$. In this situation we use the first algorithm to orient edges in that graph.

The time complexity of the second algorithm depends on the algorithm chosen for the maximum flow problem. If we choose the best known Ford-Fulkerson algorithm, then the time complexity of second algorithm is $O(|E| \cdot f)$, where f is the value of the maximum flow.

4 Conclusion

We have two different algorithms to solve the problem of the optimal orientation of almost regular graph. One of them with time complexity $O(|E|)$ is asymptotically as fast as it can be, because we always need to go through all edges if we want to set their orientation. But this algorithm does not find the best orientation if additional conditions are not satisfied. The second algorithm is slower, but it finds the optimal orientation of every almost regular graph. It remains to consider, which algorithm for the maximum flow problem will be the best in our case, since there are lots of algorithms and their time complexity depends on different parameters.

We also tried to somehow generalize our definition of almost regular graph, but it turned out that even if we change the condition from $\Delta(G) - \delta(G) \leq 2$ to $\Delta(G) - \delta(G) \leq 3$, then the problem starts to be much more complex and the algorithms described in this paper will not be always sufficient to find the optimal orientation.

Results of our work on almost regular graphs were presented at the conference Grafy 2018 in Prague.

Acknowledgments

This work was supported by The Ministry of Education, Youth and Sports from the National Programme of Sustainability (NPU II) project “IT4Innovations excellence in science – LQ1602”.

References

1. YUCHI, A., E. MIYANO, H. ONO and K. ZENMYO. Graph orientation algorithms to minimize the maximum outdegree. In: *12th Computing: The Australasian Theory Symposium*. Hobart: Australian Computer Society, 2006, pp. 11–20. ISBN 1-920682-33-3.
2. VENKATESWARAN, V. Minimizing maximum indegree. *Discrete Applied Mathematics*. 2004, vol. 143, iss. 1–3, pp. 374–378. ISSN 0166-218X. DOI: 10.1016/j.dam.2003.07.007.
3. CHROBAK, M. and D. EPPSTEIN. Planar orientations with low out-degree and compaction of adjacency matrices. *Theoretical Computer Science*. 1991, vol. 86, iss. 2, pp. 243–266. ISSN 0304-3975. DOI: 10.1016/0304-3975(91)90020-3.
4. Eulerian path. In: *Wikipedia: the free encyclopedia* [online]. San Francisco (CA): Wikimedia Foundation, 2001- [cit. 2018-07-25]. https://en.wikipedia.org/wiki/Eulerian_path#Hierholzer's_algorithm.

Optical Vehicle-to-Vehicle (V2V) Communication: Analysis of Beam Homogeneity DRL Jaguar XK

Peter Hajduk and Vladimír Vašínek

Department of Telecommunications, FEECS,
VŠB – Technical University of Ostrava, 17. listopadu 15,
708 33 Ostrava – Poruba, Czech Republic
{peter.hajduk.st2, vladimir.vasinek}@vsb.cz

Abstract. The article focuses on the implementation of vehicle to vehicle (V2V) communication technology in the field of road traffic safety, by way of light-emitting diodes (LED), which serve for the transmission of an optical signal within the range of the visible optical radiation (VLC). LED technology is nowadays used standardly in higher versions of car headlights and tail-lights, where it fulfills signaling functions as well as headlight functions. The future of V2V technology lies in the hybrid application of optical wireless communication which utilises LED sources on the side of the optical transmitter and a camera system (OCI, optical communication imaging sensor) on the side of the receiver, along with mobile technologies transmitting information about the state and character of the roadway. The authors of the work carried out research in the area to verify the possibility of implementing the function of a DRL headlight in a Jaguar XK model 2011 in V2V communication, with the homogeneity demands for the specific function of the headlight in mind.

Keywords: Beam homogeneity; VLC; Bias-Tee; V2V communication.

1 Introduction

Optical wireless data transfer between vehicles (V2V) is a new field of research, based on VLC technology. This technology is undergoing dynamic growth, as a result of the European Union's effort to react to the rapid increase in the frequency of road traffic accidents. The emphasis is put on raising active and passive safety, and therefore on the two basics of external automobile lighting – to see and be seen. The concept of road traffic safety is supported by research conducted by premier automotive manufacturers (BMW, Audi), where the applying of hybrid V2V communication is assumed. In this concept, mobile technologies transmit information about the roadway at greater distances (fog, rain), with OWC used for data transfer at shorter distances, about sudden changes in the roadway, when a quick response of the system >190ms (braking, change of direction) is important. Naturally, the utilisation of an optical V2V communication system opens up a series of problems. These include the necessity of integrating the modulator into the electronic control units of a headlight, as well as its placement in built-up and housing development areas. Another issue is the ful-

filling of legal regulations concerning the individual functions of a headlight, along with the homogeneity of a specific function determined by the car manufacturer [4].

2 Optical V2V communication system

Research in the field of optical communication between vehicles (V2V) is expanding mainly in conjunction with the light-emitting LED diode for optical wireless communication (OWC). The optical source utilising the LED diode represents an appropriate OWC device for transmitting an optical signal within the visible spectrum of the VLC, with the possibility of modulating LED at high transmission speeds, with a long operational lifespan, effectiveness, and allowing automobile designers to create concepts typical for individual marques. This technology is commonly utilised in tail-lights, brake lights, headlights or in traffic signaling [1].

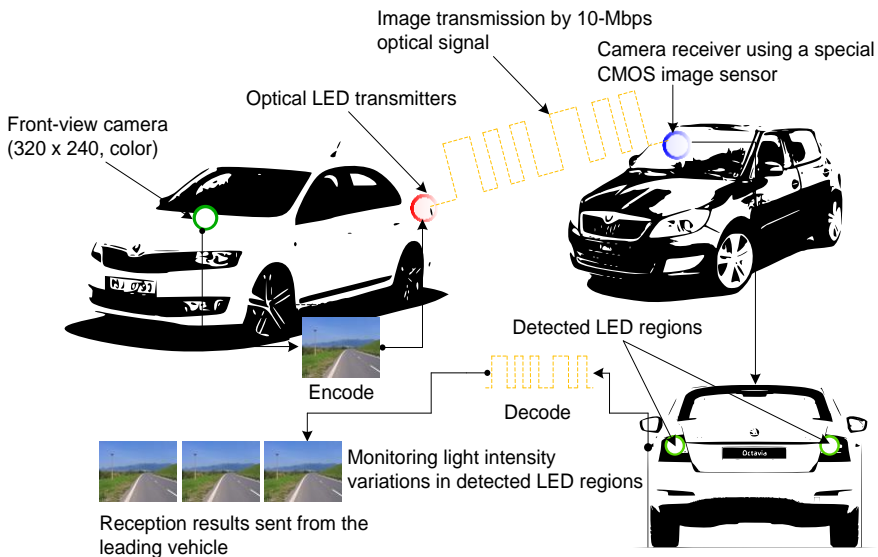


Fig. 1. Illustration of the optical V2V communication system.

The optical signal receiver in OWC automobile systems is comprised of a camera device utilising a special CMOS image sensor, referred to as a communication image sensor (OCI, optical communication image) [2]. The OCI uses so-called communication pixels (CPx), specialized for high-speed receiving of an optical signal. In addition to that, it contains an input circuit that reacts to intense light sources, e.g. LED, thus facilitating their detection. This means that the OWC technology uses a camera (an image sensor) providing non-crosstalk communication with multiple-access LED without a complex protocol and processing, preventing the mixing of an optical signal with noise, such as directly falling rays of sunlight. The applying of a camera system as a part of V2V communication also counts with the utilisation of camera systems, which are currently being used in the automotive industry for safety and comfort applications.

3 Optical V2V transmitter

The proposed concept of an optical transmitter within the context of the transfer concept is influenced by regulation ECE R 87, which is intended for the automotive industry and concerns the function of the DRL (daytime running lamp) daily lighting of a vehicle. Therefore, the optical transmitter factors in the decrease of optical radiation intensity in cases of applying advanced modulation formats, which could have transmission rate negative influence on the function of the headlight from a perspective of the lamp legality in road traffic.

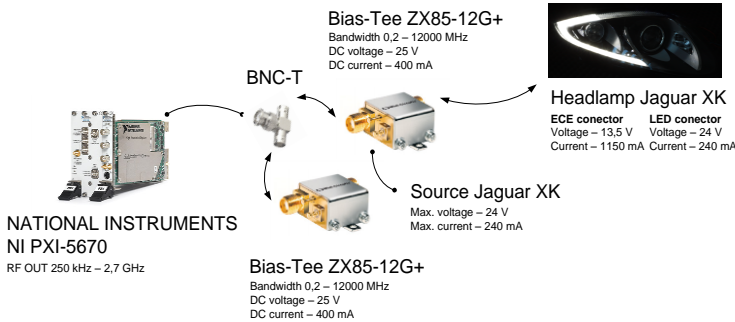


Fig. 2. Design concept of optical transmitter system DRL Jaguar XK model 2011.

The Bias-Tee ZX85-12G+ device in the proposed transmission system concept serves for the merging of an unidirectional signal on the DC port with the radio frequency signal on the RF port [3]. The combined RF+DC signal is used for setting the work point of the modulation of the individual LED segments of a DRL to a mean value of $I_{F(s)} = 240$ mA. The DC port feed is implemented via the control electronics of the headlight.

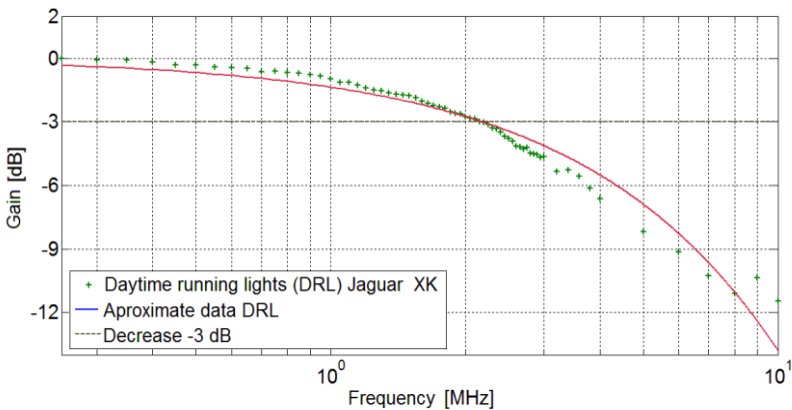


Fig. 3. Results of measurements optical output DRL Jaguar XK.

4 Measurement

The analysis of the beam homogeneity of a DRL headlight radiated optical radiation was carried out in an experimental dark testing room at the reference distance 2m on the testing stabilization part. Testing of the DRL daytime lighting proceeded at a maximum voltage of $U_F = 13,5 \text{ V}$ and environmental temperature of $T_a = 25 \text{ °C}$. Brightness analysis was done by camera with monochrome chip and RGB filter. Due to the high dynamics of the light, a brightness photo is made several times at different exposure times (at least 12 shots) and then these photos are combined into a brightness map. The first image must be made without any saturated pixels [4].

Images captured by the camera are converted to brightness values and the chip from which the readings are read must be correctly calibrated. The calibration is performed in such a way that the values correspond to cd.m^2 . RGB values that have to be converted to CIE (x, y, z) are always recorded. The ratio between the weakest and the strongest point of a given function cannot be greater than 1: 3.

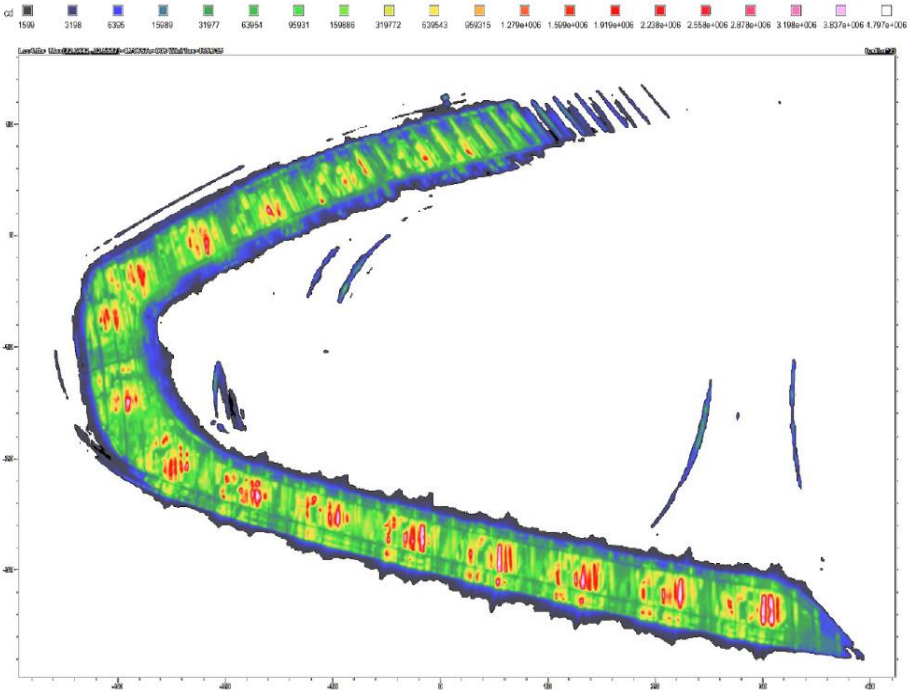


Fig. 4. Results of brightness map of the function DRL.

According to the brightness map of the DRL headlamp with the original control electronics, the MAX point (X: 22.3; Y: -32.6) reaches the highest brightness value of 4,797 Mcd. The resulting ratio between the strongest and the weakest point of the function is in the customer tolerance range and hence the DRL (EL) satisfies the homogeneity condition.

5 Conclusion

The goal of this article was to carry out an analysis of the feasibility of implementing a homologated headlight, intended for road traffic, in V2V communication as an optical transmitter in the transfer concept, with the use of advanced modulation formats. In our case, the headlight was that of Jaguar XK, where the DRL function was used, with the original control electronics. Optical wireless communication achieved the maximum transfer speed of 7,8 Mbit/s, at a carrier frequency of 2 MHz and a modulation format of 64-QAM. The resultant brightness analysis proves, that a headlight supplemented with an active modulation system complies with customer requirement of homogeneity condition without any impact on ratio between the strongest and the weakest point of the function. The MAX point (X: 22.3; Y: -32.6) reached the highest brightness value of 4,797 Mcd, and so the modified version of the headlight is eligible for implementation in road traffic.

6 References

1. TAKAI, Isamu, Tomohisa HARADA, Michinori ANDOH, Keita YASUTOMI, Keiichiro KAGAWA a Shoji KAWAHITO. Optical Vehicle-to-Vehicle Communication System Using LED Transmitter and Camera Receiver. IEEE Photonics Journal. 2014, vol. 6, issue 5, s. 1-14. DOI: 10.1109/jphot.2014.2352620.
2. M. S. Z. Sarker et al., "Design and implementation of a CMOS light pulse receiver cell array for spatial optical communications," Sensors, vol. 11, no. 2, pp. 2056–2076, Feb. 2011.
3. MINI-CIRCUITS. Coaxial Bias-Tee: ZX85-12G+. Brooklyn, NY. Dostupné z: <http://194.75.38.69/pdfs/ZX85-12G+.pdf>.
4. HAJDUK, Peter. *Study effect of LED modulation on photometric quantities and beam homogeneity from automotive lighting*. Ostrava, 2015. Master thesis. Vysoká škola báňská - Technická univerzita Ostrava - VŠB-TUO.

Implementation of a Thermally Loaded EDFA Amplifier into a WDM-PON Optical Network

Jakub Kolář¹, Jan Látal¹, Anirban Dhar², and Zdeněk Wilček¹

¹Department of Telecommunications, FEECS,
VŠB – Technical University of Ostrava, 17. listopadu 15,
708 33 Ostrava – Poruba, Czech Republic
jakub.kolar@vsb.cz

²Fiber Optics & Photonics Division, CSIR-Central Glass & Ceramic Research
Institute, 196 Raja. S. C. Mullick Road, Jadavpur, Kolkata-700 032, West-Bengal,
India anirband@cgcri.res.in

Abstract. With deployment and continuous development of optical routes, the issues concerning the thermal loading of erbium-doped optical fibres become more and more relevant. As we were able to see a significant expansion of optical communication systems in the recent years, it was also necessary to find ways for bridging longer distances between individual points of the optical route. Modern optical telecommunication routes mainly use the DWDM system and optical transmission in the C and L bands. For this purpose, optical amplifiers that are mainly based on erbium doping are used. The aim of this paper is to point out the issues associated with the implementation of erbium-doped amplifying fibres into optical transmission routes that are made using the WDM-PON technology, with regard to the thermal load of these amplifying fibres.

Keywords: WDM-PON · Er³⁺ · Second keyword · temperature · Amplification · McCumber equation.

1 Introduction

Nowadays, we can see ever-increasing demands on optical transmission networks. The increasing demands are not only for higher transmission speeds, but also for the vital network capabilities that will enable to bridge longer distances. When a signal travels through an optical fibre, it is gradually attenuated by the effects of various physical or external influences. For this reason, it is sensible to insert optical amplifiers into the transmission route. There are various kinds of optical amplifiers available and one of them is an EDFA amplifier. The EDFA amplifiers are very often used in optical routes, primarily due to their properties and the resulting gain. There is also continuous development and improvements in the area of EDFA amplifiers, especially with the doped fibres used in them [1]. However, typical problems in constructing routes are the losses, which are caused by the laying of an optical distribution network or by its poorly secured active elements.

It is the importance of securing the active elements sufficiently, especially with regard to the changes of climatic conditions, that can play the essential role in the correct functionality of the entire system. The active components are usually installed in telecommunication nodes, which have sufficient temperature stabilization provided by conditioning units with additional backup power supplies. The same is true for the installation of optical amplifiers, which are mostly implemented in the same place with the active elements, provided that they serve as power or end amplifiers in the optical route [2]. There are effects of temperature differences on optical filters, radiation sources and optical amplifiers, which are well known. For these purposes, additional temperature sensing electronic circuits are placed in optical amplifiers, and their task is to balance the temperature gradients in case a change is sensed. Temperature dependence of an EDFA amplifier may pose a substantial problem, as the temperature affects the gain of the amplifier. In case the amplifier is deployed in DWDM operation, where it amplifies a few dozens of channels at the same time, it is very inconvenient if the gain in the individual channels changes. The changes in gains of the individual channels can cause even higher impact of non-linear effects in the optical fibres, and consequently deteriorate the communication across the entire transmission chain [3], [4].

2 Measurement and Measuring Workplace

A workplace for testing the thermal load of erbium-based amplifying optic fibres was created using a copper cube that consisted of two parts. The copper material was chosen for its very good thermal conductivity, which is $393 \text{ W} \cdot \text{mK}^{-1}$. Both parts of the copper cube can be easily separated to insert the amplifying fibres. One half of the cube has a milled-out groove where the amplifying fibres can be placed. After a fibre was inserted into the groove, the remaining space was filled with heat-conducting paste, not only to increase the heat transfer from outside into the copper cube, but also to prevent water condensation in the temperature chamber. To produce the de-sired temperature with good distribution, four Peltier cells were used. Cooling of Peltier cells was provided by copper coolers made for computer chipsets. After the fibre was inserted into the groove and covered by the heat-conducting paste, the copper cover was attached. For measuring the temperature inside the temperature chamber we used a sensing system with a distributed temperature sensor. This was a commercially available distributed temperature sensing system. The system can measure temperatures along the entire length of the sensor fibre with a resolution of $0.01 \text{ }^\circ\text{C}$ per 1 meter of the optical fibre. Thanks to this system, we were able to assess the homogeneity of the temperature distribution inside the copper cube. An integral part of our workplace was formed by a pumping source, namely LD Pirelli E2-980, which was able to provide a pumping power of up to 125 mW at the wavelength of 980 nm, and also the use of a WDM coupler or an isolator. The complete connection of the designed erbium-doped amplifier was then placed on the Thorlabs board and incorporated into the overall system with all components designed for

our measurement. This solution provides ideal conditions for all specified measurements and at the same time satisfies the condition of ability to move it, i.e. the mobility of the entire measuring station. The complete connection is shown in the following photograph (see Fig. 1).

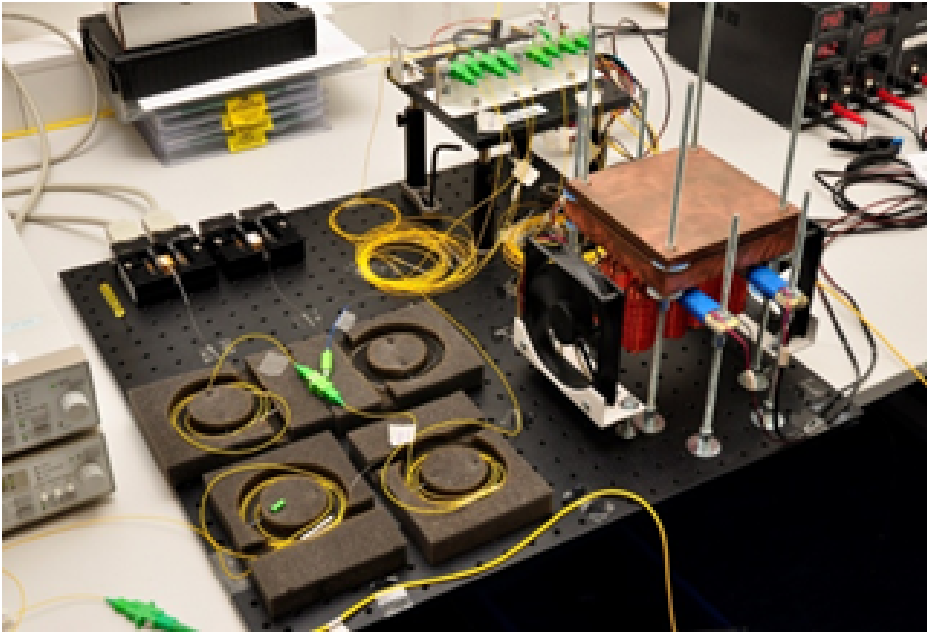


Fig. 1. Complete connection of the measuring station (front view).

For testing of the amplifying ability of experimental erbium-doped fibres depending on the temperature during connection to WDM-PON network, we used OLT unit designated as EAST 1100 from LG Nortel company. Further, it was necessary to use the athermal directional coupler AWG designated as WPF 1132c from LG Nortel company. As ONU units we used 6 end units designated EARU 1112, again from the same producer, LG Nortel company. To approximate a real topology as closely as possible, we created a transmission path measuring 13.292 km. The total transmission loss in the path is 10.37 dB. After setting of OLT unit EAST 1110, as well as six end units EARU 1112, it was necessary to connect and put to operation the whole experimental WDM-PON network. After completion and testing of functionality of experimental WDM-PON network, it was necessary to connect EDFA designed by us. EDFA was connected into the path in co-propagation direction in C band. Subsequently, spectrometer EXFO FTB-500 with module 7200D was connected to the output of splitter, through which 10 % of input signal is transmitted, and the output of individual channels before EDFA amplifier was measured so that it is possible to compare the level of signal power before amplification. During the measurement, spectrometer EXFO

FTB-500 with module 7200D was connected behind the amplified and connected again to the splitter through which 10 % of input signal is transmitted. The following image (see Fig. 2) below shows the scheme of experimental WDM-PON network.

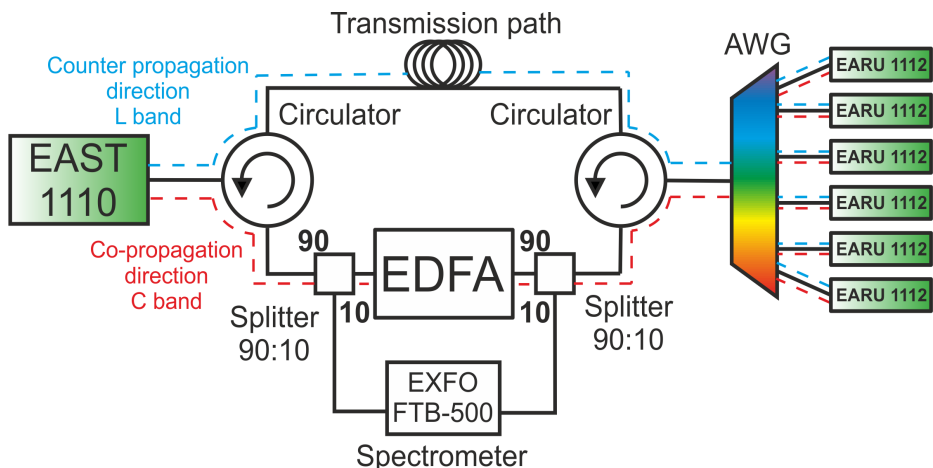


Fig. 2. Experimental connection of testing WDM-PON network with connected EDFA amplifier.

3 Measurement Evaluation

In order to compare individual fibres and enable better evaluation of the measured data, the fibres were mutually compared for two chosen temperatures, specifically, 25 °C and 90 °C. The results of this comparison were represented in individual graphs (see Fig. 3 and Fig. 4) below. In these graphs is shown behaviour of the experimental fibres within real topology. Experimental erbium-doped fibres were first compared with each other at 25 °C temperature and 100 mW output. We can see (see Fig. 3) that erbium-doped SGAE-1 fibre achieved the best level of amplification of output power in these parameters. The value of amplification for individual channels ranges from 20 to 25 dBm. Erbium-doped SGAE-2 fibre has a similar amplification curve as SGAE-1 fibre. When comparing the levels of amplification, however, erbium-doped SGAE-2 fibre achieves worse results than SGAE-1 fibre. The difference is 2-3 dBm for wavelengths ranging from 1540 nm to 1565 nm. The difference is higher between wavelengths 1530 nm and 1540 nm, specifically 5-6 dBm compared to erbium-doped SGAE-1 fibre. When we look closer at erbium-doped SAE-1 fibre, we can notice that the amplification curve is absolutely different from the above-described fibres SGAE-1 and SGAE-2. It is obvious from the amplification curve

that erbium-doped SAE-1 fibre is not excited sufficiently to amplify signal adequately in the entire C band. We can see in (see Fig. 3) that this insufficient excitement is manifested especially for wavelengths ranging from 1530 nm to 1540 nm, with a big difference in the amplification level apparent in the comparison of fibres SGAE-1 and SGAE-2. Insufficient amplification of this erbium-doped SAE-1 fibre is given by two factors. First, the high inserted attenuation of the fibre itself, which is 10 dB for 980 nm wavelength, and 20 dB for 1530 nm wavelength. Second, insufficient pump power for this fibre. As for erbium-doped SAE-2 fibre, we can see that the amplifying ability of the fibre is fully attenuated. Compared to other fibres, and in comparison with the value of power at the input of EDFA, we can see in (see Fig. 4) that this SAE-2 fibre attenuates signal in the entire C band. This is given, similarly as in case of SAE-1 fibre, by the value of inserted attenuation of the fibre itself, as well as by insufficient pump power for this fibre. The value of inserted attenuation for SAE-2 fibre is 15 dB for 980 nm wavelength, and as much as 30 dB for 1530 nm wavelength. Comparison of individual erbium-doped fibres at 100 mW pump power exposed to 90 °C temperature is available in (see Fig. 4). We can see that 90 °C temperature attenuated the level of output almost equally and for all erbium-doped fibres, approximately by 1-3 dBm. It is clear that temperature caused higher attenuation in erbium-doped SAE-2 fibre, both in C band, where not even the last two channels are distinguishable, and in L band, which is attenuated even more.

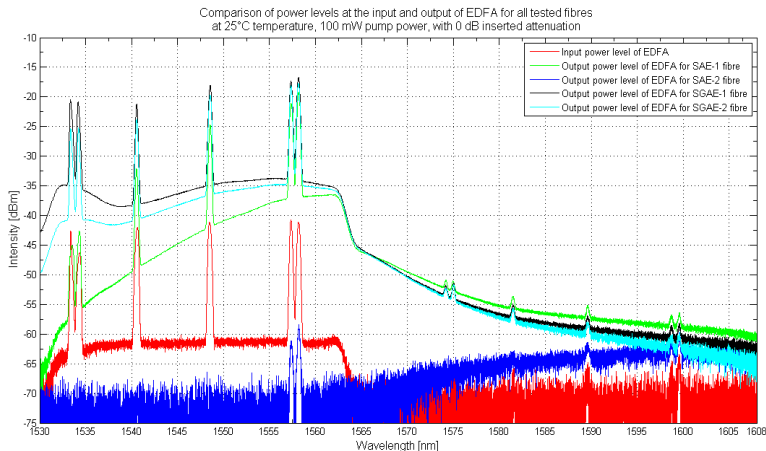


Fig. 3. Comparison of the power levels at the input and output of EDFA for all tested fibres at 25 °C temperatures, 100 mW pump power and with 0 dB inserted attenuation.

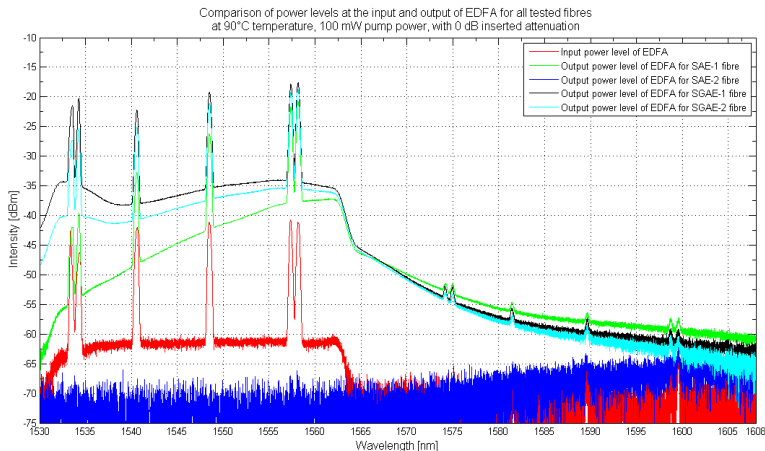


Fig. 4. Comparison of the power levels at the input and output of EDFA for all tested fibres at 90 °C temperature, 100 mW pump power and with 0 dB inserted attenuation.

4 Conclusions

Within our measurements, we have described the issues associated with the implementation of erbium-doped amplifying fibres into optical transmission routes that are made using the WDM-PON technology, with regard to the thermal load of these amplifying fibres. The real measured values, plotted in the graphs in (see Fig. 3 and Fig. 4), have thus confirmed the theoretical assumptions that increasing temperature produces decreasing gain of EDFA amplifiers or EDF fibres. In the future, we would like to perform further measurements for other temperatures, including their negative values, and subsequently compare the results with simulations made in the OptiWave OptiSystem application.

References

1. Bobrovs, V: EDFA application research in WDM communication systems. *Elektronika ir Elektrotechnika* **19**(2) 92-96 (2013)
2. Kihara, M.: Influence of Wavelength and Temperature Changes on Optical Performance of Fiber Joints With Small Gap. *IEEE Photonics Technology Letters* **18**(20), 2120-2122 (2006)
3. Putrina, J., Olonkins S., Bobrovs, V.: Investigation of in-line EDFA performance dependence on channel spacing in WDM transmission systems. In: *Proceedings - 2016 Advances in Wireless and Optical Communications (RTUWO 2016) IEEE, Riga (2016)*. <https://doi.org/10.1109/RTUWO.2016.7821848>
4. Yucel, M.: Determination of minimum temperature coefficient of C band EDFA. *Journal of Applied Sciences* **8**(23) 4464-4467 (2008)

Measurement of bulb lamp parameters made from PDMS and luminophore

Martin Novák

Department of Telecommunications, FEECS,
VŠB – Technical University of Ostrava, 17. listopadu 15,
708 33 Ostrava – Poruba, Czech Republic
martin.novak.st@vsb.cz

Abstract. The paper describes a method of manufacturing a bulb lamp made of polydimethylsiloxane and a yellow YAG luminophore. The biggest enemy of lighting systems is undoubtedly the temperature because the temperature affects the key parameters of the device. It is therefore important to know the temperature characteristics of the device. The contribution also mentions the influence of temperature on the color temperature of the luminaire. The proposed system can be used in the automotive industry or where there is a risk of electromagnetic interference (EMI).

Keywords: Polydimethylsiloxane, PDMS, luminophore, YAG, temperature characteristic, chromaticity temperature

1 Introduction

Polydimethylsiloxane (PDMS) is a transparent polymeric material that is one of the so-called silicone rubbers. Silicone rubbers are supplied mainly in the liquid phase with various viscosities, and they are transferred to the solid-state by vulcanizing using a suitable vulcanizing (curing) agent. Rubbers can vulcanize at a standard (room) temperature or higher temperatures (up to 160 °C), and at the same time, it offers the possibility of vulcanizing the mixture under pressure or without pressure. If vulcanization takes place at a higher temperature (80 °C up to 160 °C) and in pressure, dibenzyl of peroxide is used as the vulcanizing agent, and the entire process is carried out in the hydraulic presses. The bis (2,4, -dichlorobenzyl) of peroxide is used as the catalyst at pressureless vulcanization at a higher temperature. Catalyst (vulcanizing agent) is connected to the end of the macromolecule, and its residues are deactivated by neutralization after the polymerization or are washed out with water. Subsequently, residues of monomer are removed by distillation in the vacuum. The catalyst can influence the molecular weight, but in practice, concentrations of below 0.01 % are recommended, thereby the higher thermal stability of the resulting product is assured.

The chromaticity temperature T_c is equal to the temperature of the black radiant whose radiation has the same chromaticity as the considered radiation. The color space specified by the International Commission on Illumination is the CIE XYZ

space from which chromaticity diagram CIE x, y (Figure 1) is derived. The chromaticity diagram of the RGB color space is a subset of Yxy space and is defined by a triangle whose the tops are the primary colors of monochromatic light sources R (700 nm), G (546.1 nm) and B (435.8 nm). White light is defined in chromaticity temperature ranges from 2700 K to 6500 K.

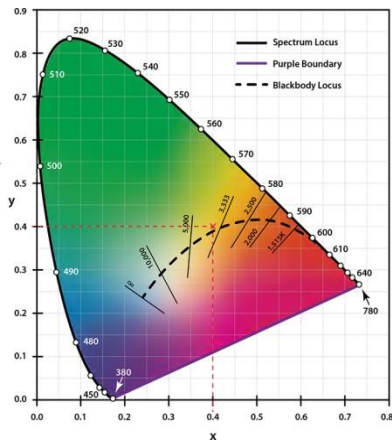


Fig. 1: A chromaticity diagram of the XYZ colorimetric system in the rectangular coordinates (x, y).

2 Sample preparation and methodics of measurement

The incandescent lamp was made from two-component silicone rubber called Sylgard 184 because it has ideal viscosity (5500 mPas) for our purposes. In a low viscosity solution, luminophore particles would clump at the bottom of the casting mould, since polymer vulcanization takes place for about 60 minutes at 100 °C. For high viscosity, it would probably not be possible to ensure a homogeneous distribution of luminophore particles, or this process would take too long. Using KERN PCB precision laboratory scales, the necessary amount of PDMS, into which the recommended curing agent was added, was weighed. Immediately after the addition of the curing agent, vulcanization begins, because this particular type of rubber can be cured even at room temperature. The prepared mixture was immersed in an ultrasonic bath for 15 minutes to degasify the mixture and to further homogenize the PDMS and the curing agent. Garnet luminophore $Y_3Al_5O_{12}:Ce^{3+}$ in a defined weight ratio was fed into the mixture and the mixture thus prepared was placed into a rotary shaker for 120 minutes to ensure a homogeneous distribution of the YAG luminophore in PDMS. The resulting homogeneous mixture was applied to a bulb-shaped glass mould in which we had implemented pre-prepared cylindrical light guide structures of the same material having a length of 25 mm and a diameter of 5 mm. The final shape of the incandescent lamp was placed in a temperature box to accelerate the vulcanization of the polymer (100 °C). At the last stage, the sample was subjected to 48-hour relaxation in a stable environment. The same procedure was repeated for other lamps. Figure 2 shows the final incandescent lamp made from PDMS with a yellow YAG luminophore.



Fig. 2: An incandescent lamp made from PDMS.

The measuring station contains a 5 W laser source with a central wavelength of 455 nm, active cooling, an air aperture and a power supply. The measuring side consists of two temperature sensors (referred to as S_1 and S_2) and probes for chromaticity temperature measurement. The temperature sensors are of the K type; the manufacturer guarantees a resolution of 0.1 °C and an accuracy of 0.5 °C in the temperature range of -50 to +1300 °C. To read the temperature, the CEM DT-613 digital thermometer, which displays data from two measuring probes at the same time, was used. To assess the chromaticity temperature, a USB4000 spectrometer with a dynamic range of 3.4×10^6 enabling measurement in the wavelength range from 200 to 1100 nm was used. Measurement of one lamp was conducted continuously for 12 hours, and every 20 minutes the temperature at defined points and the colour temperature of the output white light were recorded. Figure 3 shows the complete layout of the measuring station.

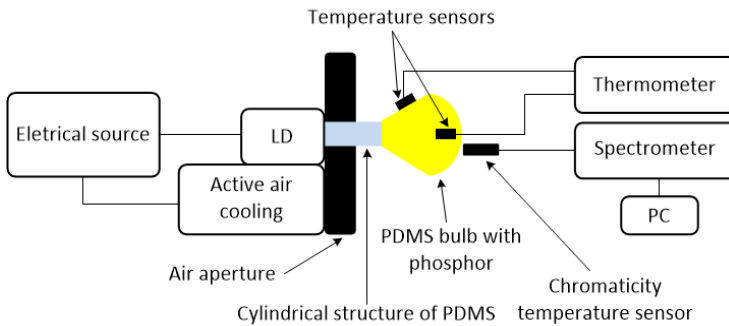


Fig. 3: The layout of the measuring station.

3 Results

The weight relationship between the luminophore and PDMS was chosen based on past experience so that the resulting chromaticity temperature ranged in typical values for cooler tones of white light. Thirty incandescent lamps were produced from each weight ratio, i.e. the statistical data set includes the results measured on 210 samples. The graphs were produced based on average values.

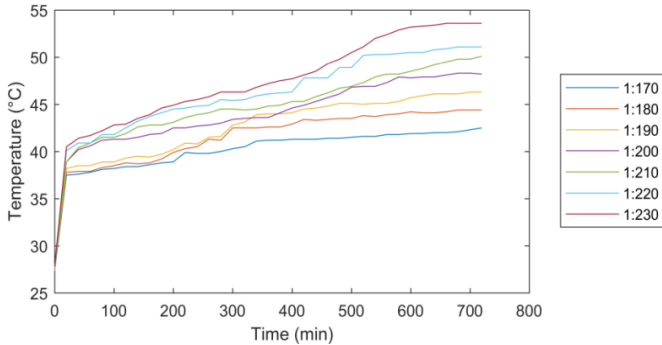


Fig. 4: Temperature characteristics of the lamp (S₁).

Figure 4 shows the temperature characteristics measured by the S₁ sensor located in the centre of the incandescent lamp. If an initial temperature (27.3 °C) that we recorded immediately after the activation of the light source is not included in the data set, the difference between the minimum and maximum values for the lowest weight ratio is 5 °C. At the highest weight ratio, the temperature increased by 13.1 °C.

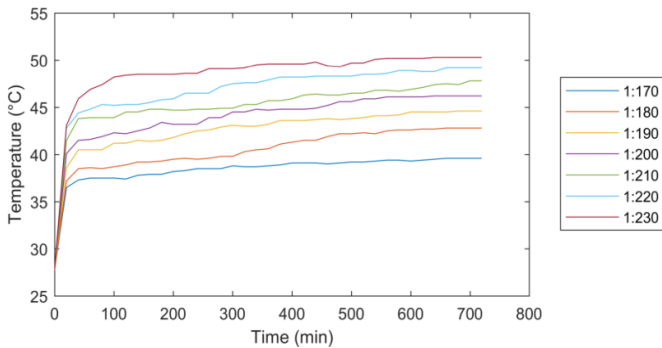


Fig. 5: Temperature characteristics of the lamp (S₂).

Figure 5 shows the temperature characteristics measured by the S₂ sensor located 2 mm under the surface of the lamp. The initial temperature of 27.7 °C is not again included in the statistical data set. At this measurement point, the temperatures do not reach the same values as in the previous case; in the middle of the lamp, heating is higher. The differences between the minimum and maximum temperatures are smaller by approximately a half with higher weight ratios. This is due to the good thermal conductivity of the polymer (0.146 W m⁻¹ K⁻¹); there is heat dissipation at the polymer/air interface.

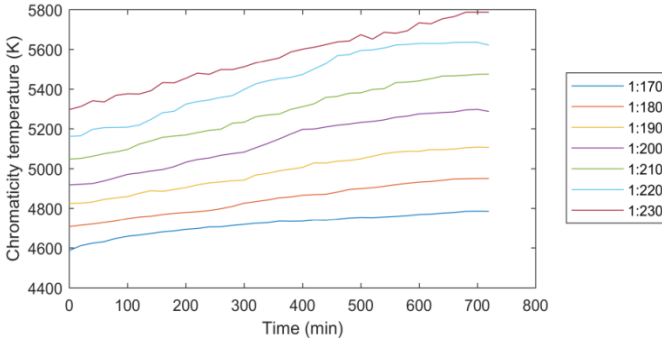


Fig. 6: Chromaticity temperature waveform.

The chromaticity temperature of the bulb lamp varies with the rising temperature of the luminaire because the efficiency of the conversion to light energy is reduced at the warming luminophore. The weight ratio 1:170 shows the difference between a minimum and a maximum value of 199 K, and the difference is 490 K for the weight ratio of 1:230 (Figure 6).

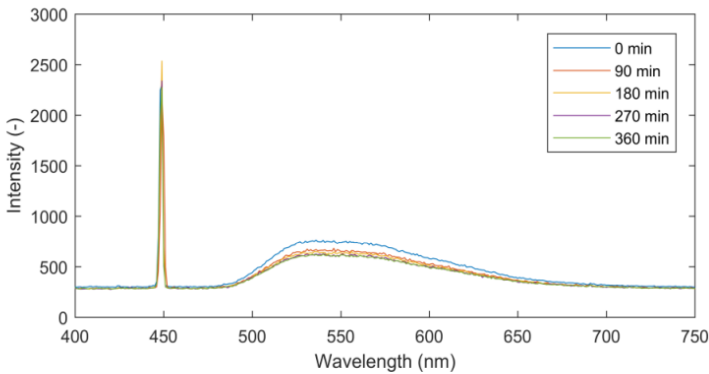


Fig. 7: Spectral dependence of a lamp with a weight ratio of 1:170.

Figure 7 shows spectral behaviour of incandescent lamps with a weight ratio of 1:170. It can be seen that the intensity of radiation decreases with the increasing time or temperature. The biggest difference in the decrease is recorded after 90 minutes; later, the decreases are not so considerable. The same trend applies to other weight ratios; therefore, we state only one weight ratio. Only five spectra are shown in the graph because the other spectra overlap.

4 Conclusion

The functionality of the device has been verified for seven different weight ratios of the luminophore. The dimensions of the lamp correspond to a standard car bulb

designed for turn indicators of a two-track vehicle with a length of 30 mm and a width of 25 mm in the widest part. The results show that the designed lamp is thermally stable in time. The highest temperature (53.6 °C) was recorded in the middle of the lamp by sensor S_1; below the surface of the lamp, the highest temperature was slightly lower than 50.3 °C. Convectional lamps generate a significantly higher temperature at the point of illumination, often above 130 °C, thus significantly reducing their service life. In our solution, we can separate the light source from the illuminating part, so the heat generated from the light source does not interfere with the illumination part. Especially in the automotive industry, it is considered a great advantage because headlights generate a lot of heat in a small space. Chromaticity temperature of lamps changes only slightly over time; the human eye is not sensitive enough to notice this change.

5 Publications

The above results were published at the SPIE conference in Warsaw in 2017. The whole concept of an incandescent light bulb is patented within the Czech Republic.

6 Projects

1. Project GUARDSENSE II - Comprehensive security and critical infrastructure facilities addressed fiber optic sensors using modern information systems.
2. Project SIDAS - Intelligent collision detection and signaling system for increased line safety.
3. Project TACR II - Intelligent communication and lighting modules.
4. Project MPO - Biosignal measuring and processing equipment using fiber optic sensors.

7 References

1. L. C. Chen, W. W. Lin, J. W. Chen, "Fabrication of GaN-Based White Light-Emitting Diodes on Yttrium Aluminum Garnet-Polydimethylsiloxane Flexible Substrates," *Advances in Materials Science and Engineering*, vol. 2015, art. no. 537163, 2015.
2. T. Güner, U. Şentürk, M. M. Demir, "Optical enhancement of phosphor-converted wLEDs using glass beads," *Optical Materials*, vol. 72, pp. 769-774, 2017.
3. H. D. Zhao, H.-D. Y. Y. Yao, et. al., "Display the CIE 1931 color chromaticity diagram with digital image processing," *Proceedings of SPIE - The International Society for Optical Engineering*, vol. 9045, art. no. 904510, 2013.

YAG:Ce Phosphor Powders in Visible Light Communication Systems

Tomáš Stratil, Jan Vitásek and Vladimír Vašínek

Department of Telecommunications, FEECS,
VŠB – Technical University of Ostrava, 17. listopadu 15,
708 33 Ostrava – Poruba, Czech Republic
{tomas.stratil, jan.vitasek, vladimir.vasinek}@vsb.cz

Abstract. This article deals with a comparison of illumination and communication characteristics of white light which is created by excitation of phosphor powder by blue power LED. There are tested two phosphor powders with little different chemical composition. The communication parameters are rise, fall, and photoluminescence decay times. Illumination parameters are colour coordinates and Colour Correlated Temperature. These characteristics are important for VLC technology. The phosphor powders were mixed with Poly-Di-Methyl-Siloxane (PDMS).

Keywords: blue LED, YAG:Ce, white light, Visible Light Communication, VLC.

1 Introduction

Light Emitting Diodes (LEDs) are more and more used in everyday life. LED light bulbs and LED strips are used inside, LEDs are used in headlamps and tail lamps of cars, are used in lamps for street illumination. The classical light bulbs and fluorescent lamps are gradually replaced by LED light sources due to their better features and characteristics. If we compare the classical and LED illumination sources, we can say that LEDs reach much higher efficiency and their further improvements are expected. The other advantages of the LEDs are their longer lifetime, a smaller and compact size, minimum heat generation compared with the classical illumination sources, higher tolerance to humidity, and lower power consumption [1–4]. The other advantage of LEDs is their possible using for communication purposes. LEDs could be fast switched on and off in comparison to the classical light bulbs and fluorescent lamps. Therefore, the LEDs could be applied in automotive for Car-to-Car (C2C) communication and Car-to-Infrastructure (C2I) communication. Great potential is placed in Visible Light Communication (VLC) which should replace the Wi-Fi in the future. VLC technology combines two functions together, illumination and communication [1, 5–8]. Creation of white light in LEDs is possible by two methods. The first method uses three colour chips (red, green and blue). Correct setting of intensity levels makes white light. This method is called as Colour Mixing, LEDs are labelled as RGB-LEDs. The other method is based on a conversion of light. A

blue light emitting chip excites a yellow phosphor; a part of the blue light is converted in the yellow light which together with rest of blue light create white light. YAG:Ce materials are used as a converter. These LEDs are labelled as pc-LEDs (phosphor-converted) [1–3]. The disadvantage of the pc-LEDs is a photoluminescence (PL) decay. This article deals with features of white light created by the phosphor-converted method. We kept at disposal two YAG:Ce phosphor powders with little different chemical composition, QMK58/F-U2 (Y3Al5O12:Ce3+) and QUMK58/F-D1 ((Y,Gd)3Al5O12:Ce). Manufacturer of these phosphor powders is Phosphor Technology Ltd. These phosphor powders were mixed with Poly-Di-Methyl-Siloxane (PDMS) [9] polymer in the same weight concentration 1:35. The phosphor powders were excited by the blue power LED H2A1-H450 [10]. The results parameters were final spectra, colour coordinates x , y and also Correlated Colour Temperature (CCT). The parameters in communication domain was a rise time, fall time and PL decay time.

2 Photoluminescence in a phosphor powder

After light excitation by correct wavelengths, the electron transitions 5d-4f happen in YAG:Ce phosphor powders with large emission spectrum. Ce3+ has a valence electron configuration of 4f1, which gives rise to the 2F5/2 and 2F7/2 low-lying energy states. Consequently, the visible emission is a composite of two bands due to an electronic transition from the lowest lying 5d energy level down to the 2F5/2 and 2F7/2 states. Since the emission is due to an allowed 5d-4f electronic transition, it has a short lifetime of ca. 20 ns [11]. The Ce3+ activator ions substitute some of the Y3+ ions which are coordinated by eight O2- anions in the host lattice of YAG. The Ce3+ ions consequently occupy sites of D2 point group symmetry and the resulting crystal field causes the energies of the 5d orbitals to be split [12, 13]. Five absorption bands at 204.6, 225.4, 261, 339.7 and 457.5 nm were observed in the absorption spectrum of YAG:Ce by Tomiki et al. [14] which were assigned to transitions from the 2F5/2 ground state to each of the 5d levels. YAG:Ce phosphors can contain together with yttrium Y also Gadolinium Gd. Gd3+ ions are larger than Y3+ which causes a red shift of the Ce3+ emission due to the increased crystal field. Conversely, substitution of Al3+ ions for the larger Gd3+ ions on the octahedral sites gives a blue shift due to a weaker crystal field for the Ce3+ ions [11].

2.1 Experimental arrangement

We needed to create some layer with phosphor powders. For this purpose, we used Poly-Di-Methyl-Siloxane (PDMS) names Sylgard 184 [9]. The Sylgard 184 has two components, a PDMS base and a curing agent. The phosphor powder was added to the Sylgard 184 in weight ratio 1:35. The mixture PDMS base-curing agent-phosphor was put in the laboratory shaker for the uniform distribution of all components. The heat hardening happens at temperature around 85° C, it takes 30 minutes. The PDMS is optically transparent from the near UV up

to NIR region of the spectra. For the measurement, we used a reflector [15] for power LEDs. The mixture of PDMS+phosphor powder was poured into Petri dish. The output aperture of the reflector was also placed in Petri dish. After hardening, it the reflector was a 2 mm thin layer of PDMS+phosphor powder, Fig. 1.

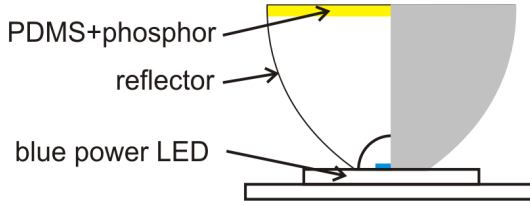


Fig. 1: PDMS+phosphor powder in a reflector.

The blue power LED H2A1-H450 (peak wavelength 450 nm and FWHM 35 nm by forward current 350 mA) [10] was continually supplied by forward current from 50 mA to 350 mA with step 50 mA through a High Power Mounts TCLDM9 (Thorlabs) and Benchtop LD Current Controller LDC240C (Thorlabs). The total optical spectrum, colour coordinates x , y , and CCT was recorded for each forward current by the spectrometer Avantes HS2048XL together with an integrating sphere.

The blue power LED H2A1-H450 [10] was modulated by a square signal (frequency 150 kHz, U_{max} 10V, U_{min} 0V). The power LED was supplied through High Power Mounts TCLDM9 (Thorlabs) and Benchtop LD Current Controller LDC240C (150 mA). The square signal was lead to TCLDM9 through RF input (50Ω). That means, the high level was 350 mA ($0.150+10/50$), the low level was 150 mA. The photodetector was PDA36A-EC (Thorlabs), and output of this photodetector was connected to the oscilloscope LeCroy 204Xi, which automatically detected rise and fall edges. The rise time is time, in which the intensity of signal rises from 0.1 to 0.9. Likewise, fall time is time, in which the intensity of signal falls from 0.9 to 0.1. The PL decay time is time, in which the intensity of signal falls from 1.0 to 0.386 [14].

2.2 Illumination characteristics results

The forward current of the excitation blue LED was gradually increased from 50 mA to 350 mA. At first, we measured the phosphor powder QMK58/F-U2. The measured values are summarized in Table 1. The same measurement was done with the phosphor powder QUMK58/F-D1, which includes moreover Gd element. The results are in Table 2. Figure 2 shows the final spectra of both phosphor powders, Fig. 3 shows measured x and y values in diagram CIE1931.

Table 1: Illumination characteristics of the phosphor powder QMK58/F-U2.

If (mA)	50	100	150	200	250	300	350
x (-)	0.3723	0.3711	0.3701	0.3692	0.3684	0.3679	0.3675
y (-)	0.459	0.4483	0.4454	0.4430	0.4411	0.4398	0.4392
CCT (K)	4567.0	4580.8	4594.4	4606.4	4617.1	4625.7	4632.1

Table 2: Illumination characteristics of the phosphor powder QUMK58/F-D1.

If (mA)	50	100	150	200	250	300	350
x (-)	0.3756	0.3735	0.3716	0.3701	0.3690	0.3684	0.3689
y (-)	0.3826	0.3778	0.3740	0.3709	0.3687	0.3672	0.3672
CCT (K)	4176.4	4206.4	4235.9	4260.7	4280.9	4290.0	4274.4

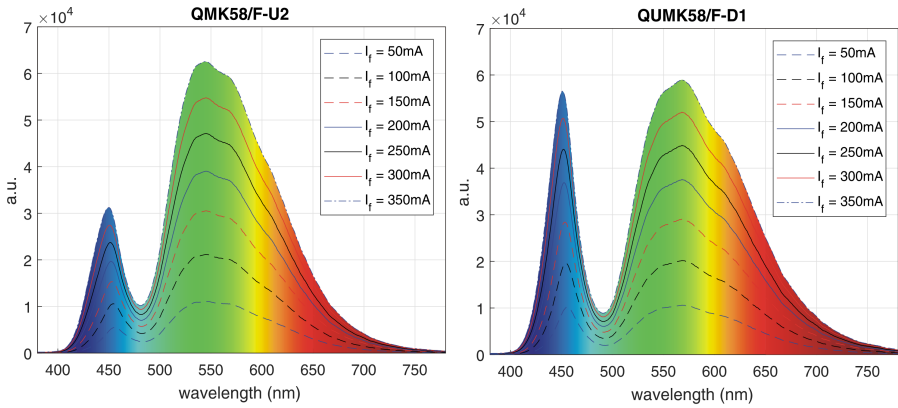


Fig. 2: White spectra with phosphor powders QMK58/F-U2 (left) and QUMK58/F-D1 (right).

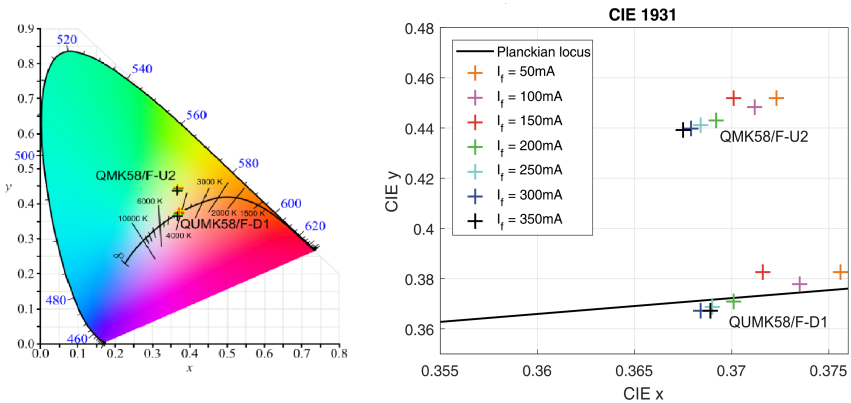


Fig. 3: White spectra with phosphor powders QMK58/F-U2 (left) and QUMK58/F-D1 (right).

2.3 Communication characteristics results

The exciting LED was modulated by the square signal described above. Measured values of rise, fall and PL decay times are in Table 3. Figure 4 shows a fall time and PL decay time of the phosphor powder QUMK58/F-D1.

Table 3: Rise, fall and PL decay times of phosphor powders QMK58/F-U2 and QUMK58/F-D1.

	rise time t_r (ns)	fall time t_f (ns)	decay time t_d (ns)
QMK58/F-U2	115.72	122.97	78.80
QUMK58/F-D1	118.38	121.58	81.60

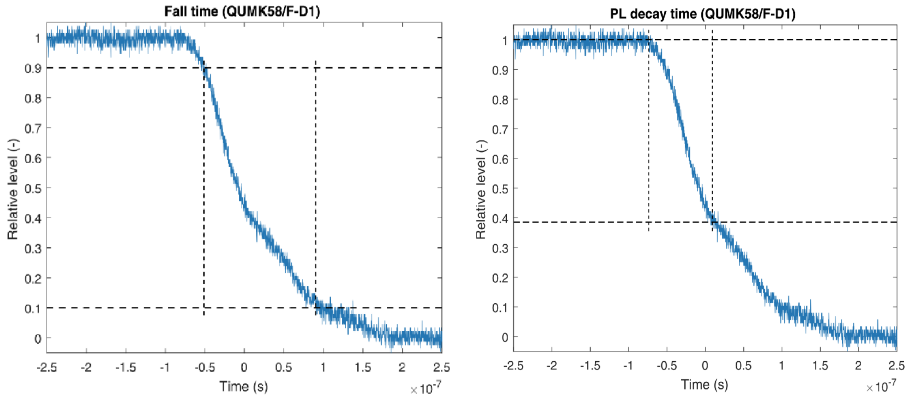


Fig. 4: Fall (left) and PL decay (right) times of the phosphor powder QUMK58/F-D1.

3 Discussion

The illumination characteristics of both phosphor powders are very similar. The CCT changed minimally with increasing forward current. The change could be calculated according to the relation (1), which is derived from the relative error

$$\Delta(\%) = \frac{CCT_{I_f=50mA} - CCT_{I_f=350mA}}{CCT_{I_f=350mA}} \quad (1)$$

where $CCT_{I_f=50mA}$ is the value of CCT measured by forward current 50 mA and $CCT_{I_f=350mA}$ is the value of CCT measured by forward current 350 mA.

The difference Δ of CCT was 1.5% (QMK58/F-U2) and 2.3% (QUMK58/F-D1) respectively. These changes are very small and human eye is not able to recognize them. The CCT independence on the forward current is very good for modulation because the CCT stays practically constant. The CCT of the phosphor powder QMK58/F-U2 is cooler than QUMK58/F-D1. The average CCTs were 4603.4K (QMK58/F-U2) and 4246.4K (QUMK58/F-D1) respectively. Therefore, both phosphor powders are usable for illumination purposes. Also, we can see the spectral red shift in QUMK58/F-D1 caused by Gd in Fig. 2. Therefore, the CCT of the QUMK58/F-D1 is warmer. The communication characteristics of both phosphor powders are also very similar. The PL decay times are longer than is mentioned in books but this is probably caused by modulation features of the exciting power LED.

4 Conclusion

This article describes testing of two YAG:Ce phosphor powders for using in VLC. The tested parameters were illumination characteristics (spectra, colour coordinates and CCT) and communication characteristics (rise, fall and PL decay times). The used excitation light source was the blue power LED. Both phosphor powders created white light which is usable for illumination purposes. The average CCTs were 4603.4K and 4246.4K respectively, which is close to a day light. The communication characteristics were also very similar, there were not found any important difference between both phosphor powders. We can say, that both phosphor powders could be used for illumination and communication purposes.

References

1. E. F. Schubert: Light-Emitting Diodes, *Cambridge University Press*, Cambridge, 2006.
2. T. Novak, B. Socha, Z. Carbol, K. Sokansky: Luminance evaluation of LED indoor luminaires for workspaces lighting, in *Proceedings of the 13th International Scientific Conference Electric Power Engineering 2012*, Brno, Czech Republic, May 2012.
3. R. Baleja, J. Sumpich, P. Bos, B. Helstynova, K. Sokansky, T. Novak: Comparison of LED properties, compact fluorescent bulbs and bulbs in residential areas, in *Proceedings of the 16th International Scientific Conference Electric Power Engineering 2015*, Kouty nad Desnou, Czech Republic, doi: 10.1109/EPE.2015.7161181.
4. T. Stratil, P. Koudelka, R. Martinek, T. Novak: Active Pre-Equalizer for Broadband over Visible Light, *Advances in Electrical and Electronic Engineering*, vol. 15, no. 3, pp. 553-560, March 2017, doi: 10.15598/aeec.v15i3.2210.
5. S. Arnon: Optimised optical wireless car-to-traffic-light communication, *Transactions on Emerging Telecommunications Technologies*, vol. 25, iss. 6, pp. 660-665, Jun 2014, doi: 10.1002/ett.2817.
6. B.W. Kim, S.Y. Jung: Vehicle Positioning Scheme using V2V and V2I Visible Light Communications, in *IEEE 83rd Vehicular Technology Conference*, IEEE, Nanjing, pp. 1-5, 2016, doi: 10.1109/VTCSpring.2016.7504526.

7. N. D. Q. Anh, T. H. Q. Minh and N. H. K. Nhan: Enhancing Lighting Performance of White LED Lamps by Green Emitting Ce,Tb Phosphor, *Advances in Electrical and Electronic Engineering*, vol. 14, no. 5, pp. 609-614, Dec. 2016, doi: 10.15598/aeec.v14i5.1795.
8. P. Jing, W. Huang, L. Chen: Car-to-Pedestrian Communication Safety System Based on the Vehicular Ad-Hoc Network Environment: *A Systematic Review*, Information, vol. 8, iss. 4, pp. 1-8, Dec 2017, doi: 10.3390/info8040127.
9. Sylgard 184 Silicone Elastomer Kit, Dow Corning [online], available at: [http : //www.dowcorning.com/applications/search/default.aspx?R = 131EN](http://www.dowcorning.com/applications/search/default.aspx?R=131EN).
10. H2A1-H450, Roithner Lasertechnik [online], [http : //www.roithner – laser.com/datasheets/led_highsingle/h2a1 – h450.pdf](http://www.roithner-laser.com/datasheets/led_highsingle/h2a1-h450.pdf).
11. R. Withnall, J. Silver, Handbook of Visual Display Technology: Luminescence of Phosphors, Springer, Berlin, 2012, pp. 1013-1028.
12. T. Teplicky, M. Danisova, M. Valica, D. Chorvat, A. Marcek Chorvatova: Fluorescence Properties of Chlorella sp. Algae, *Advances in Electrical and Electronic Engineering*, vol. 15, no. 2, pp. 352-357, June 2017, doi: 10.15598/aeec.v15i2.2015.
13. X. Xiao, H. Tang, T. Zhang, W. Chen, W. Chen, D. Wu, R. Wang, K. Wang: Improving the modulation bandwidth of LED by CdSe/ZnS quantum dots for visible light communication, *Optics Express*, vol. 24, iss. 19, pp. 21577—21586, 2016, doi: 10.1364/OE.24.021577.
14. T. Tomiki, H. Akamine, M. Gushiken, Y. Kinjoh, M. Miyazato, T. Miyazato, N. Toyokawa, M. Hiraoka, N. Hirata, Y. Ganaha, T. Futemma: Ce³⁺ Centres in Y₃Al₅O₁₂ (YAG) Single Crystals, *Journal of the Physical Society of Japan*, vol. 60, iss. 7, pp. 2437—2445, 1991, doi: 10.1143/JPSJ.60.2437.
15. Power LED reflectors, *Roithner LaserTechnik* [online], [http : //www.roithner – laser.com/datasheets/led_optics/clp17cr_lp20cr.pdf](http://www.roithner-laser.com/datasheets/led_optics/clp17cr_lp20cr.pdf).

Measurement of IPTV qualitative parameters on EPON/VDSL2 topology

Zdeněk Wilček and Jan Látal

Department of Telecommunications, FEECS,
VŠB – Technical University of Ostrava, 17. listopadu 15,
708 33 Ostrava – Poruba, Czech Republic
zdenek.wilcek.st@vsb.cz

Abstract. The future of telecommunication networks lies in the area of multimedia services that are offered to end customers. The article discusses the possibilities of deploying IPTV service for a hybrid type of telecommunication topology, which is formed by EPON/VDSL2 systems. The advantage of such topologies is the use of already existing telecommunication network and verification of qualitative features of the distributed IPTV data flows at the same moment. Therefore, the main outputs of this article are the possibilities of distributing data packets by means of multicast or unicast operations. The basic qualitative parameters of the video and data flows (PSNR, MSE, and SSIM) were evaluated with the help of the software tool - MSU Video Quality Measurement Tool.

Keywords: EPON, VDSL2, IPTV, PSNR, MSE, SSIM, unicast, multicast, MPEG.

1 Introduction

Nowadays the analogue broadcast is gradually coming to an end and the developing digital broadcast is ascending. The digital broadcast has several forms – satellite broadcast (DVB-S, DVB-S2), cable broadcast (DVB-C/2), digital terrestrial broadcast (DVB-T/2), and mobile broadcast (DVB-H/2). Another way to monitor the digital broadcast is to use IPTV technology. For the end user, the IPTV service seems to be and works as a standard television broadcast. From the point of view of an IPTV provider, the service represents processing and secure provision of the video content/streaming by means of data networks that are based on the IP protocol [1,2,3]. As the demand for multimedia services grows, it is strictly necessary for telecommunication operators to dimension their transmission networks with respect to meeting QoS parameters. This has already posed a problem as the operators are extensively trying to use the possibilities of already existing telecommunication infrastructures for distribution of broadband services. Nevertheless, there are problems with older system types, such as xDSL technology that should have played a different role in the past. Although the EPON networks are preferentially installed as access networks through FTTx, within the FTTE_x, the FTTC can be the xDSL systems for end users. However, the

problem starts now because such systems operate with completely different methods, and the coexistence of the EPON/xDSL hybrid topology hides some risks in the form of, for instance, the loss of packets due to attenuation along the route or time delays, etc.

2 Methods For Determining The Quality Of IPTV

There is a number of recommendations for the assessment of the image quality and video signal. One of the best known ones is, e.g. ITU-T P.910. The advantage of this measurement is that one can describe the image based on the reality and, as a result, the information that is imperceptible to the human eye is limited. Subjective measurement is influenced by a number of factors and it is difficult to carry out repeated subjective measurement. There are a few approaches to measure the IPTV quality, e.g. MSE, PSNR, SSIM, MDI or MPQM (Moving Pictures Quality Metric) from the range of objective methods. Within the scope of our measurements we primarily focused on the objective methods for the IPTV quality assessment, specifically on the MSE, PSNR and SSIM that are described in more detail below and the actually measured values are provided in the subsequent chapters [4, 5, 6].

2.1 MSE (Mean Square Error)

The MSE represents the mean square error of the received video signal in comparison with the original one. This formula is used for the calculation:

$$MSE = \frac{1}{MN} \sum_{j=0}^{M-1} \sum_{i=0}^{N-1} (x_{ij} - y_{ij})^2 \quad (1)$$

where x is the original image, y is the received image, elements i, j are the elements of the image matrix, M is the number of pixels per image height, and N is the number of pixels per image width.

2.2 PSNR (Peak Signal to Noise Ratio)

The PSNR represents the ratio between the highest value and the MSE and is expressed on the basis of the formula:

$$PSNR = 10 \times \log_{10} \left(\frac{m^2}{MSE} \right) = 20 \times \log_{10}(m) - 10 \times \log_{10}(MSE) \quad (2)$$

where m is the maximum value, which a pixel can receive.

2.3 SSIM (Structural Similarity Index)

The SSIM parameter takes into account the human visual system. It measures the similarity between two images. The SSIM was designed to improve traditional metrics,

such as the MSE and PSNR, which proved to be in contradiction with human perception. The reference values are in the interval of <0,1>, where 0 represents a zero relation to the original image, and is achieved when comparing two identical images.

$$SSIM(x, y) = [l(x, y)]^\alpha [c(x, y)]^\beta [s(x, y)]^\gamma \tag{3}$$

The element $l(x, y)$ is used to compare the signal brightness, element $c(x, y)$ compares the signal contrast, and $s(x, y)$ is used to measure the structural correlation.

3 IPTV Quality Measurement

The software tool MSU Video Quality Measurement Tool was used for our purposes to measure the qualitative parameters of IPTV services on a real route. By using the objective methods SSIM, PSNR and MSE it evaluates the quality of delivered or distributed video flows in the given topology of the telecommunication network. In case of the hybrid topology of the network and IPTV broadcasting, the unicast and multicast operation was investigated with respect to the type of the tested video sample. In the Table 1 the properties of the used video samples are specified.

Table 1. Video samples for IPTV testing.

Testing IPTV	Video sample parameters			
	File	Frames/sec.	Resolution	Codec
MPEG-2 HD	MPEG	59	1280×720	MPEG-2
MPEG-4 HD	AVI	23	1280×720	MPEG-4
MPEG-2 SD	MPEG	25	720×576	MPEG-2

4 IMPLEMENTED TOPOLOGY FOR MEASURING IPTV QUALITATIVE PARAMETERS

It was necessary to use two topologies for the IPTV measurement. The first connection was used for the unicast operation and the second one for the multicast operation.

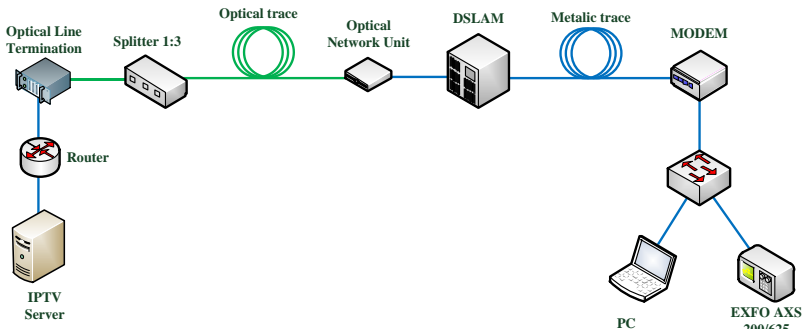


Fig. 1. Topology of hybrid network EPON/VDSL2 – multicast operation.

The given topologies were created from an optical and metallic part, where the optical part, which was formed by optical paths created by fibres G.652B, was variable with a setting of 0 to 10 km, and the metallic part was selected up to 100 meters. By using the VLC Player in broadcast mode the IPTV video flows are distributed to the EPON/VDSL2 hybrid topology to end units (PC) / EXFO AXS 200/625 measuring device. At the end of the network, there is a participating computer, which detects and processes the operation into the visual form by means of the VLC Player programme. As an active system the OLT unit of the EPON technology type 2 with the following basic parameters was used: transmission rate of 1 Gbps or 1.25 Gbps, where 250 Mbps is used for overhead needed for data transmission and administration [1].

5 MSU VIDEO QUALITY MEASUREMENT TOOL

Testing by means of the software was performed by comparing the streaming videos (see samples in Table 1) recorded by the VLC player to the original video. The samples were compared by using the objective methods MSE, PSNR, and SSIM. The higher the value of the MSE, the more different the sample is from the original video. Regarding the PSNR parameter, the sample is the same as the original video if the value is 100 dB. The lower the PSNR value, the less similar the tested samples are. The SSIM parameter takes into account the human visual system. The value 1 means the match of the compared samples. The value 0 indicates the zero relation to the original image.

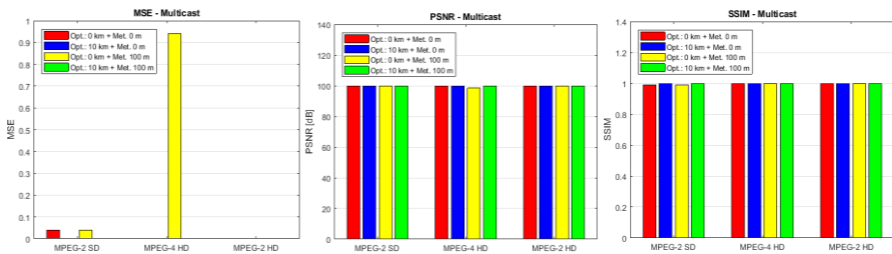


Fig. 2. The values of the MSE (left), **Fig. 3.** PSNR (centre) and **Fig. 4.** SSIM (right) parameters for multicast operation.

In Figures 2-4 we can observe the effect of the route length on the MSE, PSNR and SSIM values. Regarding the multicast operation on the EPON/VDSL2, we can clearly see that the operation is not affected by the length of the route. This indicates that the transmission capabilities of the system are sufficiently dimensioned to transmit all types of video samples. In the Figure 2 we can see that the MPEG4-HD video achieves only the value MSE 0.9 at 100 meters of a metallic path, when the attenuation of the metallic path appears.

It is necessary to take into account that the HD video flows are very dependent on the bandwidth provided for the transmission. The value is almost zero for the remaining combinations of route lengths as well as for other types SD/HD MPEG-2 videos. The PSNR value is close to the value 100 dB and the SSIM is almost equal (see Figure 3

and 4). In case of the unicast operation we can observe changes in the form of an increase of the MSE values, when the deviation of the received video signal from the original one is considerable for all types of tested samples, see Figure 5. This also applies to the other qualitative parameters PSNR and SSIM, see Figures 6 and 7.

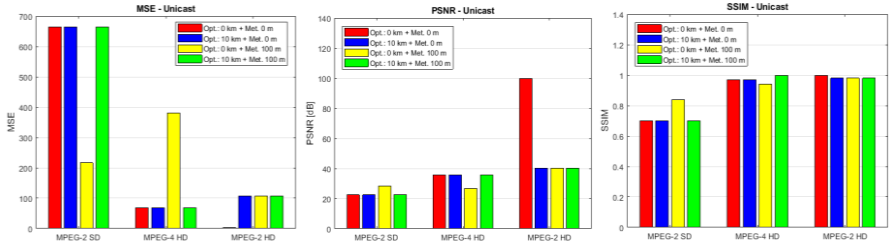


Fig. 5. The values of the MSE (left), **Fig. 6.** PSNR (centre) and **Fig. 7.** SSIM (right) parameters for unicast operation.

In the Figures 6 and 7 we can see that changes of these parameters in comparison with the tested routes and types of the chosen video flow/sample. As we can see in the Figure 5, the MSE is growing considerably for the video sample with the codec MPEG-2 SD at three variants of the network topology, when only one topology with the minimum optical path length and the 100m metallic part has a low MSE value. The MSE value grew to 664 and the PSNR dropped to 22.5 dB. The completely opposite situation occurs in the sample, when the codec MPEG-4 HD for the MSE is used. Then the situation of the MPEG-2 HD sample, when the MSE shows the same or similar values for the topologies with the set route lengths, is also interesting. Regarding the PSNR, see Figure 6, all the samples more or less behave similarly, only the MPEG-2 HD with the minimum route length setting of the tested routes, the maximum match of the video appears. The last testing is then via the SSIM, see Figure 7, when it is possible to observe very similar tendencies for all tested video samples and simulated routes. Only in case of the SD video, the SSIM drops to 0.7.

6 CONCLUSION

The future of the IPTV or Triple Play is unquestionable with respect to increasing demands of end users for this service. With the development of 5G the more massive use of multimedia data transmission will take place and telecommunication operators must be prepared to face this fact. The article describes the possibilities of distribution of different video types and compression codecs with regard to simulated path lengths for the optical or metallic parts of the distribution network. The EPON/VDSL2 hybrid network appears to be viable if more video flows are not used on the given line at one moment. They would overload the bandwidth and thus degrade the QoS and QoE parameters. It was also pointed out that the IPTV multicast operation is far more convenient than the unicast, which imposes greater requirements on the telecommunication network.

7 References

1. L. G. Kazovsky, N. Cheng, W. Shaw, D. Gutierrez and Wong Shing-Wa, *Broadband Optical Access Networks*. Canada: Wiley, 2011. pp. 283. ISBN 978-0-470- 18235-2.
2. R. Agalliu and M. Lucki, “Transmission Transparency and Potential Convergence of Optical Network Solutions at the Physical Layer for Bit Rates from 2.5 Gbps to 256 Gbps,” *Advances in Electrical And Electronic Engineering*, vol. 15, pp. 877–884, 2018.
3. C. Burtscher, D. Seyringer and M. Lucki, “Comparison of Splitting Properties of Various 1x16 Splitters,” *Advances in Electrical And Electronic Engineering*, vol.15, pp. 107 –113, 2017.
4. S. Winkler and P. Mohandas, “The Evolution of Video Quality Measurement: From PSNR to Hybrid Metrics,” in *IEEE Transactions on Broadcasting*, vol. 54, pp. 660–668, 2008.
5. Z. Wang, A.C. Bovik, H.R. Sheikh and E.P. Simoncelli, “Image quality assessment: from error visibility to structural similarity,” *IEEE Transactions on Image Processing*, vol.13, pp. 600–612, 2004.
6. H. R. Sheikh and A.C. Bovik, “Image information and visual quality,” *IEEE Transactions on Image Processing*, vol. 15, pp. 430–444, 2006.

Path Loss Predictions

Yahia Zakaria^{1,2} and Lubomír Ivánek¹

¹Department of Electrical Engineering, FEECS,
VŠB – Technical University of Ostrava, 17. listopadu 15,
708 33 Ostrava – Poruba, Czech Republic
{yahia.salem.st, lubomir.ivanek}@vsb.cz

²Engineering Research Division, National Research Centre (NRC), Ministry of
Scientific Research, P.O. 12622, Cairo, Egypt
yahia.zakaria1982@gmail.com

Abstract.

Abstract— The paper presents a simple power law path loss model according to path loss dependence on various channel models. It is obvious that the interaction between the electromagnetic waves and the environment reduces the signal strength, which is sent from transmitter to receiver that causes the path loss.

Keywords: Path Loss; Interaction;

1 Introduction

Propagation models can be grossly categorized into three types; empirical, deterministic and statistical. Empirical models are those based on observations and measurements [1]. These models are mainly used to predict the path loss. Also, empirical models can be split into two subcategories namely, time dispersive and non-time dispersive [2]. An example of time dispersive is the Stanford University Interim (SUI) channel models which developed under the Institute of Electrical and Electronic Engineers (IEEE) 802.16 working group [3]. On the other hand, COST 231 Hata model is an example of non-time dispersive empirical models [4].

Path loss calculation is one of the major factors that we have to estimate. Furthermore, path loss can be defined as the ratio of the transmitted to received power, usually expressed as the following form in decibels. Measurements done in environments which sharing similar characteristics have shown that the path loss $PL(d_i)$ is a random variable that has a lognormal distribution around a mean value $PL(d_0)$, which expressed in dB as Log-Normal Shadowing Model, [5]:

$$PL(d) = PL(d_0) + 10 n \log_{10} \left(\frac{d}{d_0} \right) \quad (1)$$

where

d is the distance;

d_0 is the reference point at 1km;

n is the path loss exponent.

We have to note that for free space loss the path loss exponent is equal to two. Moreover, the path loss exponent is valuable since it shows the rate of increase of path loss with respect to distance.

2 Measured values

Based on the measurements, we calculated the power losses that are in Tab. 1 for Eldok region and Tab. 2 for Shubra region. Parameter d is the distance of the measured site from the transmitter.

Table 1. Path Loss for Eldok region

d_i [m]	12	21	33	51	80	120	198	310	374	780
PL [dB]	61	75	68	89	69	132	76	95	63	144

Table 2. Path Loss for Shubra region

d_i [m]	12	20	32	51	80	120	199	315	495	798
PL [dB]	51	84	59	49	86	112	72	84	59	132

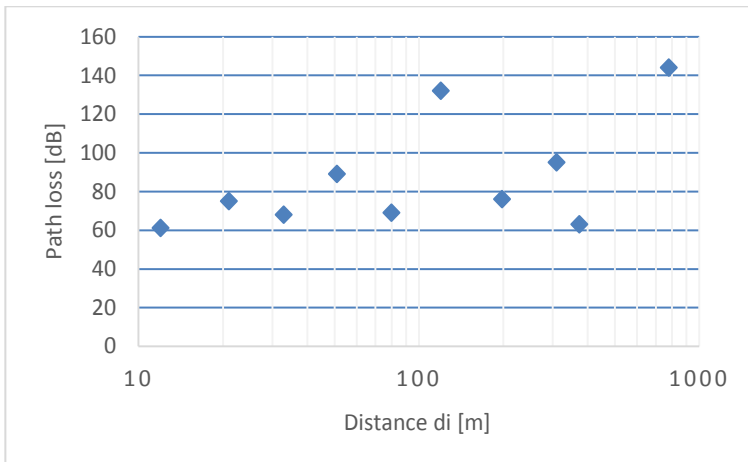


Fig. 1. Path Loss in Eldok region

The following figures show measured path loss for Eldok and Shubra regions. Related to path loss analysis and parameter adjustment, all the samples further than 10 meters from the transmitter were recorded. The path loss for Eldok and Shubra regions are shown in Fig. 1 and Fig. 2, respectively.

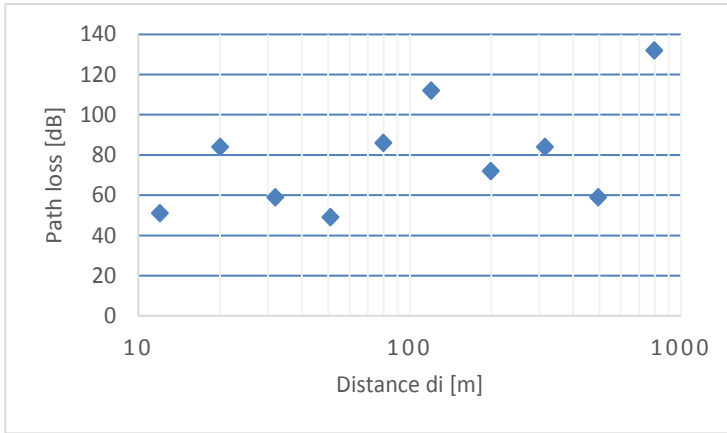


Fig. 2. Path Loss in Shubra region

3 Calculation of path loss by regression

By taking into consideration the regression analysis of the measured values, the following models are obtained to evaluate the path loss in Eldok and Shubra zones:

Linear model Eldok: $PL = 0,074 d + 72,554$ (2)

Shubra: $PL = 0,059 d + 66,284$ (3)

Exponential model: Eldok: $PL = 72,471e^{0,0007d}$ (4)

Shubra: $PL = 65,305 e^{0,0007d}$ (5)

Logarithmic model: Eldok: $PL = 11,763 \ln d + 33,403$ (6)

Shubra: $PL = 10,11 \ln d + 32,312$ (7)

4 Log-Normal Shadowing Model - determining Exponent n in Equation

A simple power law path loss model as in equation (1) was chosen for predicting the distance of a reliable communication between two mobiles.

Thus, in order to determine exponent n in equation (1), it was necessary to have a table of PL dependence on the distance d with the same step of quantity d.

Using linear regression analysis, the path loss exponent n, can be determined by minimizing (in a mean square error, sense) the difference between measured and predicted values of equation (1) to yield:

$$n = \frac{\sum_{i=1}^k [PL(d_i) - PL(d_0)]}{\sum_{i=1}^k 10 \log \left(\frac{d_i}{d_0} \right)} \tag{8}$$

where the term $PL(d_i)$ represents measured path loss and expression in brackets represents predicted path loss and k is the number of measured data or sample points. Distance $d_0 = 100$ m.

Attention must be paid to the difference between $PL(d_i) - PL(d_0)$, which is an error term with respect to n , and the sum of the mean squared error $\varepsilon(n)$. This error is given by the following equation:

$$\varepsilon(n) = \sum_{i=1}^k \left[PL(d_i) - \left(PL(d_0) + 10n \log\left(\frac{d_i}{d_0}\right) \right) \right]^2 = \sum_{i=1}^k [a + nb]^2 \tag{9}$$

where

$$a = PL(d_i) - PL(d_0) \tag{10}$$

$$b = -10 \log\left(\frac{d_i}{d_0}\right) \tag{11}$$

and

$$c = a + nb \tag{12}$$

Then

$$\varepsilon(n) = c^2 = a^2 + 2ab + b^2 \tag{13}$$

Then, we obtain the value of n by minimizing the Mean Square Error (MSE) by equating the derivative of equation to zero.

$$\frac{\partial \varepsilon(n)}{\partial n} = 0 \tag{14}$$

After derivation the following equation applies:

Eldok: $2.1132n - 6428 = 0$

Shurba: $2.1173,8n - 6646,5 = 0$

Therefore n is

Eldok: $n = 2,839$

Shurba: $n = 2,831$

The following figure presents the comparison of the evaluated values for urban area.

5 Conclusion

A comparison of the results of the Log-Normal Shadowing Model - equation (1) and the measured values is in the figures 3 and 4.

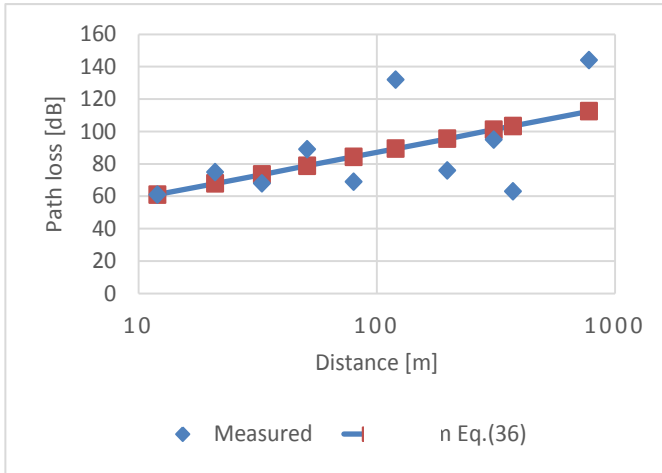


Fig. 3. Comparison of the results Eq.(1) and measured values - Eldok

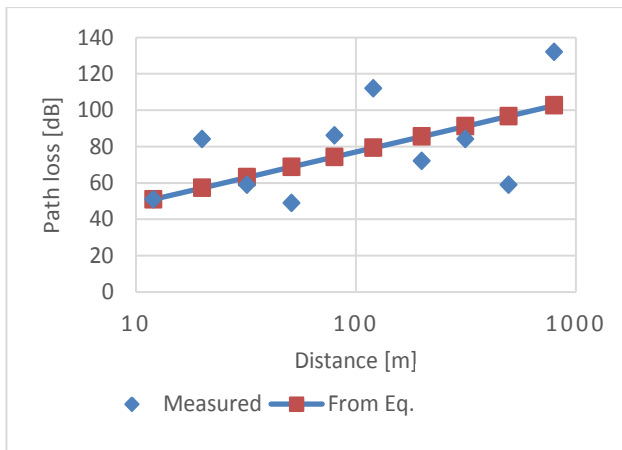


Fig. 4. Comparison of the results Eq.(1) and measured values - Shubra

By referring to the above calculations, we found that Eldok region perfectly suits the value of $n = 2.84$, and Shubra region suits the value of $n = 2.83$.

6 References

1. H. R. Anderson, Fixed Broadband Wireless System Design. John Wiley & Co., 2003.
2. M. Kumari, T. Yadav, et al “Comparative Study of Path Loss Models in Different Environments” IJEST, Vol. 3 No. 4, Apr 2011.

3. V.Erceg, K V S Hari, et al., “Channel models for fixed wireless applications,” tech. rep., IEEE 802.16 Broadband wireless access working group, Jan 2001.
4. Y. Zakaria, L. Ivanek, “Performance Evaluation of Channel Propagation Models and Developed Model for Mobile Communication”, American Journal of Applied Sciences, vol. 14, issue. 2, pp. 349-357, 2017.
5. Alam, Md et al. “Performance Evaluation of Different Frequency Bands of WiMAX and Their Selection Procedure”, International Journal of Advanced Science and Technology, vol. 62, pp. 1-18, 2014.
6. Y. Zakaria, L. Ivanek, “Propagation Modelling of Path Loss Models for Wireless Communication in Urban and Rural Environments at 1800 GSM Frequency Band”, International Journal of Advances of Electrical and Electronic Engineering, vol. 14, no. 2, pp. 139-144, June 2016.

The fiber-optic sensor as a detector of weak seismic waves

Stanislav Žabka

Department of Telecommunications, FEECS,
VŠB – Technical University of Ostrava, 17. listopadu 15,
708 33 Ostrava – Poruba, Czech Republic
stanislav.zabka@vsb.cz

Abstract. This article deals with the theme of the seismic fiber-optic sensor. The sensor is based on optical fibers and uses the principle of phase modulation of interfering radiation propagating inside the optical fiber caused by seismic waves (earthquake). The basic advantage of the presented solution against the conventional seismographic sensors is the possibility of implementing the sensor on the surface of the monitored environment. Also, this article summarizes the author's activities during two years of his study, his research and development activities related to the studies and research projects.

Keywords: optical fiber, web presentation, sensors

1 Introduction

Allow me to introduce myself. My name is Mr. Stanislav Zabka. I am a doctoral student at the Faculty of Electrical Engineering and Computer Science at the Technical University of Ostrava. My education program is called Computer Science, Communication Technology and Applied Mathematics and field of study called Communication Technology. I am also working (part-time job) as Java developer in big software corporation and I am using these skills to achieve the best results when it comes to create software which handles and computes big data from sensors. In my second year of study I am extending my knowledge in communication technologies, especially fiber-optical sensors. I am part of several projects from the field of fiber-optics especially focused on the detecting of weak seismic waves. To the date 7/2018, I have a total of 11 accepted or published publications and 2 utility models.

2 About my project and dissertation work

During the first and second year of my study, I was to design a measurement scheme and forms for the creation of FBG sensor which can be used to monitoring the electrical current. Also, I prepared a simulation of parameters of the prototype of the FBG sensor. Now I am working in the laboratory on practical tests which have given the first functional answers. Except this I worked on the project where I am focusing on created the software which handles and computes big data from the seismic fiber-optic sensor. Also, with my colleagues, we proposed a measuring sensor, please see Figures.

List of Reference tags:

1. Input interface 1
2. Output interface 2
3. Polymer housing
4. Single-fiber optical fiber
5. Optical coupler 1
6. Optical coupler 2
7. Sensor part of the sensor
8. Sensor detection side
9. Insulation part of the sensor

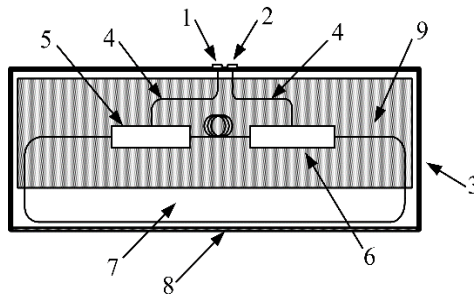


Fig. 1. The proposed basic scheme of the seismic fiber-optic sensor.

The sensor is based on optical fibers and uses the principle of phase modulation of interfering radiation propagating inside the optical fiber caused by seismic waves (earthquake). The resulting optical radiation intensity is proportional to the magnitude of phase change between light beams spreading through the interferometer. The output is represented in the voltage (which is proportional to the total output of the captured light - i.e. the phase). The sensor is designed to detect weak seismic waves within a wide range (up to 60 Hz). Seismic waves arise from any sudden deformation of the natural environment and may be caused, for example, by earthquakes, explosions, human activities and the like [1-2]. Figure 2 shows an example of a time recording representing the detection of vibration-acoustic waves caused by the human activity. Figure 3 represents a 3D spectrum of captured seismic waves caused by the human activity.

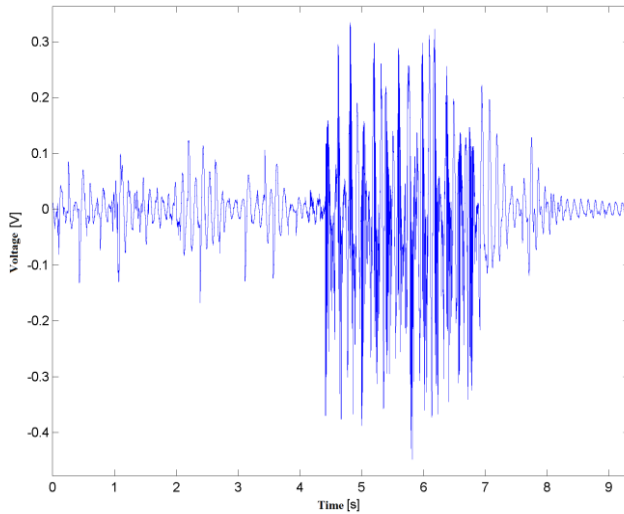


Fig. 2. Time recording representing the detection of vibration-acoustic waves.

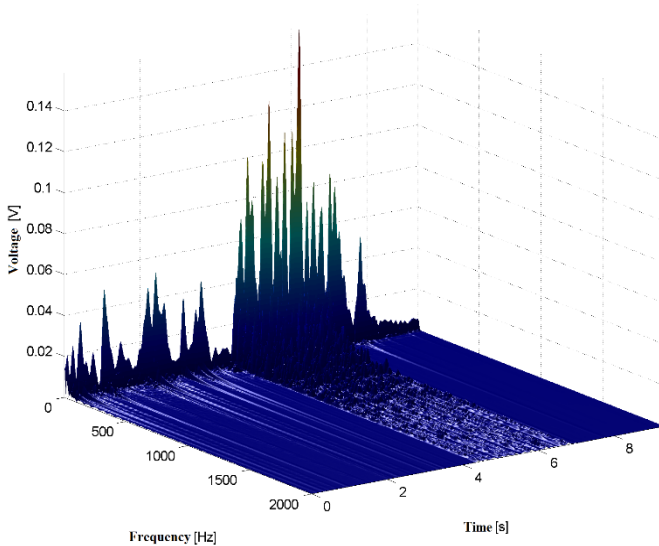


Fig. 3. Example of 3D spectrum of the captured seismic waves.

The basic advantage of the presented solution against the conventional seismographic sensors [3] is the possibility of implementing the sensor on the surface of the monitored environment, the sensor does not need to be implemented into the natural environment.

3 Projects

As part of my studies, I was actively involved in solving 3 projects, namely:

1. Measuring the weight of trash bins, while being lifted by truck: We were using optical fibers and sensor to detect deformation of fiber attached to lifting arm. We did many measurements to get reference values. Then I prepared software that calculates other missing values such as the weight of trash.
2. SGS SP2017/79 - New types of photonic systems for IoT.
3. SGS SP2018/184 - Optical communication technologies and sensors

4 Publications activities

From the date 9/2016 since to the date 8/2017, I have a total of 11 accepted or published publications and 2 utility models. As I mentioned above I am creating a software which handles and computes big data from sensors (medicine sensors, sensors for traffic, security, and etc.).

5 Pedagogic part and other activities at the Department of Telecommunications

In summer semesters, I was part of courses UDKT (Introduction to Communication Technologies). It should be for me a preparation for next semester, where I need to handle lessons by myself. I helped with preparation of class and leading students during their practical activities. I had to handle several devices that are part of laboratories for this subject.

6 Future work

In the third year of my study, I will be focusing on measurements with the proposed FBG current sensor. Also, I will be focusing on the projects, my doctoral thesis, and I will prepare 2 publications which will corresponding to the topic of my dissertation topic.

7 References

1. Pisco, M., Bruno, F.A., Galluzzo, D., Nardone, L., Gruca, G., Rijnveld, N., Bianco, F., Cutolo, A., Cusano, A., "Opto-mechanical lab-on-fibre seismic sensors detected the Norcia earthquake," (2018) *Scientific Reports*, 8 (1).
2. Reitano, D., Falsaperla, S., Musacchio, G., Merenda, R., "Awareness on seismic risk: How can augmented reality help," (2019) *Geotechnical, Geological and Earthquake Engineering*, 47, pp. 485-492.
3. Buchen, J., Marquardt, H., Speziale, S., Kawazoe, T., Boffa Ballaran, T., Kurnosov, A., "High-pressure single-crystal elasticity of wadsleyite and the seismic signature of water in the shallow transition zone," (2018) *Earth and Planetary Science Letters*, 498, pp. 77-87.

Use of a Flying Platform for Measuring of Electromagnetic Fields

Lukasz Miszuda

Opole University of Technology,
Faculty of Electrical Engineering, Automatic Control and Informatics,
Institute of Computer Science, Prószkowska 76, 45-758 Opole, Poland
lukaszmiszuda@wp.pl

***Abstract.** Nowadays, humans are surrounded by more and more devices that artificially generate an electromagnetic field. According to law, supervision of the level of the electromagnetic field requires specific measurements. Measurement performed by traditional methods have several limitations, which come from the infrastructure and time taken to perform the measurement. New methods of measurement are being developed in order to execute the research relatively quickly and repeatedly without any limitations. One of the methods is to use a flying mobile measurement platform.*

Keywords: electromagnetic field, flying platform, measuring

1 Introduction

Direct influence of the electromagnetic field on a human being may cause numerous threats to health or safety. A person who is within the electromagnetic field is exposed to the presence of a magnetic field and an induced electric fields caused by electrical currents flowing through the body.

In the body of a person exposed to such fields some biophysical effects of the following form may occur [8]:

- stimulation of nervous or muscular tissue (in the case of interaction of fields with frequencies not exceeding a few megahertz),
- increase in tissue temperature (in the case of interaction of fields with mega- or gigahertz frequencies),

Human beings usually are not able to feel the direct effect of the electromagnetic field on their organisms. According to studies [8], the effects of the electromagnetic field may have other consequences that can be revealed with a time delay, especially during strong exposures.

The influence of the electromagnetic field can also have an indirect impact on people, interpreted as contact currents that flow through the

human body touching a metal object that has a different electrical potential due to the electromagnetic field impact on it [8].

The effects of the indirect impact of the electromagnetic field can also be [8]:

- interference with electronic devices, including medical equipment, electronic implants (such as cardiac pacemakers) and medical devices for permanent wearing on the body (such as infusion pumps)
- a threat to the functioning of passive metal implants
- damage to magnetic storage media.

In the environment that surrounds us, the problem of measuring the electromagnetic field without restrictions coming from the infrastructure and various external conditions has not yet been solved. The generality of infrastructure is now a very big problem when performing an electromagnetic field measurement, because it is not possible to take measurements very close to the source of the electromagnetic field. The main sources of the electromagnetic field can be, for example: high voltage lines, which during transmission create around themselves an artificial EM field, transformer stations, mobile phone stations, RTV transmitters [8].

2 Measurement of the electromagnetic field

Nowadays, man cannot imagine life without electricity anymore. In the early years no one was thinking about the influence of the electromagnetic field and radio waves on living organisms. With time, however, an increasing number of people began to pay attention to the levels of electromagnetic radiation produced by a man, which more and more surrounds our communities [3]. According to the Act of 27 April 2001 - Environmental Protection Law (unified text Journal of Laws 2013, 1232 with subsequent amendments), electromagnetic fields are defined as electric, magnetic and electromagnetic fields with frequencies range from 0 Hz up to 300 GHz. The evaluation of electromagnetic field levels in the environment is carried out as part of the State Environmental Monitoring. The Voivodship Inspector for Environmental Protection conducts periodic studies of the levels of electromagnetic fields in the environment. The number of measuring stations, the type of areas on which measurements are carried out and their frequency is specified in the Regulation of the Minister of Environment of Novem-

ber 12, 2007 on the range and manner of conducting periodic tests of electromagnetic fields in the environment (Journal of Laws No. 221, item 1645). The regulation defines three basic categories of sites on which PEM monitoring should be carried out:

1. *Central districts of settlements or cities with a population of over 50,000*
2. *Other (smaller) cities,*
3. *Rural areas.*

For each of the above mentioned area categories there are selected 45 measuring points - a total of 135 points. Measurements at the selected points are repeated after each full, 3-year measurement cycle. Within one year, measurements are made in 45 points (15 per area category). Measurements at each point are performed once a year.

Detailed values of permissible intensity of radiation fields have been specified in the ordinance of the Minister of the Environment dated October 30, 2003 on the permissible levels of electromagnetic fields in the environment and ways to check compliance with these levels (Journal of Laws No. 192, item 1883). According to the Regulation, acceptable levels of electromagnetic fields have been designated for "sites dedicated for development" and "places accessible to the public" and refer to different ranges of field frequencies from 50 Hz up to 300 GHz.

From the point of view of environmental monitoring the most important aspect is the frequency range, which might be from 3MHz to 3000MHz. The permissible electromagnetic field intensity for a given range is $E = 7\text{V/m}$ for the electrical component and $S=0.1\text{W/m}^2$ for the power density. They are many times more stringent than the WHO recommendations and ICNIRP limits adopted by the EU (from 28 V/m to 61 V/m, depending on the frequency) [11].

The magnitude of measured values of electromagnetic field (PEM) intensities is the resultant of the number of sources and their power.

Performed measurements are carried out on the basis of legal regulations [9].

3 Mobile measurement of electromagnetic field

Currently, in times of rapid development of automation and its interference in various areas of our lives, also measurements of the elec-

tromagnetic field are carried out using it to a greater or lesser extent. The use of sensors placed on cars affects the availability of measurements. The sensor placed on the roof of a car is limited by environmental and technical conditions where the car can reach. (Fig. 1) Measurement can be performed relatively quickly and systematically, moving a given vehicle according to predetermined roads. The data transmitted by the sensor also have such parameters as the GPS network data so that the measurement results can be placed on the map and compared with measurements made at another time, in the same place.



Fig.1 Vehicle with a sensor placed on the roof [4]

The next step towards a greater automation of the measurements of the electromagnetic field is the use of a flying platform, under which the sensor were mounted. Currently manufactured sensors, from a technical point of view, can be placed on flying platforms. Performing measurements using a flying platform is the solution to one of the currently unresolved problems, which is the lack of barriers related to the availability of the area. The flying platform has unquestionable freedom of movement in the field. Unpaved roads or places which cannot be reached by a car are no longer a problem. The flight route can be planned in advance and performed without the direct presence of the person supervising the flight. As a result, the “pilot” is not exposed to the fields being measurement. Measurements can theoretically be per-

formed without time limits 24h/365 days. The only limitation are the weather conditions. The sensor moving on the platform has one more advantage, it has the ability to catalog a large area within a relatively short time. Due to this, the measurement performed in a dozen of defined points for each area can be extended to a much larger number of measuring points, thus increasing the quality of the measurement.

The measurements of the intensity of the electromagnetic field plays an important role in relation to the conducted research on the implantation of the electromagnetic network and phone transmitters in close proximity to residential buildings and the influence of the intensity of the electromagnetic field on living organisms.

According to the concept of mobile network systems, the entire field handled by a given network is divided into areas ("cells") presented on propagation maps with the use of hexagons including base transceiver stations (BTS) located in the center. The communication between a moving cell phone user in the most popular GSM 900 network and the base station takes place in the 890-915 MHz bandwidth and between the base station and phone - in the 935-960 MHz bandwidth. Individual "cells" may possess a diameter from a few hundred meters in office centers up to more than a dozen kilometers in areas of a low population density. This means that in large urban agglomerations in order for a network to work properly it requires the functioning of 30-50 base stations which, taking into consideration the presence of three providers on the market (plusGSM, EraGSM, and Idea Centertel), results in a quite vast number of radiation sources.

The configuration of a base station depends on its purpose and location. In cities, sector antennas are usually installed in such a manner so that the main radiation beams are directed in three or four directions, thus ensuring an almost even cover of the entire cell in terms of the radio signal. In terms of base stations located in rural areas as well as near the main road and railroad trails, sector antennas are installed on lattice or concrete-steel towers (photos 1 and 2), and directed at one or two azimuths. It also sometimes happens that some stations include omni-directional radiation antennas.

4 Conclusion

The use of flying platforms to perform measurements of the electromagnetic field is a very good alternative to traditional methods. Thanks to UAV, it is possible to carry out measurements on a larger area in a much shorter period of time. The measurement is not limited by infrastructural barriers, therefore the measurement can be made close to the source of the electromagnetic field. The measurement route, once planned, can be repeated several times in different periods to make the analysis more transparent. By applying colors to the measurement results you can quickly determine how the intensity of the electromagnetic field changes at a given point. The basic advantage of the measurement based on the autonomous unit is the ability to perform measurement of the fields distribution for the magnetic and electrical components. Thanks to the point measurement of the area, it is possible to generate a spatial grid of the fields distribution, which has been difficult so far.

The flying unit is able to study points that were previously unattainable. It would be advisable to use many UAV units controlled by the "Boids" algorithm, which would allow to make measurements with a high density of measurement points [1;2].

5 References

1. Beni G., Wang J.: Swarm Intelligence, Proceedings of the Seventh Annual Meeting of the Robotic Society of Japan, pp. 425-428, RSJ Press, Tokyo, 1989.
2. Eberhart R., Kennedy J.: Particle swarm optimization, Proceedings of the International Conference on Neural Network, pp. 1942-1948, 1995.
3. Kasprzyk R., Butlewski R., *Pole elektromagnetyczne jako czynnik szkodliwy w przemyśle elektroenergetycznym*, Zeszyty Naukowe Politechniki Poznańskiej. Organizacja i Zarządzanie” 2013 ; nr 59
4. <http://www.wavecontrol.com/rfsafety/en/> (available: 16.05.2018).
5. http://www.wios.lodz.pl/Monitoring_promieniowania_elektromagnetycznego_PEM,38 (available: 20.04.2018).
6. <https://www.piiit.org.pl/wazne/pem> (available: 10.05.2018).
7. Tomczykowski J.: Sieci energetyczne pięciu największych operatorów. Energia Elektryczna nr 5/2015, s. 23-25.
8. <http://archiwum.ciop.pl/26003.html> (available: 3.03.2018).
9. http://www.opole.pios.gov.pl/wms/Pliki/2017/Ocena_wynikow_pomiarow_monitoringowych_PEM_za_rok_2016.pdf (available: 21.02.2018).
10. <https://www.aspen-electronics.com/wcrange.html>(available: 10.04.2018).
11. <http://www.who.int/mediacentre/factsheets/fs193/en/> (available: 10.04.2018).

Spectral analysis of high-voltage lines surroundings

Jakub Osuchowski

Opole University of Technology,
Faculty of Electrical Engineering, Automatic Control and Informatics,
Institute of Computer Science, Prószkowska 76, 45-758 Opole, Poland
jakub.osuchowski@gmail.com

Abstract. The purpose of the work is to outline problems related to the multi-spectral analysis of the environment of the power line. In addition, the article contains a spectral data description. An important element of the article is presentation of spectral data analysis methods. A review of the possibilities of spectral image acquisition for the need of power line diagnostics is also presented.

Keywords: Power Line, Image Recognition, Image Processing, Multispectral Imaging.

1 Introduction

Maintenance and vegetation control of several hundreds of kilometers of power line is time-intensive and very expensive. For this purpose the spectral satellite images can be used. The use of this kind of data makes inspection of high-voltage lines faster and more accurate, but unfortunately these pictures are quite difficult to analyze. The last few decades have seen a surge in the significance of electrical energy in the economy and society as a whole. With that surge grew the requirements concerning the continuity of power supply. As all technical objects, power lines are subject to the ageing process and failures, which are a natural result of their exploitation. In order to ensure continuous supply of energy, operators of an electrical grid are obliged to make regular preventive inspections, whose main goal is to evaluate the technical condition of power lines. Due to the specificity of transmission infrastructure (vast area, complex structure, exposure to various forms of impact etc.), this is a complicated and time-consuming task requiring expert knowledge and the application of suitable technical measures. The development of various machine vision technologies for the observation of public space and conservation of various objects, accompanied by a rapid growth of communication systems, create premises for their broad application in

power engineering [1], [2], [3], [4], [5] in combination with the computer image analysis technology. Comprehensive recognition of the state of infrastructure objects visible in digital images allows for a broad spectrum of potential applications, such as precise measurement of the position of the structural components of power lines, monitoring that supports emergency population warnings or, indeed, regular maintenance checks and localization of damage to transmission and distribution networks. Spectral data can be considered as a 3d matrix (cube), where X and Y are length and width and λ is the length of the light wave [6]. An example of a spectral cube is shown in Figure 1.

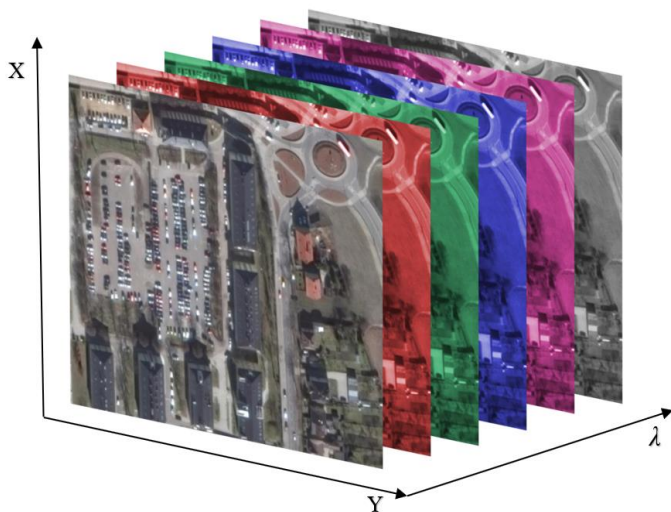


Fig. 1. Spectral cube example

Spectral data for the diagnosis of high voltage power lines can be obtained in two different ways. From the flight (helicopter or drone) or using the satellite. Using satellite images, larger groups of objects can be identified and analyzed.

2 Acquiring multispectral images for diagnostic purposes

One of the ways to create databases for remote sensing systems are satellite images. The satellite image is a photography of a part of the Earth's surface registered by the satellite. Its main advantage are small geometrical distortions. Using satellite images, you can identify larger groups of objects, such as land use forms. Satellite images are registered in the so-called an optical window, or spectrum of electromagnetic waves,

transmitted through the Earth's atmosphere. A pioneer in the field of constant observation of the terrestrial globe was the American system called Landsat. This system is currently operational, and the entire Landsat program has eight versions of the satellites. The main instruments on board the satellite are Operational Land Imager (OLI) and Thermal InfraRed Sensor (TIRS). They enable the surface of the Earth to be imaged with a resolution of up to 30 m in visible and near infrared light, up to 100 m in thermal (medium) infrared and obtaining panchromatic images with a resolution of 15 m. The channels recorded by the Landsat 8 satellite are shown in Table 1.

Table 1. Spectral channels recorded by the Landsat 8 satellite.

Channels	Wavelength (μm)	Resolution (m)
1 - Ultra Blue	0.435 - 0.451	30
2 - Blue	0.452 - 0.512	30
3 - Green	0.533 - 0.590	30
4 - Red	0.636 - 0.673	30
5 - Near Infrared	0.851 - 0.879	30
6 - SWIR 1	1.566 - 1.651	30
7 - SWIR 2	2.107 - 2.294	30
8 - Panchromatic	0.503 - 0.676	15
9 - Cirrus	1.363 - 1.384	30
10 - Infrared 1	10.60 - 11.19	100
11 - Infrared 2	11.50 - 12.51	100

The effects of the Landsat system are one of the most commonly used satellite images in the world. Nevertheless, the termination of the program is being talked about more often due to the emergence of more effective and accurate satellite imaging systems. However, this system has certainly set a new direction in the development of satellite programs for the purpose of observing the Earth's surface and analyzing the collected data [7].

3 Methods for spectral data analysis

Spectral data are usually subjected to a variety of computer operations. Four groups of processing methods can be separated. The first of these is pre-filtration, which allows to remove distortions and interference and is also used for image calibration. Initial image corrections can be divided into radiometric and geometric corrections. Radiometric correction is done to reduce or correct errors in the digital numbers of images.

The process improves the interpretability and quality of remote sensed data. Radiometric calibration and correction are particularly important when comparing data sets over a multiple time periods. The energy that sensors onboard aircrafts or satellites record can differ from the actual energy emitted or reflected from a surface on the ground. This is due to the sun's azimuth and elevation and atmospheric conditions that can influence the observed energy. Therefore, in order to obtain the real ground irradiance or reflectance, radiometric errors must be corrected for. Geometric corrections consist in removing image distortions caused by the motion of the imaging sensor and fitting the image in the desired coordinate system from the user's point of view [8].

The second group of methods is strengthening of the mapping, which include: contrast enhancing, color compositions creating and digital filtration. Strengthening the contrast of the image increases its visual interpretation. However, since it involves modifying the original registered pixel brightness, the image after this operation can not be used in the classification process. The combination of three spectral channels, recorded in the appropriate bands of electromagnetic radiation, gives the opportunity to create so-called composition of colorful satellite images. Color compositions are often used as the primary source of information about the depicted area. Color compositions enable easier recognition of terrain objects thanks to their colors and their tones, instead of shades of gray [8].

The third group are classification methods. Classification is a process in which the interpretation of images is carried out in a semi-automated manner, using a computer system. In the automatic classification of spectral images algorithms such as the Support Vector Machine (SVM) are often used. Thanks to the use of this algorithm, it is possible to detect many threats to high voltage lines such as: dangerous human activity, groundwater, diseased trees, poor ground quality etc.

An example of an operation from an image transformation group can be, for example, transformations called vegetation indexes [9], [10]. It has the following form, and the image of high voltage line obtained thanks to these transformation is shown in Figure 2.

$$NDVI = \frac{NIR - RED}{NIR + RED}$$

Where: NIR - infrared channel, RED - red channel.

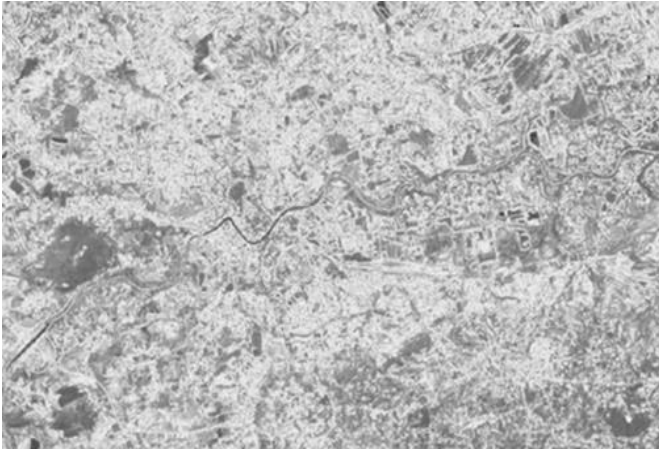


Fig. 2. Normalized Differential Index of Vegetation.

The image of the vegetation index can be interpreted in such a way that the higher the value of this index, the larger is the biomass existing in a given place.

4 Conclusion

Early detection of overhead line insulators failures is critical to avoid costly downtimes of whole high voltage power line. Spectral data has a very wide spectrum of applications and numerous methods for their analysis. Spectral imaging, UAV vehicles or satellites and digital image processing methods may be in the future used to create complete and autonomous systems for identification of threats to high-voltage lines resulting from its immediate environment.

5 References

1. Zator, S., Michalski, P., Lasar, M.: Linking chromatic images with spatial data. PAK, vol. 11, pp. 962-964. (2012)
2. Zator, S., Michalski, P.: Pomiar zmian topologii obiektów na podstawie wyznaczania parametrów położenia markerów. PAK, vol. 12, pp. 1480-1482. (2011)
3. Tomaszewski, M., Krawiec, M.: Detection of linear objects based on computer vision and Hough transform, *Przegląd Elektrotechniczny (Electrical Review)*, vol. 88 10b (2012)
4. Osuchowski, J.: Insulator detection based on hog features descriptor, *Przegląd Naukowo-Metodyczny Edukacja dla Bezpieczeństwa*, vol. 34, pp. 1176-1186, (2017)
5. Zator, S., Gasz, R.: A analysis of the geometry HV power line uploaded with used high resolution images. PPM pp. 127-130 (2014)

6. Frank M., Pan Z., Raber B., Lenart C.: Vegetation management of utility corridors using high-resolution hyperspectral imaging and LIDAR, 2nd Workshop on Hyperspectral Image and Signal Processing, pp. 3-6, (2010)
7. John F. Bolton, Full spectral imaging: a revisited approach to remote sensing, „Proceedings of SPIE”, International Society for Optics and Photonics, (2004)
8. Krukar M., Przygotowanie zdjęć satelitarnych i darmowych baz danych do analizy wielospektralnej w programie ILWIS
9. Matikainen L., Lehtomäki M., Ahokas E., Hyyppä J., Karjalainen M., Jaakkola A., Kukkoa A., Heinonen T., Remote sensing methods for power line corridor surveys, ISPRS Journal of Photogrammetry and Remote Sensing”, vol. 119, pp. 10-31, (2016)
10. Bunting, P., Lucas, R.: The delineation of tree crowns in Australian mixed species forests using hyperspectral Compact Airborne Spectrographic Imager (CASI) data. Remote Sensing of Environment, 101(2), pp. 230–248, (2006)

Analysis of Improvement in Reaction Time With Prolonged Use of Android System Devices

Agnieszka Rozanska

Opole University of Technology,
Faculty of Electrical Engineering, Automatic Control and Informatics,
Institute of Computer Science, Prószkowska 76, 45-758 Opole, Poland
a.rozanska92@gmail.com

Abstract. In this paper author describes advantages and disadvantages of prolonged use of devices with an Android operating system. Reaction time of volunteers is properly tested with an application implemented in Java in Android Studio. Application created in this study was made specifically for these tests. Quantitative study revealed many advantages about prolonged use of Android devices.

Keywords: Android · reaction time · Java.

1 Introduction

Android is a mobile operating system created in California in 2003 and it was called Android Project. Developers intended to create advanced system for digital cameras, but later on the project evolved into an operating system for a prototype phone, that was running a pre-release version of Android system, called Sooner [1]. In 2005 Google bought Android Inc. for at least \$50 million [2] with its key employees and it was being developed by Google ever since.

Android is based on Linux kernel and open source software to minimize costs of creating this operating system. It is designed specifically for devices with touchscreen, such as tablets and smartphones. In 2005, Google developed Android system for devices, e.g. cars and even watches. There are many other variants of the Android operating system and these are used commonly on game consoles, digital cameras and PCs and such variety is available thanks to the Android open source project that lets people use core code of Android operating system to create something on their own [3]. Core code of Android system is licensed under the Apache License. Android is the most popular OS on smartphones since year 2011, and on tablets since 2013. As of June 2018, the Google Play store features over 3.3 million applications and games [4].

2 Quantitative study

This chapter includes information about the acquisition process of reaction time data while interacting with an Android system device. A description of the test setup is given below.

Setup for recording reaction time data of people was done by implementing and installing application created specifically for this study. Application was developed using Android Studio and was installed on following Android devices: devices from Samsung Galaxy series Note, S8 and S9, MyPhone Infinity series and Lenovo devices. The developed application was running as a background process on a smartphone and was sending a reminder twice a day for ten days at the same time 10:00 AM and 07:00 PM to play a simple game of tapping a red dot five times on a screen as fast as the person could. Screenshot of the game is presented in Fig. 1. Game was optimized to be playable on every smartphone, with attention to the MyPhone Infinity series, because of the lowest parameters of all of the devices available at this study.

Seven people took the tests and they were asked to do a single task twice a day for ten days. The implemented application showed a red circle at random location on the screen without using 5% of the screen counting from the border of it, because the red dot will not be fully visible otherwise. At this moment timer starts to count down the time in milliseconds. The person has to tap the red button and the time between showing the red dot and person tapping is saved. After three seconds, another red dot is shown at other random location on the screen.

After taking all of the measurements, whole file with all of the time measured in milliseconds is saved as a *.txt file format with a persons ID number from 1 to 10, day when the reaction time is measured and hour of measuring. Acquired data is collected and presented in Table 1 below. Columns show every person that agreed to take part in the study, and rows contain the day of the measurements. Each single person has two measured times for each day first measurement is for 10:00 AM and second 07:00 PM. Last row, called Difference, is for showing difference between the first and the last day of acquired data. The positive value of the difference means positive learning resulting in better reaction time. This data is discussed in the Results section.

3 Results

As seen on the Table 1, at the beginning of the test most of the participants were able to click on the dot with reaction time between 300-450 milliseconds on average value. From the first day to the day four, participants didn't show much progress in shortening reaction time, but after fourth day there is a visible progress. After everyday usage of the implemented application, majority of testers were able to shorten their reaction time, and the overall results are shown in the last line of the Table 1.

4 Conclusion

In this paper author described an analysis of users reaction time. Proper testing procedure for this study and results were given. This research may be useful

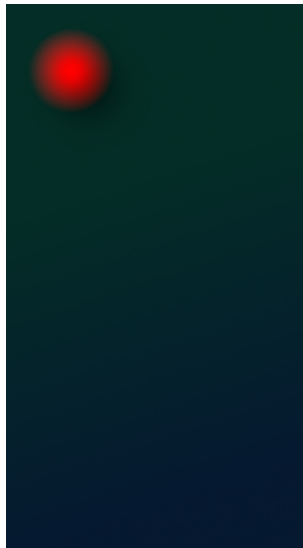


Fig. 1. Screenshot of an application developed for the study. The GUI of the application was created full-screen on the smartphone to prevent errors by tapping for example on return button

Table 1. Time measurement results in milliseconds.

Day/Person	01	02	03	04	05	06	07
Day 1	238/220	361/327	336/324	363/335	375/421	384/359	479/415
Day 2	236/251	278/224	389/411	226/271	362/395	388/372	351/332
Day 3	239/233	335/428	395/403	245/229	368/374	395/413	369/327
Day 4	217/225	376/322	412/342	271/200	455/397	352/331	389/327
Day 5	162/167	354/316	358/349	225/217	410/338	371/333	310/319
Day 6	203/174	338/329	324/355	241/226	487/442	324/310	285/224
Day 7	171/189	286/288	227/213	205/133	406/336	395/362	300/289
Day 8	164/168	264/225	248/229	271/284	441/496	354/362	221/287
Day 9	159/155	269/210	269/210	259/226	457/392	334/320	269/342
Day 10	162/166	244/213	196/225	243/280	443/398	359/306	288/219
Difference	76/54	117/96	140/99	120/55	-68/23	25/53	191/196

for readers willing to understand how helpful everyday usage of Android smartphone can be in the decrease of reaction time. The goal of authors research is to show positive aspects of everyday use of a smartphone with an Android system. The study revealed that the majority of the volunteers were able to learn to have better response time. Lower differences in some of the testers can be explained in many ways, e.g. that these people could be in worse health condition, had hard days at work, etc. and these aspects can have a huge impact on the results. The future work involves a research on the field of natural Human-Machine Interaction. Research will include optimizing interface [5] of the tablet of humanoid robot Pepper [6].

References

1. Android central: Google Sooner prototype appears, shows off one Googles first prototype builds of Android, <https://www.androidcentral.com/google-sooner-prototype-appears-shows-one-googles-first-prototype-builds-android>. Last accessed 20 Aug 2018
2. NY Times: A Murky Road Ahead for Android, Despite Market Dominance, <https://www.nytimes.com/2015/05/28/technology/personaltech/a-murky-road-ahead-for-android-despite-market-dominance.html>. Last accessed 23 Aug 2018
3. Google: Welcome to the Android Open Source Project!, <https://source.android.com/>. Last accessed 23 Aug 2018
4. Statista: Number of Google Play Store apps 2018, <https://www.statista.com/statistics/266210/number-of-available-applications-in-the-google-play-store/>. Last accessed 21 Aug 2018
5. Raska A., Podpora M.: Making eye contact with a robot exploring user experience in interacting with Pepper, in: Hunek W., Paszkiel Sz.: Biomedical Engineering and Neuroscience, Proceedings of the 3rd International Scientific Conference on Brain-Computer Interfaces, Advances in Intelligent Systems and Computing book series (AISC, volume 720), Springer, pp. 172-183, 2018, DOI: 10.1007/978-3-319-75025-5
6. SoftBank Robotics: Find out more about Pepper, <https://www.ald.softbankrobotics.com/en/cool-robots/pepper/find-out-more-about-pepper>. Last accessed 19 Aug 2018

Crypto Mining Energy Consumption Problem

Sławomir Szymocha

Opole University of Technology,
Faculty of Electrical Engineering, Automatic Control and Informatics,
Institute of Computer Science, Prószkowska 76, 45-758 Opole, Poland
slawekszymocha@gmail.com

Abstract. In his article the author presents the problem of huge demand for electricity needed by the new market related to cryptocurrencies. The development of this area has initiated an sales avalanche of equipment to be used as so-called "Diggers". Every kilowatt used by this type of device has the goal to bring a definite profit to the owner. However, due to the fact that the ratio of the "prize" to the amount of energy absorbed is very variable, the final effect cannot be determined. The devices used to maintain the network of cryptocurrencies are very often not designed for such purpose, which means that a very large part of energy is dissipated in the form of heat. The multiplicity of the demand for energy needed to maintain a whole network of cryptocurrency can be compared to the energy needs of some countries. The author proposes to use renewable energy sources to power the distributed network of nodes. The surplus energy of photovoltaic devices can be used for cryptocurrency mining purposes.

Keywords: Crypto Mining, Energy Consumption, Crypto Mining Network,

1 Introduction

One of the main assumptions for the development of electronic circuits is their evolution. By this concept we understand miniaturization, reduction of energy consumption and increase of computing possibilities. The increase in the number of our world's population results in a continuous growth in electricity demand. In order to meet this phenomenon, producers try to make devices with a lower consumption of electricity. Each of these devices performs a specific activity by absorbing a fixed dose of electricity. The popularisation of crypto-currencies caused a devaluation of the relationship between the energy expenditure and the result obtained. So-called "miners" by performing on their devices a predetermined sequence of mathematical operations wanting to obtain a certain digital value. [1] The amount of the reward that will be granted

to a "miner" depends on the number of operations that it can carry out within an hour, and on the number of people participating in a given moment. Mathematical operations of this type can be performed on various types of devices, starting from specialized integrated circuits, designed for such purpose stationary computers and ending with single-plate raspberry PI computers. [2]

2 Energy consumed by cryptocurrency network devices

Along with the price increase in cryptocurrencies, the number of people willing to make money from them increased. A significant part of the interested parties decided to independently "extract" the electronic currency. The easiest way to do this was to use already existing equipment or purchase a new one, usually advanced graphics cards. [2] The increase in the popularity of cryptocurrencies was the same as the increase in energy demand in the given time (Fig 1) [3]



Fig. 1. Bitcoin Energy Consumption chart [3]

This trend is still maintained, the demand is constantly growing in line with the energy expenditure of countries or global credit card systems. (Fig 2) [3]



Fig. 2. Bitcoin network versus VISA network average consumption [3]

The ever-increasing demand for energy designed for bitcoin networks is currently 52 TWh, which exceeds the demand of Portugal, Peru and Ireland. Keeping this trend in July 2019 will outstrip the demand in the United States of America. [4] One transaction absorbs around 460.27 of carbon dioxide, and the trend is increasing. Most of the large mines are powered by power grids connected to coal-fired power plants, e.g. in China. [3]

Another important aspect is the maladjustment of traffic loads to the existing electricity grid. The increase in the energy demand in some regions has doubled. Adding new devices to the grid can cause overloading and increase the risk of its failure. This is very noticeable in areas where the network grid is very old or poorly developed. [5] In the most critical phase this may lead to an avalanche effect. [6] If you consider a micro scale, a home or factory installation may fail, if an unaware user starts to connect high-power devices by himself. Often, due to the lack of professional literature on the construction of devices designed for cryptocurrency mining, knowledge on this subject is obtained from online guides. Instructions of this type very often omit issues related to safety and protection against electricity shocks, fire or the correct working conditions of such devices. [7]

It is possible to successfully use existing prosumer micro installations to supply network nodes. It is necessary to take into account the off grid zone units or installations which do not use their full energy Potential. Excess energy which cannot be used for own needs or cannot be sold can be used to supply specific equipment. The device will start generating profits even if will be work by several hours a day. Installation consisting of a panel, a battery, charging regulator and weather sensors can be successfully fitted with a copying unit. (Fig. 3) It is very important to pay attention to the time in what the PV installation produces redundant energy. The designated times will be the times of the copying device.



Fig. 3. Air measurement unit with cryptocurrency mining machine (uP PC) [9]

3 Conclusion

Users of the cryptocurrency network very often make alterations to electric installations or ICT infrastructure without proper knowledge. Lack of technical knowledge very often ends up with accidents and equipment damage. [8] Cryptotransaction is a very young technology, which needs to be optimized in many aspects. Special attention should be paid to the hardware layer, the devices used for cryptocurrencies absorb huge amounts of electricity. Each MWh used means, that 823,257 kg of CO₂ has been emitted into the atmosphere [9], thus devices adapted to work with cryptocurrencies networks should be used. It is necessary to design the system and software so that its efficiency is as large as possible. It may be advisable to use renewable energy to power devices using the cryptocurrency network. This will

reduce the traffic load on the power grid and the risk of overload failure. The author's design demonstrates the possibility of managing the excess energy obtained from the solar powered measurement unit for the purpose of supplying the cryptocurrency network device. This treatment allows you to take full advantage of the energy possibilities of the power system, thus reducing the costs and production of CO₂ into the air.

4 References

1. MIRZAYI S. MEHRZAD M.: Bitcoin, An SWOT Analysis, 7th International Conference on Computer and Knowledge Engineering, 2017
2. Prometheus MMS, Be a BITCOIN Millionaire: Beginner to master, Bitcoin Energy Consumption Index <https://digiconomist.net/bitcoin-energy-consumption> [access: 22.04.2018]
3. Bitcoin's electricity consumption problem; <https://www.drax.com/technology/bitcoins-electricity-consumption-problem/> [access: 22.04.2018]
4. McGraw Hill Education, Electrical Power Distribution: Case Studies from Distribution Reform, Upgrades and Management (DRUM) Program; Pvt Ltd, 2012 – 264
5. JIAN G. L., XINZHOU D., XINGYING C., XIANGQIAN T., XIAOQING Z., SHIMING X.: Fault Location and Service Restoration for Electrical Distribution Systems; John Wiley & Sons, 28 mar 2016 – 256
6. MILLER R.: Fire at Bitcoin Mine Destroys Equipment; Nov 06, 2014; <https://gizmodo.com/a-huge-fire-took-out-a-bitcoin-mining-operation-1655981855>; [access: 22.04.2018]
7. Bitcoin mining causes huge fire in block of flats: Eight apartments destroyed in Russia; <http://bitcoin-newswire.com/2018/02/09/bitcoin-mining-causes-huge-fire-in-block-of-flats-eight-apartments-destroyed-in-russia-world-news/> ; [access: 22.04.2018]
8. Raport KOBiZE; WSKAŹNIK I EMISYJNOŚCI CO₂ DLA ENERGII ELEKTRYCZNEJ U ODBIORCÓW KOŃCOWCH , na podstawie informacji zawartych w Krajowej bazie o emisjach gazów cieplarnianych i innych substancji za 2014 rok
9. Own study

Author Index

- Andrešič, David, 178
- Bača, Jakub, 57, 63
Bailová, Michaela, 190
Baleja, Richard, 1
Běčák, Petr, 7
Běloch, Michal, 196
Bilík, Petr, 135
Blažek, Vojtěch, 13
Borová, Monika, 98
- Cigánek, Jiří, 21
Cigánková, Barbora, 178
- Dhar, Anirban, 240
Dočekal, Tomáš, 104
- Foltyn, Ladislav, 201
- Golembiovský, Matěj, 112
- Hajduk, Peter, 235
Halfar, Radek, 118
Harach, Tomáš, 69
- Chamrád, Petr, 63
Chlebiš, Petr, 92
- Ivánek, Lubomír, 265
- Jahan, Ibrahim S., 27
Janečko, Tomáš, 165
Janošová, Karolína, 123
Jaroš, René, 129
- Klein, Tomáš, 75
Kolář, Jakub, 240
Kolařík, Jakub, 135
Kořený, Martin, 81
Kouřil, Daniel, 63
Kovář, Petr, 230
Kravčenko, Michal, 230
Krbeček, Matěj, 230
Kubesa, Michael, 230
Kučera, Radek, 207
- Látal, Jan, 240, 259
Lazecký, David, 33
- Machů, Tomáš, 39
Martinek, Radek, 129, 135
Miszuda, Łukasz, 276
Mišák, Stanislav, 27
- Novák, Martin, 246
Novák, Tomáš, 1, 7
Novosád, Ladislav, 45
- Oczka, David, 142
Ondraczka, Tomáš, 147
Osuchowski, Jakub, 282
Ožana, Štěpán, 104
- Pacholek, Jan, 207
Paláček, Stanislav, 213
Petružela, Michal, 13
Praužek, Michal, 98, 123
Przeczek, Samuel, 86
- Raiman, Tom, 219
Rozanska, Agnieszka, 288
- Seroiszka, Petr, 51
Silber, Adam, 230
Šimkanič, Radek, 171
Sokanský, Karel, 1, 7
Stratil, Tomáš, 252
Strossa, Jan, 92
Szymocha, Sławomir, 292
- Šaloun, Petr, 178
Škovránek, Jiří, 153
Štefanský, Jakub, 135
- Urbanczyk, Tomáš, 159
- Vašínek, Vladimír, 235, 252
Vitásek, Jan, 252
Vrtková, Adéla, 224
Vysocký, Jan, 13
- Wilček, Zdeněk, 240, 259
- Zakaria, Yahia, 265
Zatloukal, Filip, 184
Závada, Jakub, 230
- Žabka, Stanislav, 271

Editors: Michal Krátký, Jiří Dvorský, Pavel Moravec
Dept. of Computer Science
VŠB – Technical University of Ostrava

Title: WOFEX 2018

Place, year, edition: Ostrava, 2018, 1st

Page count: 310

Edit: VŠB – Technical University of Ostrava,
17. listopadu 15, 708 33 Ostrava-Poruba
Czech Republic

Impression: 200

Not for sale.

ISBN 978-80-248-4206-6